# Single and Multi-Exciton Dynamics in Nanoscale Semiconductors

by

Colby Peyton Steiner

B.S. in Chemistry
University of California at Berkeley, 2010

Submitted to the Department of Chemistry
in Partial Fulfillment of the Requirements for the Degree of

DOCTOR OF PHILOSOPHY IN PHYSICAL CHEMISTRY
at the
MASSACHUSETTS INSTITUTE OF TECHNOLOGY

June 2016



Signature of Author: .....
Department of Chemistry
May 3, 2016

Certified by: .....
Keith A. Nelson
Haslam & Dewey Professor of Chemistry
Thesis Supervisor

Accepted by: .....
Robert W. Field
Haslam & Dewey Professor of Chemistry
Chairman, Departmental Committee on Graduate Students

This doctoral thesis has been examined by
a Committee of the Department of Chemistry as follows:

Professor Robert G. Griffin .....
Chairman, Thesis Committee
Professor of Chemistry

Professor Keith A. Nelson .....
Thesis Supervisor
Haslam & Dewey Professor of Chemistry

Professor Moungi G. Bawendi .....
Thesis Committee Member
Lester Wolfe Professor of Chemistry

# Single and Multi-Exciton Dynamics in Nanoscale Semiconductors

by

Colby Peyton Steiner

Submitted to the Department of Chemistry
on May 3, 2016, in partial fulfillment of
the requirements for the degree of
Doctor of Philosophy in Physical Chemistry.

## Abstract

Recent advancements in the synthesis and fabrication of nanoscale semiconductors and optoelectronic devices are revolutionizing an array of industries. Nonlinear spectroscopy is a powerful tool for studying the unique optical and electronic properties of these semiconductors. This thesis describes experiments using a unique multi-dimensional spectrometer to study three semiconductors: double-walled J-aggregate nanotubes, cuprous oxide, and monolayer transition metal dichalcogenides.

First, we use two-dimensional correlation spectroscopy and cryogenic tunneling electron microscopy to correlate the excitonic and structural properties of J-aggregate nanotubes in solution. We observe weak coupling between inner and outer wall excitons in both isolated and bundled nanotubes. We also use two-dimensional rephasing spectroscopy to measure the homogeneous and inhomogeneous linewidths in solution at 295 K and in a glass at 10 K and determine dynamic and static disorder dominate, respectively. In addition, we observe photo-induced damage and recovery of nanotubes in the solid state.

Quantum process tomography is used to unambiguously elucidate the single-exciton dynamics of J-aggregate nanotubes in solution. Inversion of spectroscopic signals from eight transient grating experiments completely characterizes the time evolution of the single-exciton density matrix by determining the process matrix. We confirm the weak coupling of inner and outer wall excitons and observe no contributions from non-secular processes.

Second, we use two-quantum spectroscopy to make the first experimental observation of two-exciton correlations (i.e. biexcitons) in cuprous oxide. The direct measurement of two-exciton correlations supports the proposed mechanism of biexciton-Auger recombination for the efficient suppression of the Bose-Einstein condensation of excitons.

Third, we use two-dimensional rephasing spectroscopy to observe substantial inhomogeneous broadening due to large static disorder in monolayer transition metal dichalcogenides. We also use two-dimensional correlation spectroscopy to reveal interactions of excitons with in-plane optical and acoustic phonons. Lastly, we use one- and two-quantum spectroscopy to

measure unprecedentedly large inorganic, biexciton binding energies due to reduced dielectric screening in the atomically thin limit.

The exciton and phonon dynamics revealed in these experiments contribute to our understanding of the elementary excitations in organic and inorganic nanostructured semiconductors. It is our hope these insights will help guide the design of next generation devices utilizing nanoscale semiconductors.

Thesis Supervisor: Keith A. Nelson
Title: Haslam & Dewey Professor of Chemistry

## Acknowledgements

First and foremost, I want to dedicate this thesis to my grandparents Stuart and Sylvia Steiner. My grandfather never had the opportunity to finish his PhD, so I want to share this accomplishment with him. He died before I was old enough to share our mutual love for science, so I hope to honor him now with this thesis. My grandmother was also the most encouraging and kind person I have ever known. I never questioned her unconditional love and support. She died just before I was admitted to MIT, but I know she would have been incredibly proud and would have continued to support me in every step of graduate school.

There are so many people who contributed to the completion of this thesis: some through productive conversations, some by performing research along side me, some for keeping me sane, and some for simply bringing a smile to my face by having one on yours. There are too many people to thank by name; so please know that if I call you friend, then you are greatly loved and appreciated.

To Keith, thank you for having the most infectious enthusiasm for science I have ever had the privilege of working with. When I was applying to graduate school, there was no one at MIT or elsewhere I wanted to work for more than you. I'm so glad I had the opportunity to work and learn under your tutelage. Your intuitive way of thinking about the world has completely changed the way I think. Thank you for the constant guidance, support, and encouragement over the last six years.

To the cohort I entered the Nelson group with in 2010: Jeff, Sam, and Yongbao, it has been a pleasure to take classes and perform research along side you for so many years. Watching you grow has inspired me and helped me to see and celebrate my own development. Jeff, I am so glad to call you one of my best friends and it was an honor to stand beside you on your wedding day. I wish you and Beci all joy and love for many years to come. Also, you owe me $50 for our bet. Sam, you are one of the most brilliant scientists I have ever known and you are completely selfless with your knowledge and your time. I can't wait to see all the great things you do. Yongbao, I can't imagine a better person to have shared a lab with for six years. You have no fear of the unknown or of trying new things, thank you for helping feel and do the same.

To my thesis writing cohort: Sam, Ben, and Jenn, thank you for not killing me when I was at my craziest. Ben, you are my voice of reason and constant lifeline to sanity. Thank you for always listening to rants and insecurities. I hope in some small way I was able to return the favor. Jenn, thank you for always being real and honest. It allowed me to be me, which was a priceless gift.

To my mentors: Patrick and Dylan, thank you for taking me under your wing and teaching me everything you know. Patrick, your dry and crude humor always made me laugh when I needed it most—though you probably don't know what I'm talking about. Dylan, you are more than a mentor or friend. You are my brother. This thesis is as much your accomplishment as it is mine. I would never have been able to do it without you. And to your better half, Lemon, I don't know where I'd be without you either.

To my younger and older apprentices: Joseph and Jake, thank you for teaching me more than I ever taught you and for giving me the confidence to continue doing research when things didn't work. You are both talented scientists and great friends.

To the Nelson group past and present: Brad, Harold, Johanna, Kara, Kit, Nate, Sharly,

Steph, thank you for the memories and all those productive and not-so-productive conversations. Kara, thank you for reminding me that shit is always gonna done git. Nate, I hope you never stop Beliebing. Steph, I will always bear the scars of your valuable friendship. The Full Nelson, it was a pleasure to play volleyball with you for so many years. I'm so glad we finally won a championship!

Thank you to all my collaborators both near and far. Dörthe Eisele, Justin Caram, Sandra Doria, and Moungi Bawendi at MIT and Xiaofeng Fu and Daniela Nicastro at Brandeis University for your collaboration on the J-aggregate nanotubes experiments. Joel Yuen-Zhou, Jacob Krich, and Alán Aspuru-Guzik at Harvard University for your collaboration on the quantum process tomography experiments. Laszlo Frazer, Kelvin Chang, and Kenneth Poeppelmeier at Northwestern University for your collaboration on the cuprous oxide experiments. Edbert Sie and Nuh Gedik at MIT and Yi-Hsien Lee at the National Tsing Hua University for your collaboration on the monolayer transition metal dichalcogenides experiments. Andrei Tokmakoff, Gabriela Shlau-Cohen, and Thomas Feurer, thank you for giving so much of your time and for more helpful conversations than I can count.

Much of my PhD was spent managing the renovation of building 2. So I also want to thank Marty Deluga from Facilities and Bob Dooley, Mike Canal, and Blake Wilcox from Bond Brothers for making the process as painless as possible. Building 2 is beautiful and it is all because of you.

I also need to thank my community outside of MIT. The support I received from the people at Park Street Church and Reality Boston has been invaluable. I have made so many lifelong friends and some of you I consider family.

Jonathan, thank you for being my best friend and roommate these last five years. Your understanding and support has made all the difference. Thank you for freezing in the winter and boiling in the summer along side me. I'm so glad we didn't have to put duct tape down the middle of the apartment and that neither of us has left Boston, gotten married, or died yet.

Lastly, I need to thank Kaylyn. You are the most patient and gracious human being I have ever met. And you are the best model of Christ's love I could ever know. Thank you for being patient every time I was physically present but mentally absent. Thank you for being understanding every time I broke down. Thank you for being gracious every time the stress got to me. I have now idea why you put up with me, but thank you for always being there.

# Contents

# List of Figures

# List of Tables

# Chapter 1

# Introduction

In recent decades, advancements in the fabrication and synthesis of nanoscale materials has lead to new and interesting physics. The unique properties of nanoscale semiconductors make them promising media for more efficient optical and electronic devices [1, 2]. Indeed, engineers are already utilizing organic and inorganic, nanostructured semiconductors in a variety of devices, including photovoltaics [3, 4, 5], photodetectors [6, 7, 8], light emitting diodes [9, 10, 11, 12, 13], diode lasers [14, 15, 16, 17], optical switches [18, 19, 20], and transistors [21, 22, 23, 24].

In particular, we are interested in new nanostructured materials for application in solar cells and other photovoltaic devices in order to improve light harvesting efficiencies and decrease the economic costs of renewable energy. Solar energy is the most promising source of renewable power as the Earth receives as much energy from the sun in one hour as is consumed globally in a year [25]. Biology has evolved over millions of years to take advantage of this nearly infinite energy source and efficiently harvest light. Much can be learned from photosynthetic systems to help guide the design of better solar cells, photovoltaic devices, and their active media [26, 27, 28, 29]. Most interestingly, experimental evidence suggests the high efficiencies in biological light harvesting systems is due to electronic coherences and the correlated protein dynamics that protect them[30, 31, 32, 33]. Photosynthetic complexes

are rich with both classical and quantum mechanics, which must be carefully tailored in synthetic devices to produce high light harvesting efficiencies [34, 35].

The complexity of biological light harvesting systems often makes them difficult to study. So, there has been great interest in understanding synthetic analogs of photosynthetic complexes, which are much easier to study due to less convoluted dynamics. Multichromophoric systems, such as J-aggregates, have been of particular interest because their electronic couplings and supramolecular structure are similar to naturally occurring chlorosomes [36, 37, 38]. In chapters 5 and 6, we discuss experiments using multi-dimensional optical spectroscopy and transient grating measurements to interrogate electronic coupling and dynamics in a double-walled J-aggregate nanotube.

Multi-dimensional optical spectroscopy is a power tool for measuring electronic coherence and dynamics, electronic interactions with vibrational modes and the environment, homogeneous and inhomogeneous linewidths, multi-particle states, and much more [39, 40, 41]. Multi-dimensional spectroscopy has been used to characterize electronic dynamics in a variety of system including: photosynthetic complexes [42, 43, 44, 45, 46], J-aggregates [47, 48, 49, 50, 51], conjugated polymers [52, 53, 54], singlet fission materials [55], nitrogen-vacancy centers [56], monolayer transition metal dichalcogenides [57], inorganic quantum wells [58, 59, 60, 61, 62, 63], quantum dots [64, 65, 66, 67, 68], and much more. However, it is often difficult to separate electronic and vibronic contributions to multi-dimensional signals, even when they are deconvolved over a second frequency axis. Thus, theoretical studies have been undertaken to learn how to accurately interpret spectroscopic signals [69, 70, 71, 72]. Currently, the experimental evidence for electronic coherences in photosynthetic complexes using ultrafast spectroscopy has sparked a debate over whether electronic coherences can occur under incoherent excitation. Both experimental and theoretical studies have provided contradicting results, so the debate continues to be hotly contested [73, 74, 75].

The fundamental electronic excitations in most biological light harvesting systems, J-aggregates, and other semiconductors are correlated electron-hole pairs, called excitons. Ex-

citons are bosonic quasi-particles that can undergo, among other processes, Bose-Einstein condensation [76, 77, 78, 79]. Insight into Bose-Einstein condensation is important for understanding the related processes of superconductivity and superfluidity and their applications in new and more efficient optical and electronic devices [80, 81]. In chapter 7, we discuss the first measurement of biexcitons in cuprous oxide, which leads to the efficient suppression of Bose-Einstein condensation of excitons.

The recent isolation of monolayer transition metal dichalcogenides has brought renewed interest to these now two-dimensional materials [82]. Of particular interest to the engineering community is their transition to a direct band gap semiconductor in the monolayer limit and the emergence of coupled spin and valley physics [83, 84]. Thus, monolayer transition metal dichalcogenides are being employed as active media in a variety of electronic and optical devices [85]. Unprecedented Coulombic interactions in these atomically thin, inorganic semiconductors has also lead to important questions about their applicability in photovoltaic devices as electrons and holes must be separated in order to produce a current [86]. In chapter 8, we discuss experiments to study exciton-exciton and exciton-phonon interactions in monolayer transition metal dichalcogenides.

The outline of the thesis is as follows. In chapter 2, we first discuss the physics of excitons starting with the electronic states of the hydrogen atom and working our way to enhanced electron-hole correlations in nanostructured semiconductors. Then in chapter 3, we discuss the theory and techniques of ultrafast spectroscopy, including linear absorption, pump-probe, transient grating, and multi-dimensional measurements. In chapter 4, we discuss the specific technical design, capabilities, and limitations of our two-dimensional spectrometer that utilizes diffraction-based spatiotemporal pulse shaping and the calibrations necessary to perform an ultrafast experiment. Chapters 5 through 8 describe experiments exploring exciton-phonon and exciton-exciton interactions in a variety of organic and inorganic, nanostructured semiconductors. In chapter 5, we determine the coupling between inner and outer wall excitons in isolated and bundled double-walled J-aggregate nanotubes in solution. We

also explore the processes leading to exciton dephasing in solution at room temperature and in a glass at cryogenic temperature, as well as the photo-induced damage and recovery observed in the solid state. In chapter 6, we utilize quantum process tomography to unambiguously elucidate the single-exciton dynamics in isolated J-aggregate nanotubes. In chapter 7, we make the first direct experimental measurement of biexcitons in cuprous oxide and provide evidence to support a biexciton-Auger mechanism that effectively suppresses the Bose-Einstein condensation of excitons. In chapter 8, we discuss preliminary experiments exploring the strength of exciton-phonon and exciton-exciton interactions in monolayer transition metal dichalcogenides. Finally in chapter 9, we conclude and discuss outlooks for new ultrafast spectroscopic experiments to further our understanding excitons on the nanoscale.

# Chapter 2

# Excitons in Nanoscale Semiconductors

In chapter 2, we will discuss the physics of the elementary solid state excitation relevant in most optoelectronic devices: the electron-hole quasiparticle called an exciton. In particular, we are interested in exciton properties and dynamics when semiconductors are structured on the nanoscale. Thus, we will work our way from a discussion of the electronic structure of the hydrogen atom, up to the $H_2^+$ molecule, and finally to semiconductors in the solid state. In doing so, we will describe how excitons are formed and their classifications. Subsequently, we will discuss how excitons interact with each other, other charged species, and crystal lattice vibrations (i.e. phonons). Finally, we will consider how excitonic states are perturbed due to confinement on the nanoscale, starting with a discussion of particle-in-a-box states.

## 2.1 The Hydrogen Atom

In atoms, electrons occupy localized orbitals with discrete energy levels [87]. The Hamiltonian of the hydrogen atom consists of an electron kinetic energy term and a Coulombic potential energy term describing the electron and proton interaction:

$$\hat{H} = -\frac{\hbar^2}{2\mu}\nabla^2 - \frac{e^2}{4\pi\varepsilon_0 r} \tag{2.1}$$

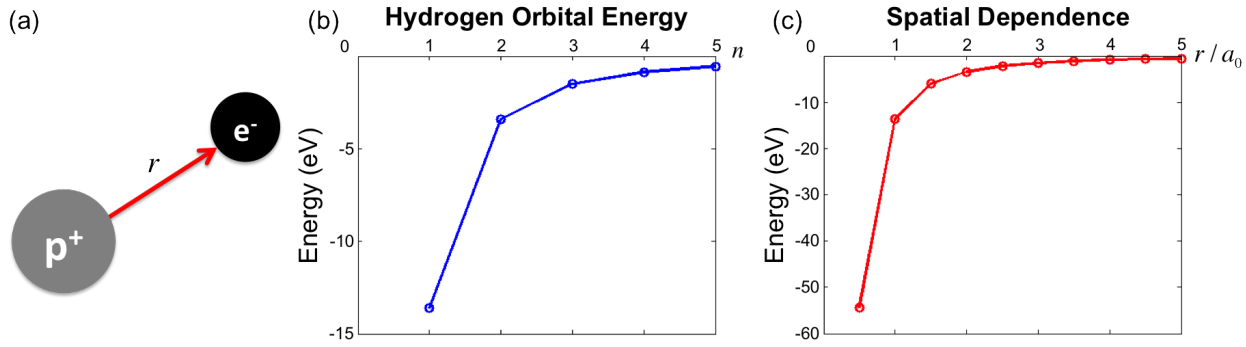


Figure 2.1: Hydrogen atomic orbitals. (a) Hydrogen atom diagram, where $p^+$ and $e^-$ are the proton and electron, respectively, and $r$ is the distance between them. (b) Atomic orbital energies as a function of the principal quantum number $n$. (c) Spatial dependence of the $n = 1$ atomic orbital energies on the electron radius $r$.

where $\hbar$ is Planck's constant, $\mu = m_p m_e / (m_p + m_e) \approx m_e$ is the reduced mass of the proton $m_p$ and electron $m_e$, $\nabla^2$ is the del operator, $e$ is the charge of an electron, $\varepsilon_0$ is the permittivity of free space, and $r$ is the distance between the electron and proton that is illustrated in figure 2.1a. Solving the Schrödinger equation, $\hat{H}\Psi = E\Psi$, results in a three dimensional wavefunction that is separable into a radial component and spherical harmonics using polar coordinates:

$$\Psi(r, \theta, \phi) = \psi_l^m(r)\, Y_l^m(\theta, \phi) \tag{2.2}$$

and is defined by the principal, azimuthal, and magnetic quantum numbers $n$, $l$, and $m$, respectively. The energies of the atomic orbitals or Rydberg states are dependent on the principal quantum number:

$$E_n = -\frac{\hbar^2}{2m_e a_0^2}\frac{1}{n^2} = -\frac{R_y}{n^2} \tag{2.3}$$

where $a_0 = 4\pi\varepsilon_0\hbar^2/m_e e^2$ is the Bohr radius, which defines the most probable distance between the proton and electron in the lowest lying $1s$ atomic orbital, and $R_y = \hbar^2/2m_e a_0^2$ is the Rydberg constant. Figures 2.1b and 2.1c illustrate the atomic orbital energy dependence on the principal quantum number and proton-electron radius, respectively.

When a single $H$ atom is optically excited, the electron is promoted from the lowest lying

$1s$ orbital into a higher lying orbital. The electronic transition is described by:

$$\langle \Psi_f(r) | \hat{\mu}_{if}(r) | \Psi_i(r) \rangle = \int \Psi_f^*(r) \, \hat{\mu}_{if}(r) \, \Psi_i(r) \, d^3r \tag{2.4}$$

where $\Psi_i(r)$ and $\Psi_f(r)$ are the wavefunctions of the initial and final states and $\hat{\mu}_{if}(r)$ is the transition dipole moment between them. In order for the integral to be non-zero, the initial and final state wavefunctions must be a pair of even and odd functions. This optical selection rule allows only transitions between atomic orbitals of even and odd azimuthal (i.e. orbital angular momentum) quantum number $\ell$ to occur.

## 2.2 The Hydrogen Molecule

In the simplest molecular case, where two protons are bound by one electron, the electronic Hamiltonian of the $H_2^+$ molecule in atomic units and under the Born-Oppenheimer approximation takes the form:

$$\hat{H}_{el}\left(\overrightarrow{R}_a, \overrightarrow{R}_b, \overrightarrow{r}\right) = -\frac{1}{2}\nabla_r^2 - \frac{1}{\left|\overrightarrow{R}_a - \overrightarrow{r}\right|} - \frac{1}{\left|\overrightarrow{R}_b - \overrightarrow{r}\right|} + \frac{1}{\left|\overrightarrow{R}_a - \overrightarrow{R}_b\right|} \tag{2.5}$$

where $\overrightarrow{r}$ is the dynamic position of the electron and $\overrightarrow{R}_i$ is the fixed position of the hydrogen atom $H_i$, illustrated in figure 2.2a [87]. The first term in equation 2.5 is the electron kinetic energy, the second and third terms are the attractive electron-proton Coulombic interactions, and the final term is the repulsive proton-proton Coulombic interaction. The second, third, and fourth terms are collectively called the potential energy $\hat{V}_{ab}$. The Schrödinger equation for the electronic Hamiltonian of the $H_2^+$ atom, $\hat{H}_{el}\left(\overrightarrow{R}\right)\Psi\left(\overrightarrow{r}, \overrightarrow{R}\right) = E_{el}\left(\overrightarrow{R}\right)\Psi\left(\overrightarrow{r}, \overrightarrow{R}\right)$, is dependent on the dynamic position of the electron and fixed positions of the nuclei. Solving the Schrödinger equation, the lowest lying molecular orbitals are linear combinations of the atomic orbitals of hydrogen, illustrated in figure 2.2c:

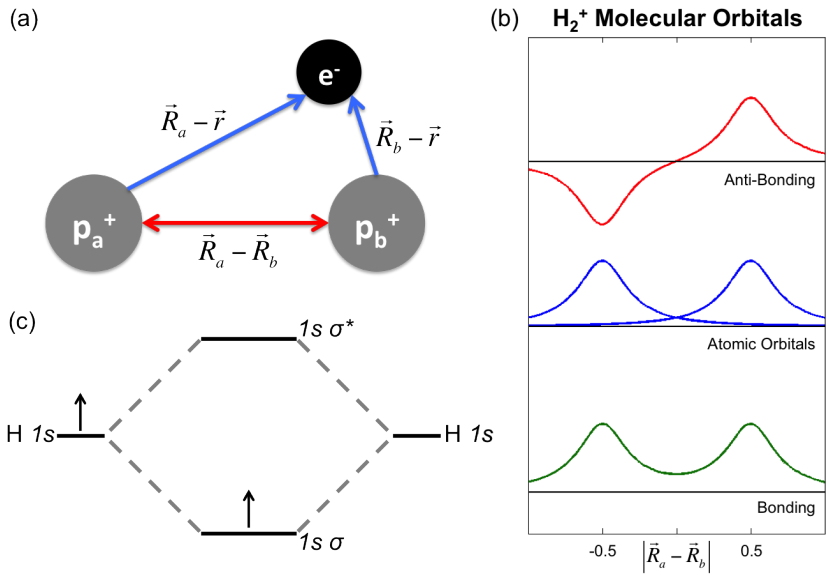


Figure 2.2: Hydrogen $H_2^+$ molecular orbitals. (a) Hydrogen molecule diagram, where $p_i^+$ and $e^-$ are the protons and electron, respectively, and $\overrightarrow{R}_i$ and $\overrightarrow{r}$ are their positions, respectively. (b) Molecular orbital diagram where the $1s$ $\sigma$ bonding and $1s$ $\sigma^*$ anti-bonding molecular orbitals are linear combinations of the two $1s$ hydrogen atomic orbitals. (c) $H$ $1s$ atomic orbitals and $H_2^+$ $1s$ molecular bonding and anti-bonding orbitals.

$$\Psi_\pm\left(\overrightarrow{r},\overrightarrow{R}\right) = c_a\left(\overrightarrow{R}\right)\phi_a\left(\overrightarrow{r},\overrightarrow{R}\right) \pm c_b\left(\overrightarrow{R}\right)\phi_b\left(\overrightarrow{r},\overrightarrow{R}\right) \tag{2.6}$$

where $\Psi_\pm\left(\overrightarrow{r},\overrightarrow{R}\right)$ are the bonding and anti-bonding molecular orbitals, $c_a = c_b = 1/\sqrt{2}$ are the coefficients describing the linear combination, and $\phi_i\left(\overrightarrow{r},\overrightarrow{R}\right)$ are the atomic orbitals of $H_i$. The energies of the molecular orbitals, illustrated in figure 2.2b, depend on the positions of the hydrogen atoms:

$$E_\pm\left(\overrightarrow{R}\right) = -\frac{E\left(\overrightarrow{R}\right) \pm V_{ab}\left(\overrightarrow{R}\right)}{1 \pm S_{ab}\left(\overrightarrow{R}\right)} \tag{2.7}$$

$$\begin{aligned} E\left(\overrightarrow{R}\right) &= \left\langle \phi\left(\overrightarrow{r},\overrightarrow{R}\right) \middle| \hat{H}_{el}\left(\overrightarrow{r},\overrightarrow{R}\right) \middle| \phi\left(\overrightarrow{r},\overrightarrow{R}\right) \right\rangle \\ &= \int \phi^*\left(\overrightarrow{r},\overrightarrow{R}\right)\hat{H}_{el}\left(\overrightarrow{r},\overrightarrow{R}\right)\phi\left(\overrightarrow{r},\overrightarrow{R}\right) d^3\overrightarrow{r} \end{aligned} \tag{2.8}$$

$$V_{ab}\left(\overrightarrow{R}\right) = \left\langle \phi_b\left(\overrightarrow{r},\overrightarrow{R}\right)\left|\hat{V}_{ab}\left(\overrightarrow{r},\overrightarrow{R}\right)\right|\phi_a\left(\overrightarrow{r},\overrightarrow{R}\right)\right\rangle$$
$$= \int \phi_b^*\left(\overrightarrow{r},\overrightarrow{R}\right)\hat{V}_{ab}\left(\overrightarrow{r},\overrightarrow{R}\right)\phi_a\left(\overrightarrow{r},\overrightarrow{R}\right)d^3\overrightarrow{r} \tag{2.9}$$

$$S_{ab}\left(\overrightarrow{R}\right) = \left\langle \phi_b\left(\overrightarrow{r},\overrightarrow{R}\right)\left|\phi_a\left(\overrightarrow{r},\overrightarrow{R}\right)\right\rangle\right.$$
$$= \int \phi_b^*\left(\overrightarrow{r},\overrightarrow{R}\right)\phi_a\left(\overrightarrow{r},\overrightarrow{R}\right)d^3\overrightarrow{r} \tag{2.10}$$

where $E\left(\overrightarrow{R}\right)$ is the atomic orbital energy, $V_{ab}\left(\overrightarrow{R}\right)$ is the expectation value of the electron potential energy, and $S_{ab}\left(\overrightarrow{R}\right)$ is the atomic orbital overlap of the hydrogen atoms $H_a(\overrightarrow{R}_a)$ and $H_b(\overrightarrow{R}_b)$. Optical excitations in molecules are described identically to those in atoms:

$$\left\langle \Psi_f\left(\overrightarrow{r},\overrightarrow{R}\right)\left|\hat{\mu}_{if}\left(\overrightarrow{r},\overrightarrow{R}\right)\right|\Psi_i\left(\overrightarrow{r},\overrightarrow{R}\right)\right\rangle \tag{2.11}$$

where the transition dipole moment $\hat{\mu}_{if}\left(\overrightarrow{r},\overrightarrow{R}\right)$ connects the initial and final molecular orbitals $\Psi_i\left(\overrightarrow{r},\overrightarrow{R}\right)$ and $\Psi_f\left(\overrightarrow{r},\overrightarrow{R}\right)$. Thus, the same optical selection rule applies and only allows transitions between molecular orbitals of different symmetry to occur.

## 2.3 Solid State Materials

In a crystalline solid, the electronic structure is described by many electrons in a periodic potential, illustrated in figure 2.3a [88]. The Hamiltonian of a crystalline solid takes the form:

$$\hat{H} = -\sum_i \frac{\hbar^2}{2m_e}\nabla_i^2 + \sum_i U\left(\overrightarrow{r}_i\right) + \sum_{i<j}\frac{e^2}{\left|\overrightarrow{r}_i - \overrightarrow{r}_j\right|} \tag{2.12}$$

where the first term describes the electron kinetic energies and $\hbar$ is Planck's constant and $m_e$ the electron mass, the second term the attractive electron-nuclei Coulombic interactions and $\overrightarrow{r}_i$ are the electron positions, and the third term the repulsive electron-electron Coulombic interactions and $e$ is the electron charge. The wavefunctions take the form of

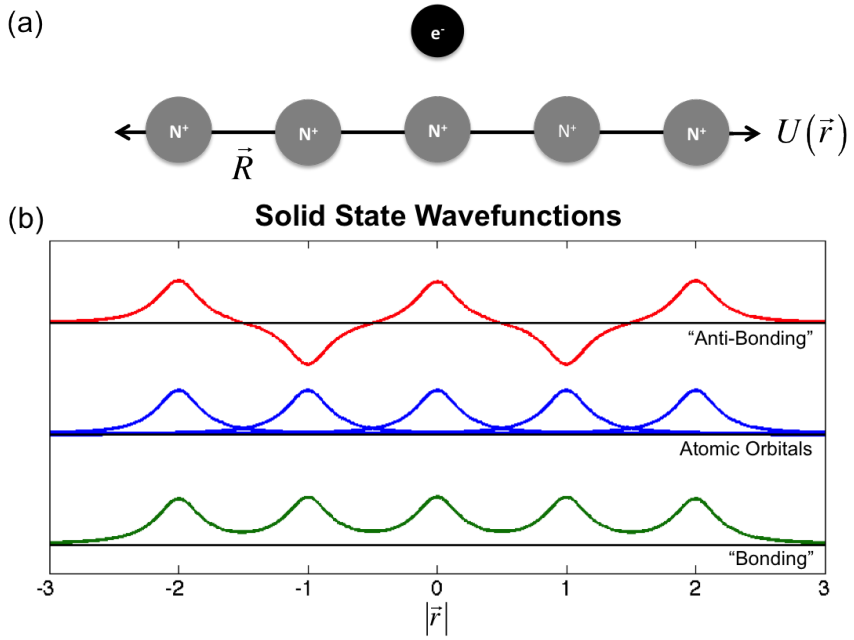


Figure 2.3: Solid state wavefunctions. (a) Solid state diagram in one dimension, where $N^+$ and $e^-$ are the nuclei and electron, respectively, and $\overrightarrow{R}$ and $\overrightarrow{r}$ are their positions, respectively. (b) Nuclei atomic orbitals and solid state "bonding" and "anti-bonding" orbitals.

anti-symmetrized products of the localized atomic orbitals $\phi$, shown in figure 2.3b:

$$\Psi = \hat{\alpha} \prod_i \phi \left( \overrightarrow{r}_i - \overrightarrow{R}_i \right) \tag{2.13}$$

where $\hat{\alpha}$ is the anti-symmetrization operator and $\overrightarrow{R}_i$ are the nuclei positions.

The full Hamiltonian of a crystalline solid is extremely complicated. However, the eigenstates and eigenvalues can be calculated using a periodic, one-electron Hamiltonian

$$\hat{H} = \frac{\hbar^2}{2m_e} \nabla^2 + U\left(\overrightarrow{r}\right) \tag{2.14}$$

where $U(\overrightarrow{r}) = U(\overrightarrow{r} + \overrightarrow{R})$ is the periodic potential defined by the lattice vector $\overrightarrow{R}$ (i.e. the inter-unit cell distance). In this method, the repulsive electron-electron interactions described in the second term of equation 2.12 must be added back in to accurately described the electron dynamics. The one-electron eigenstates are products of a plane wave and periodic function

as described by Bloch's theorem

$$\psi_{nk}\left(\overrightarrow{r}\right) = \exp\left[i\overrightarrow{k}\cdot\overrightarrow{r}\right] u_{nk}\left(\overrightarrow{r}\right) \tag{2.15}$$

where $\overrightarrow{k} = 2\pi/\overrightarrow{R}$ is the wavevector describing the periodicity of the crystal lattice and $u_{nk}$ is a periodic function that takes the form of the contributing atomic orbitals of each nucleus. Due to the periodicity of the crystal lattice, the eigenstates have the special property that $\psi\left(\overrightarrow{r}+\overrightarrow{R}\right) = \exp\left[i\overrightarrow{k}\cdot\overrightarrow{R}\right]\psi\left(\overrightarrow{r}\right)$.

The Schrödinger equation of a crystalline solid thus reduces to $\hat{H}u_{nk}\left(\overrightarrow{r}\right) = E_{nk}u_{nk}\left(\overrightarrow{r}\right)$. Like the eigenstates, the periodic function also has the special property that $u_{nk}\left(\overrightarrow{r}\right) = u_{nk}\left(\overrightarrow{r}+\overrightarrow{R}\right)$. In the solid state, $n$ is a discrete quantum number describing the electronic state and $\overrightarrow{k}$ is a continuous quantum number describing the crystal momentum. The eigenvalues of a solid state material become continuous electronic energy bands dependent on the crystal lattice structure and elemental composition of the material.

As in the case of atoms and molecules, the same optical selection rule continues to apply and only allows transitions between electronic bands of different symmetry.

### 2.3.1 Semiconductors

In a semiconductor, low lying electronic bands are completely filled and there is an energy gap between the highest lying, occupied valence band and the lowest lying, unoccupied conduction band. The band gap energy is typically less than or equal to $2\,eV$. As the band gap energy increases, the material becomes an insulator and as the band gap energy goes to zero (i.e. incomplete filling of an electronic band), the material becomes a metal. The band gap can either be direct or indirect, where the highest lying valence band maximum and lowest lying conduction band minimum have the same or different wavevector $k$, respectively. In general, direct band gap semiconductors are substantially more optically active than indirect semiconductors because the latter require phonons play a role in excitation and

emission processes in order to conserve crystal momentum.

Optical excitation of a direct band gap semiconductor promotes an electron from a filled valence band into an unoccupied conduction band. The promotion of a negatively charged electron into the conduction band results in a positively charged hole in the valence band due to the absence of the excited electron. Repulsion of the conduction band electron by valence band electrons localizes the excited electron near the valence band hole. Coulombic attraction between the electron and hole can bind them to form a charge neutral (bosonic) quasiparticle called an exciton, illustrated in figures 2.4a and b [89]. The energy difference between the free electron and hole states and the exciton state is called the exciton binding energy: $\Delta E_{Ex} = (E_e + E_h) - E_{Ex}$, and is typically on the order of $0.01 - 1\,eV$.

Conduction band electrons and valence band holes tend to be localized near the minimum and maximum of their respective bands, at which point the relationship between energy and wavevector (i.e. the dispersion relation) is approximately quadratic. Thus, the electronic band structure of the electron and hole can be written as:

$$E_e\left(k\right) = E_c + \frac{\hbar^2 k^2}{2m_e} \tag{2.16}$$

$$E_h\left(k\right) = E_v + \frac{\hbar^2 k^2}{2m_h} \tag{2.17}$$

where $E_c$ and $E_v$ are the minimum and maximum energies of the conduction and valence bands, respectively, and $m_e$ and $m_h$ are the electron and hole masses, respectively. A qualitative picture of the electronic band structure and exciton state is illustrated in figure 2.4b.

Intuitively, excitons can be thought of as hydrogen-like atoms, where the negatively charged electron orbits around the positively charged hole. However, there are two major differences between an exciton and a hydrogen atom. First, the electron and hole masses are comparable in magnitude, unlike atoms where there is a three order of magnitude disparity between the proton and electron masses. Second, excitons are described by the dielectric constant of the solid state material (i.e. relative permittivity), which screens the electron-

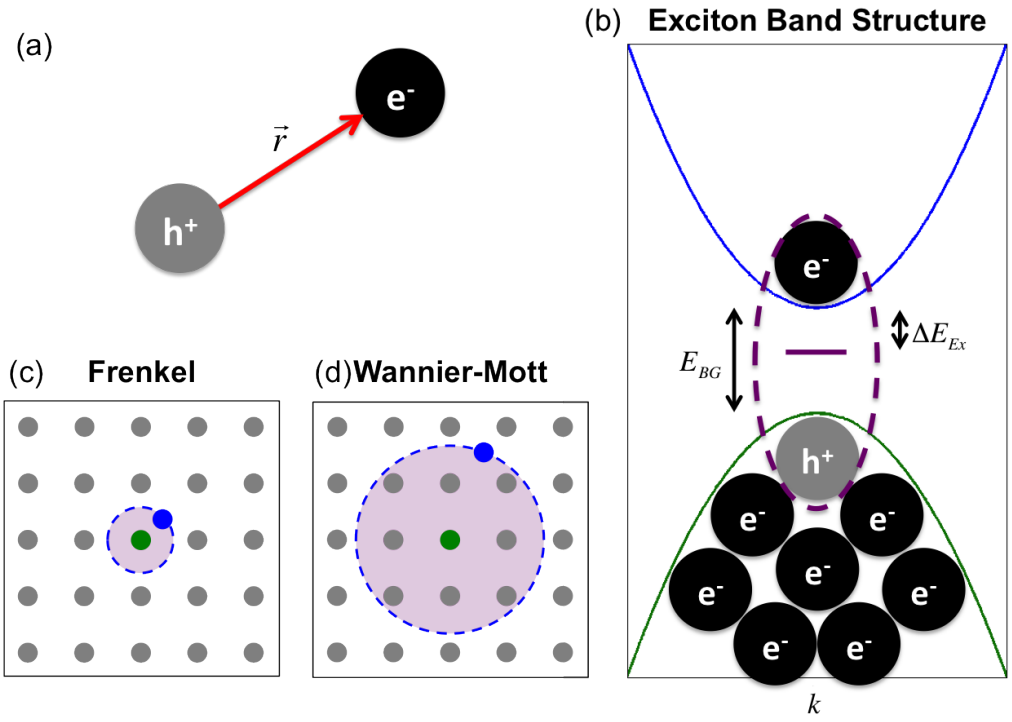


Figure 2.4: Exciton band structure. (a) Exciton diagram, where $h^+$ and $e^-$ are the hole and electron and $\overrightarrow{r}$ is the distance between them. (b) Qualitative exciton band structure with a free electron in the conduction band (blue) and a hole in the valence band (green), where $E_{BG}$ is the direct band gap energy. Electrostatic repulsion of the free electron in the conduction band by the bound electrons in the valence band localize the electron and hole near each other. The electron and hole bind due to electrostatic attraction into an exciton (purple) and are stabilized by the exciton binding energy $\Delta E_{Ex}$. (c) Frenkel excitons are characterized by small electron-hole (green and blue, respectively) radii and large exciton binding energies. (d) Wannier-Mott excitons are characterized by large electron-hole radii and small exciton binding energies.

hole interaction, rather than in a non-perturbative vacuum. Nevertheless, the similarities between excitons and hydrogen atoms are quite striking. Similar to hydrogen atoms, excitons possess Rydberg states where the energy is dependent on the quantum number $n$ and are given by:

$$\begin{aligned} E_{Ex}^{n}(k) &= E_{BG}(0) + \frac{\hbar^2 k^2}{2(m_e + m_h)} - \frac{R_y^*}{n^2} \\ &= (E_e(0) - E_h(0)) + \frac{\hbar^2 k^2}{2(m_e + m_h)} - \left(\frac{\varepsilon_0}{\varepsilon}\right)^2 \left(\frac{m^*}{m_e}\right) \frac{R_y}{n^2} \end{aligned} \tag{2.18}$$

where the first term $E_{BG}(0)$ is the band gap energy, the second term describes the electron and hole kinetic energy given by the dispersion relation, and the third term is the exciton Rydberg energy given by the exciton Rydberg constant $R_y^*$ and composed of the relative permittivity of the material $(\varepsilon/\varepsilon_0)$ and the electron-hole reduced mass $m^* = m_e m_h/(m_e + m_h)$. In this case, the first exciton Rydberg term $(n = 1)$ gives the exciton binding energy.

$$\Delta E_{Ex} = R_y^* = \left(\frac{\varepsilon_0}{\varepsilon}\right)^2 \left(\frac{m^*}{m_e}\right) R_y \tag{2.19}$$

An exciton Bohr radius can also be defined and describes the exciton delocalization or most probable distance between the electron and hole in the lowest lying $1s$ exciton state.

$$a_{Ex} = \frac{\epsilon}{\epsilon_0} \frac{m_e}{m^*} a_0 \tag{2.20}$$

#### 2.3.1.1 Frenkel Excitons

In semiconductors with small dielectric constants, electrons and holes experience little screening from each other and tend to interact strongly. In this case, the quasiparticles are classified as Frenkel excitons, shown in figure 2.4c. The delocalization of Frenkel excitons tends to be small (on the order of a unit cell) and the exciton binding energy large $(0.1 - 1\,eV)$. Examples of Frenkel excitons include those in alkali halides [90], organic molecular crystals

[91], and H- and J-aggregates [38].

#### 2.3.1.2 Wannier-Mott Excitons

In semiconductors with large dielectric constants, electrons and holes are substantially screened from each other and tend to weakly interact. In this case, the quasiparticles are classified as Wannier-Mott excitons, shown in figure 2.4d. The delocalization of Wannier-Mott excitons tends to be large (greater than a unit cell) and the exciton binding energy small $(0.01 - 0.1\, eV)$. Examples of Wannier-Mott excitons include many inorganic semiconductors including bulk group IV silicon [92] and germanium [93], III-V compounds such as pseudo two-dimensional GaAs quantum wells [94], and II-VI compounds such as ZnO nanowires [95] and CdSe quantum dots [96].

#### 2.3.1.3 Intermediate Excitons

It is important to note that Frenkel and Wannier-Mott excitons are only the extrema of a spectrum of excitons. Many systems, such as single-walled carbon nanotubes [97], lie within this spectrum. In the case of single-walled carbon nanotubes, excitons are delocalized over several nanometers due to the large dielectric constant but screening is reduced in low dimensions and allows for large exciton binding energies. Thus, excitons in single-walled carbon nanotubes possess both Frenkel and Wannier-Mott characteristics and cannot be classified as either.

## 2.4 Many-Body Interactions

Expanding the analogy of excitons to hydrogen-like atoms, excitons also form the basis of more complex excitonic "ions" and "molecules". Here, we will discuss higher-order correlations of excitons and charged particles that result from $n > 2$ particle interactions.

### 2.4.1 Trions: Excitonic Ions

Similar to atoms, excitons can form positively and negatively charged "ions" [98, 99]. Three-particle correlations of an exciton with an additional electron or hole produce positively and negatively charged excitons called trions, which are analogous to $H_2^+$ and $H^-$, respectively. A trion binding energy and Bohr radius can be defined to describe the degree of stabilization and delocalization. However, since trions are not produced directly by optical excitation, we do not observe these quasi-particles in our spectroscopic experiments.

### 2.4.2 Multi-Excitons: Excitonic Molecules

Similar to atoms, excitons can form excitonic "molecules" [61, 62, 100]. The simplest case is the four-particle correlation of identical electrons and holes called a biexciton, which is analogous to a homonuclear diatomic molecule (e.g. $H_2$). A four-particle correlation of nonequivalent electrons and holes can form called a mixed biexciton, which is analogous to a heteronuclear diatomic molecule (e.g. $HCl$). A biexciton binding energy can be defined to describe the degree of exciton-exciton stabilization:

$$\Delta E_{Bx}^{nm} = (E_{Ex}^{n} + E_{Ex}^{m}) - E_{Bx}^{nm} \tag{2.21}$$

where $E_{Bx}^{nm}$ is the energy of the biexciton composed of $n$ and $m$ excitons and $E_{Ex}^{n}$ and $E_{Ex}^{m}$ are the constituent $n$ and $m$ excitons energies. Like electrons in a molecular bond, the constituent exciton spins of a biexciton must be anti-parallel ($|\uparrow,\downarrow\rangle$ or $|\downarrow,\uparrow\rangle$) in order to bind. Excitons with parallel spins ($|\uparrow,\uparrow\rangle$ or $|\downarrow,\downarrow\rangle$) can be correlated to each other but do not exhibit a stabilizing binding energy due to the Pauli exclusion principle. Higher-order correlations of excitons can also form called multi-excitons, which are analogous to polyatomic molecules.

In our spectroscopic experiment, multi-excitons can be generated via successive electromagnetic field interactions up and down the ladder of $n$-exciton correlations. In our two-dimensional spectrometer, the phase stability amongst an arbitrary number and geometry

of pulses provides a unique capability that allows us to investigate this ladder of countable $n$-exciton correlations unlike most conventional two-dimensional spectrometers.

## 2.5 Exciton-Phonon Coupling

In the solid state, electronic structure is strongly dependent on the structure of the material. Thus, deformations in the crystal structure via collective motions of atoms or molecules in the lattice (i.e. phonons) can strongly couple to the electronic modes and modulate their eigenstates and eigenvalues [101]. This exciton-phonon coupling can be described by adding an exciton-phonon interaction term $\hat{V}_{EP}$ to the Hamiltonian:

$$\begin{aligned}\hat{H} &= \hat{H}_E + \hat{H}_P + \hat{V}_{EP} \\ &= \sum_{n,k} a^\dagger_{n,k} a_{n,k} E_n\left(\overrightarrow{k}\right) + \sum_{m,q} b^\dagger_{m,q} b_{m,q} E_m\left(\overrightarrow{q}\right) + \hat{V}_{EP}\end{aligned} \tag{2.22}$$

$$\hat{V}_{EP} = \sum_{f,i}\sum_{k',k}\sum_{m,q} V_{fk',ik,mq} \left|\Psi_f\left(\overrightarrow{k}'\right)\right\rangle \left\langle\Psi_i\left(\overrightarrow{k}\right)\right| \left(b^\dagger_{m,q} + b_{m,q}\right) \tag{2.23}$$

where $a_{n,k}$ and $a^\dagger_{n,k}$ are the creation and annihilation operators of exciton $n$ with wavevector $\overrightarrow{k}$ and $b_{m,q}$ and $b^\dagger_{m,q}$ are the creation and annihilation operators of phonon $m$ with wavevector $\overrightarrow{q}$. $V_{fk',ik,mq}$ is the coupling strength between phonon mode $m$ and exciton $i$ that results in exciton $f$, where $\overrightarrow{k}' = \overrightarrow{k} + \overrightarrow{q}$. This linear coupling term allows the creation or annihilation of a single phonon upon an electronic transition. Strong coupling between exciton and phonon modes will be discussed further in chapter 7 in our analysis of the biexciton states in cuprous oxide and chapter 8 in our discussion of monolayer transition metal dichalcogenides.

## 2.6 Excitons on the Nanoscale

When the spatial dimensions of a nanostructured semiconductor are on the order of the exciton de Broglie wavelength $\lambda = h/p$ (approximately 10 nm at room temperature), the

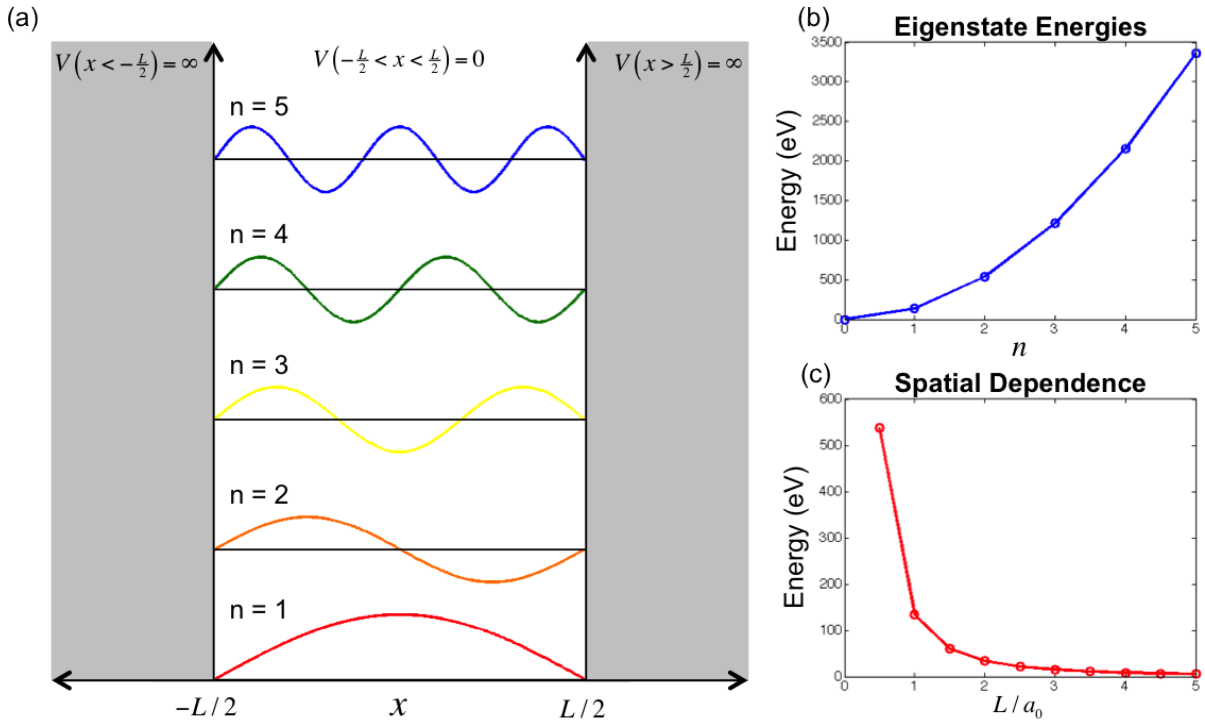


Figure 2.5: Particle-in-a-box. (a) Particle-in-a-box potential well and wavefunctions $n = 1 - 5$. (b) Eigenstate energies as a function of quantum number $n$ with, where $L = a_0$. (c) Spatial dependence of eigenstate energies on the width of the potential $L$, where $n = 1$.

exciton wavefunctions are perturbed due to constraint by the size of the material. First, we will introduce the affects of spatial confinement by considering the easiest case of a particle-in-a-box. Second, we will discuss additional affects of spatial confinement in nanostructured semiconductors in various dimensions.

### 2.6.1 Particle-in-a-Box

In the case of atoms and excitons, the Bohr radius defines the most probable distance between the positively and negatively charged particles. When a particle is spatially confined on the order of its Bohr radius, the eigenstates and eigenvalues of the system are perturbed [87]. Consider a particle in a one dimensional box of length $L$ with zero potential energy inside and infinite potential energy outside the box, illustrated in figure 2.5a.

$$\hat{V}(x) = \begin{cases} \infty, & x < -L/2 \\ 0 & -L/2 < x < L/2 \\ \infty, & x > L/2 \end{cases} \tag{2.24}$$

The Hamiltonian thus takes the form:

$$\hat{H} = -\frac{\hbar^2}{2m}\nabla^2 + \hat{V}(x) \tag{2.25}$$

where $m$ is the mass of the particle. Solving the Schrödinger equation $\hat{H}\Psi(x) = E\Psi(x)$ produces wavefunctions that are only defined inside the box, illustrated in figure 2.5a.

$$\Psi(x) = \begin{cases} 0, & x < -L/2 \\ \sin\left[k_n\left(x + \frac{L}{2}\right)\right], & -L/2 < x < L/2 \\ 0, & x > L/2 \end{cases} \tag{2.26}$$

where the spatial wavevector $k_n = n\pi/L$ defines the periodicity of the wavefunction in the box. The particle-in-a-box energies thus take the form:

$$E_n = \frac{\hbar^2 k_n^2}{2m} = \frac{\pi^2\hbar^2 n^2}{2mL^2} \tag{2.27}$$

The energy levels of the particle-in-a-box states are similar to the exciton Rydberg state energies, however there is a striking difference. The particle-in-a-box energies increase quadratically with the quantum number $n$ (figure 2.5b), while the exciton energies are inversely proportional to the second power of $n$ (figure 2.1b). While the exciton energy levels get closer together with increasing $n$, the particle-in-a-box energy levels get farther apart due to greater confinement of larger electron orbitals. However, the particle-in-a-box and exciton energies are both inversely proportional to the second power on the spatial localization, $L$ and $a_0$, respectively. Thus, both the particle-in-a-box and exciton states are stabilized by

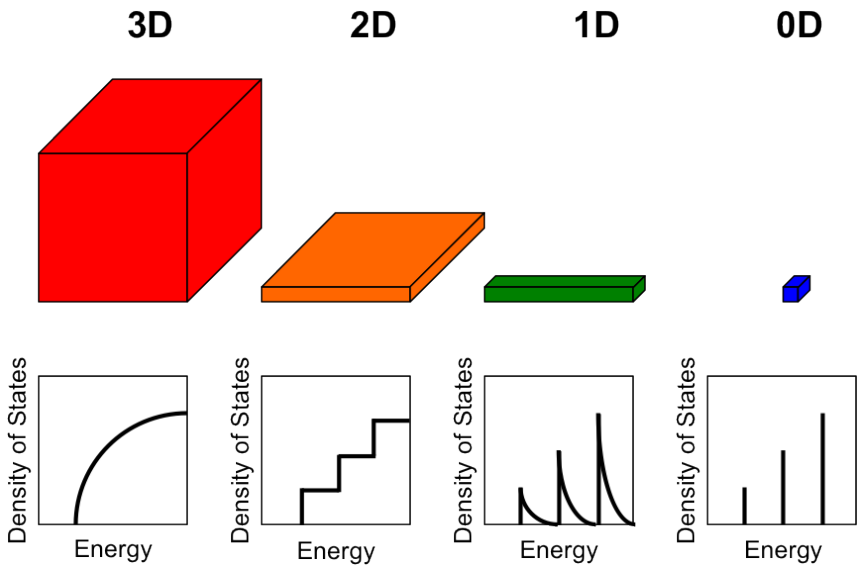


Figure 2.6: Quantum confinement. The change in the density of states with decreasing dimensionality. Oscillator strength is concentrated into narrow regions of the electromagnetic spectrum due to the increase in the crystal momentum uncertainty and a flattening of the electronic bands.

spatial delocalization.

### 2.6.2 Quantum Confinement

From the discussion of a particle-in-a-box, we learn that exciton energies increase as spatial confinement increases. Additionally, the oscillator strengths of the associated electronic transitions are concentrated into narrow regions of the electromagnetic spectrum, enhancing absorption and emission [102]. The oscillator strength concentration can be understood by considering Heisenberg's uncertainty principle: $\sigma_x \sigma_p \geq \hbar/2$. For an exciton in the bulk, the uncertainty in the crystal momentum ($\sigma_p$) is small, unlike the uncertainty in the exciton position ($\sigma_x$), due to the well defined periodicity and symmetry of the crystal. However for a spatially confined exciton, the uncertainty in the exciton position decreases as confinement increases and requires an increase in the crystal momentum uncertainty. The decrease in the crystal momentum uncertainty results in a flattening of the electronic bands and a concentration in the density of states, illustrated in figure 2.6.

The role of quantum confinement will be discussed further in chapter 8 in our measurements of the single and multi-exciton states of monolayer transition metal dichalcogenides.

# Chapter 3

# Third-Order Nonlinear Spectroscopy

In chapter 3, we will describe the spectroscopic techniques used to study excitons in nanostructured materials. First, we will begin our discussion of spectroscopy with linear absorption and the first-order response function. From there, we will generalize our discussion to third-order response functions in order to understand the theoretical principles of third-order non-linear spectroscopy. We will discuss pump-probe, transient grating, and two-dimensional spectroscopies, which have increasing numbers of experimental variables and allow new spectroscopic signals to be measured. We will also comment on higher-order two-dimensional spectroscopy. Finally, we will end by discussing excitation-induced spectroscopic artifacts.

For the theoretical description of nonlinear spectroscopy, there are a great number of texts that help form the foundation of this discussion and to which I refer the reader for additional information [41, 103, 104, 105].

Spectroscopy is the study of physical phenomena by the interaction of light and matter [106]. First, we recognize that matter is composed of charged particles (i.e. protons and electrons) and light is an electromagnetic field which can exert a force on charged particles. In the classical picture, an electromagnetic field exerts a force that depends on the form of the binding potential for the charged particles, the charge magnitudes, and the form and

amplitude of the electromagnetic field. It is this exerted force that allows light and matter to interact. Moreover, the acceleration of charged particles due to exerted electromagnetic forces allows matter to radiate new electromagnetic fields that form the heart of spectroscopy.

## 3.1 Linear Absorption Spectroscopy

In linear absorption, an electromagnetic field creates a macroscopic oscillating polarization as it propagates through a material:

$$P^{(1)}\left(\omega, \overrightarrow{k}\right) = \chi^{(1)}\left(\omega, \overrightarrow{k}\right) E_I^{(1)}\left(\omega, \overrightarrow{k}\right) \tag{3.1}$$

where $P^{(1)}\left(\omega, \overrightarrow{k}\right)$ is the first-order (linear) polarization as a function of frequency $\omega$ and wavevector $\overrightarrow{k}$, $\chi^{(1)}\left(\omega, \overrightarrow{k}\right)$ is the first-order susceptibility of the material, and $E_I^{(1)}\left(\omega, \overrightarrow{k}\right)$ is the spectral density of the incident electromagnetic field. The gradient of the generated linear polarization radiates a second electromagnetic field:

$$E_R^{(1)}\left(\omega, \overrightarrow{k}\right) = iP^{(1)}\left(\omega, \overrightarrow{k}\right) \tag{3.2}$$

that is dependent on the electronic resonances of the material. This radiating electromagnetic field is $\frac{\pi}{2}$ out of phase with the incident field and destructively interferes at the resonance energies of the material. The total electromagnetic field can be written as

$$\begin{aligned} E_{tot}^{(1)}\left(\omega, \overrightarrow{k}\right) &= E_I^{(1)}\left(\omega, \overrightarrow{k}\right) + E_R^{(1)}\left(\omega, \overrightarrow{k}\right) \\ &= E_I^{(1)}\left(\omega, \overrightarrow{k}\right)\left[1 + i\chi^{(1)}\left(\omega, \overrightarrow{k}\right)\right] \end{aligned} \tag{3.3}$$

assuming only a small change in the amplitude of the incident electromagnetic field. However, the intensity rather than the amplitude of the electromagnetic field is measured by a

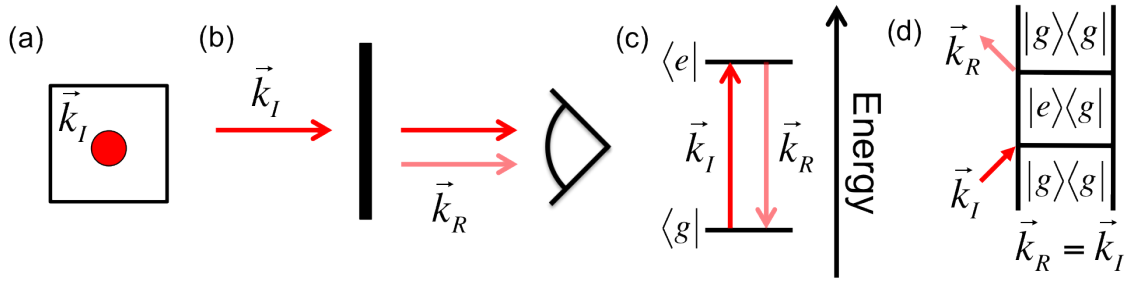


Figure 3.1: Linear absorption experiment. (a) Laser beam geometry. (b) Experimental diagram. (c) Energy level diagram. (d) Feynman diagram.

spectrometer. So, the measured spectral output takes the form

$$\begin{aligned} I_{tot}^{(1)}\left(\omega, \overrightarrow{k}\right) &= \left|E_{tot}^{(1)}\left(\omega, \overrightarrow{k}\right)\right|^2 \\ &= I_I^{(1)}\left(\omega, \overrightarrow{k}\right)\left|1+\chi^{(1)}\left(\omega, \overrightarrow{k}\right)\right|^2 \end{aligned} \tag{3.4}$$

Noting the susceptibility is a complex number $\chi^{(1)} = \chi_{\Re}^{(1)} + i\chi_{\Im}^{(1)}$ and assuming the susceptibility is small compared to the incident electromagnetic field $\chi^{(1)} \ll 1$, equation 3.4 reduces to

$$I_{tot}^{(1)}\left(\omega, \overrightarrow{k}\right) = I_I^{(1)}\left(\omega, \overrightarrow{k}\right)\left[1-2\chi_{\Im}^{(1)}\left(\omega, \overrightarrow{k}\right)\right] \tag{3.5}$$

In this case, the $1-2\chi_{\Im}^{(1)}\left(\omega, \overrightarrow{k}\right)$ term in 3.5 equation describes the destructive interference of the two electromagnetic fields and the imaginary component of the susceptibility describes the absorptive response of the material to the incident electromagnetic field. A linear absorption experiment is graphically illustrated in figure 3.1.

The susceptibility can also be recast in the time domain. The Fourier transform of the first-order susceptibility is called the linear response function:

$$R^{(1)}\left(t, \overrightarrow{k}\right) = \int_{-\infty}^{\infty} \chi^{(1)}\left(\omega, \overrightarrow{k}\right) \exp\left[-i2\pi\omega t\right] d\omega \tag{3.6}$$

The linear polarization generated in the material can also be recast in the time domain with

the temporal profile of the incident electromagnetic field $E_I^{(1)}\left(t, \overrightarrow{k}\right)$:

$$P^{(1)}\left(t, \overrightarrow{k}\right) = \int_{-\infty}^{t} R^{(1)}\left(t-\tau, \overrightarrow{k}\right) E_I^{(1)}\left(\tau, \overrightarrow{k}\right) d\tau \tag{3.7}$$

In the time domain, the linear polarization generated is a convolution of the response function with the incident electromagnetic field; while in the frequency domain, the polarization generated is the product of the susceptibility and the incident electromagnetic field. The polarization generated by the incident electromagnetic field acts as a source term that can be inserted into Maxwell's equations:

$$\nabla^2 E\left(t, \overrightarrow{k}\right) - \frac{1}{c^2}\frac{\partial^2 E\left(t, \overrightarrow{k}\right)}{\partial t^2} = \frac{4\pi}{c^2}\frac{\partial^2 P^{(1)}\left(t, \overrightarrow{k}\right)}{\partial^2 t} \tag{3.8}$$

and produces solutions for the polarization of the form

$$P^{(1)}\left(t, \overrightarrow{k}\right) = P^{(1)}(t) \exp\left[i\overrightarrow{k} \cdot \overrightarrow{r} - i\omega t\right] + c.c. \tag{3.9}$$

where $P^{(1)}(t)$ is an envelope function and radiates an electric field of the same form

$$E^{(1)}\left(t, \overrightarrow{k}\right) = E^{(1)}(t) \exp\left[i\overrightarrow{k} \cdot \overrightarrow{r} - i\omega t\right] + c.c. \tag{3.10}$$

Figure 3.2 illustrates an incident laser field, material resonance, and signal transmission in the time and frequency domains.

In the time domain, the linear polarization can be calculated using the transition dipole moment operator $\overrightarrow{\mu}(t)$ and the time-dependent density matrix $\rho(t)$:

$$P^{(1)}(t) = Tr\left(\overrightarrow{\mu}(t)\,\rho(t)\right) \tag{3.11}$$

where $Tr$ is the trace of a matrix. The density matrix can be calculated from the von

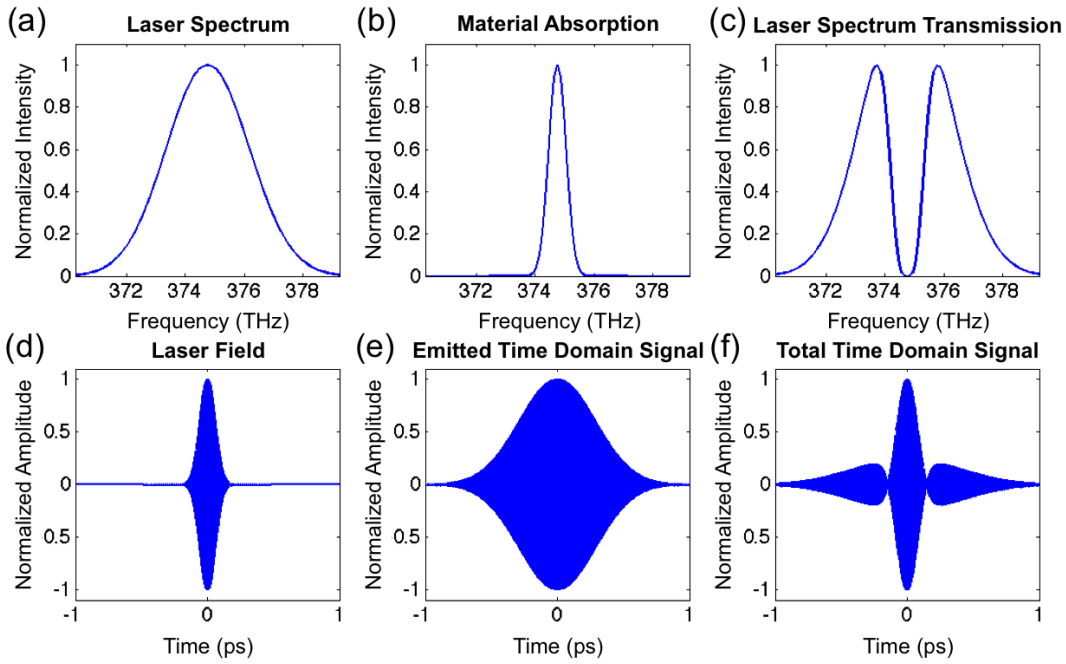


Figure 3.2: Linear absorption spectrum. (a) Incident laser spectrum. (b) Material absorption resonance. (c) Laser spectrum transmission. (d) Incident laser field. (e) Emitted time domain signal by the material. (f) Total time domain signal.

Neumann equation:

$$\rho\left(t\right)=-\frac{i}{\hbar}\int_{-\infty}^{t}dt_{1}\left[\hat{V}\left(t_{1}\right),\rho\left(0\right)\right] \tag{3.12}$$

where $[a,b]=ab-ba$ is the commutator operator and $\hat{V}\left(t\right)=-\overrightarrow{\mu}\left(t\right)\cdot\overrightarrow{E}\left(t\right)$ is the time-dependent component of the Hamiltonian, $\hat{H}\left(\mathrm{t}\right)=\hat{H}_{0}+\hat{V}\left(\mathrm{t}\right)$, describing the light-matter interaction. Substituting equation 3.12 into equation 3.11 and simplifying, we find the linear polarization can be written as

$$P^{(1)}\left(t\right)=\frac{i}{\hbar}\int_{0}^{\infty}d\tau\,E\left(t-\tau\right)Tr\left(\left[\overrightarrow{\mu}\left(\tau\right),\overrightarrow{\mu}\left(0\right)\right]\rho\left(0\right)\right) \tag{3.13}$$

with the change of variable $\tau=t-t_{1}$. Since the linear polarization is a convolution of the response function with the incident electromagnetic field, we observe that the linear response function is

$$R^{(1)}\left(\tau\right)=\frac{i}{\hbar}\theta\left(\tau\right)Tr\left(\left[\overrightarrow{\mu}\left(\tau\right),\overrightarrow{\mu}\left(0\right)\right]\rho\left(0\right)\right) \tag{3.14}$$

where $\theta(t)$ is the Heaviside step function.

Both the frequency and time domains are useful paradigms from which to understand spectroscopy. We will use both perspectives to think about nonlinear spectroscopy and understand the time-resolved experiments described in this thesis.

## 3.2 Third-Order Nonlinear Spectroscopy

With an understanding of first-order (linear) spectroscopy, we will now discuss third-order nonlinear spectroscopy. In third-order spectroscopy, we consider the case where there are three light matter interactions. In this case, the principles of linear spectroscopy are easily generalizable to higher-order. First, the polarization generated in a material by an electromagnetic field(s) can be expanded to higher-order:

$$P(\omega) = P^{(0)}(\omega) + P^{(1)}(\omega) + P^{(2)}(\omega) + P^{(3)}(\omega) + \cdots \tag{3.15}$$

$$P(t) = P^{(0)}(t) + P^{(1)}(t) + P^{(2)}(t) + P^{(3)}(t) + \cdots \tag{3.16}$$

In the frequency domain, the third-order polarization $P^{(3)}(\omega)$ in equation 3.15 can easily be written down as the product of the third-order susceptibility $\chi^{(3)}(\omega)$ and the spectral densities of the three incident electromagnetic fields:

$$P^{(3)}(\omega) = \chi^{(3)}(\omega) E_1(\omega) E_2(\omega) E_3(\omega) \tag{3.17}$$

In the time domain, the third-order polarization $P^{(3)}(t)$ in equation 3.16 is more difficult to write down as it requires the calculation of the third-order expansion of the density matrix $\rho^{(3)}(t)$ and results in a triple integral and a triple nested commutator:

$$P^{(3)}(t) = Tr\left(\overrightarrow{\mu}(t)\,\rho^{(3)}(t)\right) \tag{3.18}$$

$$\rho^{(3)}(t) = \left(-\frac{i}{\hbar}\right)^3 \int_{-\infty}^{t} dt_3 \int_{-\infty}^{t_3} dt_2 \int_{-\infty}^{t_2} dt_1 \left[-\overrightarrow{\mu}(t_3) \cdot \overrightarrow{E_3}(t_3), \right. \\ \left. \left[-\overrightarrow{\mu}(t_2) \cdot \overrightarrow{E_2}(t_2), \left[\overrightarrow{\mu}(t_1) \cdot \overrightarrow{E_1}(t_1), \rho(0)\right]\right]\right] \quad (3.19)$$

With the third-order expansion of the density matrix, we can write down the full third-order polarization:

$$P^{(3)}(t') = \left(\frac{i}{\hbar}\right)^3 \int_0^{\infty} dt \int_0^{\infty} dT \int_0^{\infty} d\tau \, \overrightarrow{E_3}(t'-t) \, \overrightarrow{E_2}(t'-t-T) \, \overrightarrow{E_1}(t'-t-T-\tau) \\ \times Tr\left(\left[\left[\left[\overrightarrow{\mu}(\tau+T+t), \overrightarrow{\mu}(\tau+T)\right], \overrightarrow{\mu}(\tau)\right], \overrightarrow{\mu}(0)\right]\rho(0)\right) \quad (3.20)$$

with the change of variables: $t_1 = t' - \tau - T - t$, $t_2 = t' - T - t$, $t_3 = t' - t$ and enforcing time ordering of the pulses $t_1 \leq t_2 \leq t_3$. Since the third-order polarization is a triple convolution of the response function with three incident electromagnetic fields, we observe from equation 3.20 that the third-order response function is

$$R^{(3)}(\tau, T, t) = \left(\frac{i}{\hbar}\right)^3 \theta(t)\,\theta(T)\,\theta(\tau)\; Tr\left(\left[\left[\left[\overrightarrow{\mu}(\tau+T+t), \overrightarrow{\mu}(\tau+T)\right], \overrightarrow{\mu}(\tau)\right], \overrightarrow{\mu}(0)\right]\rho(0)\right) \quad (3.21)$$

The triple nested commutator in equation 3.21 results in the sum of eight correlation functions at third-order: four are unique and the other four are their complex conjugates. The four unique correlation functions can be written as:

$$R^{(3)}(\tau, T, t) = \left(\frac{i}{\hbar}\right)^3 \theta(t)\,\theta(T)\,\theta(\tau) \sum_{i=1}^{4} \left[R_i^{(3)}(t, T, \tau) - R_i^{(3)*}(t, T, \tau)\right] \quad (3.22)$$

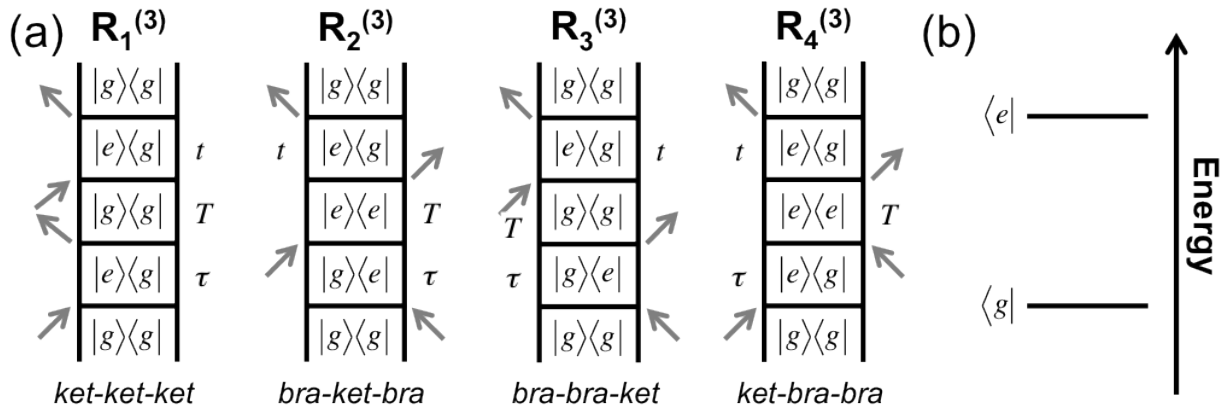


Figure 3.3: One-quantum Feynman diagrams. (a) Unique correlation functions of the third-order response function $R^{(3)}(\tau, T, t)$. (b) Two-level system energy level energy diagram.

$$R_1^{(3)}(\tau+T+t) = Tr\left[\overrightarrow{\mu}(\tau+T+t)\,\overrightarrow{\mu}(\tau+T)\,\overrightarrow{\mu}(\tau)\,\overrightarrow{\mu}(0)\,\rho(0)\right] \tag{3.23}$$

$$R_2^{(3)}(\tau+T+t) = Tr\left[\overrightarrow{\mu}(0)\,\overrightarrow{\mu}(\tau+T)\,\overrightarrow{\mu}(\tau+T+t)\,\overrightarrow{\mu}(\tau)\,\rho(0)\right] \tag{3.24}$$

$$R_3^{(3)}(\tau+T+t) = Tr\left[\overrightarrow{\mu}(0)\,\overrightarrow{\mu}(\tau)\,\overrightarrow{\mu}(\tau+T+t)\,\overrightarrow{\mu}(\tau+T)\,\rho(0)\right] \tag{3.25}$$

$$R_4^{(3)}(\tau+T+t) = Tr\left[\overrightarrow{\mu}(\tau)\,\overrightarrow{\mu}(\tau+T)\,\overrightarrow{\mu}(\tau+T+t)\,\overrightarrow{\mu}(0)\,\rho(0)\right] \tag{3.26}$$

The four correlation functions are distinct based on the number and order of their bra and ket interactions: $R_1^{(3)} = ket - ket - ket$, $R_2^{(3)} = bra - ket - bra$, $R_3^{(3)} = bra - bra - ket$, and $R_4^{(3)} = ket - bra - bra$. The Feynman diagrams of the four unique correlation functions for a two-level system are illustrated in figure 3.3.

### 3.2.1 Wavevector Matching

In general, third-order nonlinear spectroscopies involve multiple interacting beams. When the interacting beams have different geometries, their momenta (or wavevectors) must be conserved during the nonlinear process. Similarly, when the interacting pulses have finite spectral bandwidths, their energies must also be conserved. In third-order experiments, these

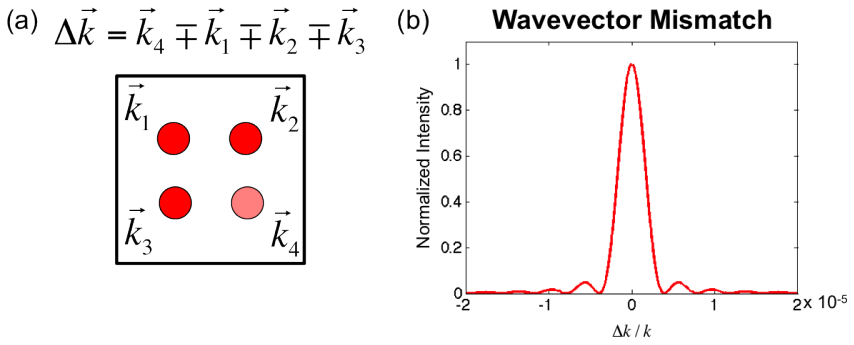


Figure 3.4: Wavevector matching. (a) BOXCARS beam geometry. (b) Wavevector mismatch dependent nonlinear signal intensity, where L = 1 μm and λ = 800 nm.

conservation laws are dependent on the nonlinear process and take the general form:

$$\overrightarrow{k}_4 = \pm\overrightarrow{k}_1 \pm \overrightarrow{k}_2 \pm \overrightarrow{k}_3 \tag{3.27}$$

$$\omega_4 = \pm\omega_1 \pm \omega_2 \pm \omega_3 \tag{3.28}$$

where $\overrightarrow{k}_i$ and $\omega_i$ are the wavevector and frequency components of beam $i$, respectively. Figure 3.4a illustrates a typical BOXCARS geometry. Energy conservation is fairly intuitive, while momentum conservation in nonlinear spectroscopy can be less so. However, it has been shown that the intensity of the nonlinear experiment strongly depends on momentum conservation:

$$I_4 \propto sinc^2\left(\frac{\Delta kL}{2\pi}\right) \tag{3.29}$$

where $\Delta k = k_4 \mp k_1 \mp k_2 \mp k_3$ is the wavevector mismatch or deviation from perfect momentum conservation and $L$ is the length of the nonlinear medium [107]. The dependence of the nonlinear signal intensity on the wavevector mismatch is illustrated in figure 3.4b.

An important consequence of momentum conservation is that signals of different nonlinear processes are radiated in different spatial directions depending on the number and type of interactions of each incident beam, called wavevector matching. Thus by controlling the geometry of the interacting beams, different third-order signals can be isolated by detection in a specific spatial direction. Additionally, the relative timing of the pulses composing

the interacting beams can be used to detect different four-wave mixing signals in the same direction–as in the case of transient grating and two-dimensional spectroscopies.

## 3.3 Nonlinear Spectroscopic Techniques

We will now discuss the most common third-order, nonlinear spectroscopies. We start with the conventional and intuitive pump-probe spectroscopy. From there, we will extend our discussion to transient grating spectroscopy. This discussion will naturally lead to a description of the four types of third-order, two-dimensional (2D) spectroscopy. Finally, we will end by generalizing our discussion of 2D spectroscopy to higher-orders.

### 3.3.1 Pump-Probe Spectroscopy

In the classical picture, pump-probe spectroscopy uses a strong pump pulse to excite a material and after some time delay a second weak probe pulse interrogates the excited state. The change in the transmission of the probe pulse (i.e. linear absorption) as a function of time delay is used to interrogate the temporal dynamics of the material. Such an experiment is graphically illustrated in figure 3.5.

In the quantum mechanical picture, two pulses are incident on a material with the first pulse contributing two field interactions and the second pulse contributing one field interaction. The first "pump" pulse (wavevector $\vec{k}_1$) creates an excited state population $|e\rangle\langle e|$, initiating population decay during the delay time $T$ between the first and second pulses. Additionally, if the excitation is coherent and the bandwidth sufficiently broad to cover multiple excited states, a coherence can be created between two excited states $|e'\rangle\langle e|$, initiating oscillations at the difference frequency $\omega_{e'e}$ and dephasing of the system during the delay time $T$. At some delay time $T$ later, the second "probe" pulse ($\vec{k}_2$) projects the system onto a coherence $|g\rangle\langle e|$ and creates a third-order polarization that radiates the pump-probe signal ($\overrightarrow{k}_{PP} = \pm\vec{k}_1 \mp \vec{k}_1 + \vec{k}_2 = \vec{k}_2$) in the direction of the probe pulse–called self-heterodyne

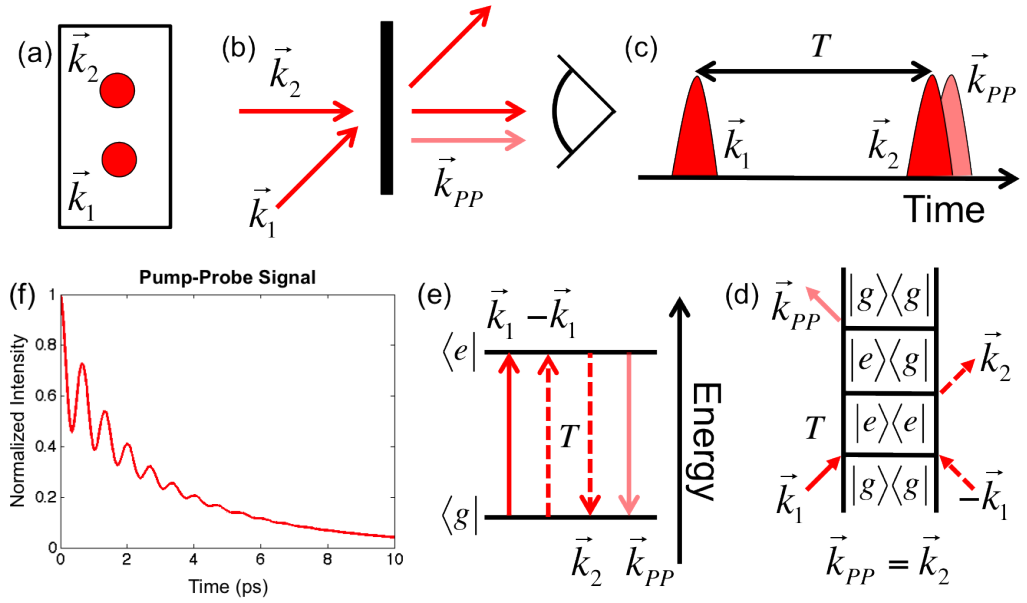


Figure 3.5: Pump-probe experiment. (a) Laser beam geometry. (b) Experimental diagram. (c) Pulse timing diagram. (d) Feynman diagram. (e) Energy level diagram. (d) Simulated emission energy-integrated pump-probe signal.

detection. In the frequency domain, the electromagnetic field amplitude of the pump-probe signal takes the form:

$$E^{(3)}_{Signal}\left(T,\omega_t\right) = i\chi^{(3)}_{PP}\left(T,\omega_t\right) E_1\left(T,\omega_t\right) E^*_1\left(T,\omega_t\right) E_2\left(T,\omega_t\right) \tag{3.30}$$

with contributions from all the correlation functions illustrated in figure 3.3 with the first time delay $\tau = 0$.

Similar to linear absorption, the pump-probe signal is locked $\frac{\pi}{2}$ out of phase from the probe pulse. Interference of the signal and probe pulses generates a change in the transmission of the probe pulse, which is measured in a spectrometer as a function of the delay time. The intensity of the transmitted electromagnetic field of the total pump-probe signal

$I^{(3)}_{PP}(T,\omega_t)$ is measured by a spectrometer. The measured spectral output takes the form:

$$\begin{aligned} I^{(3)}_{PP}(T,\omega_t) &= \left| E_2(T,\omega_t) + E^{(3)}_{Signal}(T,\omega_t) \right|^2 \\ &= I_2(T,\omega_t) - 2\chi^{(3)}_{PP:\Im}(T,\omega_t)\, I_1(T,\omega_t)\, I_2(T,\omega_t) \end{aligned} \tag{3.31}$$

under the assumption $E_1 \gg E_2 \gg \chi^{(3)}_{PP}$.

Pump-probe measurements are designed to interrogate the effect of the pump pulse on the transmittance of the probe pulse, thus the intensity change in the probe pulse $\Delta I^{(3)}_{PP}(T,\omega_t)$ is used to determine the temporal dynamics in the material:

$$\begin{aligned} \Delta I^{(3)}_{PP}(T,\omega_t) &= I^{(3)}_{PP}(T,\omega_t) - I_2(T,\omega_t) \\ &= -2\chi^{(3)}_{PP:\Im}(T,\omega_t)\, I_1(T,\omega_t)\, I_2(T,\omega_t) \end{aligned} \tag{3.32}$$

The pump-probe signal intensity in equation 3.31 and the change in probe transmission in equation 3.32 are directly analogous to the case of linear absorption in equation 3.5 under the influence of a pump pulse incident at a time delay $T$ prior to the probe pulse. The change in the transmission of the probe pulse occurs due to the imaginary (i.e. absorptive) component of the third-order susceptibility $\chi^{(3)}_{PP:\Im}$ because the electromagnetic field of the pump-probe signal is locked $\frac{\pi}{2}$ out of phase from the probe pulse.

### 3.3.2 Transient Grating Spectroscopy

In the classical picture, transient grating spectroscopy is an extension of pump-probe spectroscopy in which the pump and probe pulses are each split into two beams. First, the two time-coincident pump pulses are crossed at an angle $\theta$ in the material to create an excited state (transient) grating due to the interference of the two beams, illustrated in figure 3.6. The period of the transient grating is given by

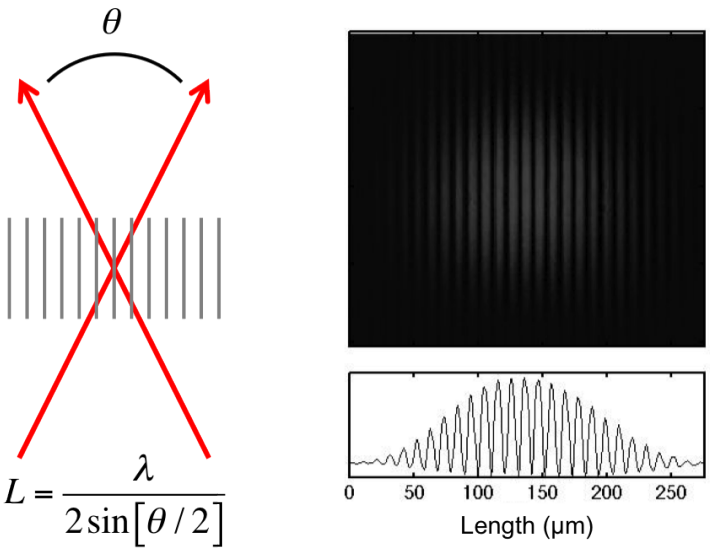


Figure 3.6: Transient grating spatial periodicity. Transient grating spatial periodicity $L = \lambda/2\sin[\theta/2]$, where $\lambda$ is the center wavelength of the two incident beams and $\theta$ is the angle between them.

$$L = \frac{\lambda}{2\sin(\theta/2)} \tag{3.33}$$

where $\lambda$ is the central wavelength of the pump pulses. At some delay time $T$ later, a third probe pulse diffracts off the excited state grating into the direction of a fourth heterodyning pulse. The change in the diffraction of the probe pulse as a function of time delay is used to measure the temporal dynamics of the material. The components of a transient grating experiment are illustrated in figure 3.7. The spatially periodicity of the transient grating can also be used to measure transport [108, 109, 110].

In the quantum mechanical picture, three pulses are incident on a material with each contributing a single field interaction. The first pulse (wavevector $\vec{k}_1$) creates a coherence between the ground state and an excited electronic state $|g\rangle\langle e|$. The second pulse ($\vec{k}_2$) is time-coincident with the first pulse ($\tau = 0$) and creates an excited state population $|e\rangle\langle e|$, initiating population decay of the system during the delay time $T$ between the second and third pulses. Additionally, if the excitation is coherent and the bandwidth of the pump pulses is sufficiently broad to cover multiple excited states, a coherence can be created

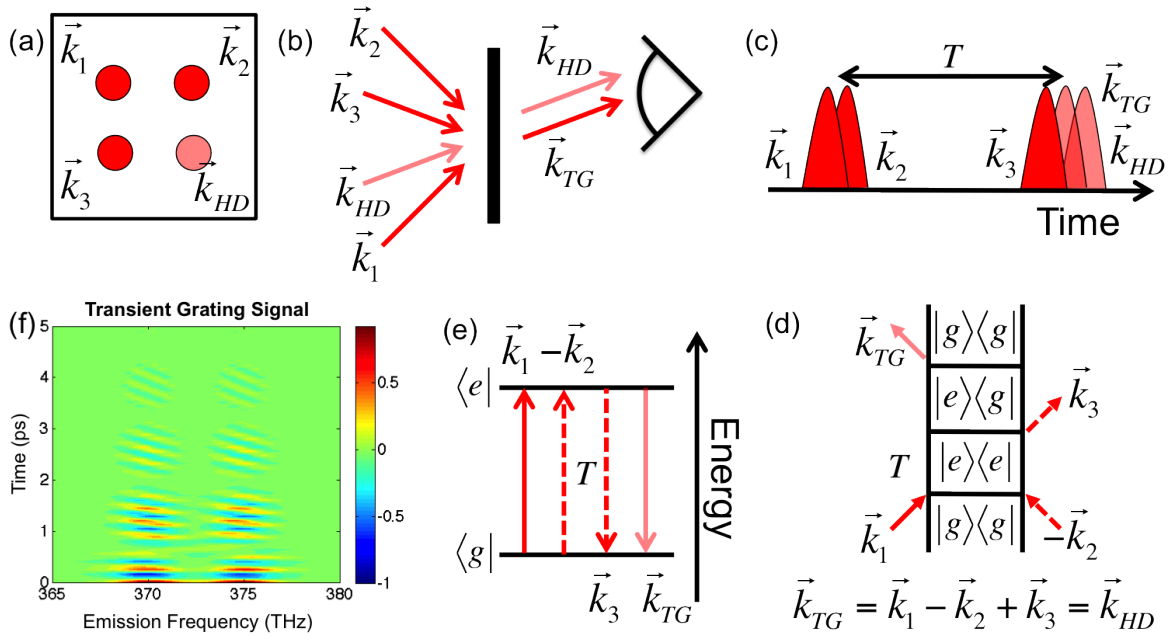


Figure 3.7: Transient grating experiment. (a) Laser beam geometry. (b) Experimental diagram. (c) Pulse timing diagram. (d) Feynman diagram. (e) Energy level diagram. (f) Simulated transient grating signal.

between two excited states $|e'\rangle\langle e|$, initiating oscillations at the difference frequency $\omega_{e'e}$ and dephasing of the system during the delay time $T$. At some delay time $T$ later, the third pulse ($\vec{k}_3$) projects the system onto a coherence $|g\rangle\langle e|$ and creates a third-order polarization that radiates the transient grating signal ($\overrightarrow{k}_{TG} = \pm\vec{k}_1 \mp \vec{k}_2 + \vec{k}_3$). The emitted signal is heterodyne-detected with a fourth pulse ($\overrightarrow{k}_4 = \overrightarrow{k}_{TG}$). In the frequency domain, the electromagnetic field amplitude of the transient grating signal takes the form:

$$E^{(3)}_{Signal}(T,\omega_t) = i\chi^{(3)}_{TG}(T,\omega_t)\, E_1(T,\omega_t)\, E_2^*(T,\omega_t)\, E_3(T,\omega_t) \tag{3.34}$$

with contributions from all the correlation functions illustrated in figure 3.3 with the first time delay $\tau = 0$.

Unlike pump-probe spectroscopy, the transient grating signal is not self-heterodyned. The phase between the signal and the fourth heterodyning pulse $\Delta\phi_{HD}$ can be experimentally controlled. Thus, the electromagnetic field intensity of the total transient grating signal

$I^{(3)}_{TG}(T,\omega_t)$ takes the form:

$$\begin{aligned} I^{(3)}_{TG}(T,\omega_t) &= \left| E_{HD}(T,\omega_t)\exp(i\Delta\phi_{HD}) + E^{(3)}_{Signal}(T,\omega_t) \right|^2 \\ &= I_{HD}(T,\omega_t) - 2\left[\chi^{(3)}_{TG:\Re}(T,\omega_t)\sin(\Delta\phi_{HD}) + \chi^{(3)}_{TG:\Im}(T,\omega_t)\cos(\Delta\phi_{HD})\right] \\ &\quad \times E_1(T,\omega_t)\,E_2^*(T,\omega_t)\,E_3(T,\omega_t)\,E^*_{HD}(T,\omega_t) \end{aligned} \tag{3.35}$$

under the assumption $E_i \gg \chi^{(3)}_{TG}$. When $\Delta\phi_{HD} = \pi\left(n+\frac{1}{2}\right)$ where $n$ is an integer, the electromagnetic field intensity of the transient grating signal is analogous to the pump-probe case (equation 3.31):

$$I^{(3)}_{TG}(T,\omega_t) = I_{HD}(T,\omega_t) - 2\chi^{(3)}_{TG:\Im}(T,\omega_t)\,E_1(T,\omega_t)\,E_2^*(T,\omega_t)\,E_3(T,\omega_t)\,E^*_{HD}(T,\omega_t) \tag{3.36}$$

and the dynamics related to the imaginary (i.e. absorptive) component of the third-order susceptibility $\chi^{(3)}_{TG:\Im}$ are measured. When $\Delta\phi_{HD} = n\pi$ where $n$ is an integer, the transient grating signal reveals the dynamics related to the real (i.e. dispersive) component of the third-order susceptibility $\chi^{(3)}_{TG:\Re}$:

$$I^{(3)}_{TG}(T,\omega_t) = I_{HD}(T,\omega_t) - 2\chi^{(3)}_{TG:\Re}(T,\omega_t)\,E_1(T,\omega_t)\,E_2^*(T,\omega_t)\,E_3(T,\omega_t)\,E^*_{HD}(T,\omega_t) \tag{3.37}$$

In transient grating spectroscopy, separation of the pump and probe pulses each into two beams creates more experimental input parameters that allow both the absorptive and dispersive components of the third-order susceptibility to be measured [111]. Additionally, the spatial periodicity of the transient grating allows measurement of transport properties. Thus, we can see that increasing the number of experimental input parameters increases the number and type of measurable spectroscopic signals.

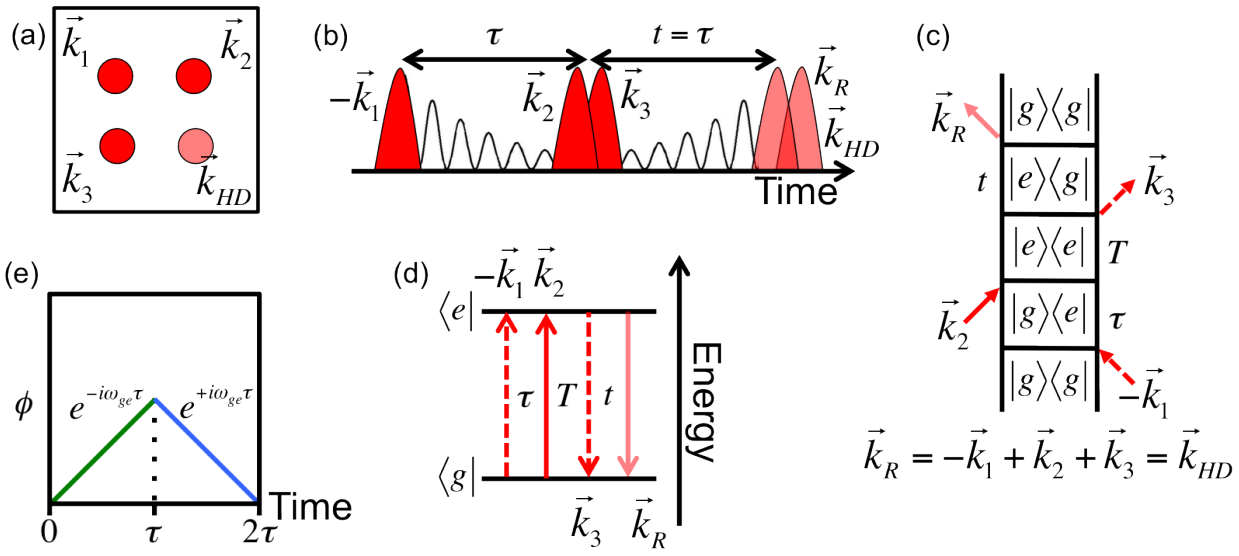


Figure 3.8: Two-dimensional rephasing experiment. (a) Laser beam geometry. (b) Pulse timing diagram. (c) Feynman diagram. (d) Energy level diagram. (e) Time-dependent phase evolution.

### 3.3.3 Two-Dimensional Rephasing (Photon Echo) Spectroscopy

In our discussion of 2D spectroscopy [39, 40], we will start with the quantum mechanical picture because the classical picture is less intuitive than those for pump-probe and transient grating spectroscopies. Before we begin, we note that 2D spectroscopy is analogous to transient grating spectroscopy in that it requires the interaction of three pulses in a material and a fourth heterodyning pulse to detect the signal. However, we increase the number of experimental input parameters by changing the time delay between the first and second pulses to measure new spectroscopic signals.

In a 2D rephasing measurement (illustrated in figure 3.8), three pulses are incident on a material with each contributing a single field interaction. The first pulse (wavevector $-\vec{k}_1$) creates a coherence between the ground and an excited electronic state $|g\rangle\langle e|$, initiating oscillations at the central frequency $\omega_{ge}$ and dephasing of the system during the excitation time $\tau$ between the first and second pulses. Subsequently, the second pulse ($\vec{k}_2$) creates an excited state population $|e\rangle\langle e|$ that decays during the population time $T$ between the second and third pulses. Additionally, if the excitation is coherent and the bandwidth of

the first two pulses is sufficiently broad to cover multiple excited states, a coherence can be created between two excited states $|e'\rangle\langle e|$, initiating oscillations at the difference frequency $\omega_{e'e}$ and dephasing of the system during the delay time $T$. Finally, the third pulse ($\vec{k}_3$) creates a coherence $|e\rangle\langle g|$, conjugate to that of the excitation time, initiating oscillations and rephasing of the inhomogeneous frequency components of the system around the central frequency $\omega_{ge}$ during the emission time $t$ after the third pulse. At time $t = \tau$, the system is rephased and the constructive superposition of the frequency components is maximized and emits a photon echo ($\overrightarrow{k}_R = -\vec{k}_1 + \vec{k}_2 + \vec{k}_3$). The emitted signal is heterodyne-detected with a fourth pulse ($\vec{k}_4 = \overrightarrow{k}_{TG}$) by spectral interferometry to recover the full electric field. In the frequency domain, the electromagnetic field amplitude of the rephasing signal takes the form:

$$E^{(3)}_{Signal}(\tau, T, \omega_t) = i\chi^{(3)}_R(\tau, T, \omega_t) E^*_1(\tau, T, \omega_t) E_2(\tau, T, \omega_t) E_3(\tau, T, \omega_t) \tag{3.38}$$

with contributions from the $R^{(3)}_2$ and $R^{(3)}_3$ correlation functions illustrated in figure 3.3.

The total rephasing signal intensity is measured by a spectrometer as a function of the excitation time, $I^{(3)}_R(\tau, T, \omega_t)$, and subsequently Fourier transformed to produce the 2D rephasing spectrum, $I^{(3)}_R(\omega_\tau, T, \omega_t)$, illustrated in figure 3.9. The electromagnetic field intensity of the rephasing signal is analogous to the transient grating case (equation 3.35) with the addition of the excitation time delay $\tau$:

$$\begin{aligned} I^{(3)}_R(\omega_t, T, \omega_t) &= I_{HD}(\omega_t, T, \omega_t) - 2\left[\chi^{(3)}_{R:\Re}(\omega_t, T, \omega_t)\sin(\phi_{HD}) + \chi^{(3)}_{R:\Im}(\omega_t, T, \omega_t)\cos(\phi_{HD})\right] \\ &\quad \times E^*_1(\omega_t, T, \omega_t) E_2(\omega_t, T, \omega_t) E_3(\omega_t, T, \omega_t) E^*_{HD}(\omega_t, T, \omega_t) \end{aligned} \tag{3.39}$$

The rephasing of the inhomogeneous components of the system during the emission time $t$ allows the homogeneous linewidth of the material resonance to be measured by 2D rephasing spectroscopy. In the 2D rephasing spectrum (figure 3.9), the diagonal and anti-diagonal linewidths correspond to the inhomogeneous ($\Gamma$) and homogeneous ($\Delta$) linewidths, respec-

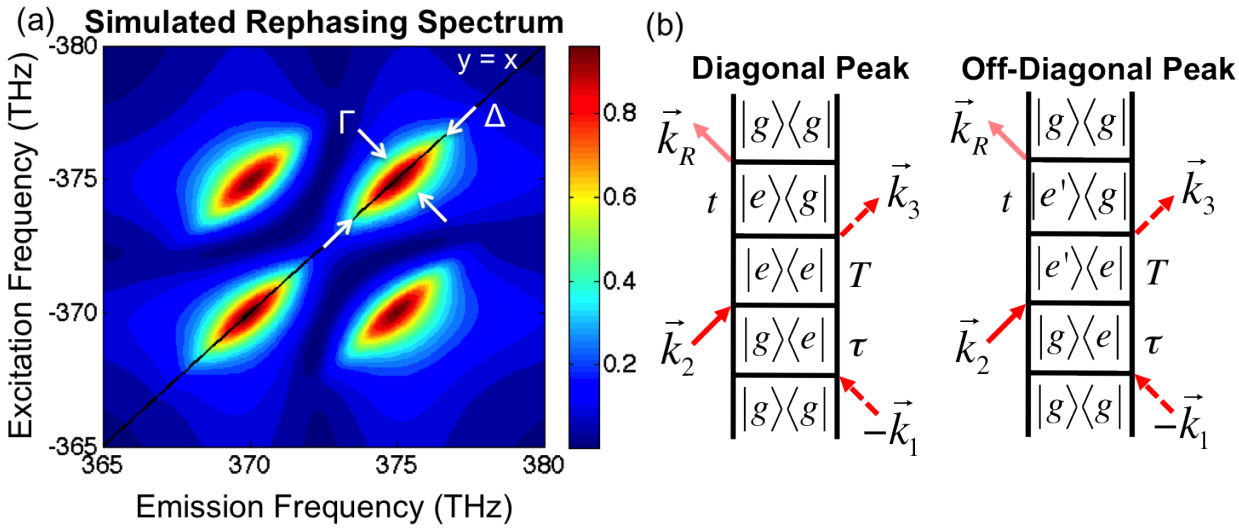


Figure 3.9: Two-dimensional rephasing spectrum. (a) Simulated rephasing spectrum reveals the homogenous Γ and inhomogeneous Δ linewidths. (b) Diagonal and off-diagonal Feynman diagrams.

tively. The ability of 2D rephasing experiments to measure homogeneous linewidths can be understood in the classical picture.

The first 2D rephasing spectroscopy experiments were performed by nuclear magnetic resonance (NMR) using electromagnetic waves in the MHz to GHz range to interrogate nuclear magnetic spin dynamics, illustrated in figure 3.10 [112]. In this experiment, a strong static magnetic field $\overrightarrow{B}$ is used to align the magnetic nuclear spins of atoms or molecules. An electromagnetic pulse perpendicular to static magnetic field aligns some of the nuclear spins in the plane. Once the electromagnetic pulse is gone, the nuclear spins in the plane begin to precess due to the torque $\overrightarrow{\tau}$ exerted on the magnetic dipole moment $\overrightarrow{\mu}_B$ by the perpendicular magnetic field, $\overrightarrow{\tau} = \overrightarrow{\mu}_B \times \overrightarrow{B}$. The angular frequency of precession can be written as $\omega_B = -\gamma B$ , where $\gamma = \frac{q}{2m}$ is the gyromagnetic ratio with $q$ the charge of the particle, $m$ the mass of the particle, and $B$ the amplitude of the static magnetic field. Because the angular frequency of precession is dependent on the charge and mass of the particle, the nuclear spins spread out according to their gyromagnetic ratios during the excitation time $\tau$. After some variable excitation time $\tau$ later, a second electromagnetic pulse antiparallel

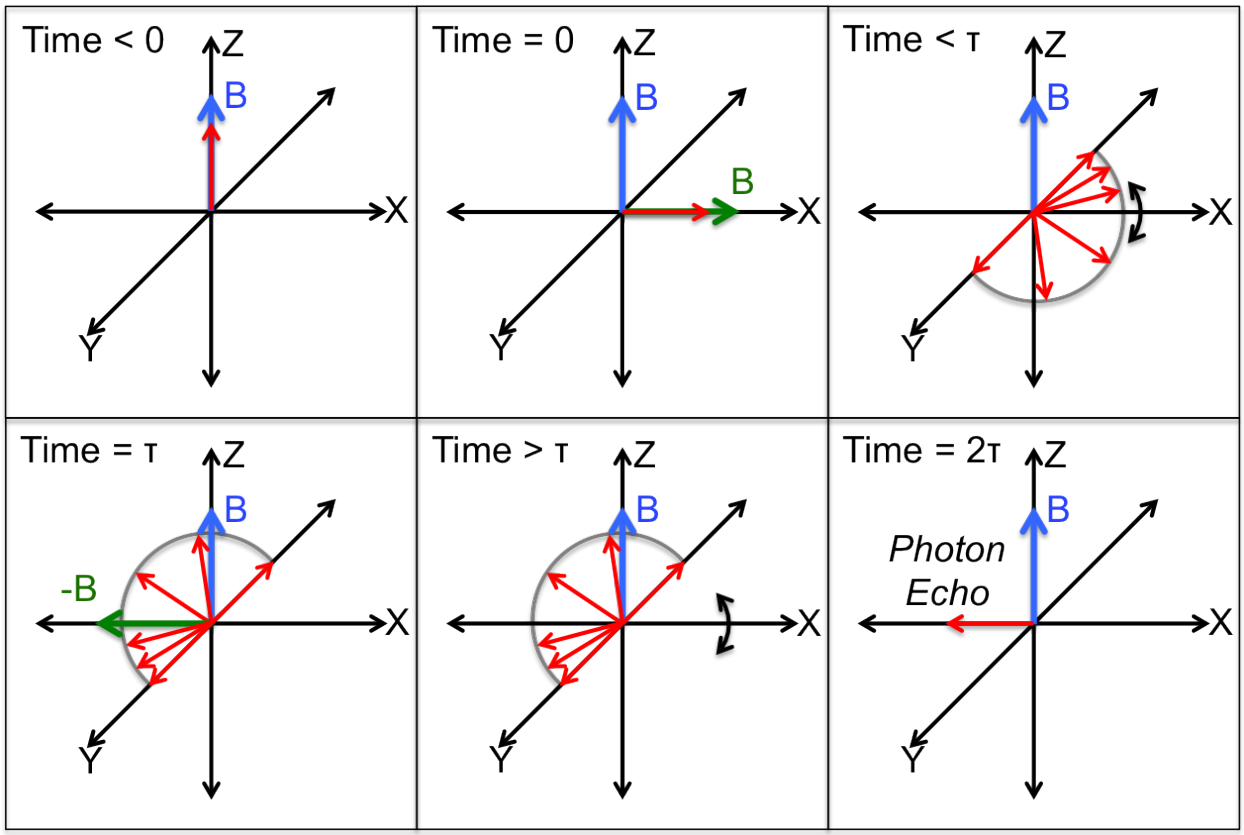


Figure 3.10: Two-dimensional spin echo in NMR. (1) Nuclear magnetic spins are aligned by a strong static field $B_z$. (2) A perpendicular magnetic pulse $B_x$ aligns a subset of nuclear spins into the $xy$ plane. (3) Nuclear spins in the $xy$ plane precess at different frequencies according to their mass and charge due to the torque exerted by the static magnetic field $B_z$. (4) At some delay time $\tau$ later, a second magnetic pulse $-B_x$ flips the nuclear spins in the $xy$ plane. (5) The nuclear spins begin to converge in the $xy$ plane. (6) At $2\tau$, the nuclear spins realign and their macroscopic oscillating polarization radiates a spin echo.

to the first pulse flips the nuclear spins in the plane. Once the electromagnetic field is gone, the nuclear spins continue to precess in the same direction. However, since the nuclear spins have been flipped in the plane, the nuclear spins begin to converge during the emission time $t$. When $t = \tau$, the nuclear spins are realigned in the plane and their macroscopic oscillating polarization emits a photon echo.

2D rephasing experiments of excited electronic states are analogous to the case of nuclear magnetic spins in NMR. The first pulse ($-\vec{k}_1$) creates multiple excited state coherences that initiate oscillations at their resonance frequencies. During the excitation time $\tau$, the system dephases due to differences in the resonance frequencies. After some variable excitation time $\tau$ later, the second ($\vec{k}_2$) and third ($\vec{k}_3$) pulses ($T = 0$) "flip" the system by creating the coherences conjugate to those during the excitation time. During the excitation time $t$, the system rephases. When $t = \tau$, the rephasing of the excited states is maximized and their macroscopic oscillating polarization emits a photon echo.

### 3.3.4 Two-Dimensional Non-Rephasing Spectroscopy

In a 2D non-rephasing measurement (illustrated in figure 3.11), three pulses are incident on a material with each contributing a single field interaction. The first pulse (wavevector $\vec{k}_1$) creates a coherence between the ground and an excited electronic state $|e\rangle\langle g|$ , initiating oscillations at the central frequency $\omega_{eg}$ and dephasing of the system during the excitation time $\tau$ between the first and second pulses. Subsequently, the second pulse ($-\vec{k}_2$) creates an excited state population $|e\rangle\langle e|$ that decays during the population time $T$ between the second and third pulses. Additionally, if the excitation is coherent and the bandwidth of the first two pulses is sufficiently broad to cover multiple excited states, a coherence can be created between two excited states $|e\rangle\langle e'|$, initiating oscillations at the difference frequency $\omega_{ee'}$ and dephasing of the system during the delay time $T$. Finally, the third pulse ($\vec{k}_3$) creates a coherence $|e\rangle\langle g|$, the same as that of the excitation time, initiating oscillations and further dephasing of the system during the emission time $t$ after the third pulse. During the emission

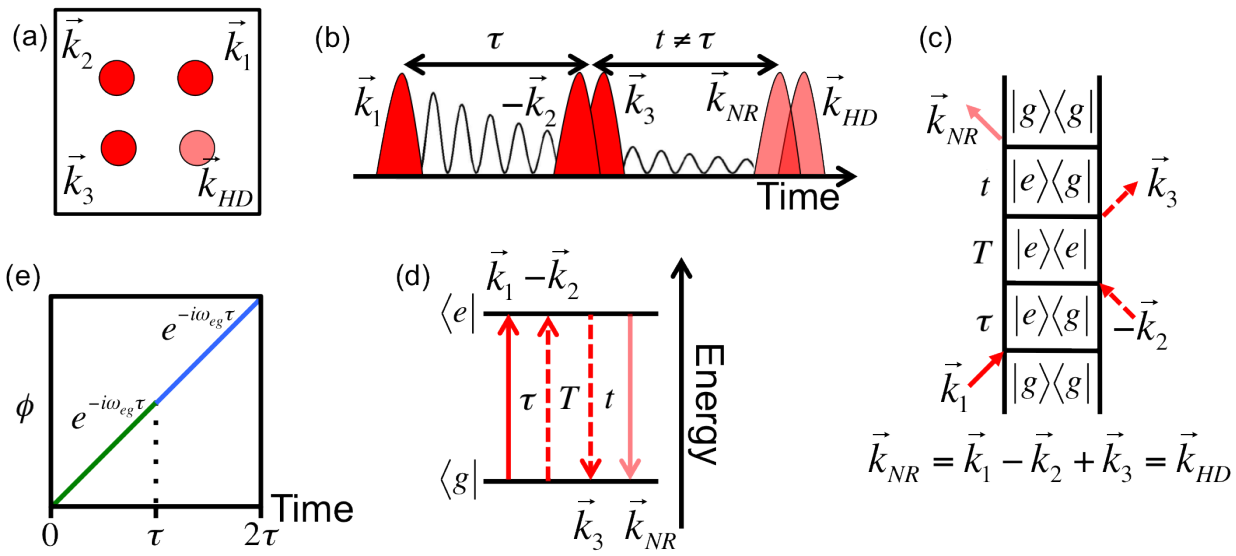


Figure 3.11: Two-dimensional non-rephasing experiment. (a) Laser beam geometry. (b) Pulse timing diagram. (c) Feynman diagram. (d) Energy level diagram. (e) Time-dependent phase evolution.

time $t$, the third-order polarization generated by the three incident pulses radiates to produce the non-rephasing signal ($\vec{k}_{NR} = \vec{k}_1 - \vec{k}_2 + \vec{k}_3$). The emitted signal is heterodyne-detected with a fourth pulse ($\vec{k}_4 = \vec{k}_{NR}$) by spectral interferometry to recover the full electric field. In the frequency domain, the electromagnetic field amplitude of the non-rephasing signal takes the form:

$$E^{(3)}_{Signal}(\tau, T, \omega_t) = i\chi^{(3)}_{NR}(\tau, T, \omega_t)\, E_1(\tau, T, \omega_t)\, E_2^*(\tau, T, \omega_t)\, E_3(\tau, T, \omega_t) \tag{3.40}$$

with contributions from the $R_1^{(3)}$ and $R_4^{(3)}$ correlation functions illustrated in figure 3.3.

The emitted signal is measured by a spectrometer as a function of the excitation time, $I^{(3)}_{NR}(\tau, T, \omega_t)$, and subsequently Fourier transformed to produce the 2D non-rephasing spectrum, $I^{(3)}_{R}(\omega_\tau, T, \omega_t)$, illustrated in figure 3.12. The electromagnetic field intensity of the non-rephasing signal is analogous to the rephasing signal (equation 3.39):

$$\begin{aligned} I^{(3)}_{NR}(\omega_t, T, \omega_t) &= I_{HD}(\omega_t, T, \omega_t) - 2\left[\chi^{(3)}_{NR:\Re}(\omega_t, T, \omega_t)\sin(\phi_{HD}) + \chi^{(3)}_{NR:\Im}(\omega_t, T, \omega_t)\cos(\phi_{HD})\right] \\ &\quad \times E_1(\omega_t, T, \omega_t)\, E_2^*(\omega_t, T, \omega_t)\, E_3(\omega_t, T, \omega_t)\, E^*_{HD}(\omega_t, T, \omega_t) \end{aligned} \tag{3.41}$$

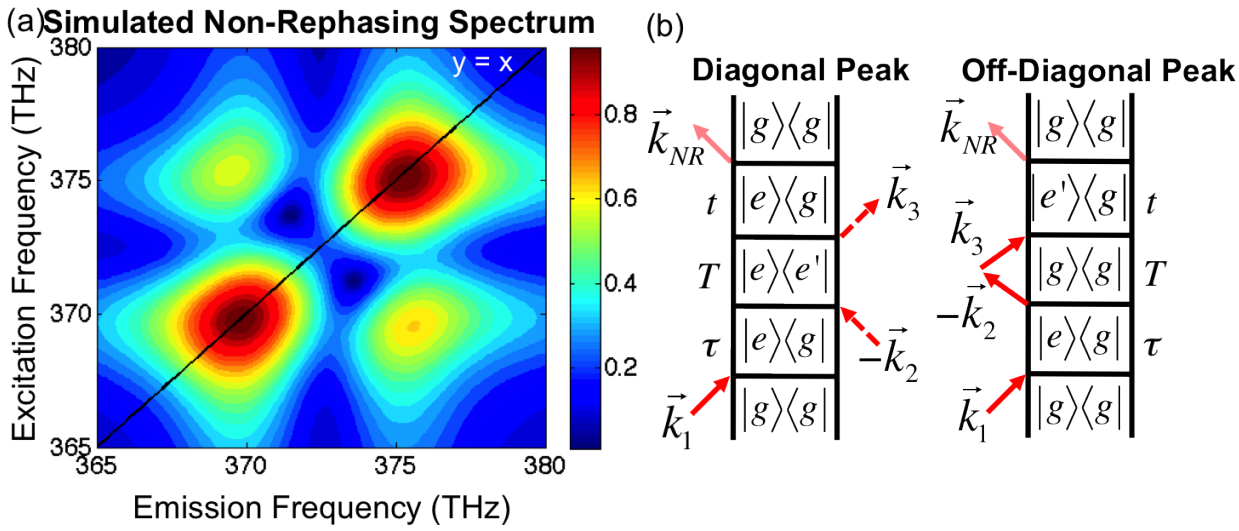


Figure 3.12: Two-dimensional non-rephasing spectrum. (a) Simulated non-rephasing spectrum. (b) Diagonal and off-diagonal Feynman diagrams.

Interpretation of 2D rephasing and non-rephasing spectra (figures 3.9 and 3.12, respectively) is very similar. Diagonal peaks correspond to spectral features in the linear absorption spectrum, while off-diagonal peaks demonstrate coupling between spectral features but do not reveal how features are coupled–often through a common ground state. By measuring multiple 2D spectra as a function of the population time $T$, population transfer and coherent coupling between excited states can be measured. Coherent coupling manifests itself differently in rephasing and non-rephasing spectra. In the rephasing spectrum, off-diagonal peaks oscillate at the difference frequency of the coupled excited states as a function of the population time $T$. In the non-rephasing spectrum, diagonal peaks oscillate. Collecting 2D spectra with sufficient population time resolution, a 3D spectrum can be generated that fully characterizes the third-order spectroscopic response of the interrogated excited states [63].

### 3.3.5 Two-Dimensional Correlation Spectroscopy

The astute reader will have noticed that neither the rephasing nor the non-rephasing 2D spectra had contributions from all the correlation functions for the third-order response function. The rephasing spectrum corresponds to the $R_1^{(3)}$ and $R_4^{(3)}$ correlation functions and

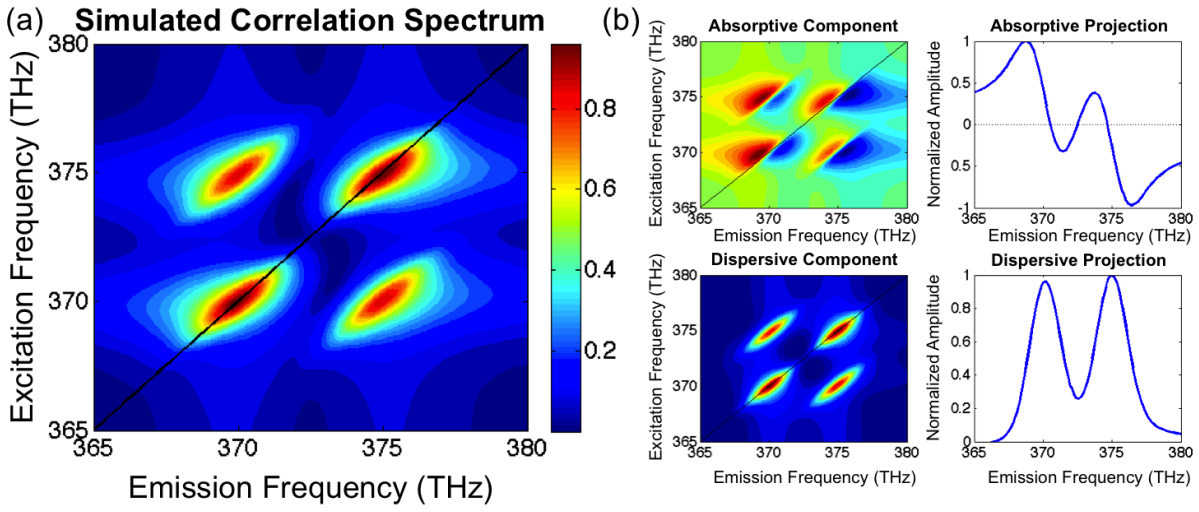


Figure 3.13: Two-dimensional correlation spectrum. (a) Simulated correlation spectrum. (b) Absorptive and dispersive components and excitation energy-integrated projections.

the non-rephasing spectrum to the $R_2^{(3)}$ and $R_3^{(3)}$ correlation functions in figure 3.3. Because neither comprises the full set of correlation functions, the 2D spectra have a phase twist and result in imaginary and real components that no longer correspond to the absorptive or dispersive components, respectively, but rather to linear combinations [113].

To separate the absorptive and dispersive components of the 2D signal, the equally weighted rephasing and non-rephasing contributions must be summed. The 2D correlation spectrum contains all the correlation functions of the third-order response, eliminating the phase twist and resulting in a spectrum for which the absorptive and dispersive components are separable. Figure 3.13 shows a 2D correlation spectrum and the separable absorptive and dispersive components of the signal.

### 3.3.6 Two-Dimensional Two-Quantum Spectroscopy

In a two-quantum measurement (illustrated in figure 3.14) [114, 61], three pulses are incident on a material with each contributing a single field interaction. The first pulse (wavevector $\overrightarrow{k}_1$) creates a coherence between the ground state and an excited electronic state $|g\rangle\langle e|$. The second pulse ($\overrightarrow{k}_2$) is time-coincident with the first pulse ($\tau = 0$) and creates a two-quantum

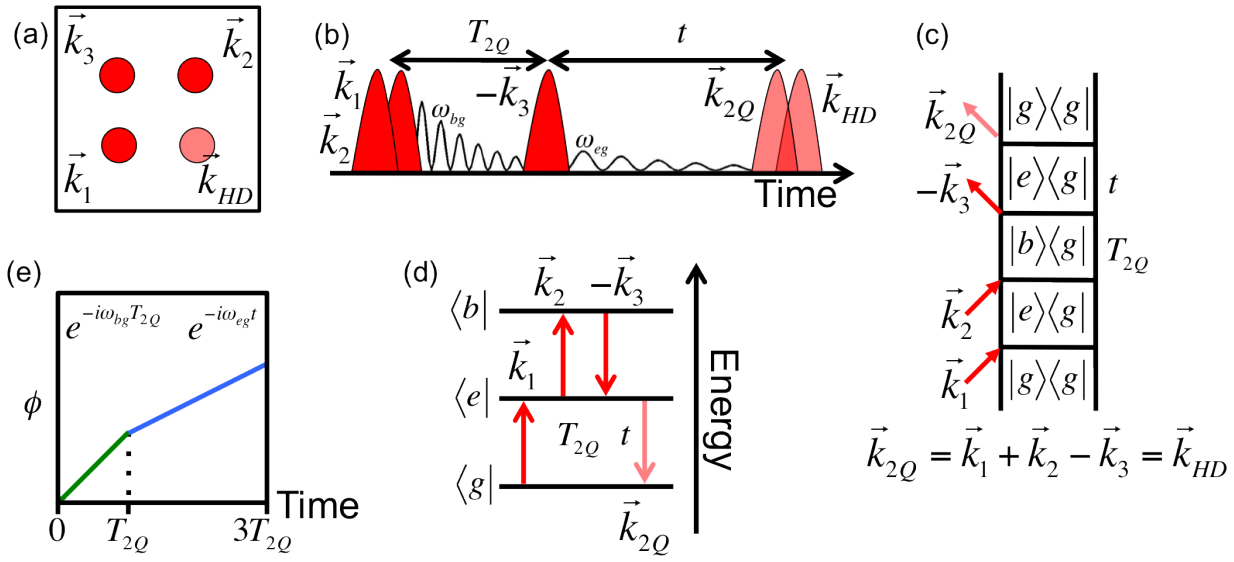


Figure 3.14: Two-dimensional two-quantum experiment. (a) Laser beam geometry. (b) Pulse timing diagram. (c) Feynman diagram. (d) Energy level diagram. (e) Time-dependent phase evolution.

coherence between the ground state and a doubly excited electronic state $|g\rangle\langle b|$, initiating oscillations at the two-quantum frequency $\omega_{gb}$. At some two-quantum time $T_{2Q}$ later, the third pulse ($-\vec{k}_3$) projects the system onto a one-quantum coherence $|g\rangle\langle e|$ and creates a third-order polarization that radiates the two-quantum signal ($\vec{k}_{2Q} = \vec{k}_1 + \vec{k}_2 - \vec{k}_3$). The emitted signal is heterodyne-detected with a fourth pulse ($\vec{k}_4 = \vec{k}_{2Q}$) by spectral interferometry to recover the full electric field. In the frequency domain, the electromagnetic field amplitude of the two-quantum signal takes the form:

$$E^{(3)}_{Signal}(0, T_{2Q}, \omega_t) = i\chi^{(3)}_{2Q}(0, T_{2Q}, \omega_t)\, E_1(0, T_{2Q}, \omega_t)\, E_2(0, T_{2Q}, \omega_t)\, E^*_3(0, T_{2Q}, \omega_t) \qquad (3.42)$$

with the related correlation functions illustrated in figure 3.15.

The emitted signal is measured by a spectrometer as a function of the two-quantum time, $I^{(3)}_{2Q}(0, T_{2Q}, \omega_t)$, and subsequently Fourier transformed to produce the two-quantum spectrum, $I^{(3)}_{2Q}(0, \omega_{2Q}, \omega_t)$, illustrated in figure 3.16. The electromagnetic field intensity of the two-quantum signal is analogous to the rephasing and non-rephasing signals (equations

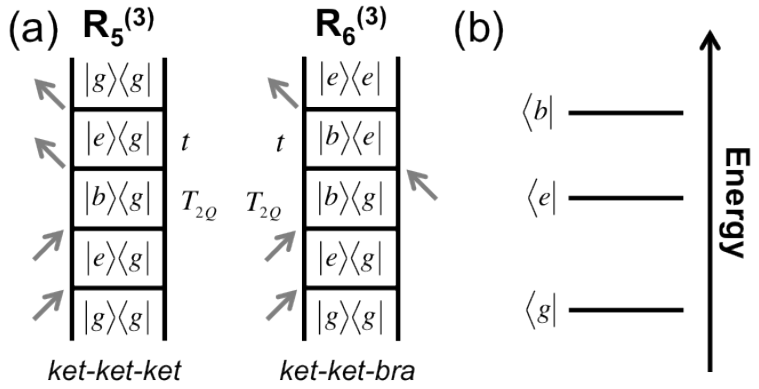


Figure 3.15: Two-quantum Feynman diagrams. (a) Unique correlation functions of the third-order, two-quantum response function $R_{2Q}^{(3)}(0, T_{2Q}, t)$. (b) Three-level system energy level energy diagram, including the ground $g$, single-exciton $e$, and biexciton $b$ manifolds.

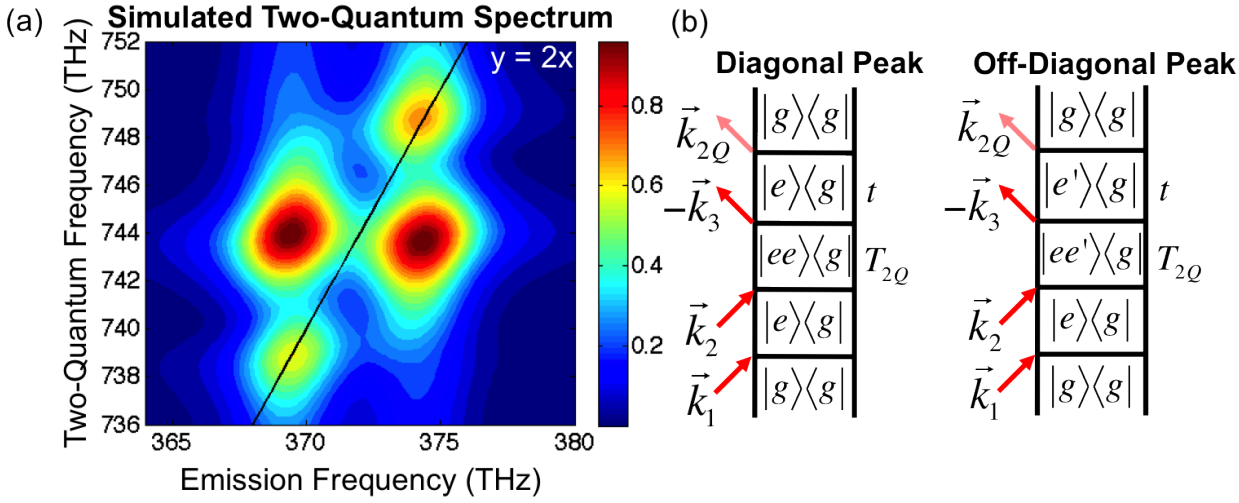


Figure 3.16: Two-dimensional two-quantum spectrum. (a) Simulated two-quantum spectrum. (b) Diagonal and off-diagonal Feynman diagrams.

3.39 and 3.41, respectively):

$$
\begin{aligned}
I_{2Q}^{(3)}\left(0,T_{2Q},\omega_t\right) &= I_{HD}\left(0,T_{2Q},\omega_t\right) \\
&\quad -2\left[\chi_{2Q:\Re}^{(3)}\left(0,T_{2Q},\omega_t\right)\sin\left(\phi_{HD}\right)+\chi_{2Q:\Im}^{(3)}\left(0,T_{2Q},\omega_t\right)\cos\left(\phi_{HD}\right)\right] \\
&\quad \times E_1\left(0,T_{2Q},\omega_t\right)E_2\left(0,T_{2Q},\omega_t\right)E_3^*\left(0,T_{2Q},\omega_t\right)E_{HD}^*\left(0,T_{2Q},\omega_t\right)
\end{aligned}
\tag{3.43}
$$

In the two-quantum spectrum, the excitation energy (called the two-quantum energy) is twice the magnitude of the rephasing and non-rephasing spectra, while the emission energy remains the same. The spectral features of two-particle correlations lie on the $y = 2x$ line rather than the $y = x$ line as in the case of one-particle correlations in the rephasing and non-rephasing spectra. Spectral features on the $y = 2x$ line correspond with two correlated particles of the same type ($AA$ correlations), while off-diagonal features correspond with two correlated particles of different types (mixed $AB$ correlations). Deviation of the two-quantum energy of the two-particle correlation from the sum of their constituent particle energies reveals the two-particle binding energy (or anharmonicity), $\Delta E_{2P} = (E_{p1} + E_{p2}) - E_{2P}$. Direct observation of two-particle correlations well separated from strong one-particle signals using 2D two-quantum spectroscopy (unlike one-quantum spectroscopies) is a fundamental experimental advantage that has revealed substantial information about the types, energetic properties, and temporal dynamics of correlated systems.

### 3.3.7 Higher-Order Multi-Quantum Spectroscopy

Correlations of more than two excitations can be measured using higher-order spectroscopies. To date, three correlated excitons in GaAs quantum wells and four correlated exciton-polaritons in GaAs quantum wells embedded in a microcavity have been measured using fifth- and seventh-order spectroscopies [62, 100]. Qualitatively, these experiments are analogous to third-order two-quantum spectroscopy. A correlation of $N$ particles can be measured with an experiment that creates an $N$-quantum coherence between the ground

and $N$-particle state $|N\rangle\langle g|$ by $N$ field interactions. The dynamics of the $N$-particle correlation are measured by the oscillations at the $N$-quantum frequency $\omega_{gN}$ and the dephasing of the system. At some $N$-quantum time $T_{NQ}$ later, $N-1$ field interactions project the system onto a one-quantum coherence $|g\rangle\langle e|$ and creates a $(2N-1)$-order polarization that radiates the $N$-quantum signal and reveals the $N$-particle correlation.

## 3.4 Spectral Lineshapes

Previously, the concept of the time-dependent density matrix was introduced via the von Neumann relation (equation 3.12) to describe the system of an ensemble of quantum states. The von Neumann relation is now recast in its derivative form to determine the kinetics of the density matrix, $\rho = \sum_{i,j} |i\rangle\langle j|$.

$$\frac{\partial \rho}{\partial t} = \frac{i}{\hbar}\left[\hat{H}, \rho\right] \tag{3.44}$$

where is $\hat{H}$ the Hamiltonian. A Hamiltonian describing the state of a quantum system under electromagnetic excitation can be written as the sum of a system Hamiltonian $\hat{H}_0$, relaxation Hamiltonian $\hat{H}_R = -\Gamma \times \rho$, and time-dependent excitation potential $\hat{V}(t) = -\overrightarrow{\mu} \times \overrightarrow{E}(t)$.

$$\begin{aligned}\hat{H} &= \hat{H}_0 + \hat{H}_R + \hat{V}(t) \\ &= \begin{bmatrix} \hbar\omega_g & 0 \\ 0 & \hbar\omega_e \end{bmatrix} - \begin{bmatrix} 0 & -\Gamma_{ge} \\ -\Gamma_{eg} & -\Gamma_{ee} \end{bmatrix} \begin{bmatrix} \rho_{gg} & \rho_{ge} \\ \rho_{eg} & \rho_{ee} \end{bmatrix} - \begin{bmatrix} 0 & \mu_{ge} \\ \mu_{eg} & 0 \end{bmatrix} E(t)\end{aligned} \tag{3.45}$$

where $\hbar\omega_n$ are the state energies, $\Gamma_{nn}$ and $\Gamma_{nm}$ the population and coherence lifetimes, $\rho_{nm}$ the density matrix elements, $\mu_{nm}$ the transition dipole moments, and $E(t)$ the exciting electromagnetic field. Substituting the Hamiltonian (equation 3.45) into the von Neumann relation (equation 3.44), the time-derivative of the density matrix for the two-level system

takes the form:

$$\frac{\partial \rho}{\partial t} = \frac{i}{\hbar}\begin{bmatrix} \Gamma_{ee}\rho_{ee} + \left(\mu_{eg}\rho_{ge} - \mu_{ge}\rho_{eg}\right) E\left(t\right) & \left(\hbar\omega_{ge} + i\Gamma_{ge}\right)\rho_{ge} + \mu_{ge}\left(\rho_{gg} - \rho_{ee}\right) E\left(t\right) \\ \left(\hbar\omega_{eg} + i\Gamma_{eg}\right)\rho_{eg} + \mu_{eg}\left(\rho_{ee} - \rho_{gg}\right) E\left(t\right) & -\Gamma_{ee}\rho_{ee} + \left(\mu_{ge}\rho_{eg} - \mu_{eg}\rho_{ge}\right) E\left(t\right) \end{bmatrix} \tag{3.46}$$

where $\omega_{nm}$ is the frequency difference between the states $n$ and $m$. The $\left(\hbar\omega_{nm} + i\Gamma_{nm}\right)\rho_{nm}$ terms determine the frequency and spectral lineshape of the excitation. The $\pm\Gamma_{nn}\rho_{nn}$ terms represent population relaxation from the excited state to the ground state. The transition dipole moment terms $\mu_{nm}$ represent the optical excitation from the ground state into and out of the excited state.

Integrating equation 3.46 produces solutions to the off-diagonal density matrix elements of the form $\rho_{ge}\left(t\right) = \exp\left[\left(i\omega_{ge} - \frac{\Gamma_{ge}}{\hbar}\right)t\right]$, whose Fourier transformations yield Lorentzian lineshapes of width $\gamma_{ge} = \frac{\Gamma_{ge}}{\hbar}$ at the central frequency $\omega_{ge}$:

$$\rho_{ge}\left(\omega\right) = \frac{1}{\pi\gamma_{ge}}\frac{\gamma_{ge}^2}{\left(\left(\omega - \omega_{ge}\right)^2 + \gamma_{ge}^2\right)} \tag{3.47}$$

### 3.4.1 Local Field Effects

Under strong field excitation, local fields are generated due to the dipole moment of electron-hole pairs (i.e. excitons) [115, 116]. Thus, the total electromagnetic field acting on the system takes the form: $E\left(t\right) = E_0\left(t\right) + E_L\left(t\right)$. Exciton states are destabilized due to the presence of the local field $E_L\left(t\right)$ [117, 118, 119]. However, local fields also induce slower system decoherence as excitations continue to be driven after the applied electromagnetic field is gone [120, 121]. These effects can be introduced phenomenologically by adding density-dependent frequency and coherence lifetimes terms into the equation 3.46:

$$\frac{\partial \rho_{ge}}{\partial t} = \left[i\left(\omega_{ge} + N\omega^{EIS}\right) - \left(\gamma_{ge} + N\gamma^{EID}\right)\right]\rho_{ge} \tag{3.48}$$

where $N$ is the excitation density, $\omega^{EIS}$ describes excitation-induced frequency shift, and $\gamma^{EID}$ describes excitation-induced dephasing.

# Chapter 4

# Experimental Setup

In chapter 4, we will first discuss the ultrafast laser system and non-collinear optical parametric amplifier used for the experiments in this thesis [122]. From there, we will describe our spatial-temporal based two-dimensional spectrometer, including the theory of temporal pulse shaping and the calibrations and other technical considerations required for an ultrafast experiment [114, 123]. Finally, we will discuss the detection methods used for nonlinear spectroscopy: rotating wave detection, spectral interferometry, phase cycling, and the phase stability of our two-dimensional spectrometer [124, 125, 126].

## 4.1 Ultrafast Laser System

The experiments described in this thesis were all performed using a Coherent Libra titanium sapphire (Ti:Sapph) regenerative amplifier system [127]. The output of the Libra was a 3.0 W, 10 kHz pulse train of approximately 100 fs pulses centered at 800 nm with a full width at half maximum of 10 nm.

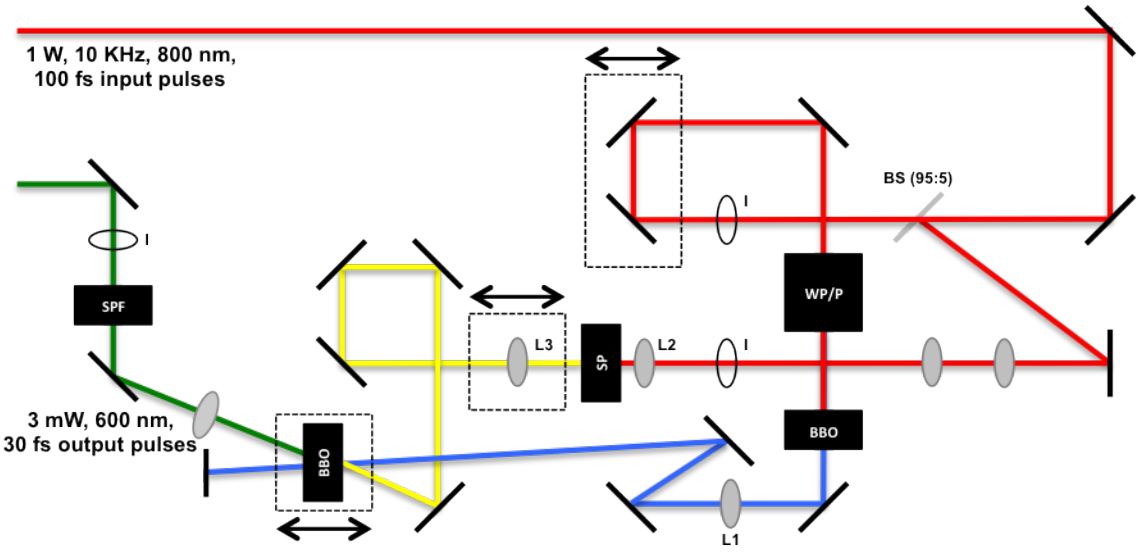


Figure 4.1: Experimental non-collinear optical parametric amplifier. 1 W of 100 fs, 800 nm pulses are incident on a 95:5 beamsplitter (BS). 95% is transmitted through the BS and onto a delay stage. The 0.95 W beam passes through a waveplate/polarizer pair (WP/P) for attenuation and then into a Beta Barium Borate crystal (BBO) for Type I second harmonic generation. The 400 nm pump beam is then focused by a 40 cm lens (L1) onto the mixing BBO for optical parametric amplification. The 0.05 W beam reflected off the BS is attenuated by an iris (I) and focused by a 3 cm lens (L2) into a sapphire plate (SP) for white light continuum generation. The white light seed beam is then single lens imaged by a 10 cm lens (L3) onto the mixing BBO for optical parametric amplification. Any 800 nm light co-propagating with the 3 mW amplified visible beam is filtered out by a shortpass filter (SPF). The spatial mode of the beam is subsequently fixed by focusing through a 200 μm pinhole and the pulse compressed and any spatial chirp corrected by a prism compressor.

## 4.2 Non-Collinear Optical Parametric Amplifier

To perform experiments throughout the visible region of the electromagnetic spectrum, the 800 nm output of the regenerative amplifier must be upconverted to the region of 500 - 700 nm.

Upconversion is accomplished by optical parametric amplification (OPA) using a non-collinear optical parametric amplifier (NOPA) [122]. First, a large fraction of the input beam is upconverted by second harmonic generation (SHG). In the experimental setup, approximately 0.95 W of the 800 nm beam is transmitted through a beamsplitter, traverses a delay stage, is attenuated by a waveplate/polarizer pair, and propagates through a Beta

Barium Borate (BBO) crystal optimized for Type I SHG to generate 400 nm light. Type I SHG is a second-order nonlinear process in which two photons at the fundamental frequency with the same polarization sum to produce one photon at twice the fundamental frequency, $\omega_{SHG} = 2\omega_F$, with a polarization orthogonal to the fundamental [107]. The process of SHG can mathematically written in the frequency domain as:

$$E(\omega_{SHG}) \sim iP^{(2)}_{SHG}(2\omega_F) = i\chi^{(2)}_{SHG} E(\omega_F) E(\omega_F) \tag{4.1}$$

where $E(\omega_{SHG})$ is the spectral amplitude of the second harmonic, $P^{(2)}_{SHG}(2\omega_F)$ is the second-order nonlinear polarization generated at the second harmonic frequency in the doubling BBO, $\chi^{(2)}_{SHG}$ is the second-order nonlinear susceptibility of the doubling BBO, and $E(\omega_F)$ is the spectral amplitude of the fundamental. Second-order nonlinear processes are only possible in non-centrosymmetric materials, such as BBO, as the crystal symmetry must allow for finite values of the second-order susceptibility.

Once the 800 nm fundamental has been upconverted to 400 nm, it must be downconverted from the ultraviolet into the visible by OPA. OPA is a second-order nonlinear process in which a strong pump beam (P) is downconverted using a weak seed beam (S) by difference frequency generation, $\omega_P = \omega_S + \omega_I$, and results in the amplification of the frequencies of the seed beam. In the nonlinear process, energy and momentum must be conserved by producing a third idler beam (I). The process of OPA can mathematically written in the frequency domain as:

$$E(\omega_S) \sim iP^{(2)}_{OPA}(\omega_S) = i\chi^{(2)}_{OPA} E(\omega_P) E(\omega_P) \tag{4.2}$$

where $E(\omega_S)$ is the spectral amplitude of the amplified seed beam, $P^{(2)}_{OPA}(\omega_S)$ is the second-order nonlinear polarization generated at the seed frequencies in the mixing BBO, and $E(\omega_P)$ is the spectral amplitude of the pump beam.

To generate the seed beam, approximately 0.05 W of the 800 nm beam is reflected off the

beam splitter, attenuated by an iris, and focused with a 3 cm lens into a 1 mm thick sapphire plate to produce a white light continuum by self-phase modulation (SPM). SPM is a second-order nonlinear process in which a large electric field intensity creates an intensity-dependent refractive index:

$$n(\omega, I) = n_0(\omega) + n^{(2)}(\omega) I \tag{4.3}$$

where $n_0(\omega)$ is the linear refractive index of a material, $n^{(2)}(\omega)$ is the second-order nonlinear refractive index, and $I$ is the electric field intensity. The intensity-dependent refractive index produced as the light propagates through the sapphire generates a phase shift in the pulse that broadens the pulse in the frequency domain and produces a supercontinuum covering the entire visible spectrum [107]. The supercontinuum is subsequently imaged with a single 10 cm lens onto the mixing BBO optimized for OPA.

The 400 nm pump beam is simultaneously focused by a 40 cm lens into the mixing BBO at an angle $\alpha$ relative to the supercontinuum. Because indices of refraction are frequency-dependent, dispersion occurs when different frequencies are generated or propagate through a material, limiting the intensity and bandwidth of the amplified light. However, BBO is birefringent so the indices of refraction along different crystallographic axes can be used to phasematch large bandwidths. The angle $\alpha$ between the pump and seed beams is chosen such that the dispersion (i.e. group velocity mismatch) between the seed and idler are matched along the direction of amplification, allowing for broadband frequency generation. In BBO for broadband generation centered at 600 nm, $\alpha$ is approximately 3.7°.

After the mixing BBO, the pump and idler beams are rejected and the amplified beam is collimated using a 15 cm lens. The remaining 800 nm light in the amplified beam is eliminated using a shortpass filter. The spatial profile of the beam is cleaned up by focusing through a 200 μm pinhole and a prism compressor is used to compress the pulses and correct for any spatial chirp generated during OPA.

With the NOPA, bandwidths spanning 500 to 700 nm can be easily achieved. However, such large bandwidths are not suitable for the rest of our experimental setup. Thus, the

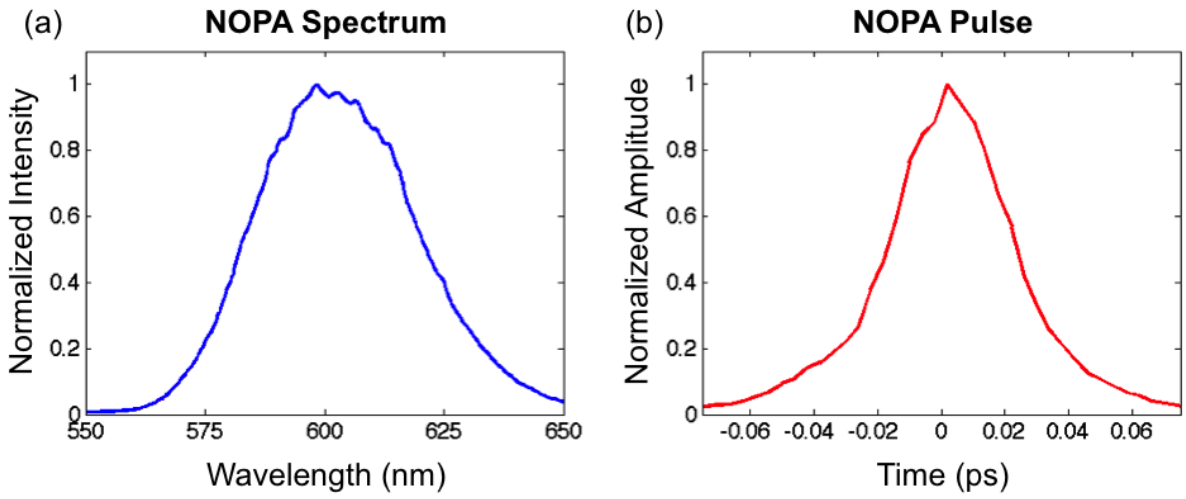


Figure 4.2: Non-collinear optical parametric amplifier output. (a) NOPA spectrum at 600 nm with a full width at half the maximum of 40 nm. (b) NOPA pulse compressed by a pair of prisms to 40 fs and measured using a second harmonic generation frequency-resolved optical gating (SHG FROG).

NOPA output bandwidth is generally limited to approximately 45 nm by introducing dispersion into the white light arm and then tuned to the desired region of the visible spectrum by the time delay between the 400 nm pump beam and the white light supercontinuum. Figure 4.2 shows a typical narrowband NOPA spectrum and the corresponding pulse in the time domain.

## 4.3 Spatio-Temporal Pulse Shaping

Once visible ultrafast pulses have been generated in the NOPA and compressed by a prism pair, the beam is routed into our two-dimensional (2D) spectrometer for multiple beam generation and temporal pulse shaping. Figure 4.3 illustrates the components and layout of the 2D spectrometer including a Hamamatsu X7550 2D liquid crystal spatial light modulator and a Princeton Instruments Action SP2300 spectrometer with a PIXIS 400 CCD

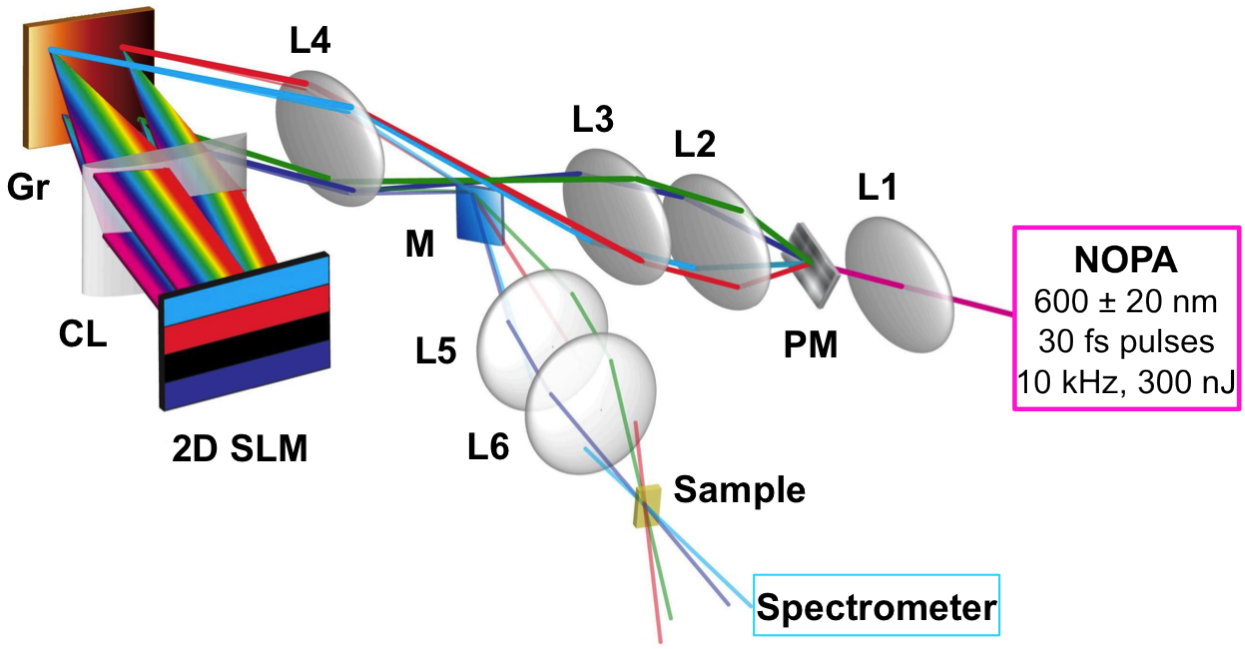


Figure 4.3: Two-dimensional spectrometer. Ultrafast laser pulses from the NOPA are focused by a lens L1 onto a phase mask (PM) to produce four beams in the BOXCARS geometry and subsequently collimated by lens L2. Lens L3 and L4 relay image the beams into the temporal pulse shaper, consisting of a grating (Gr), cylindrical lens (CL), and 2D spatial light modulator (SLM). The grating spectrally disperses the beams and the cylindrical lens focuses them onto vertically distinct regions of the 2D SLM, which controls the frequency-dependent phase of each beam. The phase-perturbed beams are then refocused by the cylindrical lens on to the grating and are compressed. Lens L4 focuses the beams onto the pick-off mirror M1 and lens L5 recollimates them. Finally, lens L6 focuses the beams onto the sample and the signal and local oscillator are detected by a spectrometer.

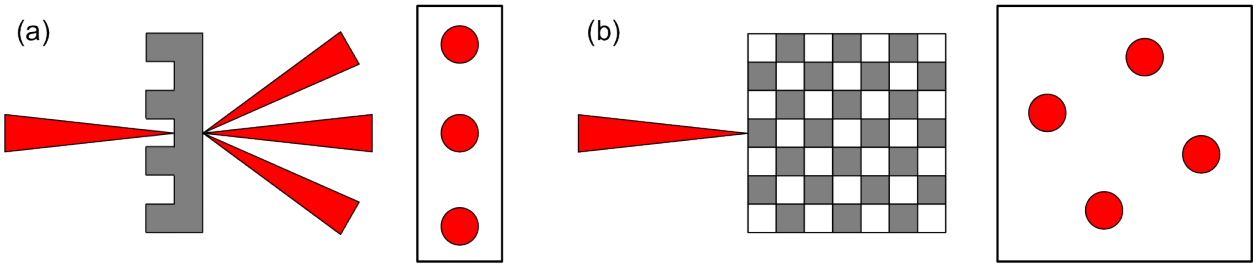


Figure 4.4: Beam pattern generation. (a) Linear three beam geometry using a 1D phase mask. (b) BOXCARS four beam geometry using a 2D phase mask.

camera.

### 4.3.1 Principles of Pulse Shaping

#### 4.3.1.1 Beam Pattern Generation

To generate multiple beams in a specified geometry, a phase mask (or low dispersion, transmissive, diffractive optic) optimized for first-order diffraction is used. A linear set of three beams can be generated by a phase mask with a square grating pattern in one dimension, figure 4.4a; a set of fours beams in the BOXCARS geometry can be generated by a phase mask with two perpendicular square grating patterns, figure 4.4b. To generate the desired beam set, the fundamental beam is focused by a lens onto the phase mask causing diffraction of the beam into multiple orders. The diffracted beams are collimated by a second lens and the desired beams for a specific geometry are imaged using common path optics to the temporal pulse shaper and subsequently to the sample position. Imaging of the phase mask pattern onto the sample position has the advantage of automatic phase matching of the wavevectors for each beam (including the local oscillator) and an increase in the measured 2D signal due to an enhancement of the phase front overlaps of the beams at the sample position [128].

#### 4.3.1.2 Temporal Pulse Shaping

From the phase mask, the beams are imaged using common path optics into a pulse shaper consisting of a plane-ruled reflectance grating, achromatic cylindrical lens, and a 2D

spatial light modulator (SLM). In the pulse shaper, the beams are spectrally dispersed by the grating, which is blazed at the center wavelength of the ultrafast pulse and has a periodicity of approximately 1,000 groves/mm. The cylindrical lens subsequently stops the divergence of the spectrum off the grating and focuses the beams onto vertically distinct positions of the 2D SLM.

The 2D SLM is a phase only device that can independently control the frequency-dependent phase $\phi_i(\omega)$ of each beam $i$. By applying a phase in the frequency domain $E_i^0(\omega)$, the temporal profile of the ultrafast pulse $E_i'(t)$ can be modified. The relation between these quantities is given by the inverse Fourier transform:

$$E_i'(t) = \int_{-\infty}^{\infty} E_i^0(\omega) \exp\left[-i\phi_i(\omega)\right] \exp\left[i\omega t\right] d\omega \tag{4.4}$$

The global phase, time delay, and first-order dispersion (temporal chirp) can be controlled by applying a constant ($\phi_i = c_i$), linear ($\phi_i(\omega) = \omega t_i$), or quadratic phase ($\phi_i(\omega) = \omega^2 t_i^2$) in the frequency domain. Figure 4.5 illustrates the affect of applying different phase functions in the frequency domain on the temporal profile of the pulse.

Due to the pixelation of the SLM ($480 \times 480$), the phase function applied to the spectral profile of the ultrafast pulse is not continuous. Similarly, the maximum grayscale value of the SLM (256) defines the number of phase values that can be applied at a given pixel. Because $\exp[i \times 0] = \exp[i \times 2\pi]$, we are able to wrap the applied phase modulo $2\pi$. Thus, the 256 grayscale values need only apply a phase from 0 to $2\pi$; however in practice, phases of 0 to approximately $2.5\pi$ are applicable.

The discreteness of the applied phase function due to the pixelation of the SLM has a number of important implications. First, there is an inherent upper bound to the time delay that can be applied to the pulse. As discussed above, a time delay results from a linear change in the phase as a function of frequency. The time delay is thus defined as:

$$t_i = \frac{\partial \phi_i(\omega)}{\partial \omega} \tag{4.5}$$

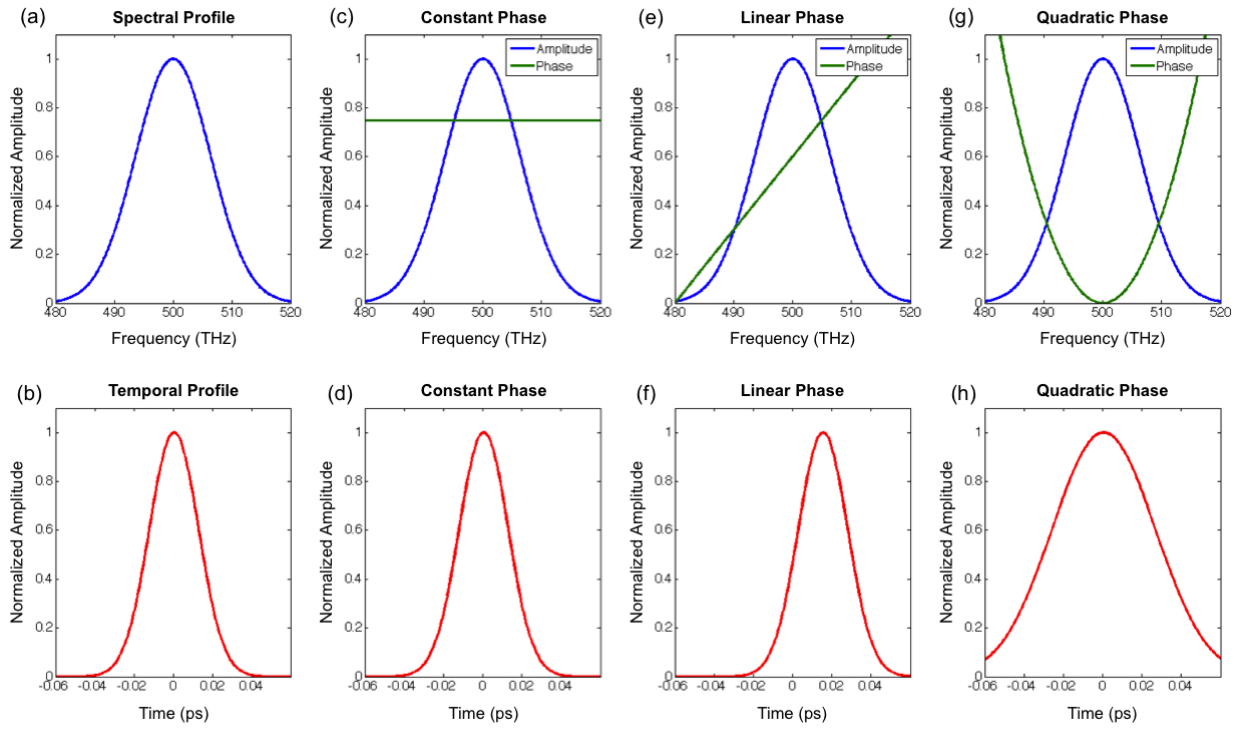


Figure 4.5: Temporal pulse shaping. (a) Spectral profile of the fundamental pulse. (b) Temporal profile of the fundamental pulse. (c) Constant phase applied to the pulse. (d) Temporal profile of the constant phase pulse. (e) Linear phase applied to the pulse. (f) Temporal profile of the delayed pulse. (g) Quadratic phase applied to the pulse. (h) Temporal profile of the chirped pulse.

where $\partial\phi_i(\omega)$ is the change in phase and $\partial\omega$ is the frequency bandwidth per pixel, defined by the grating dispersiveness and the cylindrical lens focal length. To maximize the time delay, the change in phase from pixel to pixel must be maximized. The maximum applied phase is always $2\pi$, which for a frequency bandwidth of approximately 0.03 THz per pixel, results in a maximum time delay of approximately 3 ps.

$$t_i^{max} = \frac{\partial\phi_i^{max}(\omega)}{\partial\omega} = \frac{2\pi}{2\pi \times 0.03THz} \sim 3ps \tag{4.6}$$

To increase the upper limit of the time delay, the frequency bandwidth per pixel must be decreased. However, the timescales relevant to this thesis are of electronic coherences with dephasing times on the order of hundreds of femtoseconds. Thus, a maximum time delay of 3 ps is more than sufficient.

Second, the top-hat spatial profile of the pixels creates a periodic filter in the frequency domain that causes a rapid decline in the intensity of the shaped pulse as a function of the time delay. This pulse intensity roll off is given by the Fourier transform of the spatially-filtered frequency spectrum and results in a $sinc[\pi\partial\omega t]$ intensity decline, where $\partial\omega$ is the frequency bandwidth per pixel. Similarly, the finite spectral resolution of the grating-cylindrical lens pair, $\Delta\omega$, generates a Gaussian time window $\exp[-\pi^2\Delta\omega^2 t^2]$ that also attenuates the intensity of the shaped pulse [129].

Third, the pixelation of the SLM generates a train of pulses that are separated in time by $1/\partial\omega$. These sampling replica pulses generally occur at long time delays and their amplitudes decrease as a function of time due to the Gaussian time window and sinc function just described. A train of modulator replica pulses (separated in time by the applied time delay $t$) is also generated due to phase wrapping at modulo $2\pi$ and the periodic pixel boundaries. In general, modulator replica pulses are problematic for all coherent, ultrafast spectroscopy experiments using temporal pulse shaping.

#### 4.3.1.3 Diffraction-Based Pulse Shaping

To separate the desired pulse from the modulator replica pulses, we employ a diffraction-based scheme of pulse shaping in which a sawtooth diffraction grating is applied along the vertical dimension of the 2D SLM [130]. The spatial phase (i.e. vertical position) and the amplitude of the sawtooth grating can be used to modify the frequency- and spatially-dependent phase:

$$\Phi(\omega, y) = \phi^{max}\left[\frac{1}{2} + A(\omega)\, S_d(\phi(\omega), y)\right] \tag{4.7}$$

where $\phi^{max} = 2\pi$ is the maximum achievable phase shift of the SLM, $S_d(\phi(\omega), y)$ is a sawtooth grating function of period $d$ along the $y$ dimension, and $A(\omega)$ is a frequency-dependent amplitude function that can vary between 0 and 1. In this manner, the frequency-dependent phase and amplitude of the output electric field can be modified and takes the form:

$$E_i'(\omega) \propto E_i^0(\omega) \exp[-i\phi_i(\omega)]\, sinc\left[\pi - \frac{\phi^{max}}{2} A_i(\omega)\right] \tag{4.8}$$

where $E_i^0(\omega)$ is the input electric field.

A lens at the back focal plane of the SLM focuses each diffraction order off the sawtooth grating to a vertically distinct position where the first-order alone can be picked off by a mirror and collimated. By definition, each modulator replica pulse in the train has an additional phase factor of $2\pi$. Thus, each modulator replica pulse is diffracted into a different order and only the desired pulse diffracts into the first-order. Figure 4.6 illustrates the scheme of diffraction-based pulse shaping and the applied sawtooth grating pattern.

The properties of the sawtooth grating pattern also define the minimum time delay achievable by the SLM. The minimum time delay is achieved when the phase across one period of the vertical sawtooth grating is minimized. The minimum applied phase is the maximum phase divided by the periodicity of the vertical sawtooth grating $d$, usually 6 pixels. However, pixels can also be binned in order to apply smaller phase changes over the spectral profile of the pulse. If the pixels are binned into 2 sets of 240 pixels, the minimum

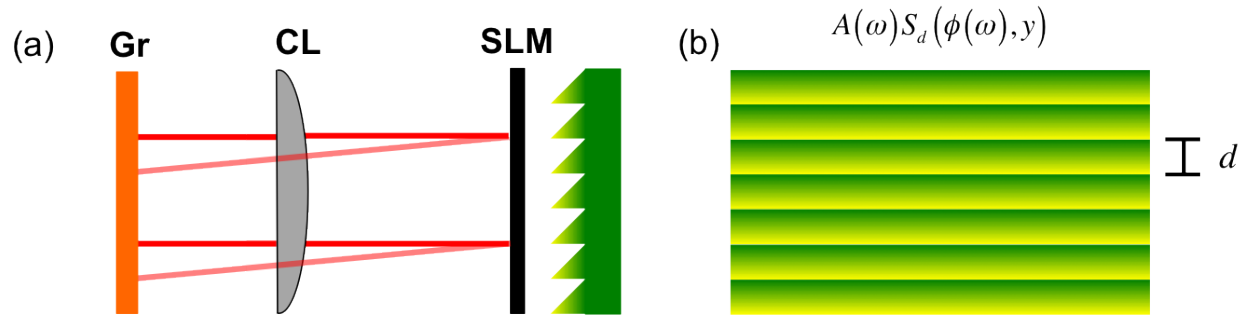


Figure 4.6: Diffraction-based pulse shaping. (a) Beams spectrally dispersed by the grating (Gr) are focused by a cylindrical lens (CL) onto the spatial light modulator (SLM). (b) The sawtooth grating pattern applied along the vertical dimension $A(\omega) S_d(\phi(\omega), y)$ with a periodicity $d$ diffracts the incoming beams into many vertically distinct spatial orders, eliminating modulator replica pulses and allowing amplitude shaping.

time delay achievable is 0.02 ps.

$$t_i^{min} = \frac{\partial \phi_i^{min}(\omega)}{\partial \omega} = \frac{(2\pi/d)/pixel}{\partial \omega} = \frac{(2\pi/6)/240}{2\pi \times 0.03THz} \sim 0.02ps \tag{4.9}$$

To decrease the time step lower limit, the frequency bandwidth per pixel or the periodicity of the vertical sawtooth grating can be increased.

Not only does diffraction-based pulse shaping have the distinct advantages of providing spectral amplitude control and elimination of unwanted modulator replica pulses, it also allows spectroscopic experiments to be performed in the rotating frame and for easy phase cycling, both of which increase the quality of measured spectroscopic signals. Rotating frame detection and phase cycling will be discussed at the end of the chapter.

### 4.3.2 Experimental Calibrations

In order to perform an ultrafast experiment, the SLM must be carefully calibrated to apply the correct frequency-dependent phase for each desired output field. Thus, the phase applied by a given grayscale value of the SLM and the frequency component of a pulse on a given pixel must be calibrated. Once the 2D SLM has been calibrated, the compression and time ordering of the pulses must be set for time-resolved experiments. Finally, the pulse intensity roll off, carrier frequency, and global phase difference between the signal and local

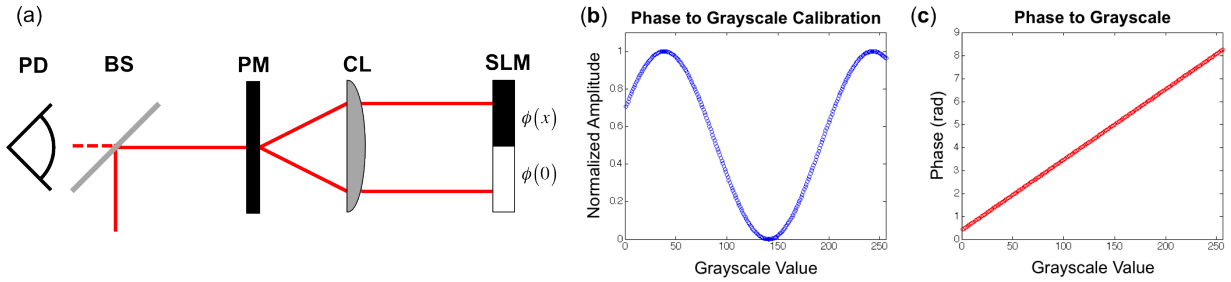


Figure 4.7: Phase-to-grayscale calibration. (a) The input beam reflects off a beamsplitter (BS) and diffracts off a linear phase mask (PM) to produce two beams. The beams are focused onto horizontally distinct regions of the 2D spatial light modulator (SLM). The phase of one beam is modified by changing the grayscale value of the SLM $\phi(x)$, while the phase of the other beam is held constant $\phi(0)$. The beams reflect off the SLM and are refocused onto the PM by the CL and are recombined. The backward propagating beams are transmitted through the BS and the interference between the beams is measured on a photodiode (PD). (b) Interference of phase-perturbed beams. (c) Extracted phase-to-grayscale calibration function.

oscillator electric fields must be measured.

#### 4.3.2.1 Phase-to-Grayscale

First, the phase applied by a given grayscale value of the SLM must be calibrated. To do this, one beam is reflected off a beam splitter and onto a 1D phase mask. Diffraction off the phase mask produces two first-order beams that are focused by a cylindrical lens onto two horizontally distinct regions of the 2D SLM. The phase of one beam is modified by changing the grayscale value of the SLM $\phi(x)$, while the phase of the other beam is held constant $\phi(0)$. The phase-perturbed and phase-constant beams reflect off the SLM and are refocused by the cylindrical lens onto the phase mask and are recombined. The backward propagating beams are transmitted through the beam splitter and their interference is measured on a photodiode as a function of the SLM grayscale value, $\cos[\phi(x)]$. From this measurement, a phase-to-grayscale calibration function can be determined to apply the correct phase to a given frequency component. Figure 4.7 illustrates the experimental setup, the raw data, and the extracted phase-to-grayscale calibration function. Once the phase-to-grayscale calibration has been completed, recalibration is not necessary unless there is a significant change in wavelength of the beam due to the frequency-dependence of the applied phase by a given

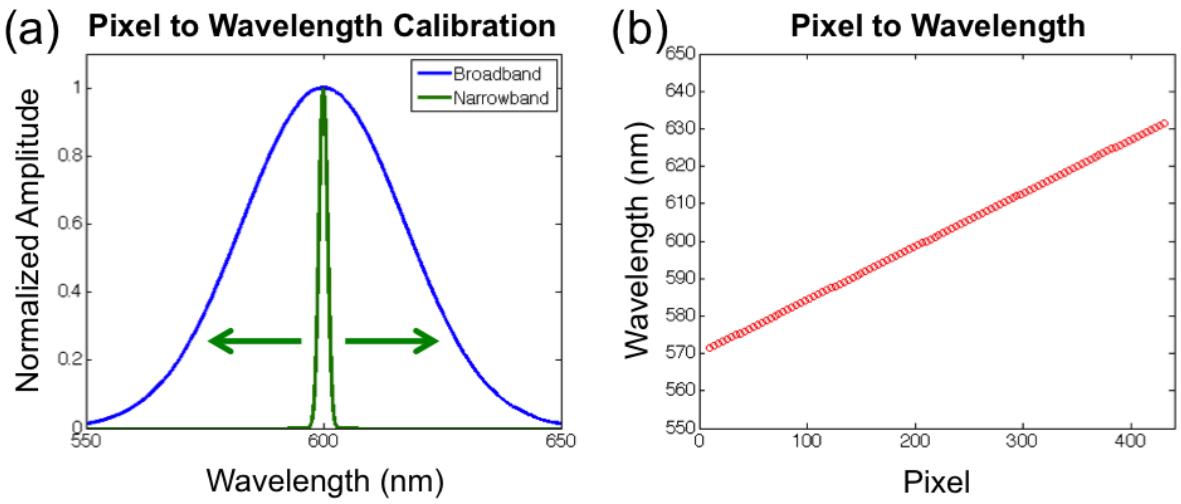


Figure 4.8: Pixel-to-wavelength calibration. (a) The three pixel-wide narrowband spectrum of the ultrafast pulse is measured across all pixels of the spatial light modulator. (b) Extracted pixel-to-wavelength calibration function.

grayscale value.

#### 4.3.2.2 Pixel-to-Wavelength

In order to control the frequency-dependent phase of an ultrafast pulse, the pixel on which a given frequency component is located must be measured. To do this, a three pixel-wide column of the sawtooth grating pattern is illuminated on the SLM. Only the frequency components on the illuminated pixels diffract, exit the pulse shaper, and are measured by the spectrometer. By sweeping the location of the illuminated pixels across the SLM and measuring the corresponding spectra, a pixel-to-wavelength calibration function can be determine. Figure 4.8 illustrates the experimental concept and an extracted pixel-to-wavelength calibration function. As the frequency components of the pulse and the alignment of the beam change daily, the pixel-to-wavelength calibration must also be performed daily.

#### 4.3.2.3 Pulse Compression and Timings

In ultrafast experiments, the compression and time ordering of pulses are critical. Propagation through transmissive optics and off the grating, cylindrical lens, and SLM (which acts as

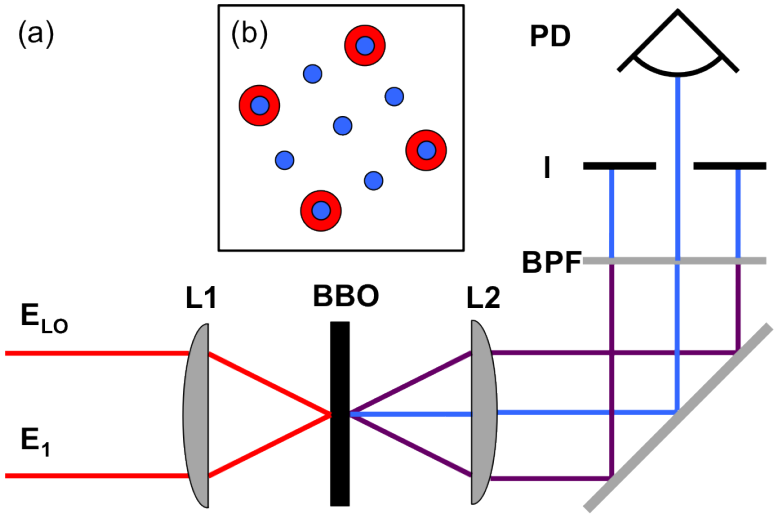


Figure 4.9: Pulse compression and timings. (a) In the cross correlation setup, two beams are focused by lens L1 into a Beta Barium Borate (BBO) crystal for second harmonic generation and are recollimated by lens L2. A bandpass filter (BPF) blocks out the fundamental light and an iris (I) isolates the cross correlation signal, which is measured by a photodiode (PD) as a function of the time delay between the two beams. (b) Cross sectional image of the four fundamental beams and all the second harmonic cross correlations.

a grating compressor) changes the compression and timing of the pulses. So, the compression and timing must be calibrated daily. First, the pulse duration of one beam is measured by second harmonic frequency-resolved optical grating (SHG FROG) and compressed using the grating and cylindrical lens in the pulse shaper [131]. Next, a BBO crystal is placed at the sample position and SHG cross-correlations of each beam with the first are measured on a photodiode as a function of time delay between the beams. The SLM is used to compress the pulses and to overlap them in time by applying quadratic and linear phase, respectively. Figure 4.9 illustrates the cross correlation setup and the second harmonic cross correlations of the four fundamental beams.

#### 4.3.2.4 Pulse Intensity Roll Off

As discussed above, the intensity of a temporally shaped pulse decreases as a function of the applied time delay. The pulse intensity roll off can be calibrated by measuring the pulse spectrum as a function of time delay, $I(\tau)$. Figure 4.10 shows a frequency-integrated pulse in-

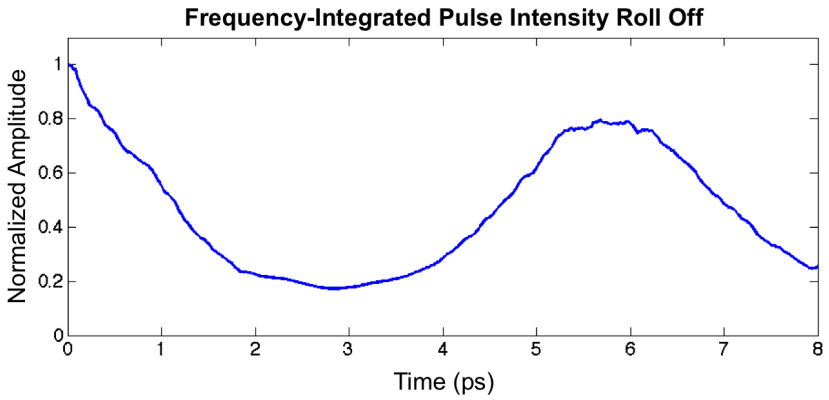


Figure 4.10: Pulse intensity roll off calibration. Frequency-integrated pulse intensity as a function of time delay, $I(\tau)$.

tensity roll off measurement. The pulse intensity roll off calibration can be used to correct for the decrease in the pulse intensity during a time-resolved experiment by dividing the 2D signal $S(\tau, 0, \omega_t)$ by the square root of the intensity roll off: $S^{IC}(\tau, 0, \omega_t) = S(\tau, 0, \omega_t) / \sqrt{I(\tau)}$. Once the pulse intensity roll off has been measured, recalibration is not necessary unless there is a significant change in the frequency bandwidth per pixel.

#### 4.3.2.5 Carrier Frequency

The precise carrier frequency of each beam must also be measured because our experiments are inherently performed in the rotating frame. To determine the carrier frequencies, each beam is temporally shaped to generate a symmetric double pulse by applying the phase function $\phi(\omega) = \cos[(\omega - \omega_c) T]$ and the interference of the two pulses is measured as a function of the delay time $T$ by a spectrometer. The phase of the carrier frequency $\omega_c$ does not change as a function of time delay and thus its corresponding frequency fringe does not move in the interferogram. Once measured, the interferogram is inverse Fourier transformed into the time-time domain and the negative time component is filtered out. The interferogram is subsequently Fourier transformed back into the frequency-time domain to recover the electric field amplitude and phase and determine the carrier frequency. This data processing technique, called spectral interferometry, will be discussed in more detail

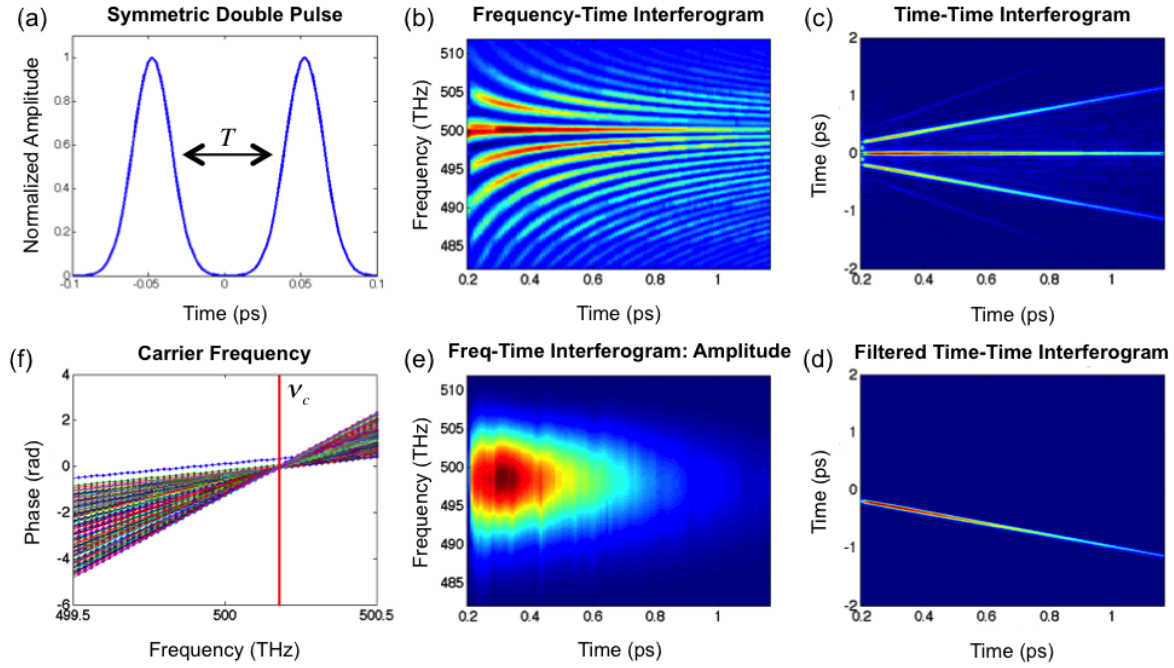


Figure 4.11: Carrier frequency calibration. (a) A symmetric double pulse is generated by applying the phase function $\phi(\omega) = \cos[(\omega - \omega_c)T]$ in the frequency domain. (b) The interference of the symmetric double pulse is measured as a function of $T$ by a spectrometer. The fringe at the carrier frequency $\omega_c$ does not move as a function of the delay time $T$. (c) The interferogram is inverse Fourier transformed into the time-time domain. (d) The negative time component is filtered out. (e) and (f) The interferogram is Fourier transformed back into the frequency-time domain to recover the amplitude and phase of the electric field and determine the carrier frequency, which does not evolve as a function of the time delay.

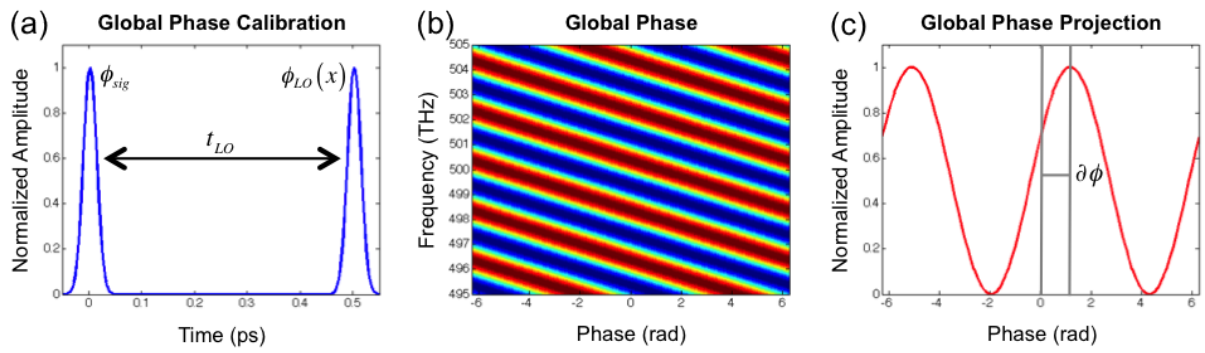


Figure 4.12: Global phase calibration. (a) Interference between the signal and local oscillator fields is measured by a spectrometer as a function of the local oscillator phase $\phi_{LO}(x)$. (b) Local oscillator phase-dependent interference. (c) The global phase difference between the signal and local oscillator fields $\partial\phi$ is extracted from the frequency-integrated interference.

at the end of the chapter. Figure 4.11 illustrates the experimental concept, the raw data, and the extraction process. Like the pixel-to-wavelength calibration, daily changes in the alignment change the carrier frequency and thus the carrier frequency calibration must be performed daily.

#### 4.3.2.6 Global Phase

To separate the absorptive and dispersive components of a spectroscopic signal, the phase difference between the signal and reference (i.e. local oscillator) beams must be determined. The global phase difference is calibrated by measuring the change in the signal-local oscillator interference as a function of the local oscillator phase $\phi_{LO}(x)$. Once the interferogram has been measured by a spectrometer, it is frequency integrated and fit to a $\cos[\phi_{LO}(x) + \partial\phi]$ function from which the global phase difference $\partial\phi$ can be determined. Figure 4.12 illustrates the experimental concept, the interferogram, and the extracted phase. Daily changes in the compression and time ordering of the pulses change the global phase difference between the signal and the local oscillator, thus the global phase calibration must be performed daily.

## 4.4 Spectroscopic Detection

### 4.4.1 Rotating Frame Detection

In temporal pulse shaping, a carrier frequency $\omega_c$ is used as a reference to control the phases of the other frequency components in the pulse. When the phase of a given frequency component is temporally shaped, it is modified relative to the carrier frequency. Thus, the phase of the carrier frequency remains constant as the phase of the other frequency components change. This subtle experimental detail has an important implication. Because the phase of the carrier frequency does not change, measurements are implicitly made in the rotating frame [124]. All oscillations measured experimentally are reduced by the carrier frequency, $\Omega = \omega - \omega_c$. Experimentally, we can thus define the Nyquist frequency for capturing the dynamics of a system and significantly reduce the required number of time steps per spectrum. This significantly reduces the time required to perform a full 2D measurement to approximately 15 minutes.

### 4.4.2 Spectral Interferometry

Spectral interferometry is a powerful tool used to characterize the electric field amplitude and phase of a spectrally resolved, non-self-heterodyned spectroscopic signal [125]. In this technique, a local oscillator $E_{LO}(\omega)$ at a time delay $t_{LO}$ relative to the spectroscopic signal $E_{Signal}(\omega)$ is used as a reference for heterodyne detection [132]. The intensity of the total spectral interferometry signal ($I_{SI}(\omega, t_{LO})$) is spectrally resolved by a spectrometer:

$$\begin{aligned} I_{SI}(\omega, t_{LO}) &= \left|E_{LO}(\omega)\exp(i\omega t_{LO}) + E_{Signal}(\omega)\right|^2 \\ &= I_{LO}(\omega) + I_{Signal}(\omega) + E_{LO}(\omega)\,E^*_{Signal}(\omega)\exp(i\omega t_{LO}) \\ &\quad + E^*_{LO}(\omega)\,E_{Signal}(\omega)\exp(-i\omega t_{LO}) \end{aligned} \tag{4.10}$$

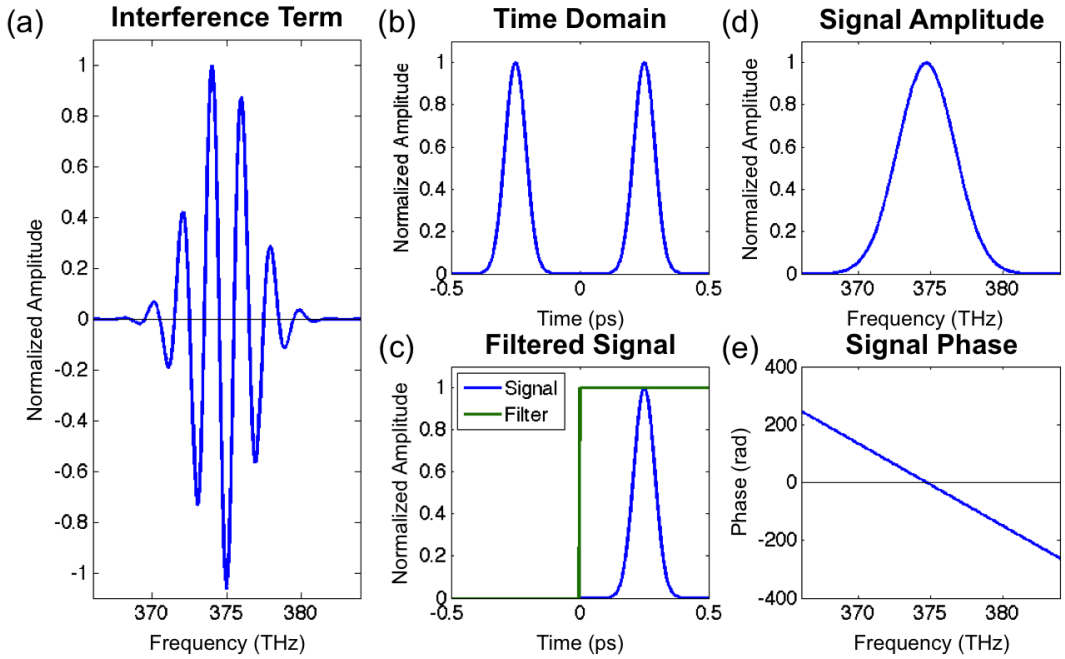


Figure 4.13: Spectral interferometry. (a) Spectral interferometry interference term in the frequency domain. (b) Interference term in the time domain. (c) Filtered interference term and heaviside step function in the time domain. (d) Signal amplitude in the frequency domain. (e) Signal phase in the frequency domain.

The interference term is isolated by subtracting the intensities of the local oscillator and signal from the total spectral interferometry signal:

$$\begin{aligned}\Delta I_{SI}(\omega, t_{LO}) &= I_{SI}(\omega, t_{LO}) - I_{LO}(\omega) - I(\omega) \\ &= E_{LO}(\omega) E^*_{Signal}(\omega) \exp(i\omega t_{LO}) + E^*_{LO}(\omega) E_{Signal}(\omega) \exp(-i\omega t_{LO}) \\ &= 2\Re\left[E^*_{LO}(\omega) E_{Signal}(\omega) \exp(-i\omega t_{LO})\right] \end{aligned} \tag{4.11}$$

Noting $C + C^* = (C_\Re + iC_\Im) + (C_\Re - iC) = 2C_\Re$.

When the interference term of the spectral interferometry signal is inverse Fourier transformed, the time domain signal is compromised of two signals at $\pm t_{LO}/2$.

$$\begin{aligned}&IFT\left\{\Re\left[E^*_{LO}(\omega) E_{Signal}(\omega) \exp(-i\omega t_{LO})\right]\right\} = \\ &\quad E^*_{LO}(t - t_{LO}/2) E_{Signal}(t - t_{LO}/2) + E^*_{LO}(-t - t_{LO}/2) E_{Signal}(-t - t_{LO}/2)\end{aligned} \tag{4.12}$$

Filtering out the negative time component with a heaviside step function $\theta(t)$ to enforce causality (i.e. emission occurs after excitation), Fourier transformation of the filtered interference term back into the frequency domain results in a complex spectrum because the complex conjugate of the spectral interferometry signal was filtered out in the time domain. Multiplication of the filtered interference term in the time domain by the phase factor $\exp(i\omega t_{LO})$ corrects for the local oscillator time delay and division by the complex conjugate of the local oscillator electric field $E^*_{LO}(\omega)$ yields the amplitude and phase of the signal electric field:

$$E_{Signal}(\omega, \phi) = \frac{FT\left\{\theta(t) \times IFT\left\{\Re\left[E^*_{LO}(\omega) E_{Signal}(\omega) \exp(-i\omega t_{LO})\right]\right\}\right\} \exp(i\omega t_{LO})}{E^*_{LO}(\omega)} \tag{4.13}$$

This method for determining the amplitude and phase of a signal electric field is illustrated in figure 4.13 on the preceding page. In this case, a signal and local oscillator with

Gaussian spectral profiles are used.

### 4.4.3 Phase Cycling

Phase cycling plays an extremely important role in 2D spectroscopy. Since experimental signals tend to be weak, phase cycling helps to suppress scatter from the exciting beams and enhance the desired signal contribution [126]. Phase cycling also performs the first step in spectral interferometry by subtracting out the local oscillator and signal intensity terms in order to retrieve the full amplitude and phase of the signal electric field.

In general, the total signal of a four beam experiment is the absolute value squared of the local oscillator, third-order signal, and three excitation electric fields:

$$\begin{aligned} I_{tot}(\omega) &= |E_{LO}(\omega)\exp[i\phi_{LO}(\omega)] + E_{Sig}(\omega)\exp[i\phi_{Sig}(\omega)] \\ &\quad + E_1(\omega)\exp[i\phi_1(\omega)] + E_2(\omega)\exp[i\phi_2(\omega)] + E_3(\omega)\exp[i\phi_3(\omega)]|^2 \\ &= I_{LO} + I_{Sig} + I_1 + I_2 + I_3 + E_{LO}E_{Sig}\cos[\phi_{LO} - \phi_{Sig}] \\ &\quad + E_{LO}E_1\cos[\phi_{LO} - \phi_1] + E_{LO}E_2\cos[\phi_{LO} - \phi_2] + E_{LO}E_3\cos[\phi_{LO} - \phi_3] \\ &\quad + E_{Sig}E_1\cos[\phi_{Sig} - \phi_1] + E_{Sig}E_2\cos[\phi_{Sig} - \phi_2] + E_{Sig}E_3\cos[\phi_{Sig} - \phi_3] \\ &\quad + E_1E_2\cos[\phi_1 - \phi_2] + E_1E_3\cos[\phi_1 - \phi_3] + E_2E_3\cos[\phi_2 - \phi_3] \end{aligned} \tag{4.14}$$

where $\phi_{Sig}(\omega) = \pm\phi_1(\omega) \pm \phi_2(\omega) \pm \phi_3(\omega)$. To recover the electric field amplitude and phase of the third-order signal by spectral interferometry, the only desired signal contribution from equation 4.14 is the $E_{LO}E_{Sig}\cos[\phi_{LO} - \phi_{Sig}]$ term. To isolate this signal, phase cycling is used to subtract out the local oscillator and signal intensity terms ($I_{LO}$ and $I_{Sig}$) and eliminate scattered contributions from the excitation beams.

First, we will consider a four-step phase cycling procedure in which the phase of each

excitation beam is individually shifted by $\pi$ and subtracted from the unperturbed signal:

$$\begin{aligned} I^{4S}(\omega) &= I_{tot} - I_{tot}(\phi_{LO}, \phi_1 + \pi, \phi_2, \phi_3) \\ &\quad - I_{tot}(\phi_{LO}, \phi_1, \phi_2 + \pi, \phi_3) - I_{tot}(\phi_{LO}, \phi_1, \phi_2, \phi_3 + \pi) \\ &= -2I_{LO} - 2I_{Sig} - 2I_1 - 2I_2 - 2I_3 + 8E_{LO}E_{Sig}\cos[\phi_{LO} - \phi_{Sig}] \\ &\quad + 4E_{Sig}E_1\cos[\phi_{Sig} - \phi_1] + 4E_{Sig}E_2\cos[\phi_{Sig} - \phi_2] + 4E_{Sig}E_3\cos[\phi_{Sig} - \phi_3] \\ &\quad + 4E_1E_2\cos[\phi_1 - \phi_2] + 4E_1E_3\cos[\phi_1 - \phi_3] + 4E_2E_3\cos[\phi_2 - \phi_3] \end{aligned} \tag{4.15}$$

With four-step phase cycling, the $E_{LO}E_i\cos[\phi_{LO} - \phi_i]$ terms, where $i = 1, 2, 3$, are eliminated and the desired signal contribution is enhanced by a factor of 8.

To eliminate additional undesired signal contributions, the logical extension of four-step phase cycling is a seven-step phase cycling procedure in which the phase of each pair of excitation beams is shifted by $\pi$ and added to the four-step phase cycling signal.

$$\begin{aligned} I^{7S}(\omega) &= I^{4S} + I_{tot}(\phi_{LO}, \phi_1 + \pi, \phi_2 + \pi, \phi_3) \\ &\quad + I_{tot}(\phi_{LO}, \phi_1 + \pi, \phi_2 + \pi, \phi_3) + I_{tot}(\phi_{LO}, \phi_1, \phi_2 + \pi, \phi_3 + \pi) \\ &= I_{LO} + I_{Sig} + I_1 + I_2 + I_3 + 14E_{LO}E_{Sig}\cos[\phi_{LO} - \phi_{Sig}] \\ &\quad - 2E_{LO}E_1\cos[\phi_{LO} - \phi_1] - 2E_{LO}E_2\cos[\phi_{LO} - \phi_2] - 2E_{LO}E_3\cos[\phi_{LO} - \phi_3] \\ &\quad + 2E_{Sig}E_1\cos[\phi_{Sig} - \phi_1] + 2E_{Sig}E_2\cos[\phi_{Sig} - \phi_2] + 2E_{Sig}E_3\cos[\phi_{Sig} - \phi_3] \\ &\quad + 2E_1E_2\cos[\phi_1 - \phi_2] + 2E_1E_3\cos[\phi_1 - \phi_3] + 2E_2E_3\cos[\phi_2 - \phi_3] \end{aligned} \tag{4.16}$$

Equation 4.16 reveals that seven-step phase cycling increases the number of undesired contributions but also increases the enhancement of the desired signal term to a factor of 14.

Adding an eighth phase cycling step in which the phases of all the excitation beams are shifted by $\pi$ and subtracted from the seven-step phase cycling signal, the desired signal

contribution can be isolated.

$$\begin{aligned} I^{8S}(\omega) &= I^{7S} - I_{tot}(\phi_{LO}, \phi_1 + \pi, \phi_2 + \pi, \phi_3 + \pi) \\ &= 16 E_{LO} E_{Sig} \cos[\phi_{LO} - \phi_{Sig}] \end{aligned} \tag{4.17}$$

Indeed, the eight-step phase cycling procedure subtracts out the local oscillator and signal intensity terms, eliminates scatter from the excitation beams, and enhances the desired signal contribution by a factor of 16.

### 4.4.4 Phase Stability

Using common path optics and 2D temporal pulse shaping, the phases of an arbitrary number and geometry of beams are passively stabilized [133]. In our experimental setup, the phase stability is better than $\lambda/100$ over more than several hours. Strong phase stability between all beams is a distinct advantage of our 2D spectrometer. The phase stability allows us to perform two-quantum, three-dimensional, and higher-order measurements that most conventional 2D spectrometers are incapable of performing.

# Chapter 5

# Morphology and Excitonic Coupling in Double-Walled J-Aggregate Nanotubes

In chapter 5, we characterize the coupling between the inner and outer wall excitons of double-walled J-aggregate nanotubes. For our experiments, we take great care to ensure our samples are comprised of only isolated or bundled nanotubes in order to determine the effects of higher-order morphology on excitonic coupling. First, linear absorption spectra are correlated to morphology using cryogenic electron tunneling microscopy. Then, we use linear absorption to characterize nanotube morphology and measure two-dimensional spectra of isolated, bundled, and mixed nanotubes in solution. Finally, we characterize mixed nanotube samples in glass at cryogenic temperature.

Synthesis of the solution-based nanotubes was performed at MIT by Dörthe Eisele in the group of Moungi Bawendi. Synthesis of the glass nanotubes was also performed at MIT by Justin Caram and Sandra Doria in the Bawendi group. Cryogenic tunneling electron microscopy was performed at Brandeis University by Xiaofeng Fu in the group of Daniela Nicastro. Two-dimensional spectroscopy of solution-based nanotubes was performed by myself and Dylan Arias; two-dimensional spectroscopy of glass nanotubes was performed by myself and Jake Siegel.

## 5.1 Theory of Molecular Aggregates

The simplest exciton in a molecular aggregate is formed by a dimer coupled through its transition dipole moments [134, 38]. The Hamiltonian for the dimeric exciton states is determined by the lowest lying excited state energy of the molecular constituents $E$ and the dipole-dipole coupling strength $J$:

$$H = \begin{bmatrix} \mathrm{E} & \mathrm{J} \\ J & E \end{bmatrix} \tag{5.1}$$

$$J = \frac{\mu_1 \mu_2}{4\pi\epsilon_r R^3} \left(1 - 3\cos^2\theta\right) \tag{5.2}$$

The coupling strength is defined by the relative permittivity of the molecular constituents $\epsilon_r$, the magnitudes of their transition dipole moments $\mu_i$, and the distance $R$ and angle $\theta$ between them, as illustrated in figure 5.1a. Coupling of the excited state molecular orbitals produces two Frenkel exciton states where the lower energy (i.e. bonding-like) wavefunction is the sum of the molecular orbitals and the higher energy (i.e. antibonding-like) wavefunction is the difference. The exciton state with in-phase molecular wavefunctions contains most of the oscillator strength because the individual dipoles act as an enhanced single dipole moment, while the exciton state with out-of-phase molecular wavefunctions contains little oscillator strength due to destructive interference of the dipole moments.

Coupling of the excited molecular states is strongly dependent on the relative angle between the transition dipole moments, shown in green in figure 5.1b. When $\theta = 0$, the coupling between the molecules is negative and the lowest lying energy state is characterized by in-phase wavefunctions and dipoles aligned head-to-tail. The exciton absorption is red-shifted from the molecular excited state energy and the dimer is called a J-aggregate, illustrated in figure 5.1c. As the angle between the dipoles increases and dipole-dipole coupling becomes positive, the wavefunctions of the higher lying energy state become in-phase and the dipoles align side-by-side. When $\theta = \pi/2$, the exciton absorption is blue-shifted from the molecular

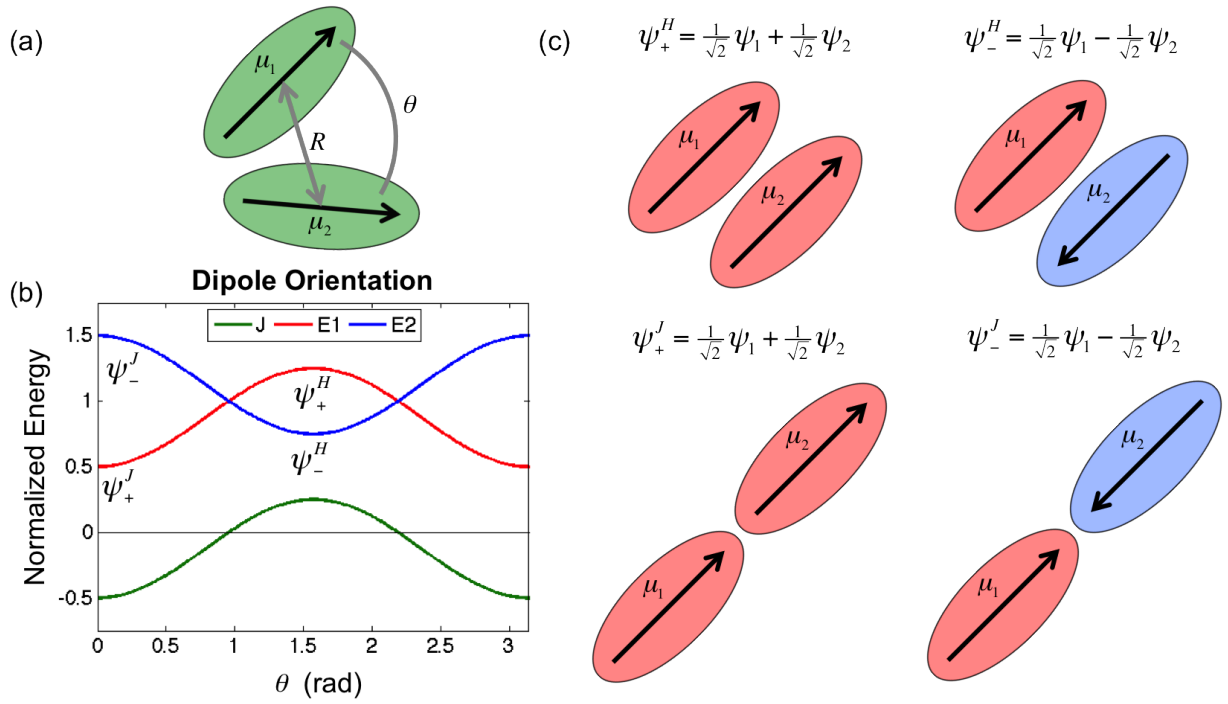


Figure 5.1: Coupled molecular dimer. (a) Transition dipole moments $\mu_1$ and $\mu_2$ of molecules 1 and 2 are separated by $R$ and oriented at angle $\theta$. (b) Angle-dependent dipole-dipole coupling and eigenstate energies. (c) Molecular dimer wavefunctions for the J- and H-aggregates $\psi^J_\pm$ and $\psi^H_\pm$, respectively.

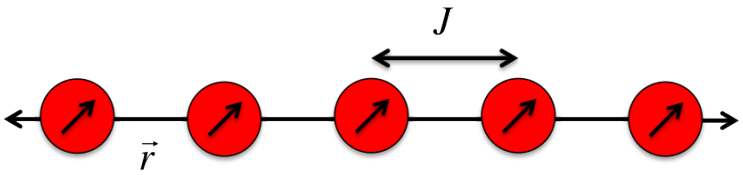


Figure 5.2: Linear J-aggregate. Linear J-aggregates possess molecular dipole moments oriented parallel to one another in a chain, which are separated by $\vec{r}$ and have a nearest-neighbor interaction strength $J$.

excited state energy and the dimer is called an H-aggregate, illustrated in figure 5.1c.

### 5.1.1 Linear J-Aggregates

The coupled dimer model can be easily extended to linear J-aggregates where many two-level molecules are aligned in one dimension and couple to form delocalized exciton states, illustrated in figure 5.2 [135]. The Frenkel exciton Hamiltonian takes the form:

$$\hat{H} = \sum_{p} E_p B_p^{\dagger} B_p + \sum_{p,q} V_{pq} B_p^{\dagger} B_q \tag{5.3}$$

$$V_{pq} = -\frac{J}{|\vec{r}_p - \vec{r}_q|^3} \tag{5.4}$$

where $E_p$ is the excited state molecular orbital energy of molecule $p$, $B_p^{\dagger}$ and $B_p$ are the creation and annihilation operators for an exciton on molecule $p$ (under the constraint there can be at most one exciton per molecule), and $V_{pq}$ is the dipole-dipole coupling between molecules $p$ and $q$ at $\vec{r}_p$ and $\vec{r}_q$ with nearest-neighbor interaction strength $J$.

In the idealized linear model, J-aggregates are homogeneous and intermolecular coupling is restricted to nearest neighbors. Under this condition, the solutions to the exciton wavefunctions, energies, and transition dipole intensities take the form:

$$|\Psi_k\rangle = \sqrt{\frac{2}{N+1}} \sum_{p} \sin\left[\frac{kp\pi}{N+1}\right] |\psi_p\rangle \tag{5.5}$$

$$E_k = E + 2J\cos\left[\frac{k\pi}{N+1}\right] \tag{5.6}$$

$$I_k = \left(1-(-1)^k\right)\frac{\mu^2}{N+1}\cot^2\left[\frac{k\pi}{2\,(N+1)}\right] \tag{5.7}$$

where $k$ is the crystal wavevector, $N$ is the number of coupled molecules in the J-aggregate, and $|\psi_p\rangle$ are the molecular wavefunctions of molecule $p$. Similar to particle-in-a-box states, the J-aggregate wavefunctions have a sinusoidal form that is characterized by the exciton delocalization. Large spatial delocalization is favorable and substantially stabilizes the exciton by lowering the J-aggregate energy. It also substantially increases the macroscopic transition dipole moment.

### 5.1.2 J-Aggregate Nanotubes

In some cases, the physical structure of molecules allows complex aggregate structures to form in solution, including sheets, rods, and ribbons. In chapters 5 and 6, we study J-aggregates that form double-walled nanotubes [136, 137, 138]. Such nanotubes can be modeled by wrapping a conventional planar J-aggregate into a cylinder of the appropriate radius, illustrated in figure 5.3a. In this model, molecules of length $a$ and thickness $d$ are arranged in a brick lattice defined by the basis vectors $\overrightarrow{a}_1$ and $\overrightarrow{a}_2$, where the displacing shift $s$ between molecules in adjacent rows determines the dipole-dipole coupling and the type of aggregation. The planar structure is then wrapped along a wrapping vector $\overrightarrow{C} = \mathrm{n}_1\overrightarrow{a}_1 + \mathrm{n}_2\overrightarrow{a}_2$, where $n_i$ is an integer, to create a cylinder of the appropriate radius $R$, where $\left|\overrightarrow{C}\right| = 2\pi R$ by normal Euclidean geometry. The vector $\overrightarrow{Z}$ defines the long axis of the cylinder and $\theta$ the angle between the molecular transition dipole moments and the long axis [139, 140].

In the theoretical description of J-aggregate nanotubes, each molecule is characterized by a vector defining its transition dipole moment $\overrightarrow{\mu}$. The Frenkel Hamiltonian of the J-

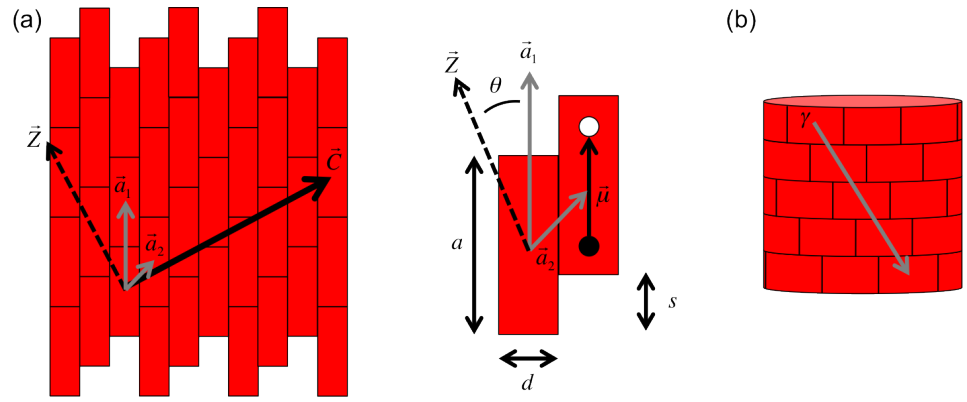


Figure 5.3: J-aggregate nanotubes. (a) Brick lattice defined by the basis vectors $\vec{a}_1$ and $\vec{a}_2$, where $a$ is the length, $d$ the thickness, and $s$ the displacing shift between molecules. The planar aggregate is wrapped along the wrapping vector $\vec{C} = \mathrm{n}_1 \vec{a}_1 + \mathrm{n}_2 \vec{a}_2$, where $n_i$ is an integer, to create a cylinder of the appropriate radius $R$ and $\vec{Z}$ defines the long axis of the cylinder and $\theta$ the angle between the molecular transition dipole moments $\vec{\mu}$ and the long axis. (b) J-aggregate nanotube composed of a stack of $N_1$ equidistant rings containing $N_2$ equidistant molecules and characterized by a helical angle $\gamma$ between rings.

aggregate nanotube has the familiar form:

$$\hat{H} = \sum_p E_p B_p^\dagger B_p + \sum_{p,q} V_{pq} B_p^\dagger B_q \tag{5.8}$$

$$V_{pq} = \frac{\vec{\mu}_p \cdot \vec{\mu}_q}{|\vec{r}_p - \vec{r}_q|^3} - 3\frac{(\vec{\mu}_p \cdot \vec{r}_{pq})(\vec{\mu}_q \cdot \vec{r}_{pq})}{|\vec{r}_p - \vec{r}_q|^5} \tag{5.9}$$

where $V_{pq}$ is the dipole-dipole coupling and is dependent on the distance $\vec{r}_p - \vec{r}_q$ and orientation between the dipole moments $\vec{\mu}_p$ and $\vec{\mu}_q$ of molecules $p$ and $q$, respectively. The exciton wavefunction take the form:

$$|\Psi_k\rangle = \sum_p \psi_k(p) B_p^\dagger |g\rangle \tag{5.10}$$

where $k$ is a general quantum number, $\psi_k(p)$ are the single exciton eigenvectors, and $|g\rangle$ is the exciton ground state.

J-aggregate nanotubes can be modeled equivalently by a stack of $N_1$ equidistant rings containing $N_2$ equidistant molecules with each ring rotated by a helical angle $\gamma$, illustrated

in figure 5.3b. In this case, the Hamiltonian is separable into a one-dimensional longitudinal contribution of the $N_1$ rings (with the same solutions of the linear J-aggregate model described in equations 5.5-5.7) and radial contributions from the independent rings with Bloch wavefunctions:

$$|\Psi_{k_2}\rangle = \exp\left[i2\pi k_2 n_2/N_2\right] \tag{5.11}$$

where $k_2 = 0, \pm 1, \ldots, N_2/2$ and $n_2$ is the position of a molecule in the ring [141]. The three-dimensional structure of the nanotube produces three excitons bands $K = (k_1, k_2)$: a longitudinal band characterized by wavevector $k_1$ and two degenerate radial bands characterized by wavevectors $\pm k_2$. Moreover, their linear absorption spectra are dominated by these three $K$ states: $(1, 0)$ a superradiant state polarized along the long axis and $(0, \pm 1)$ two degenerate states polarized perpendicular to the long axis.

## 5.2 Double-Walled J-Aggregate Nanotubes

In our experiments, we study J-aggregates formed by the self-assembly of 3,3'-bis(2-sulfopropyl) 5,5',6,6'-tetrachloro 1,1'-dioctylbenzimidacarbocyanine 18 ($C_8S_3$) monomers in water, illustrated in figure 5.4a. $C_3S_8$ monomers consist of three important structural areas [142]. The conjugated backbone of the isocyanine dye (dark grey) largely determines the electronic structure of the monomer, while the hydrophobic alkyl sidechains (light grey) and hydrophilic sulfate groups (red) create regions of differing hydrophobicity and drive self-assembly in water. $C_3S_8$ is first dissolved in methanol to prepare a monomer solution that exhibits broad absorption around 520 nm, shown in figure 5.4b.

### 5.2.1 Isolated Nanotubes

Upon dilution of the monomer solution to a final 9:1 water:methanol ratio, $C_3S_8$ self-assembles to form J-aggregate double-walled nanotubes, illustrated in figure 5.4c. The linear absorption of the J-aggregate nanotubes (figure 5.4b) exhibits the characteristic red-shift and

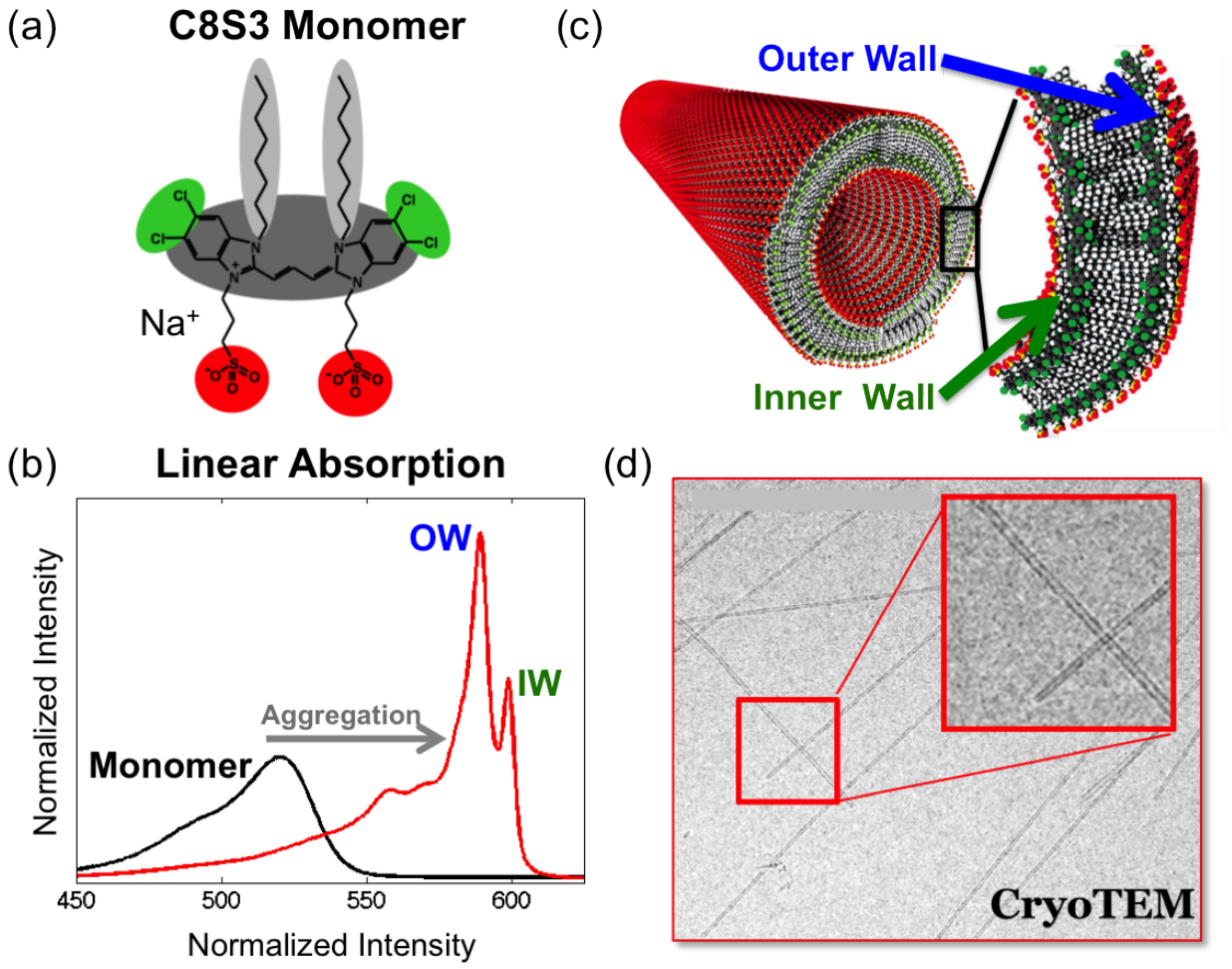


Figure 5.4: Isolated J-aggregate nanotubes. (a) 3,3'-bis(2-sulfopropyl) 5,5',6,6'-tetrachloro 1,1'-dioctylbenzimidacarbocyanine 18 ($C_3S_8$) monomers, composed of a conjugated cyanine backbone (dark grey), hydrophobic alkyl chains (light grey), hydrophilic sulfate groups (red), and sodium counter ions. (b) Monomer (black) and isolated nanotube (red) linear absorption. The 599 nm and 589 nm J-aggregate peaks correspond to excitons on the inner and outer walls, respectively. (c) Double-walled J-aggregate nanotube with characteristic inner and outer walls. (d) Cryogenic tunneling electron microscopy of isolated nanotubes reveals an inner wall diameter of 6 nm and an outer wall diameter of 13 nm (with a wall-to-wall separation of 3-4 nm) and lengths up to a few microns.

lineshape narrowing due to coupling of the electronic states when the isocyanine backbones stack in parallel [36, 143, 144, 145]. Upon aggregation, two distinct excitonic bands form at 599 nm and 589 nm, which have been previously determined to arise from inner and outer wall excitons, respectively [146]. Weaker, higher energy exciton bands also exist as discussed in the theoretical description of J-aggregate nanotubes. The most important of these higher energy exciton bands appears at 583 nm as a shoulder to the 589 nm peak. From cryogenic tunneling electron microscopy (cryo-TEM), the structure of isolated $C_3S_8$ nanotubes has been determined to consist of a 6 nm diameter inner wall and a 13 nm diameter outer wall separated by approximately 3-4 nm (corresponding to the alkyl chain length), shown in figure 5.4d. The nanotubes grow up to microns in length and are homogeneous along the entire length [147].

### 5.2.2 Bundled Nanotubes

Upon aging of isolated nanotubes, bundles of nanotubes form and exhibit their own characteristic linear absorption, shown in figure 5.5a. The inner wall peak lightly red-shifts to 603 nm and is slightly broadened. Additionally, a new broad, higher energy peak appears at 578 nm. Cryo-TEM, shown in figure 5.5b, reveals that bundled nanotube ensembles are far less homogeneous than isolated nanotubes. Bundles were composed of 6 to 12 nanotubes and appeared in two morphologies: straight and twisted, shown in figure 5.5d. Straight bundles were characterized by multiple nanotubes running parallel to one another along their entire length, while twisted bundles exhibited curvature along their length for which a unique twisting angle could be defined.

To determine the high-order morphology of the bundles, a series of TEM images was taken at different angles between the electron beam and sample in order to reconstruct the full three-dimensional structure. From the spatial reconstruction, a cross-sectional slice of a bundle can be well determined, one example of which is shown in figure 5.5d. The average center-to-center distance between nanotubes in a bundle is 9 nm, which is inconsistent with a

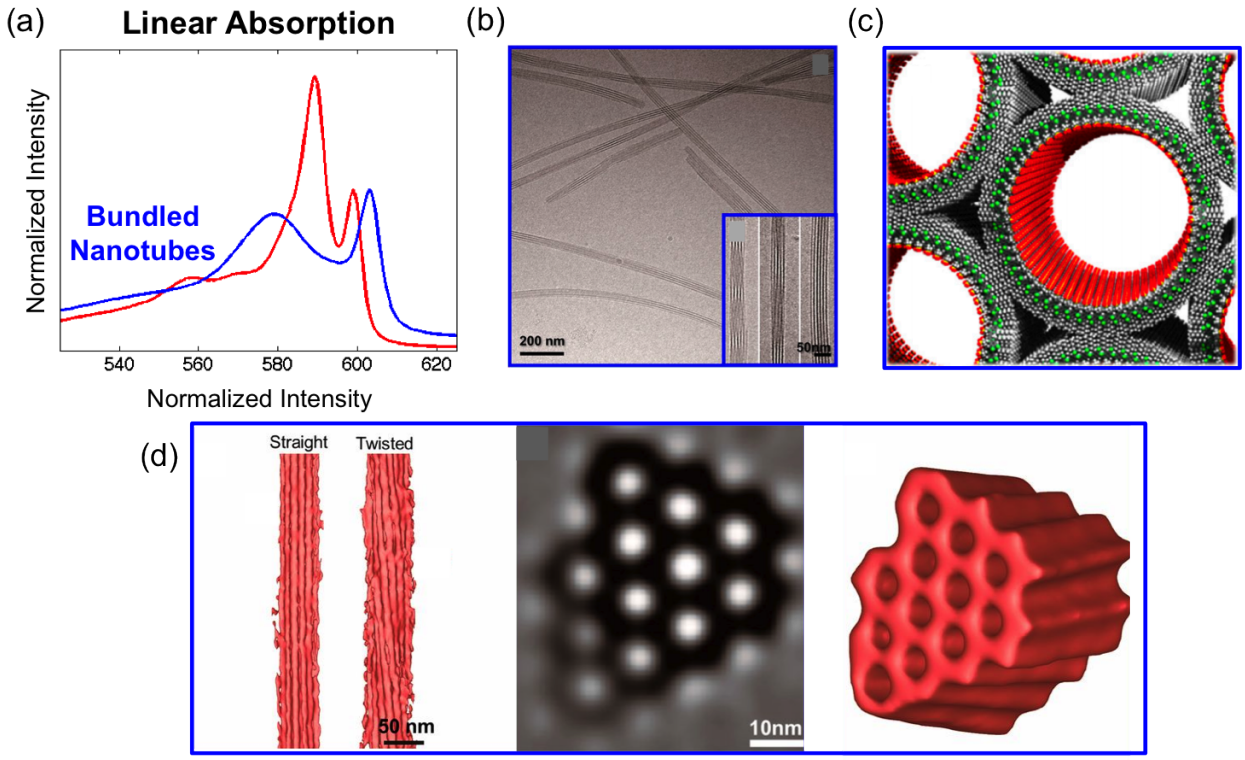


Figure 5.5: Bundled J-aggregate nanotubes. (a) Linear absorption of isolated (red) and bundled (blue) nanotubes. The 603 nm and 578 nm bundled nanotube peaks originate from inner wall excitons polarized parallel and perpendicular to the long axis of the bundle, respectively. (b) Cryogenic tunneling electron microscopy of bundled nanotubes. (c) Graphical representation of bundled inner wall nanotubes. (d) Three dimensional reconstructions of straight and twisted bundles, cross-sectional slice of a twisted bundle, and reconstruction of the cross-sectional slice.

bundle of double-walled nanotubes. However, the center-to-center distance is consistent with a bundle of inner wall nanotubes. In order to maintain its morphology, the bundled inner wall nanotubes would require an amorphous "outer wall" surrounding the entire bundle due to the hydrophobicity of the alkyl sidechains. Assuming there is substantial disorder in the amorphous outer wall, its spectral features should not exhibit the characteristic red-shifting and line narrowing of J-aggregation. Thus, we hypothesize the well-defined spectral features in the linear absorption spectrum of bundled nanotubes, shown in figure 5.5a, arise solely from inner wall nanotubes.

#### 5.2.2.1 Linear Dichroism

To determine the transition dipole moment orientations in isolated and bundled nanotubes, we measured reduced linear dichroism spectra: $LD_R = \left(A_{\parallel} - A_{\perp}\right) / \left(A_{\parallel} + A_{\perp}\right)$ [148]. In this experiment, nanotubes were flowed through a cell which caused their long axis to align along the direction of flow due to their large length to diameter ratio, illustrated in figure 5.6a. Absorption of light polarized parallel $\left(A_{\parallel}\right)$ and perpendicular $(A_{\perp})$ to the flow direction (also labelled $H(||)$ and $V(\perp)$, respectively) was then measured. A linear dichroism of 1 indicates a transition dipole moment polarized perfectly parallel to the flow direction and -1 indicates polarization perfectly perpendicular to the flow direction. A linear dichroism of 0 indicates a transition dipole moment that is either isotropic or polarized $45^{\mathrm{o}}$ relative to the flow direction.

The reduced linear dichroism of the isolated nanotubes shown in figure 5.6b demonstrates the strong inner and outer wall transitions at 599 nm and 589 nm, respectively, are polarized mainly parallel to the long axis of the nanotubes, while the small shoulder at 583 nm is polarized mainly perpendicular. The reduced linear dichroism of the bundled nanotubes shown in figure 5.6c demonstrates that the strong transition at 603 nm is polarized mainly parallel to the long axis of the bundles, while the weak transition at 578 nm is polarized mainly perpendicular .

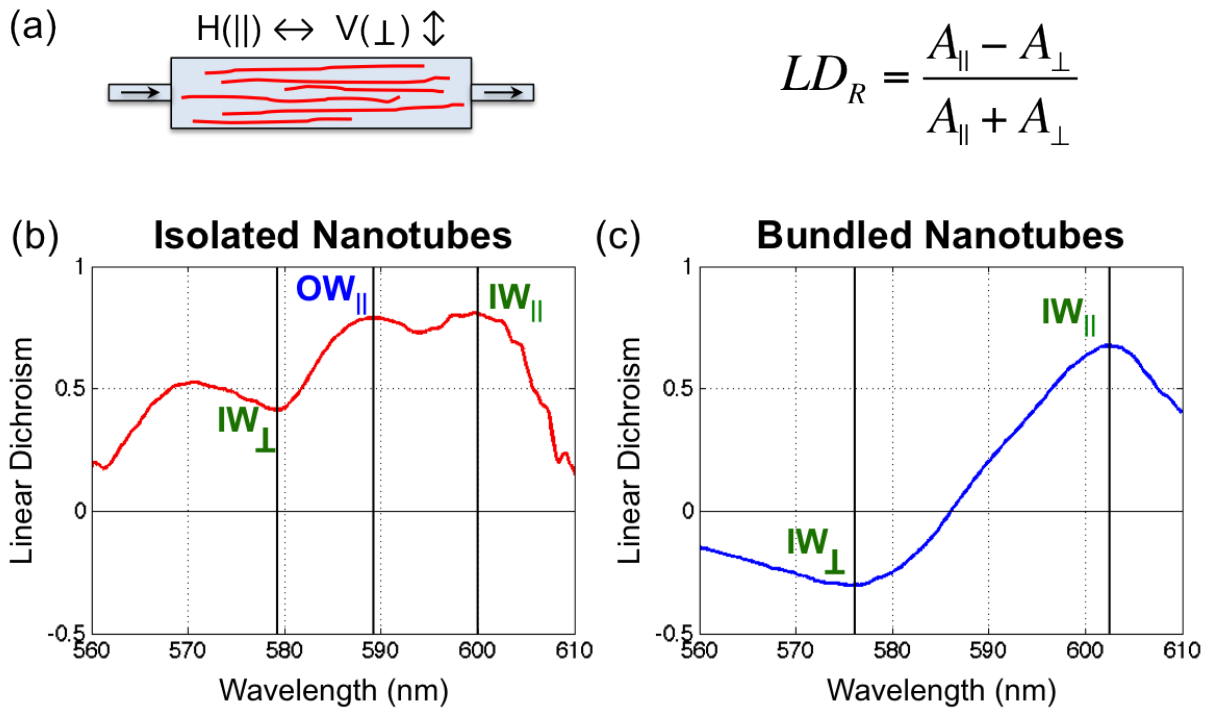


Figure 5.6: Reduced linear dichroism. (a) Nanotubes flown through a cell align along the flow direction, parallel to the laser polarization $H(||)$ and perpendicular to the laser polarization $V(\perp)$. (b) Reduced linear dichroism of isolated nanotubes. The two strong inner and outer wall transitions at 599 nm and 589 nm, respectively, are polarized mainly parallel to the long nanotube axis. A third, weak shoulder at 583 nm is polarized mainly perpendicular to the long axis of the nanotube. (c) Reduced linear dichroism of bundled nanotubes. The lower energy transition at 603 nm is polarized mainly parallel to the long bundle axis. The higher energy transition at 578 nm is polarized mainly perpendicular to the long axis of the bundles.

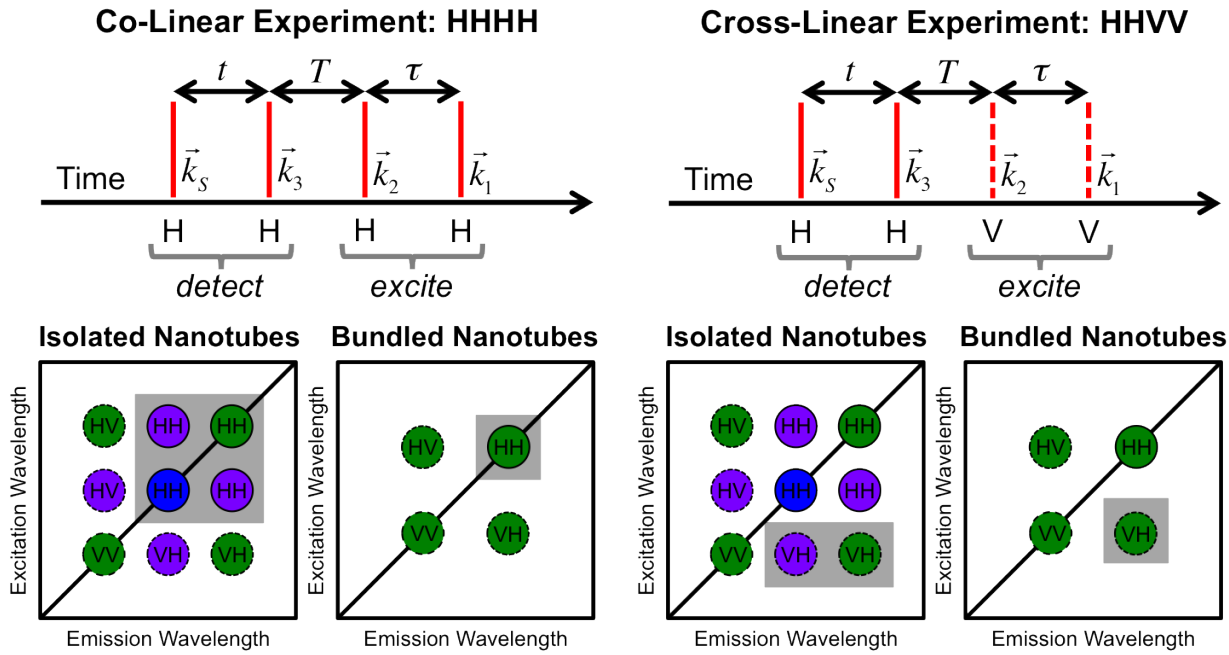


Figure 5.7: Polarization-controlled two-dimensional experiments. Co-linear experiments utilize pulses with parallel polarizations ($H$) to excite and detect excitons with parallel transition dipole moments, which enhances diagonal peaks. Cross-linear experiments utilize pulses with perpendicular polarizations to excite ($V$) and detect ($H$) excitons with perpendicular transition dipole moments, which enhances crosspeaks between perpendicularly polarized states. Isolated and bundled nanotube co-linear and cross-linear 2D spectra with the enhanced peaks indicated in grey.

## 5.3 Morphology and Excitonic Coupling

From linear absorption and linear dichroism, the structural origin and orientation of the spectral features in double-walled J-aggregate nanotubes has been determined. In the isolated nanotubes, the two strongest spectral features at 599 nm and 589 nm have been shown to originate from the inner and outer walls, respectively. Previous chemical oxidation experiments also demonstrated at most weak coupling between excitons on the inner and outer walls [146]. However, these experiments were only indirect measurements of exciton coupling. Thus, we use two-dimensional (2D) spectroscopy to directly measure the coupling of excitons in double-walled J-aggregate nanotubes.

In our experiments, we utilize polarization control to interrogate exciton states with different transition dipole moment orientations as illustrated in figure 5.7. Polarization-

controlled experiments require orientated transition dipole moments, thus the nanotubes are flowed through a cell to align their long axes parallel to the direction of flow in the same manner as the linear dichroism experiments. We perform two types of polarization-controlled 2D experiments: co-linear and cross-linear. Co-linear 2D experiments use laser fields with all parallel polarizations to excite and detect excitons with the same transition dipole moment orientation, enhancing the diagonal peaks of excitons with transition dipole moments parallel to the laser field polarization. Cross-linear 2D experiments use pairs of laser fields with perpendicular polarizations to excite and detect excitons with perpendicular transition dipole moments, enhancing the crosspeaks between excitons with perpendicular transition dipole moments.

Co-linear and cross-linear 2D spectra in isolated and bundled nanotubes are illustrated in figure 5.7. The 2D measurements of isolated nanotubes interrogate two excitons with transition dipole moments parallel and one exciton perpendicular to the long axis of the nanotubes. The co-linear experiment interrogates the diagonal peaks of excitons with the parallel transition dipole moments and their crosspeaks. The cross-linear experiment interrogates the crosspeaks between excitons with perpendicular transition dipole moments. The 2D measurements of bundled nanotubes interrogate one exciton with a transition dipole moment parallel and one exciton perpendicular to the long axis of the bundles. The co-linear experiment interrogates the diagonal peak of the exciton with the parallel transition dipole moment. The cross-linear experiments interrogates the crosspeak between the excitons with perpendicular transition dipole moments. The co-linear and cross-linear spectra for isolated and bundled nanotubes are illustrated in figure 5.7 with a light grey box indicating the peak enhancement in each experimental case.

Many two-dimensional experiments have been performed on J-aggregate nanotubes previously [149, 47, 48, 150, 151, 49]. However, the appropriate care was not taken to ensure only a single nanotube morphology was interrogated in each of these studies. Because linear dichroism and linear absorption have proven to be reliable methods for determining nan-

otube morphology, we used both techniques throughout the synthesis and 2D experiments to ensure samples contained only the desired morphology.

### 5.3.1 Isolated Nanotubes

First, the co-linear 2D spectrum of isolated nanotubes was measured with the polarization of the incident laser fields parallel to the flow direction. The co-linear 2D spectrum in figure 5.8a reveals two diagonal peaks at 599 nm and 589 nm associated with the inner and outer wall excitons polarized parallel to the long axis of the nanotube. A weak crosspeak between the two peaks is also clearly visible, revealing weak inter-wall coupling between excitons on the inner and outer walls.

Second, the cross-linear 2D spectrum of isolated nanotubes was measured with the polarization of the exciting laser fields parallel and the detecting laser fields perpendicular to the flow direction. The cross-linear 2D spectrum in figure 5.8c reveals the same inner and outer wall diagonal peaks at 599 nm and 589 nm, respectively. However, now there is a much stronger crosspeak shifted to lower excitation wavelength. This strong crosspeak appears between the 599 nm inner wall peak and the weak 583 nm shoulder of the outer wall peak.

The reduced linear dichroism revealed this shoulder is polarized perpendicular to the long axis of the nanotube, explaining the appearance of the new crosspeak between the perpendicularly polarized exciton states due to the orthogonality of the incident laser fields. However, the 583 nm diagonal peak still does not appear because the exciting laser fields are perpendicular to the transition dipole moment. Additionally, the weak crosspeak between inner and outer wall excitons can still be observed as a small shoulder to higher excitation wavelength.

As discussed previously, the theoretical description of J-aggregate nanotubes determined that three exciton bands form due to their three-dimensional cylindrical structure: one perpendicular to the long axis and two perpendicular. In double-walled nanotubes, two sets of three exciton bands should exist and correspond to each wall. The 583 nm shoulder is

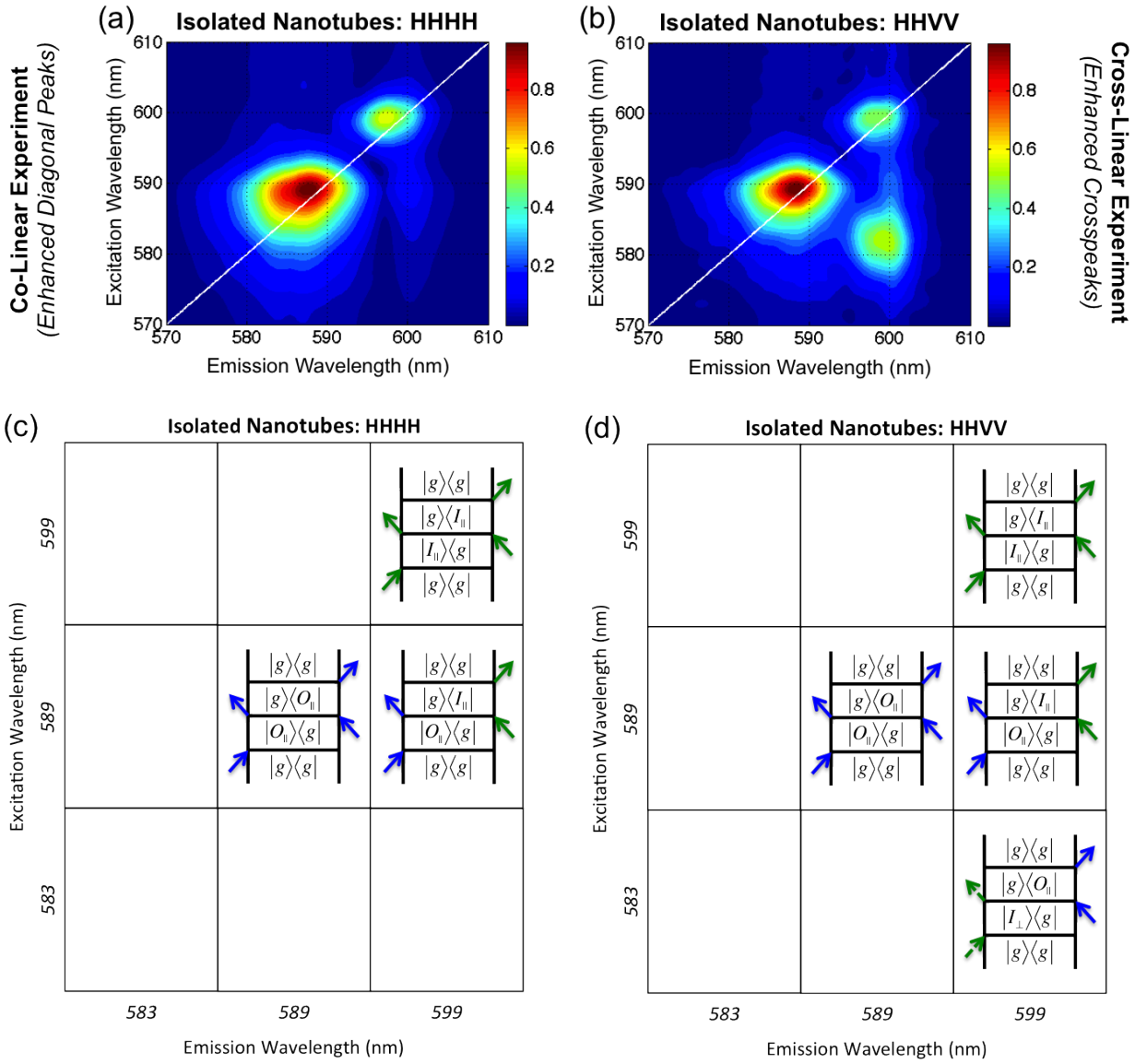


Figure 5.8: Isolated nanotube two-dimensional correlation spectra. (a) Co-linear 2D correlation spectrum of isolated nanotubes (enhancing the diagonal peaks) reveals weak coupling between inner and outer wall peaks at 599 nm and 589 nm. (b) Cross-linear 2D correlation spectrum of isolated nanotubes (enhancing the crosspeaks) reveals strong coupling between perpendicular inner wall peaks at 599 nm and 583 nm. (c) Co-linear 2D rephasing spectrum Feynman diagrams (stimulated emission only), where green and blue arrows denotes transitions at 599 nm and 589 nm, respectively, and solid and dashed arrows denote transition dipole moment interactions parallel and perpendicular to the long axis of the nanotubes, respectively. (d) Cross-linear 2D rephasing spectrum Feynman diagrams.

the lowest energy peak polarized perpendicular to the long axis of the nanotube and thus we expect it to originate from the same state as the lowest energy peak polarized parallel to the long axis, i.e. the inner wall. Strong exciton coupling between the 583 nm and 599 nm peaks also supports the assignment of the 583 nm peak to an inner wall exciton. The co-linear 2D spectrum revealed weak coupling between parallel inner and outer wall excitons, thus strong coupling is similarly unlikely between perpendicular excitons on different walls. So, we assign the 583 nm peak to an inner wall exciton polarized perpendicular to the long axis of the nanotube, revealing strong intra-wall coupling of excitons in isolated nanotubes.

### 5.3.2 Bundled Nanotubes

Third, the co-linear 2D spectrum of bundled nanotubes was measured with the polarization of the incident laser fields parallel to the flow direction. The co-linear spectrum in figure 5.9a reveals a strong diagonal peak at 603 nm and a weak diagonal peak at 578 nm, corresponding with the linear absorption of the bundled nanotubes. The linear dichroism revealed these peaks are polarized parallel and perpendicular to the long axis of the bundle, respectively, and are likely associated with excitons on the bundled inner walls. The transition dipole moment orientation and laser field polarization explains the relative amplitude of the two peaks in the co-linear 2D spectrum. A weak crosspeak between the two peaks is also observed.

Fourth, the cross-linear 2D spectrum of bundled nanotubes was measured with the polarization of the exciting laser fields parallel and the detecting laser fields perpendicular to the flow direction. The cross-linear 2D spectrum in figure 5.9c reveals the same 603 nm diagonal peak but with much weaker amplitude as the exciting laser fields are now perpendicular to the transition dipole moment. However, the crosspeak has much stronger amplitude as the detecting laser fields are now parallel to transition dipole moment of the 578 nm peak.

We assume both the 603 nm and 578 nm peaks originate from the inner wall and there is no spectral contribution from the amorphous outer wall. Thus in direct comparison to the cross-linear 2D spectrum of isolated nanotubes, the strong crosspeak in the bundled

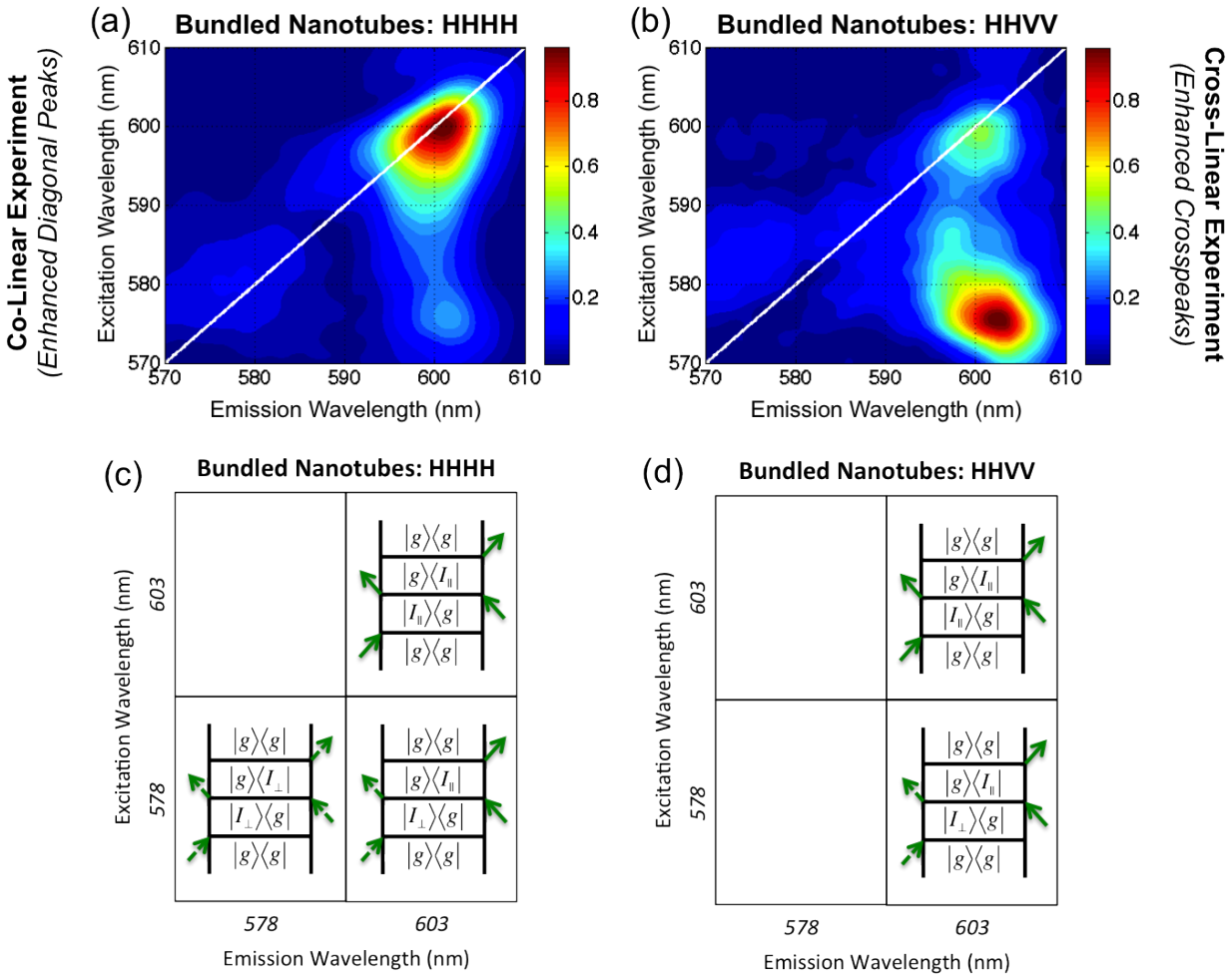


Figure 5.9: Bundled nanotube two-dimensional correlation spectra. (a) Co-linear 2D correlation spectrum of bundled nanotubes (enhancing the diagonal peaks) reveals coupling between perpendicular inner wall excitons at 603 nm and 578 nm. (b) Cross-linear 2D correlation spectrum of bundled nanotubes (enhancing the crosspeaks) reveals strong coupling between perpendicular inner wall excitons at 603 nm and 578 nm. (c) Co-linear 2D rephasing spectrum Feynman diagrams (stimulated emission only), where solid and dashed arrows denote transition dipole moment interactions parallel and perpendicular to the long axis of the bundles, respectively. (d) Cross-linear 2D rephasing spectrum Feynman diagrams.

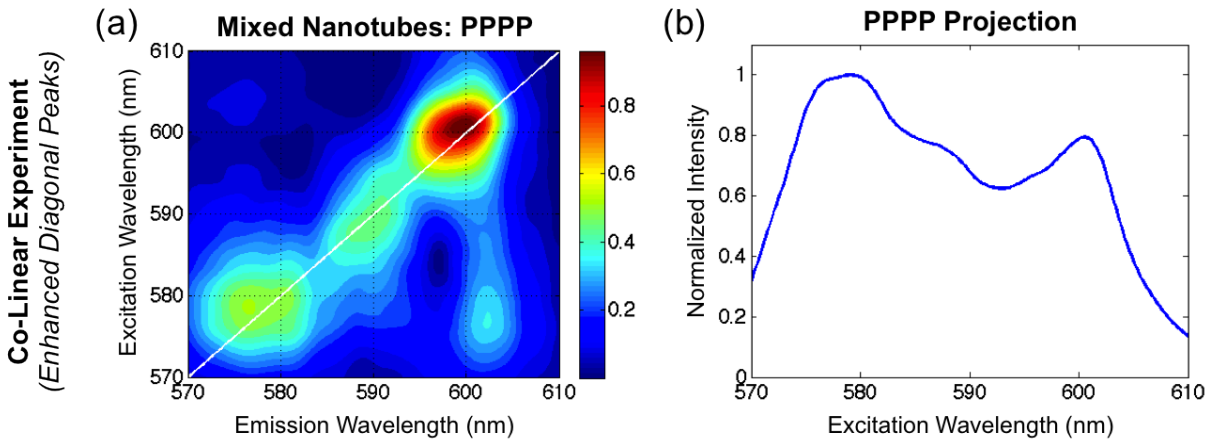


Figure 5.10: Mixed nanotube two-dimensional correlation spectrum. (a) Co-linear 2D correlation spectrum of mixed nanotubes (enhancing the diagonal peaks) with incident laser polarizations P = 45$^{o}$ between $H(||)$ and $V(\perp)$. Co-linear 2D spectrum reveals no crosspeak between excitons on isolated nanotubes and bundled nanotubes, demonstrating they are distinct physical and electronic systems in solution. (b) Emission energy-integrated projection of co-linear 2D correlation spectrum onto the excitation axis.

nanotube spectrum also reveals strong coupling between intra-wall excitons.

### 5.3.3 Mixed Nanotubes

Finally, the co-linear 2D spectrum of a mixed sample of isolated and bundled nanotubes was measured with the polarization of the incident laser fields 45$^{o}$ relative to the flow direction, allowing contributions from all the spectral features. The co-linear 2D spectrum in figure 5.10 reveals three diagonal peaks. The 600 nm peak arises from excitons on the inner walls of isolated (599 nm) and bundled (603 nm) nanotubes polarized parallel to the long axes. The 589 nm peak arises primarily from excitons on the outer wall of isolated nanotubes. The 578 nm peak arises primarily from excitons on the inner walls of bundled nanotubes polarized perpendicular to the long axis of the bundle. Additionally, a single crosspeak is observed between the bundled nanotube diagonal peaks (578 nm, 603 nm). However, no crosspeaks are observed between excitons on isolated and bundled nanotubes, which clearly demonstrates the two morphologies are physically and electronically distinct systems in solution.

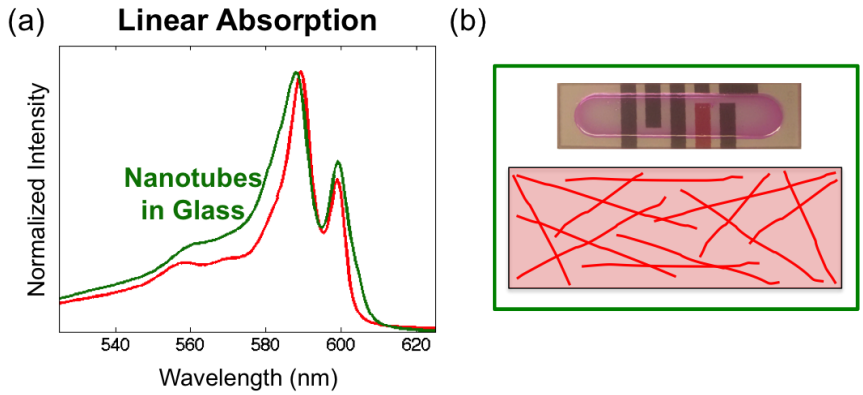


Figure 5.11: Glass J-aggregate nanotubes. (a) Glass (green) and solution-based isolated (red) nanotube linear absorption. Nanotubes are embedded in glass formed by a sucrose:trehalose matrix. Glass nanotubes exhibit lineshape broadening and contributions from isolated and bundled nanotubes. (b) Glass nanotubes are isotropically oriented in the micro-cuvette.

## 5.4 Double-Walled J-Aggregate Nanotubes at Low Temperature

To perform experiments at low temperature, J-aggregate nanotubes must be preserved in the solid state while maintaining their self-assembled structure, higher-order morphology, and optical and electronic properties. A supersaturated solution of a 1:1 mixture of sucrose and trehalose was used to prepare J-aggregate nanotubes in a glass, which is formed by a sugar matrix [152, 153, 154]. First, the solution-based nanotubes were diluted by 50% with the supersaturated sugar solution. Then, a thin layer of the nanotube-sugar solution was drop cast onto a micro-cuvette. Finally, the thin layer of the nanotube-sugar solution was exposed to vacuum for 24 hours to evaporate the water and form a glass with the nanotubes imbedded in the sugar matrix.

Sucrose and trehalose sugar matrices have been frequently used to form glasses of proteins and other biologically-relevant molecules while retaining their structure. The linear absorption of a J-aggregate nanotube glass shown in figure 5.11a demonstrates that the nanotubes maintain their optical properties upon glass formation. Compared to the linear absorption of isolated nanotubes in solution, the glass linewidths are slightly broadened and the higher

wavelength shoulder of the inner wall peak at 599 nm indicates that some bundled nanotubes are also present. However, the self-assembled structure and higher-order morphology of the nanotubes is unlikely to change significantly in the glass since the linear absorption of the isolated nanotubes (figure 5.4c) changes drastically due to the small perturbation of bundling (figure 5.5a).

Additionally, J-aggregate nanotubes are not aligned during glass formation and are isotropically oriented in the micro-cuvette, illustrated in figure 5.11b. Thus, polarization-controlled experiments are not possible since alignment of the nanotubes and their transition dipole moments is required. Our collaborators in the Bawendi group are currently working on a method to orient the glass nanotubes by flowing the supersaturated sugar and nanotube solution during the evaporation step of the synthesis.

### 5.4.1 Exciton Dephasing

With J-aggregate nanotubes in the solid state, temperature-dependent experiments can easily be performed outside the range of 273 to 373 K. We used 2D rephasing spectroscopy to measure the temperature-dependent homogeneous (i.e. anti-diagonal) and inhomogeneous (i.e. diagonal) linewidths and investigate the mechanisms of exciton dephasing. First, we performed 2D experiments on glass nanotubes at 10 K and measured the linewidths of the inner and outer wall peaks of isolated nanotubes at 594 nm and 584 nm, respectively, and the inner wall peak of bundled nanotubes at 596 nm. The rephasing spectrum of the glass nanotubes is shown in figure 5.12a and the homogeneous and inhomogeneous linewidths are summarized in table 5.1. The rephasing spectrum at 10 K revealed inhomogeneously broadened lineshapes for all three peaks. At low temperature, few vibrational or phonon modes are populated due to low thermal energy, thus exciton dephasing is dominated by static disorder in the glass nanotubes.

Second, we performed 2D experiments on solution-based isolated nanotubes at 295 K and measured the linewidths of the inner and outer walls peaks at 597 nm and 587 nm,

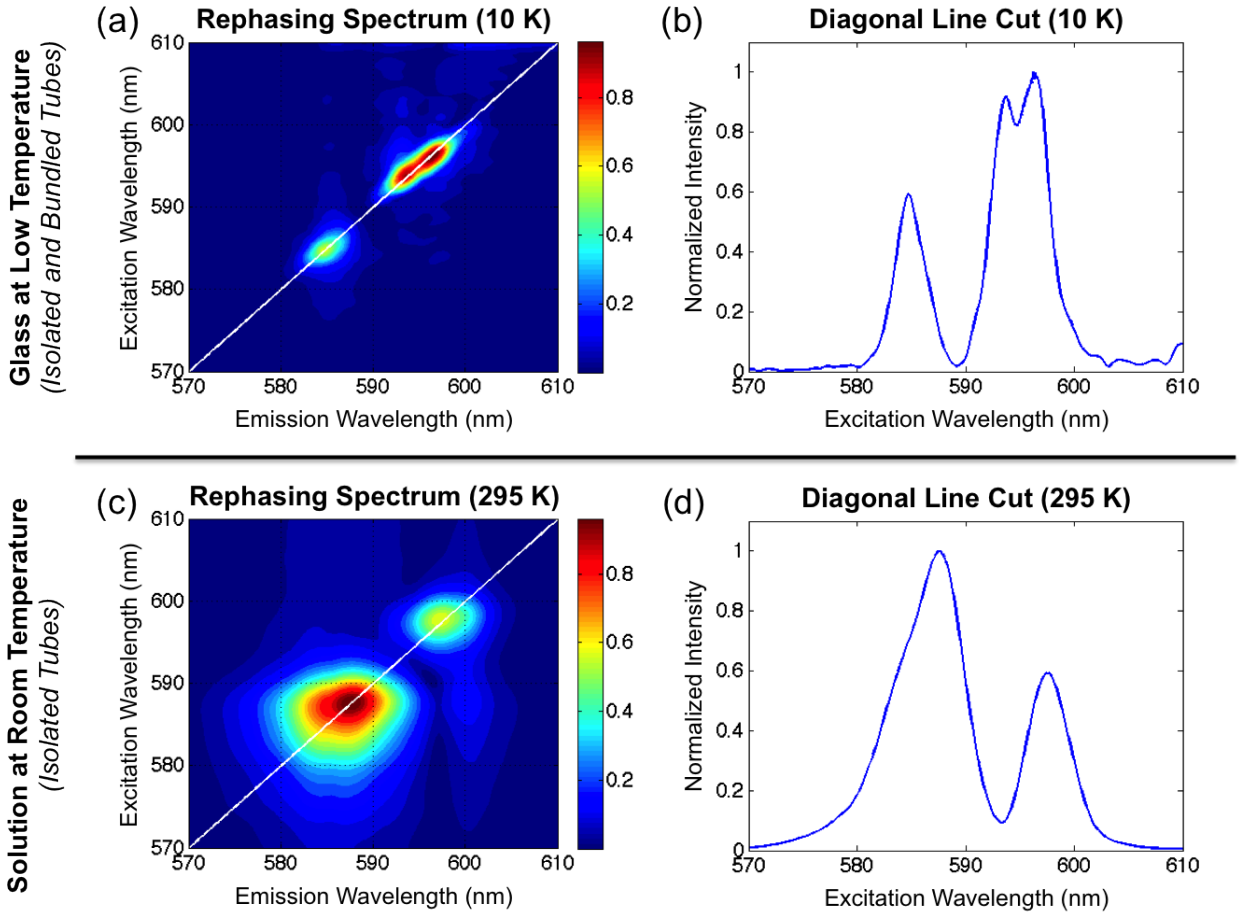


Figure 5.12: Homogeneous and inhomogeneous linewidths at room and cryogenic temperatures. (a) Rephasing spectrum of glass nanotubes (isolated and bundled) at 10 K. (b) Diagonal line cut of the rephasing spectrum at 10 K. (c) Rephasing spectrum of solution-based isolated nanotubes at 295 K. (d) Diagonal cut of the rephasing spectrum at 295 K.

**Linewidths at Cryogenic and Room Temperatures**

| Peak | Solution Linewidths at 295 K | |
|---|---|---|
| | Inhomog. | Homog. |
| 587 nm | 5.4 nm | 4.6 nm |
| 597 nm | 4.2 nm | 4.2 nm |

| Peak | Glass Linewidths at 10 K | |
|---|---|---|
| | Inhomog. | Homog. |
| 584 nm | 3.0 nm | 1.8 nm |
| 594 nm | 2.6 nm | 1.5 nm |
| 596 nm | 2.8 nm | 1.5 nm |

Table 5.1: Homogeneous and inhomogeneous linewidths of J-aggregate nanotubes at room and cryogenic temperatures. Homogeneous and inhomogeneous linewidths of glass nanotubes at 10 K, including the inner and outer wall peaks of isolated nanotubes at 594 nm and 584 nm, respectively, and the inner wall peak of bundled nanotubes at 596 nm. Homogeneous and inhomogeneous linewidths of solution-based isolated nanotubes at 295 K, including the inner and outer wall peaks at 597 nm and 587 nm, respectively.

respectively. The rephasing spectrum of the isolated nanotubes is shown in figure 5.12c and the homogeneous and inhomogeneous linewidths are summarized in table 5.1. The rephasing spectrum at 295 K revealed homogeneously broadened lineshapes for both peaks. At room temperature, many vibrational or phonon modes can be populated due to high thermal energy, thus exciton dephasing is dominated by dynamic disorder due to molecular motion in the nanotubes and solvent.

These results are in direct contrast to previous experiments on thin-film, planar J-aggregates that demonstrated dynamic disorder is the primary contributor to exciton dephasing at both room and cryogenic temperatures [155]. However, we compare glass and solution-based nanotubes at 10 K and 295 K, respectively. The dominance of static disorder in contributing to exciton dephasing at 10 K in glass nanotubes may be due to the sucrose-trehalose matrix. The control experiment of comparing the homogeneous and inhomogeneous linewidths of either glass or solution-based nanotubes at room and cryogenic temperatures is not possible due photo-induced degradation and freezing, respectively.

### 5.4.2 Photo-Induced Degradation and Recovery

Organic semiconductors under high excitation fluences commonly exhibit photo-induced changes due to processes such as exciton-exciton annihilation and charge accumulation [156, 157]. Room temperature measurements of glass J-aggregate nanotubes were not possible due to photodegradation by the ultrafast laser pulses. Photodegradation also occurred at cryogenic temperatures and the lowest possible excitation fluences but was slow enough to not significantly disrupt the 2D measurements.

We studied the effects of photodegradation in glass nanotubes at 10 K by continuously measuring 2D rephasing spectra on the same spot and observing how the spectra changed. Each 2D spectrum took approximately 30 minutes to acquire. The three 2D spectra shown in figure 5.13a represent 90 minutes of continuous irradiation. In these 2D spectra, we observe the three spectral peaks shift to lower wavelength and inhomogeneously broaden

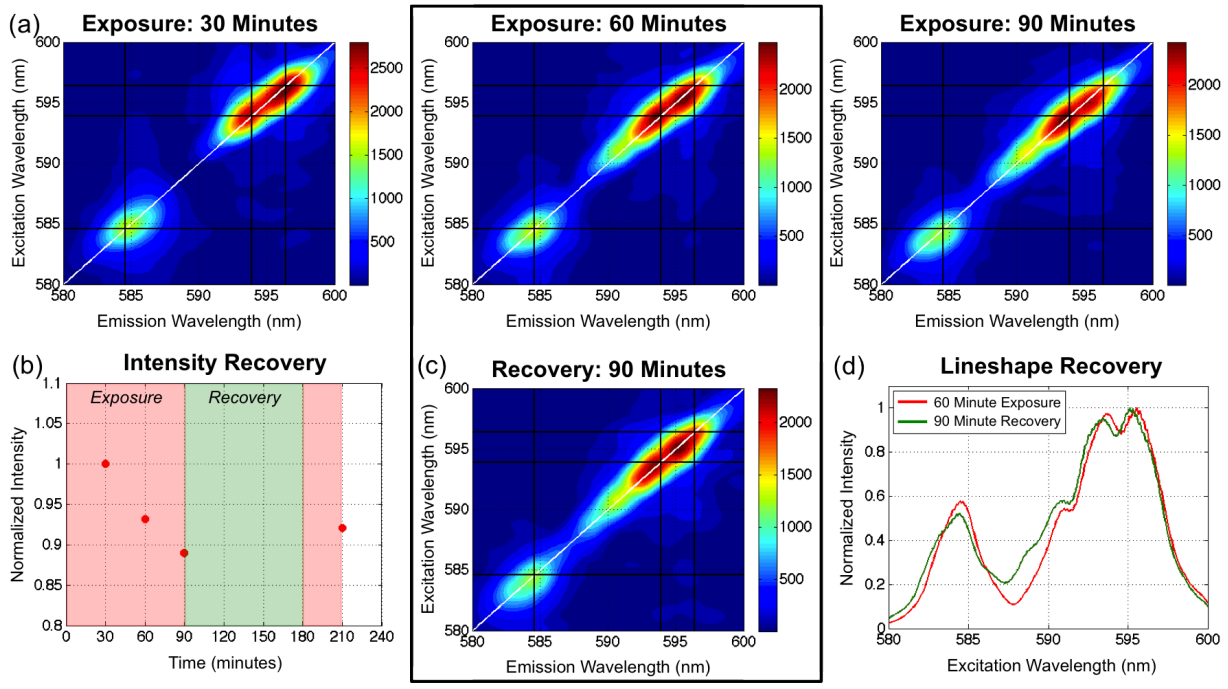


Figure 5.13: Photo-induced degradation and recovery. (a) Irradiation of glass nanotube sample at 10 K for 90 minutes followed by (c) a 90 minute recovery and 30 minutes of re-irradiation. (b) Signal intensity decays as a function of irradiation time but returns after a recovery time. (d) Spectral lineshape after 90 minutes of irradiation and recovery is the same as after 60 minutes of irradiation.

as a function of the irradiation time. Figure 5.13b also reveals that the total intensity of the 2D signal decays as a function of the irradiation time. Next, we allowed the sample to recover by turning off the irradiation for 90 minutes, i.e. the original irradiation time. We then performed a final 2D rephasing measurement on the same spot, shown in figure 5.13c, which required an additional 30 minutes of irradiation. In figure 5.13b, we observe there is a recovery in the total 2D signal intensity, while in figure 5.13d, we observe that the spectral lineshape after 90 minutes of recovery is similar to the lineshape after 60 minutes of irradiation. Thus, we observe a recovery in both the signal intensity and spectral lineshape after 90 minutes of non-irradiation.

While the exact mechanism of photodegradation and recovery is still not understood, we have learned that the process is not completely irreversible and thus does not occur due to any significant change in the nanotube structure or dipole-dipole couplings between monomers.

Additionally, our collaborators in the Bawendi group are currently investigating the control of superradiance via optical excitation and the mechanism of photodegradation and recovery in glass nanotubes using linear spectroscopy. Previous studies of a dispersively doped organic dye 1-amino-2-methylanthraquinone (Orange 11) in poly(methyl methacrylate) (PMMA)–analogous to J-aggregate nanotubes in a sucrose-trehalose matrix–also demonstrated self-healing after photodegradation [158, 159, 160]. The proposed mechanism for photodegradation and recovery was dimerization or aggregation of Orange 11 molecules in the solid state, which required high dyes concentrations. Though this mechanism is unlikely in our system, these experiments set a precedent for the recovery of optical properties via self-healing after photodegradation due to energetic disordering of the system. However, charge accumulation in the glass nanotubes is a likely mechanism for photodegradation and energetic disordering.

## 5.5 Two-Exciton States in Double-Walled J-Aggregate Nanotubes

Once we characterized the exciton couplings and homogeneous linewidths of single excitons, we measured the two-quantum spectra of both solution-based and glass nanotubes to investigate their two-exciton states.

In the solution-based experiment, isolated nanotubes were flowed through a flow cell to align their long axes to the direction of flow. Co-linear measurements were then performed with the incident laser polarizations parallel to the direction of flow. Under these conditions, only correlations between exciton states polarized parallel to the long axis of the nanotubes (i.e. 599 nm and 598 nm) are interrogated. Figure 5.14a shows the co-linear, two-quantum spectrum of solution-based isolated nanotubes at room temperature. The pure inner and outer wall biexciton states are clearly visible at the two-quantum wavelengths 300 nm and 296 nm, respectively. Both peaks are significantly elongated along the two-quantum axis. The small shoulders to higher wavelength of the pure outer wall biexciton and lower wave-

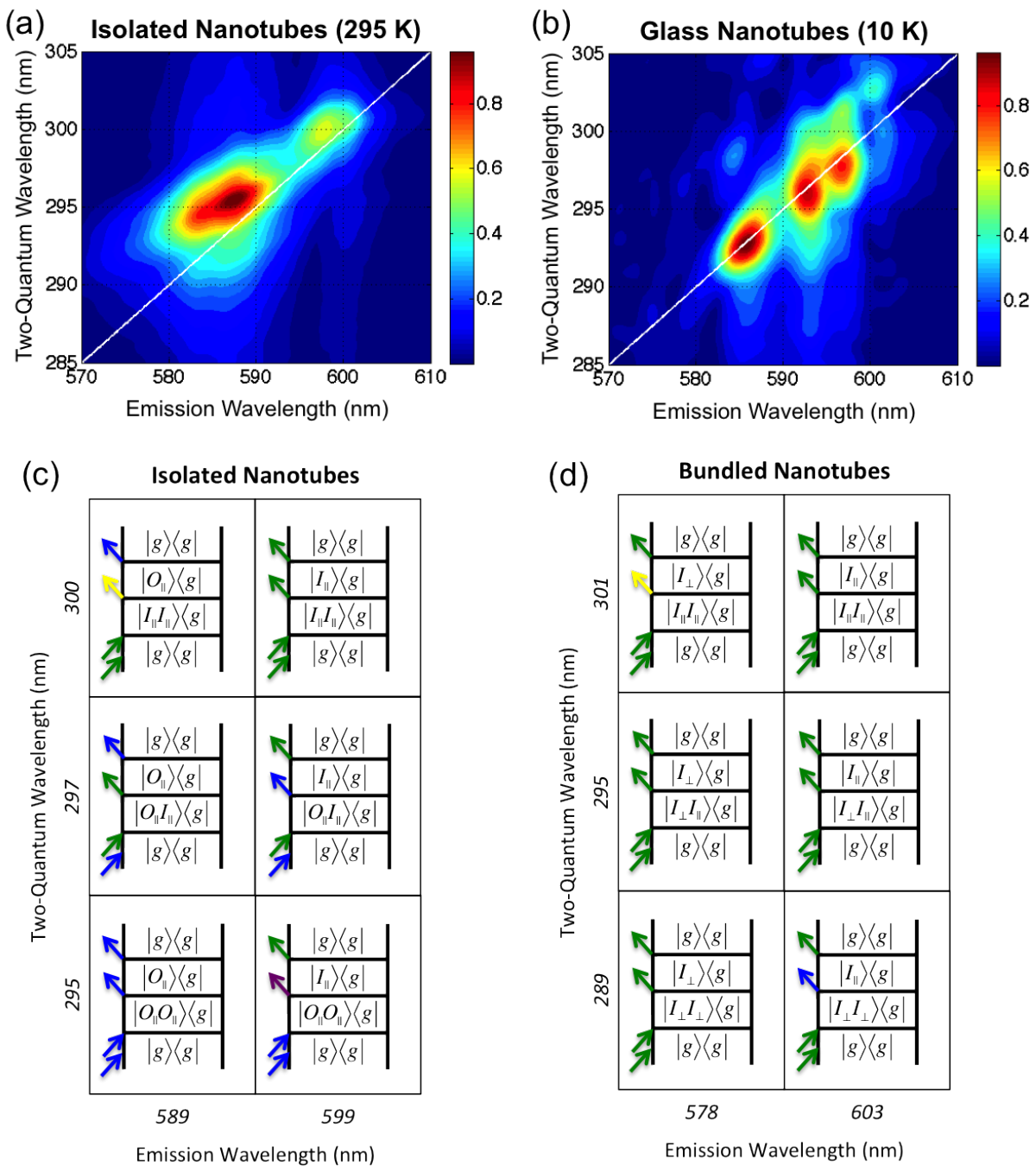


Figure 5.14: Two-dimensional two-quantum spectra. (a) Two-exciton states in isolated nanotubes at 295 K. The pure inner and outer wall biexcitons are observed at the two-quantum wavelengths 300 nm and 296 nm, respectively. (b) Two-exciton states in glass nanotubes at 10 K. The pure inner and outer wall biexcitons of isolated nanotubes are observed at the two-quantum wavelengths 298 and 293 nm, respectively, and the pure inner wall biexciton of the bundled nanotubes is observed at 296 nm. (c) Isolated nanotube two-quantum spectrum Feynman diagrams (stimulated emission only), where green and blue arrows denote transitions at 599 nm and 589 nm, respectively, and yellow and purple arrows denote transition between $|O_{||}\rangle \leftrightarrow |I_{||}I_{||}\rangle$ and $|I_{||}\rangle \leftrightarrow |O_{||}O_{||}\rangle$, respectively. (d) Bundled nanotube two-quantum spectrum Feynman diagrams.

length of the pure inner wall biexciton suggest mixed inner and outer wall biexcitons may exist, which requires at least weak inter-wall exciton coupling. However, these shoulders span much further than the 298 nm mixed biexciton two-quantum wavelength and extend from 293 nm to 305 nm. Spectral density beyond the mixed biexciton states suggests there may be a transition dipole moment between a single exciton on one wall and a biexciton on the other wall, i.e. $|I\rangle \rightarrow |OO\rangle$ and $|O\rangle \rightarrow |II\rangle$, which also requires inter-wall exciton coupling. Three-dimensional two-quantum measurements could unambiguously determine if the these transition dipole exist by peaks at $(\omega_X, \omega_{YY}, \omega)$. We mention this rather intriguing possibility because experiments using transient grating measurements to perform quantum process tomography on isolated J-aggregate nanotubes in chapter 6 also suggest these transition dipole moments may exist.

In the glass experiment, the samples contained both isolated and bundled nanotubes isotropically oriented and cooled to 10 K. Figure 5.14b shows the co-linear, two-quantum spectrum of glass nanotubes at 10 K. The pure inner and outer wall biexciton states of the isolated nanotubes are clearly visible at 298 nm and 293 nm, respectively. The pure inner wall biexciton state of the bundled nanotubes is also clearly visible at 296 nm. Overall, the two-quantum spectra of the solution-based and glass nanotubes are similar, revealing the same exciton-exciton interactions and suggesting similar excitonic couplings. However, isolated nanotube at room temperature have a large positive biexciton binding energy and fast biexciton dephasing times compared to glass nanotubes at 10 K, which have a nominal biexciton binding energy.

## 5.6 Conclusions

In this chapter, we used linear absorption as an indicator of the higher-order morphology of double-walled J-aggregate nanotubes. First, we measured the excitonic coupling in solution-based isolated and bundled nanotubes and in both cases observed strong intra-wall and weak

inter-wall exciton coupling. Additionally, two-quantum spectroscopy revealed the presence of pure inner and outer wall biexciton states and a mixed inner and outer wall biexciton state, which again suggested at least weak inter-wall exciton coupling. Investigations into mixed isolated and bundled nanotubes revealed the two morphologies are physically and electronically distinct species in solution. Second, we discovered that J-aggregate nanotubes maintain their self-assembled structure and optical and electronic properties when formed into a glass using a sucrose-trehalose sugar matrix. Temperature-dependent measurements of the homogeneous and inhomogeneous linewidths revealed dynamic and static disorder dominant exciton dephasing at room and cryogenic temperatures, respectively. Investigations into the photo-induced degradation of glass J-aggregate nanotubes at 10 K also demonstrated recovery of their optical properties via self-healing.

# Chapter 6

# Quantum Process Tomography of Single-Exciton Dynamics in Double-Walled J-Aggregate Nanotubes

In chapter 6, we unambiguously elucidate the single-exciton dynamics in double-walled J-aggregate nanotubes via quantum process tomography using a precisely designed set of narrowband transient grating experiments. For these experiments, J-aggregate nanotubes were synthesized by Dörthe Eisele in the group of Moungi Bawendi at MIT. The transient grating measurements were conducted by Dylan Arias and myself. Quantum process tomography was performed by Joel Yuen-Zhou in the group of Alán Aspuru-Guzik at Harvard University.

First, we will explain why quantum process tomography is a useful tool for elucidating complex quantum dynamics and discuss its general concepts. Second, we will consider the secular dynamics of a two-level system. Third, we will describe our transient grating experiments and explain how quantum dynamics are unambiguously extracted from these data. Finally, we will discuss the quantum dynamics revealed by quantum process tomography for the single-exciton manifold of double-walled J-aggregate nanotubes.

## 6.1 System-Bath Interactions in the Condensed Phase

The temporal dynamics of quantum systems in the condensed phase are often characterized by complex intra- and inter-system dynamics in and amongst ensemble components, interactions of the system with the environment (or bath), and environmental dynamics [41]. In such cases, the quantum system is generally described by a Hamiltonian that involves separating these interactions using the assumption there is weak coupling between the system and the bath:

$$\hat{H} = \hat{H}_S + \hat{H}_B + \hat{H}_{SB} \tag{6.1}$$

where $\hat{H}_S$ is the Hamiltonian describing the intra- and inter-system dynamics, $\hat{H}_B$ describes the bath dynamics, and $\hat{H}_{SB}$ describes the weakly-coupled system-bath interaction. In the condensed phase, the system dynamics of the ensemble, the bath dynamics of the solvent, and their interactions are generally complex and construction of a Hamiltonian that accurately describes the quantum dynamics of the total system can be difficult. Generally, a Markovian approximation is made which assumes the bath relaxation time is much faster than the relaxation time of the system due to its interaction with the bath, $\tau_S \gg \tau_B$. This approximation requires the system relaxation be stochastic (i.e a random process) but does not reduce the complexity of the system-bath Hamiltonian enough to make it easily tractable. In addition, accurate interpretation of even the simplest time-resolved spectroscopic experiments can be difficult as multiple quantum processes often contribute to single spectral features and separation of these contributions is generally impossible from a single spectroscopic experiment [71, 161, 162].

## 6.2 Quantum Process Tomography

A new approach for understanding the temporal dynamics of complex quantum systems comes from the field of quantum information processing called quantum process tomography

(QPT) [163, 164, 165, 72]. The goal of QPT is to completely elucidate the time-dependent density matrix of a system $\rho(T)$ by using a precisely designed set of spectroscopic experiments [166]. In QPT, the quantum dynamics of the system are characterized by a time-dependent process matrix $\chi(T)$ [different from the susceptibility in chapter 3] that describes the evolution of an initially prepared quantum state at time zero $\rho(0)$ to a final state at some time $T$ later $\rho(T)$. In this paradigm, the process matrix characterizes all the system and bath dynamics and interactions and acts on the system as a linear transformation between its initial and final states:

$$\rho(T) = \chi(T)\,\rho(0) \tag{6.2}$$

In spectroscopic experiments, an initial state $\rho(0)$ is prepared by a set of excitation pulses, $\chi(T)$ propagates the density matrix during time $T$, and the final state $\rho(T)$ is interrogated by a set of detection pulses. When expanded into the basis states of the system, equation 6.2 takes the form:

$$\rho_{cd}(T) = \sum_{ab} \chi_{cdab}(T)\,\rho_{ab}(0) \tag{6.3}$$

where the time-dependent process matrix element $\chi_{cdab}(T)$ describes the conversion of the initially prepared density matrix element $\rho_{ab}(0)$ into the final density matrix element $\rho_{cd}(T)$ at some time $T$. Thus, process matrix elements of the form $\chi_{aaaa}$ describe the decay of a population (i.e. diagonal density matrix element) state $a$, $\chi_{abab}$ describe the decay of a coherence (i.e. off-diagonal density matrix element) between states $a$ and $b$, and $\chi_{bbaa}$ describe the population transfer from state $a$ to state $b$. The process matrix elements $\chi_{bcaa}$, $\chi_{ccab}$, and $\chi_{cdab}$ also describe the non-secular processes of population-to-coherence transfer, coherence-to-population transfer, and coherence transfer, respectively.

To perform QPT, a precisely designed set of spectroscopic experiments is used to selectively prepare every possible initial state and measure their conversion into every possible final state [167, 168, 169]. In this procedure, the construction of an accurate Hamiltonian for the total system is unnecessary because all the quantum dynamics are extracted directly

from the spectroscopic measurements. However, a basic model for the system and an accurate understanding of the linear absorption spectrum is necessary to interpret the results of QPT. In this chapter, we use QPT to study the single-exciton dynamics of double-walled J-aggregate nanotubes, which were extensively studied and well characterized by linear and two-dimensional spectroscopy in chapter 5. While QPT has been previously used to study the quantum dynamics of spins, qubits, ions, and optical lattices, our experiments are the first performed on a molecular or supramolecular system, in the condensed phase, or at room temperature [170, 171, 172, 173, 174, 175].

## 6.3 Secular Dynamics of a Two-Level System

To acquire a basic understanding of the quantum dynamics underlying a complex condensed phase system, we will consider the case of a two-level excited state system and explore its secular dynamics: population decay and transfer and coherence decay (i.e. dephasing). In our model system, we define the excited states $a$ and $b$ with energies $\hbar\omega_a$ and $\hbar\omega_b$, respectively, where $\omega_a > \omega_b$ and $\omega_{ab} = \omega_a - \omega_b$ is the difference frequency between the states.

$$E = \hbar \begin{bmatrix} \omega_b & \omega_{ba} \\ \omega_{ab} & \omega_a \end{bmatrix} \tag{6.4}$$

The density matrix of the excited states thus takes the form:

$$\rho = \begin{bmatrix} |b\rangle\langle b| & |b\rangle\langle a| \\ |a\rangle\langle b| & |a\rangle\langle a| \end{bmatrix} \tag{6.5}$$

where the diagonal matrix elements $|x\rangle\langle x|$ describe excited state populations and the off-diagonal matrix elements $|x\rangle\langle y|$ describe coherences between the excited states. We also define a rate matrix $R$ characterizing the time constants for each excited state population

and coherence decay and transfer process:

$$R = \begin{bmatrix} R_{bbbb} & R_{aabb} & R_{abbb} & R_{babb} \\ R_{bbaa} & R_{aaaa} & R_{abaa} & R_{baaa} \\ R_{bbab} & R_{aaab} & R_{abab} & R_{baab} \\ R_{bbba} & R_{aaba} & R_{abba} & R_{baba} \end{bmatrix} \tag{6.6}$$

Now, the temporal dynamics of the excited populations and coherences can be described using normal chemical kinetics. The population kinetics take the form:

$$\dot{\rho}_{aa}(t) = R_{aabb}\rho_{bb}(t) - R_{bbaa}\rho_{aa}(t) \tag{6.7}$$

$$\dot{\rho}_{bb}(t) = R_{bbaa}\rho_{aa}(t) - R_{aabb}\rho_{bb}(t) \tag{6.8}$$

where the change in each population is described by the transfer into (i.e. positive) and out of (i.e. negative) each state. If we assume uphill population transfer does not occur (i.e. $R_{aabb} = 0$), the time derivatives of the excited state populations reduce to:

$$\dot{\rho}_{aa}(t) = -R_{bbaa}\rho_{aa}(t) \tag{6.9}$$

$$\dot{\rho}_{bb}(t) = R_{bbaa}\rho_{aa}(t) \tag{6.10}$$

In this case, the population dynamics are completely defined by the downhill population transfer rate from excited state $a$ to $b$ ($R_{bbaa}$). Integrating the differential equations using the initial condition that the excited state population begins in state $a$ (i.e. $\rho_{aa}(0) = 1$ and $\rho_{bb}(0) = 0$), the kinetics for the excited state populations can be explicitly defined.

$$\rho_{aa}(t) = \exp[-R_{bbaa}t] \tag{6.11}$$

$$\rho_{bb}(t) = 1 - \exp[-R_{bbaa}t] \tag{6.12}$$

Under these initial conditions, the population in excited state $a$ starts at 1 and decays

exponentially, while the population in excited state $b$ starts at 0 and simultaneously rises exponentially on the timescale $1/R_{bbaa}$ due to downhill population transfer. We implicitly assume the decay rate between the excited and ground states is much slower than the transfer rate between excited states and thus, in a short time approximation, decay to the ground state is does not occur.

Similar to the temporal dynamics of the populations, the kinetics of the coherences can be written down and take the form:

$$\dot{\rho}_{ab}(t) = -(i\omega_{ab} + R_{abab})\,\rho_{ab}(t) \tag{6.13}$$

$$\dot{\rho}_{ba}(t) = -(i\omega_{ba} + R_{baba})\,\rho_{ba}(t) \tag{6.14}$$

We note $\dot{\rho}_{ab}(t) = \dot{\rho}^{*}_{ba}(t)$ because the density matrix is Hermitian (i.e. self-adjoint). Integrating the differential equation using the initial condition that the amplitude of the coherences is unity (i.e. $\rho_{ab}(0) = \rho_{ba}(0) = 1$), the kinetics for the excited state coherences can be explicitly defined.

$$\rho_{ab}(t) = \rho^{*}_{ba}(t) = \exp\left[-(i\omega_{ab} + R_{abab})\,t\right] \tag{6.15}$$

Under these initial conditions, the excited state coherences start at 1, oscillates at the difference frequency $\omega_{ab} = -\omega_{ba}$, and dephases exponentially on the timescale $1/R_{abab} = 1/R_{baba}$.

## 6.4 Narrowband Transient Grating Experiments

With a basic understanding of the secular dynamics of a two-level excited state system, we can now describe the transient grating measurements used for QPT. To elucidate the process matrix of a quantum system, the spectroscopic experiments must selectively excite every possible quantum state (both populations and coherences) and selectively detect their evolution into every other quantum state. In our experimental design, we use transient grating spectroscopy to achieve the excitation and detection selectively required by QPT. To

describe our experimental measurements, we will consider the case of two optically accessible excited states $a$ and $b$ with non-overlapping absorption spectra. First, two narrowband pump pulses selectively excite one of the four possible quantum states: the $|b\rangle\langle b|$ and $|a\rangle\langle a|$ excited state populations and the $|b\rangle\langle a|$ and $|a\rangle\langle b|$ excited state coherences. The first pump pulse (wavevector $-\vec{k}_1$) acts on the ket and the second pump pulse ($\vec{k}_2$) acts on the bra to prepare the desired quantum state. The crossed pump pulses create an excited state grating off which the third narrowband probe pulse ($\vec{k}_3$) scatters after a delay time $T$. The scattered probe pulse is heterodyne detected with a fourth broadband pulse ($\vec{k}_4 = -\vec{k}_1 + \vec{k}_2 + \vec{k}_3$) by spectral interferometry using a spectrometer. The central frequencies of the narrowband pump pulses determine the selectively prepared initial state, while the central frequency of the narrowband probe pulse determines the selectively detected final state. The fourth pulse does not contribute to the scattered probe signal but acts as a broadband reference to detect both elastic and inelastic probe pulse scattering and does not effect the selectively of the spectroscopic measurements. In this experimental design, eight unique measurements are required to implement QPT. We label the experiments $xyz$, where the initial state $|x\rangle\langle y|$ is selectively prepared and the state $|z\rangle$ is selectively detected and $x,\ y,\ z \in a,\ b$. Even with the excitation and detection selectively of the transient grating measurements, a single spectroscopic signal can contain contributions from multiple process matrix elements. However, the set of transient grating measurements described can be used to extract the process matrix by implementing QPT.

We use QPT to study the single-exciton dynamics of double-walled J-aggregate nanotubes, illustrated in figure 6.1a [146, 147, 176]. Our measurements are the first realization of QPT in a molecular or supramolecular system, in the condensed phase, or at room temperature. In our experiments, the nanotubes are flowed through a cell and align along the direction of flow. The excitation and detection pulses are polarized parallel to the flow direction, so only the primary inner and outer wall transitions at 16,700 and 17,000 $cm^{-1}$, respectively, are interrogated. The transient grating measurements thus elucidate the dy-

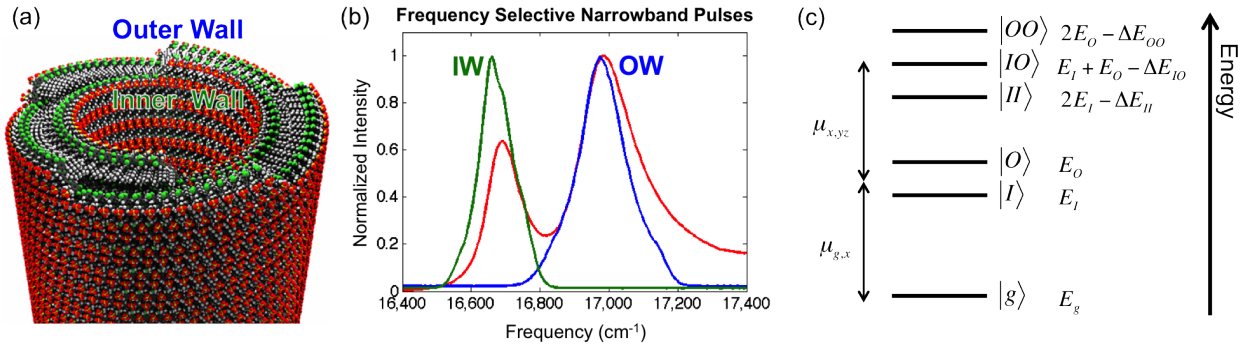


Figure 6.1: Quantum process tomography of double-walled J-aggregate nanotubes. (a) J-aggregate nanotube consisting of an inner and outer wall. (b) Linear absorption of states polarized parallel to the long axis of the nanotube (red) and the narrowband pulses resonant with the inner and outer wall absorption (green and blue, respectively) used in the narrowband transient grating measurements. (c) Energy level diagram of the J-aggregate nanotubes including the ground, one-exciton, and two-exciton manifolds. $E_x$ is the energy and $\mu_{g,x}$ the transition dipole moment between the ground $|g\rangle$ and one-exciton state $|x\rangle$. The two-exciton states $|yz\rangle$ are characterized by an additional biexciton binding energy $\Delta E_{yz}$ and the one- to two-exciton transition dipole moment $\mu_{x,yz}$.

namics of a two-level, one-exciton excited state manifold analogous to the quantum system described above. Figure 6.1b shows the linear absorption of the exciton states polarized along the long axis of the nanotube and the narrowband pulses used for excitation and detection at the central frequencies of the inner and outer wall exciton resonances. The narrowband pulses allow selective excitation and detection while maintaining a fairly high time resolution of approximately 100 fs. Two-dimensional phase and amplitude shaping of broadband pulses is used to generate and compress the frequency-selective narrowband pulses, which each had a pulse energy of approximately 0.5 nJ.

To fully elucidate the quantum dynamics of the single-exciton manifold, the ground and two-exciton manifolds must also be considered. The energy level diagram in figure 6.1c illustrates the accessible exciton states in our transient grating measurements along with their energies and transition dipole moments. These states include two pure and one mixed biexciton states $|xx\rangle$ and $|xy\rangle$, respectively, which are characterized by biexciton binding energies $\Delta E_{xy}$. The biexciton binding energies are small compared to the full width at half maximum of the linear absorption peaks, thus signals emitting from the one- and two-exciton

states are not spectrally separated and overlap in the transient grating measurements.

We performed eight transient grating measurements labelled: $OOO$, $OOI$, $IIO$, $III$, $OIO$, $OII$, $IOO$, $IOI$ (as described above). The quantum states of interest are described by the single-exciton density matrix:

$$\rho_{SE} = \begin{bmatrix} |I\rangle\langle I| & |I\rangle\langle O| \\ |O\rangle\langle I| & |O\rangle\langle O| \end{bmatrix} \tag{6.16}$$

Each quantum state is selectively prepared by the two narrowband pump pulses and their emission is selectively interrogated by the narrowband probe pulse at the central frequency of either the inner or outer wall absorption, $I$ or $O$, respectively. The raw transient grating data from the eight experiments are plotted in figure 6.2. As mentioned previously, the signals from the eight transient grating measurements do not inherently separate the elements of the process matrix. By elucidating all the possible Feynman diagrams for each measurement and allowing transfer from the initial quantum state to all other quantum states, we can determine which process matrix elements contribute to the spectroscopic signals in our experiments. Figure 6.3 shows Feynman diagrams for the preparation of each quantum state and the emission from each final state after delay time $T$–which is dependent on the central frequency of the third narrowband pulse. The full set of Feynman diagrams for our QPT experiments is provided in Appendix A. In table 6.1, we summarize the information provided by the full set of Feynman diagrams.

The process matrix elements enumerated in table 6.1 take the form $\chi_{cdab}$, where the quantum state $|a\rangle\langle b|$ evolves into state $|c\rangle\langle d|$ during the experimental delay time $T$. The process matrix elements include all secular processes: population decay $\chi_{aaaa}$, population transfer $\chi_{bbaa}$, and coherence decay $\chi_{abab}$; and non-secular processes: population-to-coherence transfer $\chi_{bcaa}$, coherence-to-population transfer $\chi_{ccab}$, and coherence transfer $\chi_{cdab}$, where $a$, $b$, $c$, $d \in I$, $O$. From table 6.1, we observe that secular and non-secular processes emit at different frequencies in each of the eight transient grating measurements. From this

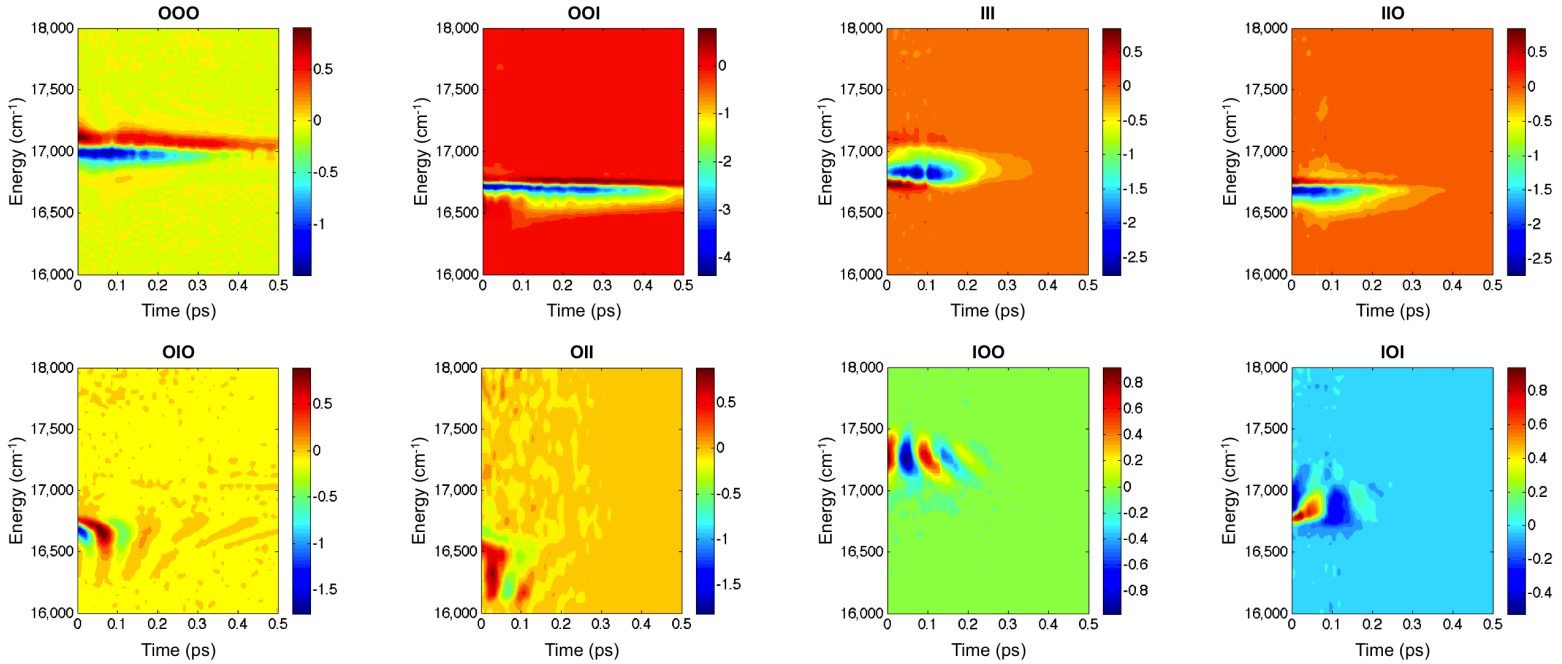


Figure 6.2: Transient grating measurements. Measurement $xyz$ is characterized by the first and second narrowband pump pulses centered at the central frequencies of states $x$ and $y$, respectively, selectively generating the initial state $|x\rangle\langle y|$ and the third narrowband probe pulse centered at the central frequency of state $z$ selectively detecting the state $|z\rangle$, where $x,\ y,\ z \in I,\ O$.

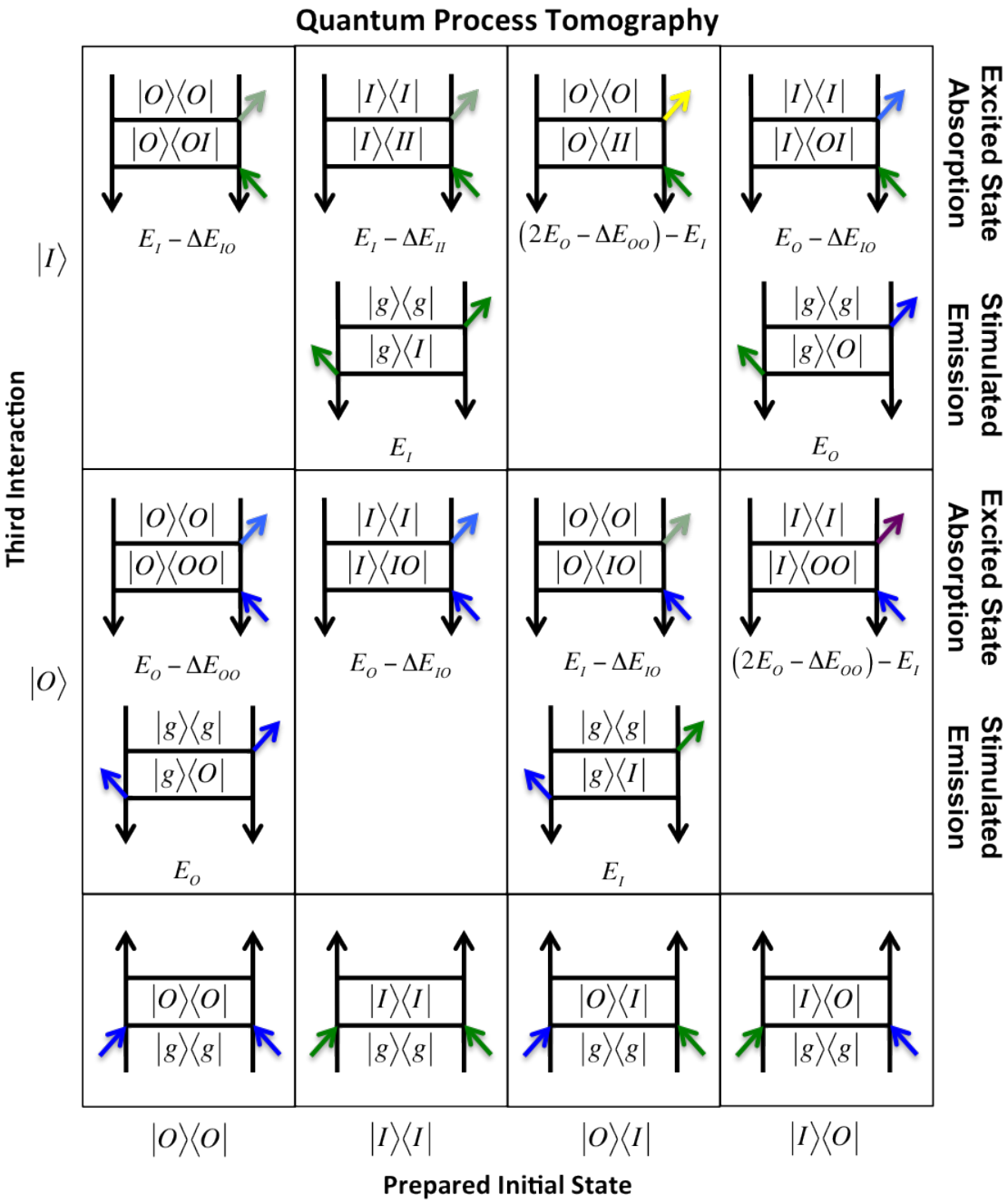


Figure 6.3: Transient grating Feynman diagrams for quantum process tomography. Bottom Row: Two narrowband pulse preparation of the initial states $|O\rangle\langle O|$, $|I\rangle\langle I|$, $|O\rangle\langle I|$, and $|I\rangle\langle O|$ followed by system evolution during the waiting time $T$. Top Rows: Third narrowband pulse-dependent emission of the final states $|O\rangle\langle O|$, $|I\rangle\langle I|$, $|O\rangle\langle I|$, and $|I\rangle\langle O|$ including stimulated emission and excited state absorption pathways, where $\Delta E_{xy}$ denotes the binding energy of the $|xy\rangle$ biexciton. Green and blue arrows indicate interactions with energies $E_I$ and $E_O$, respectively. Light green and light blue arrows indicate interactions with energies shifted by the biexciton binding energies $E_I - \Delta E$ and $E_O - \Delta E$, respectively. Yellow and purple arrows indicate interactions with energies $(2E_I - \Delta E_{II}) - E_O$ and $(2E_O - \Delta E_{OO}) - E_I$, respectively.

**Process Matrix Contributions to Transient Grating Measurements**

| Emission Frequency | $OOO$ | $OOI$ | $IIO$ | $III$ | $OIO$ | $OII$ | $IOO$ | $IOI$ |
|---|---|---|---|---|---|---|---|---|
| 1. $2E_O - \Delta E_{OO} - E_I$ | $\chi_{IOOO}$ | | $\chi_{IOII}$ | | $\chi_{IOOI}$ | | $\chi_{IOIO}$ | |
| 2. $E_O$ | $\chi_{OOOO}$ | $\chi_{IOOO}$ | $\chi_{OOII}$ | $\chi_{IOII}$ | $\chi_{OOOI}$ | $\chi_{IOOI}$ | $\chi_{OOIO}$ | $\chi_{IOIO}$ |
| 3. $E_O - \Delta E_{IO}$ | $\chi_{IIOO}$ | $\chi_{IOOO}$ | $\chi_{IIII}$ | $\chi_{IOII}$ | $\chi_{IIOI}$ | $\chi_{IOOI}$ | $\chi_{IIIO}$ | $\chi_{IOIO}$ |
| 4. $E_O - \Delta E_{OO}$ | $\chi_{OOOO}$ | | $\chi_{OOII}$ | | $\chi_{OOOI}$ | | $\chi_{OOIO}$ | |
| 5. $E_I$ | $\chi_{OIOO}$ | $\chi_{IIOO}$ | $\chi_{OIII}$ | $\chi_{IIII}$ | $\chi_{OIOI}$ | $\chi_{IIOI}$ | $\chi_{OIIO}$ | $\chi_{IIIO}$ |
| 6. $E_I - \Delta E_{IO}$ | $\chi_{OIOO}$ | $\chi_{OOOO}$ | $\chi_{OIII}$ | $\chi_{OOII}$ | $\chi_{OIOI}$ | $\chi_{OOOI}$ | $\chi_{OIIO}$ | $\chi_{OOIO}$ |
| 7. $E_I - \Delta E_{II}$ | | $\chi_{IIOO}$ | | $\chi_{IIII}$ | | $\chi_{IIOI}$ | | $\chi_{IIIO}$ |
| 8. $2E_I - \Delta E_{II} - E_O$ | | $\chi_{OIOO}$ | | $\chi_{OIII}$ | | $\chi_{OIOI}$ | | $\chi_{OIIO}$ |

Table 6.1: Process matrix contributions to transient grating measurements. The process matrix elements $\chi_{cdab}$ are categorized by their emission energy (1-8) in each transient grating measurement $xyz$. Measurement $xyz$ selectively generates the initial state $|x\rangle\langle y|$ and selectively detects state $|z\rangle$, where $x$, $y$, $z \in I$, $O$. Red process matrix elements denote non-secular processes: population-to-coherence transfer, coherence-to-population transfer, and coherence transfer.

observation, we can immediately determine from the raw transient grating data that non-secular processes are not observed in our experiments, which will be confirmed by the QPT procedure. We can also directly observe from the oscillations in the $OIO$, $OII$, $IOO$, and $IOI$ experiments that coherences between excitons on the inner and outer walls exist and thus the states must be inherently coupled.

We can write down time-dependent equations for each transient grating measurement with contributions from secular process matrix elements only, assuming no uphill population transfer (i.e. $\chi_{OOII} = 0$):

$$\begin{aligned} OOO\,(T,t) &= \chi_{OOOO}\,(T)\left[\left|\mu_{g,O}\right|^4 \exp\left[-\left(i\omega_O + \gamma_{g,O}\right)t\right]\right. \\ &\quad \left. - \left|\mu_{g,O}\right|^2 \left|\mu_{O,OO}\right|^2 \exp\left[-\left(i\left(\omega_O - \Delta\omega_{OO}\right) + \gamma_{O,OO}\right)t\right]\right] \\ &\quad -\chi_{IIOO}\,(T)\left|\mu_{g,O}\right|^2 \left|\mu_{I,IO}\right|^2 \exp\left[-\left(i\left(\omega_O - \Delta\omega_{IO}\right) + \gamma_{I,IO}\right)t\right] \qquad (6.17) \\ OOI\,(T,t) &= -\chi_{OOOO}\,(T)\left|\mu_{g,O}\right|^2 \left|\mu_{O,IO}\right|^2 \exp\left[-\left(i\omega_I - \Delta\omega_{IO} + \gamma_{O,IO}\right)t\right] \\ &\quad +\chi_{IIOO}\,(T)\left[\left|\mu_{g,O}\right|^2 \left|\mu_{g,I}\right|^2 \exp\left[-\left(i\omega_I + \gamma_{g,I}\right)t\right]\right. \\ &\quad \left. - \left|\mu_{g,O}\right|^2 \left|\mu_{I,II}\right|^2 \exp\left[-\left(i\left(\omega_I - \Delta\omega_{II}\right) + \gamma_{I,II}\right)t\right]\right] \qquad (6.18) \end{aligned}$$

$$
\begin{aligned}
IIO\left(T,t\right) &= -\chi_{IIII}\left(T\right)\left|\mu_{g,I}\right|^{2}\left|\mu_{I,IO}\right|^{2}\exp\left[-\left(i\left(\omega_{O}-\Delta\omega_{IO}\right)+\gamma_{I,IO}\right)t\right] && (6.19)\\
III\left(T,t\right) &= \chi_{IIII}\left(T\right)\left[\left|\mu_{g,I}\right|^{4}\exp\left[-\left(i\omega_{I}+\gamma_{g,I}\right)t\right]\right.\\
&\quad \left.-\left|\mu_{I}\right|^{2}\left|\mu_{I,II}\right|^{2}\exp\left[-\left(i\left(\omega_{I}-\Delta\omega_{II}\right)+\gamma_{I,II}\right)t\right]\right] && (6.20)\\
OIO\left(T,t\right) &= \chi_{OIOI}\left(T\right)\left[\left|\mu_{g,O}\mu_{g,I}\mu_{g,O}\mu_{g,I}\right|\exp\left[-\left(i\omega_{I}+\gamma_{g,I}\right)t\right]\right.\\
&\quad \left.-\left|\mu_{g,O}\mu_{g,I}\mu_{I,IO}\mu_{O,IO}\right|\exp\left[-\left(i\left(\omega_{I}-\Delta\omega_{IO}\right)+\gamma_{O,IO}\right)t\right]\right] && (6.21)\\
OII\left(T,t\right) &= -\chi_{OIOI}\left(T\right)\left|\mu_{g,O}\mu_{g,I}\mu_{I,II}\mu_{O,II}\right|\\
&\quad \times\exp\left[-\left(i\left(2\omega_{I}-\Delta\omega_{II}-\omega_{O}\right)+\gamma_{O,II}\right)t\right] && (6.22)\\
IOO\left(T,t\right) &= -\chi_{IOIO}\left(T\right)\left|\mu_{g,I}\mu_{g,O}\mu_{O,OO}\mu_{I,OO}\right|\\
&\quad \times\exp\left[-\left(i\left(2\omega_{O}-\Delta\omega_{OO}-\omega_{I}\right)+\gamma_{I,OO}\right)t\right] && (6.23)\\
IOI\left(T,t\right) &= \chi_{IOIO}\left(T\right)\left[\left|\mu_{g,I}\mu_{g,O}\mu_{g,I}\mu_{g,O}\right|\exp\left[-\left(i\omega_{O}+\gamma_{g,O}\right)t\right]\right.\\
&\quad \left.-\left|\mu_{g,I}\mu_{g,O}\mu_{O,IO}\mu_{I,IO}\right|\exp\left[-\left(i\left(\omega_{O}-\Delta\omega_{IO}\right)+\gamma_{I,IO}\right)t\right]\right] && (6.24)
\end{aligned}
$$

The initial intensity for each signal contribution is determined by the product of the relevant transition dipole moments between states $j$ and $k$, $\prod^{4}\left|\mu_{j,k}\right|$, and exist between but not within the ground state, one-, and two-exciton manifolds. The delay time dynamics are completely governed by the process matrix elements $\chi_{cdab}\left(T\right)$. The signal is determined by the radiating coherence during the emission time $t$, $\exp\left[-\left(i\omega_{j}+\gamma_{j,k}\right)t\right]$, and characterized by the exciton energies $E_{j}=\hbar\omega_{j}$ and biexciton binding energies $\Delta E_{jk}=\hbar\Delta\omega_{jk}$ and the dephasing rates $\gamma_{j,k}$ between states $j$ and $k$. The total signal for each transient grating measurement is the sum over all the contributing process matrix elements.

With the eight transient grating measurements and analytical expressions for each of the spectroscopic signals, QPT can invert the data to separate and unambiguously elucidate the dynamics of each process matrix element.

## 6.5 Signal Inversion and Process Matrix Extraction

The time-dependent signals for the transient grating measurements in equations 6.17-6.24 are composed of linear combinations of the process matrix elements and are scaled by the relevant transition dipole moments. Thus, the transient grating signals must be inverted to determine the process matrix elements.

Prior to implementing the QPT procedure, the transient grating signals were normalized to account for three variable experimental parameters. First, the signals were normalized by the relevant pulse energies for each of the three narrowband pulses. Second, the nanotubes degrade slightly over time due to pumping through the flow cell and optical excitation, so the signals were normalized by the optical density of the nanotubes by taking a linear absorption spectrum after each experiment. Finally, the transient grating signals were corrected for pulse intensity rolloff (described in chapter 4) due to time delays applied via temporal pulse shaping.

To implement the QPT procedure and extract the process matrix elements, first the transient grating signals are integrated over the emission frequency, $\int d\omega\ XYZ\left(T,\omega\right) = XYZ\left(T,t=0\right)$, yielding the time-domain signal at $t = 0$ according to Fourier transform relationships and eliminating the exponential signal terms in equations 6.17-6.24. Second, the signals with initial excited state populations (i.e. $OOY$ and $IIY$) are corrected by subtracting the signal at $T = 0$, $XXY\left(T - T_0\right) = XXY\left(T\right) - XXY\left(0\right)$, to remove interfering spectroscopic signals due to ground state bleach that do not contribute to the single-exciton dynamics. Third, the transient grating signals are inverted to generate expressions for the process matrix elements. Inversion utilizes semi-definite programming to ensure the process matrix is a linear transformation that maps physical density matrices to other physical density matrices that are Hermitian, trace preserving, and possess positive populations [177, 178].

From equations 6.19-6.24, we observe that the transient grating experiments $IIY$, $OIY$, and $IOY$ are dependent on a single process matrix element $\chi_{IIII}$, $\chi_{OIOI}$, and $\chi_{IOIO}$, respec-

tively. Thus, inversion of these process matrix elements are straightforward. From equations 6.17 and 6.18, we observe the $OOY$ experiments are coupled and depend on the process matrix elements $\chi_{OOOO}$ and $\chi_{IIOO}$. Thus, the process matrix elements $\chi_{OOOO}$ and $\chi_{IIOO}$ must be solved simultaneously, which is also straightforward but slightly more cumbersome algebraically.

The process matrix elements extracted from equations 6.17-6.24 are:

$$\chi_{OOOO}(T) = 1 + \frac{OOO(T-T_0) + \frac{\left(\frac{C_3^{OOO}C_1^{OOI}}{C_1^{OOO}-C_2^{OOO}}\right)OOO(T-T_0)+C_3^{OOO}OOI(T-T_0)}{(C_2^{OOI}-C_3^{OOI})-\left(\frac{C_3^{OOO}C_1^{OOI}}{C_1^{OOO}-C_2^{OOO}}\right)}}{(C_1^{OOO}-C_2^{OOO})} \quad (6.25)$$

$$\chi_{IIOO}(T) = \frac{OOI(T-T_0) + \left(\frac{C_1^{OOI}}{C_1^{OOO}-C_2^{OOO}}\right)OOO(T-T_0)}{(C_2^{OOI}-C_3^{OOI}) - \left(\frac{C_3^{OOO}C_1^{OOI}}{C_1^{OOO}-C_2^{OOO}}\right)} \quad (6.26)$$

$$\chi_{IIII}(T) = 1 + \frac{III(T-T_0)}{(C_1^{III}-C_2^{III})} = 1 - \frac{IIO(T-T_0)}{C_1^{IIO}} \quad (6.27)$$

$$\chi_{OIOI}(T) = = \frac{OIO(T)}{(C_1^{OIO}-C_2^{OIO})} = \frac{OII(T)}{C_1^{OII}} \quad (6.28)$$

$$\chi_{IOIO}(T) = = \frac{IOI(T)}{(C_1^{IOI}-C_2^{IOI})} = \frac{IOO(T)}{C_1^{IOO}} \quad (6.29)$$

The coefficients $c_j^{XYZ}$ are time-dependent and defined in equations 6.17-6.24 such that $XYZ(T) = \sum_j c_j^{XYZ}(t)\,\chi_j(T)$. These coefficients are products of the transition dipole moments and complex exponentials involving the transition energies and phenomenological dephasing rates. Thus, a model for the quantum system is required. A comprehensive understanding of the linear absorption spectrum (described in chapter 5 for double-walled J-aggregate nanotubes) is sufficient to characterize the system and determine the necessary parameters to calculate the time-dependent coefficients $c_j^{XYZ}$. However, extraction of the transition dipole moments from the transient grating measurements, which is robust and easy to achieve, leads to more accurate normalization of the signal contributions to compute the process matrix elements.

Because only secular dynamics and downhill energy transfer occur and population re-

laxation to the ground state is slow, the expressions for the process matrix elements in equations 6.25-6.29 are significantly reduced in complexity. The process matrix elements $\chi_{IIII}$, $\chi_{OIOI}$, and $\chi_{IOIO}$ can be singularly described by one of two transient grating measurements that provide redundant information, while the process matrix elements $\chi_{OOOO}$ and $\chi_{IIOO}$ are slightly more complex and possess contributions from two transient grating measurements. To reduce the complexity of the process matrix elements $\chi_{OOOO}$ and $\chi_{IIOO}$, we note the transient grating signal amplitude for experiment $IIO$ is nearly zero compared to other experiments. From equation 6.19, we observe the $IIO$ transient grating measurement is compromised solely of an excited state absorption pathway requiring the mixed biexciton state $|IO\rangle$, which we will assume does not contribute substantially to the transient grating signals. Thus, the coefficients $c_3^{OOO}$ and $c_1^{OOI}$ are zero and equations 6.25 and 6.26 reduce to:

$$\chi_{OOOO}(T) = 1 + \frac{OOO(T - T_0)}{(C_1^{OOO} - C_2^{OOO})} \tag{6.30}$$

$$\chi_{IIOO}(T) = \frac{OOI(T - T_0)}{(C_2^{OOI} - C_3^{OOI})} \tag{6.31}$$

If non-secular dynamics and uphill energy transfer occurred and the mixed biexciton state $|IO\rangle$ contributed, the process matrix elements would depend on many more transient grating measurements and inversion would be more cumbersome. Table 6.2 summarizes the transient grating signal contributions at a given emission frequency (where $\alpha$ is the emission frequency number defined in table 6.1) for each process matrix element if all quantum processes occurred.

**Transient Grating Signal Contributions to Process Matrix Elements**

| $\chi_{OOOO}$ | $\chi_{IIOO}$ | $\chi_{OIOO}$ | $\chi_{IOOO}$ | $\chi_{OOII}$ | $\chi_{IIII}$ | $\chi_{OIII}$ | $\chi_{IOII}$ |
|---|---|---|---|---|---|---|---|
| $OOO$ (2) | $OOO$ (3) | $OOO$ (5) | $OOO$ (1) | $IIO$ (2) | $IIO$ (3) | $IIO$ (5) | $IIO$ (1) |
| $OOO$ (4) | $OOI$ (5) | $OOO$ (6) | $OOI$ (2) | $IIO$ (4) | $III$ (5) | $IIO$ (6) | $III$ (2) |
| $OOI$ (6) | $OOI$ (7) | $OOI$ (8) | $OOI$ (3) | $III$ (6) | $III$ (7) | $III$ (8) | $III$ (3) |
| $\chi_{OOOI}$ | $\chi_{IIOI}$ | $\chi_{OIOI}$ | $\chi_{IOOI}$ | $\chi_{OOIO}$ | $\chi_{IIIO}$ | $\chi_{OIIO}$ | $\chi_{IOIO}$ |
| $OIO$ (2) | $OIO$ (3) | $OIO$ (5) | $OIO$ (1) | $IOO$ (2) | $IOO$ (3) | $IOO$ (5) | $IOO$ (1) |
| $OIO$ (4) | $OII$ (5) | $OIO$ (6) | $OII$ (2) | $IOO$ (4) | $IOI$ (5) | $IOO$ (6) | $IOI$ (2) |
| $OII$ (6) | $OII$ (7) | $OII$ (8) | $OII$ (3) | $IOI$ (6) | $IOI$ (7) | $IOI$ (8) | $IOI$ (3) |

Table 6.2: Transient grating signal contributions to process matrix elements. $xyz\,(\alpha)$ denotes the transient grating signal of experiment $xyz$ at emission frequency number $\alpha$ as defined in table 6.1. Measurement $xyz$ selectively generates the initial state $|x\rangle\langle y|$ and selectively detects state $|z\rangle$, where $x,\ y,\ z \in I,\ O$. Red process matrix elements denote non-secular processes: population-to-coherence transfer, coherence-to-population transfer, and coherence transfer.

## 6.6 Quantum Dynamics of Double-Walled J-Aggregate Nanotubes

From the raw transient grating data, we were able to directly observe that non-secular processes: population-to-coherence transfer (i.e. $\chi_{OIOO}$, $\chi_{IOOO}$, $\chi_{OIII}$, and $\chi_{IOII}$), coherence-to-population transfer (i.e. $\chi_{OOOI}$, $\chi_{IIOI}$, $\chi_{OOIO}$, and $\chi_{IIIO}$), and coherence transfer (i.e. $\chi_{IOOI}$ and $\chi_{OIIO}$), are negligible in our system. Thus, only the process matrix elements for secular processes: population decay (i.e. $\chi_{OOOO}$ and $\chi_{IIII}$), population transfer (i.e. $\chi_{IIOO}$ and $\chi_{OOII}$), and coherence decay (i.e. $\chi_{OIOI}$ and $\chi_{IOIO}$), are non-zero. All the time-dependent process matrix elements inverted from the transient grating measurements are plotted in figure 6.4.

Indeed, we observe the non-secular process matrix elements including population-to-coherence transfer, coherence-to-population transfer, and coherence transfer are all zero. The exciton population in the outer wall decays and transfers completely to the inner wall within 300 fs, observed from $\chi_{OOOO}$ and $\chi_{IIOO}$, respectively. However, the exciton population in the inner wall does not decay, $\chi_{IIII}\,(T) = 1$, due to the slow relaxation time to the ground state. Additionally, inner wall excitons do not transfer uphill to the outer wall, $\chi_{OOII}\,(T) = 0$,

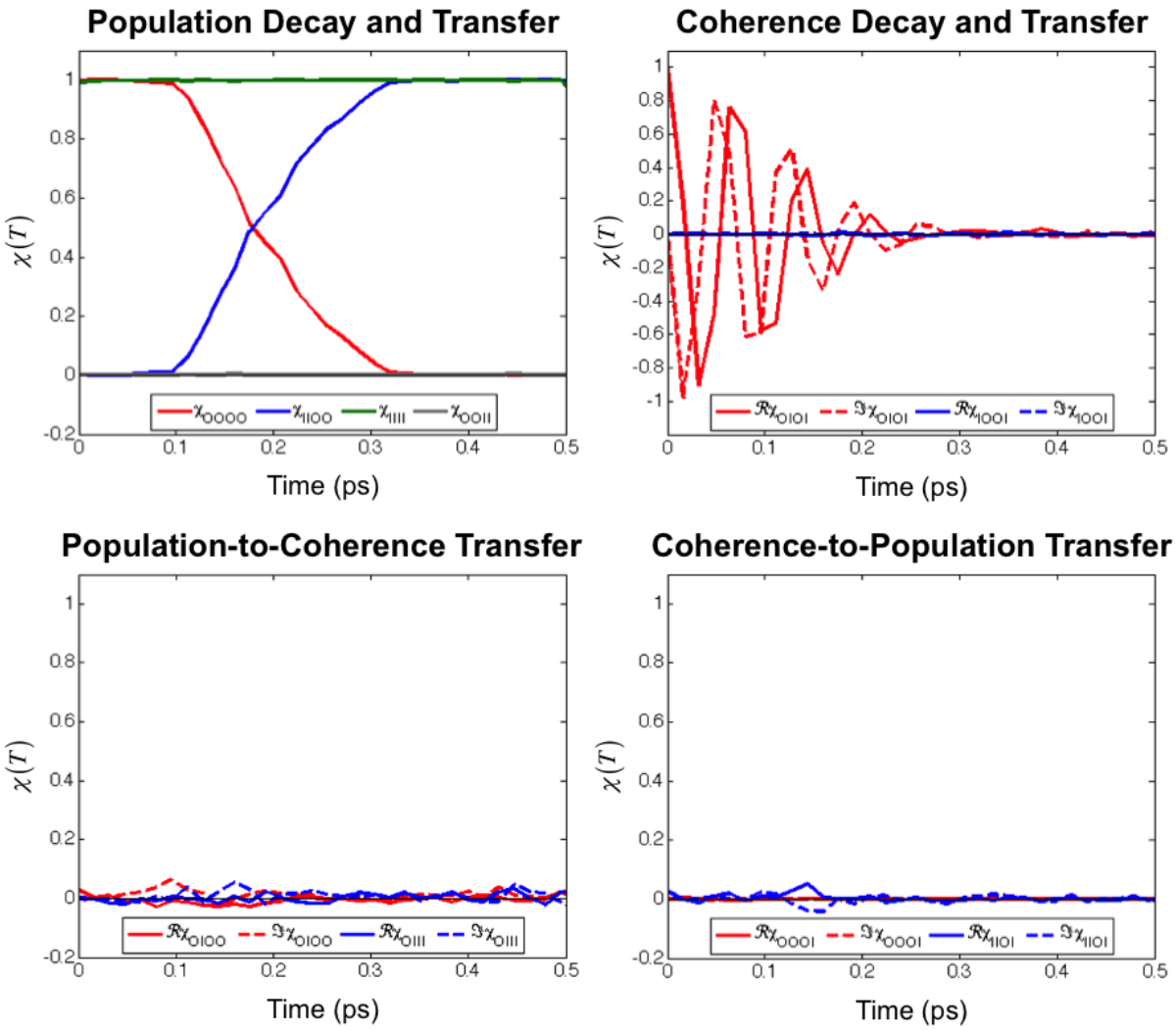


Figure 6.4: Time-dependent process matrix elements. Including secular processes: population decay ($\chi_{OOOO}$ and $\chi_{IIII}$), population transfer ($\chi_{IIOO}$ and $\chi_{OOII}$), and coherence decay ($\chi_{OIOI}$ and $\chi_{IOIO}$) and non-secular processes: population-to-coherence transfer ($\chi_{OIOO}$, $\chi_{IOOO}$, $\chi_{OIII}$, and $\chi_{IOII}$), coherence-to-population transfer ($\chi_{OOOI}$, $\chi_{IIOI}$, $\chi_{OOIO}$, and $\chi_{IIIO}$), and coherence transfer ($\chi_{IOOI}$ and $\chi_{OIIO}$). $\mathfrak{R}$ and $\mathfrak{I}$ denote the real and imaginary components of a given process matrix element.

| **Population Decay** | | | **Coherence Decay** | | |
|---|---|---|---|---|---|
| $\chi$ | Fit | Parameters | $\chi$ | Fit | Parameters |
| $\chi_{OOOO}$ | $\exp\left[-\left(T/\tau_{OO}\right)\beta_{OO}\right]$ | $\tau_{OO} = 212 \pm 8fs$<br>$\beta_{OO} = 3.3 \pm 0.4$ | $\chi_{OIOI} = \chi^*_{IOIO}$ | $\exp\left[-i\omega_{OI}T\right] \times \exp\left[-\left(T/\tau_{OI}\right)\beta_{OI}\right]$ | $2\pi/\omega_{OI} = 70 \pm 0.5fs$<br>$\tau_{OI} = 155 \pm 10fs$<br>$\beta_{OI} = 2.6 \pm 0.5$ |
| $\chi_{IIII}$ | 1 | - | | | |
| **Population Transfer** | | | **Coherence Transfer** | | |
| $\chi$ | Fit | Parameters | $\chi$ | Fit | Parameters |
| $\chi_{IIOO}$ | $1 - \exp\left[-\left(T/\tau_{OO}\right)\beta_{OO}\right]$ | $\tau_{OO} = 212 \pm 8fs$<br>$\beta_{OO} = 3.3 \pm 0.4$ | $\chi_{IOOI} = \chi^*_{OIIO}$ | 0 | - |
| $\chi_{OOII}$ | 0 | - | | | |
| **Population-to-Coherence Transfer** | | | **Coherence-to-Population Transfer** | | |
| $\chi$ | Fit | Parameters | $\chi$ | Fit | Parameters |
| $\chi_{IOOO} = \chi^*_{OIOO}$ | 0 | - | $\chi_{IIOI} = \chi^*_{IIIO}$ | 0 | - |
| $\chi_{IOII} = \chi^*_{OIII}$ | 0 | - | $\chi_{OOOI} = \chi^*_{OOIO}$ | 0 | - |

Table 6.3: Process matrix element fits and parameters. Including secular processes: population decay ($\chi_{OOOO}$ and $\chi_{IIII}$), population transfer ($\chi_{IIOO}$ and $\chi_{OOII}$), and coherence decay ($\chi_{OIOI}$ and $\chi_{IOIO}$) and non-secular processes: population-to-coherence transfer ($\chi_{OIOO}$, $\chi_{IOOO}$, $\chi_{OIII}$, and $\chi_{IOII}$), coherence-to-population transfer ($\chi_{OOOI}$, $\chi_{IIOI}$, $\chi_{OOIO}$, and $\chi_{IIIO}$), and coherence transfer ($\chi_{IOOI}$ and $\chi_{OIIO}$). The parameters $\omega_{xy}$ and $\tau_{xy}$ denote the oscillation frequency and relaxation timescale of the quantum state $|x\rangle\langle y|$ and $\beta_{xy}$ the stretching parameter for the exponential time dynamics.

because the 430 $cm^{-1}$ frequency difference is large compared to $k_BT$ at 298 K, which is 200 $cm^{-1}$. The real and imaginary components of $\chi_{OIOI}$ reveal coherences between inner and outer wall excitons oscillating at the 430 $cm^{-1}$difference frequency and lasting approximately 300 fs, signifying weak coupling between the states. Coupling between inner and outer wall excitons is also consistent with the small but measurable crosspeaks between the 16,700 and 17,000 $cm^{-1}$ inner and outer wall peaks in the two-dimensional spectra presented in chapter 5.

The data in figure 6.4 can be fit to the models derived in equations 6.11-6.15 and quantitative parameters can be determined. The fits, parameters, and error bars for each process matrix element is summarized in table 6.3. The experimental data are fit to stretched rather than standard exponentials and are characterized by the stretching parameter $\beta_x$, which we speculate is due to exponential kinetics that are embedded in Gaussian disorder.

## 6.7 Conclusions

Previous pump-probe measurements have attempted to characterize excited state population transfer and decay but were unable to unambiguously separate the inner and outer wall exciton dynamics or determine the role of biexciton states [145, 179, 151, 180]. Similarly, the two-dimensional spectra in chapter 5 could not completely separate the process matrix elements by spreading the signal over a second frequency axis as the crosspeaks include multiple contributions that evolve during the population time [47, 150, 48, 181, 176]. However, our narrowband transient grating measurements and the implementation of QPT unequivocally elucidate the single-exciton dynamics of double-walled J-aggregate nanotubes. First, we observed that non-secular processes and uphill energy transfer do not occur in our system. Second, we observed downhill energy transfer from the outer to inner wall occurred on a timescale of 212 $\pm$ 8 fs. Third, we observed weak coupling between inner and outer wall excitons characterized by dephasing on a timescale of 155 $\pm$ 10 fs. These experiments

are the first realization of QPT in a molecular or supramolecular system, in the condensed phase, or at room temperature and are the first experiments to unambiguously characterize the quantum dynamics of excitons in double-walled J-aggregate nanotubes.

# Chapter 7

# Two-Body Exciton Interactions in Cuprous Oxide

In chapter 7, we describe the first successful measurements of bi-orthoexciton coherences in cuprous oxide using two-dimensional two-quantum spectroscopy. In cuprous oxide, biexcitons are believed to drive inelastic exciton scattering but have not been detected because of strict optical selection rules that forbid radiative biexciton decay. We directly observe bi-orthoexcitons in cuprous oxide and estimate a 13 meV bi-orthoexciton binding energy, which is in the range of previous theoretical predictions, and a coherence lifetime around 70 fs. The creation or annihilation of a phonon accompanying an electronic transition also substantially increases the magnitude of the detected bi-orthoexciton coherence.

For these experiments, the cuprous oxide crystal was grown by Laszlo Frazer in the group of John Ketterson and Kelvin Chang in the group of Kenneth Poeppelmeier at Northwestern University. The two-dimensional spectroscopy measurements were conducted by Yoseob Yoon and myself.

## 7.1 Cuprous Oxide

Excitons in cuprous oxide ($Cu_2O$) are bound electron-hole pairs. The $O_h$ symmetry of $Cu_2O$ crystals and the direct gap $d$ to $s$ band transitions, which form the basis of the lowest lying "yellow" exciton series, give rise to a near-Rydberg structure [182]. However, the *1s* states deviate from the Rydberg pattern [183]. The high symmetry of the *1s* paraexciton singlet makes it optically inaccessible to all orders in the multipole expansion [184]. The 12 meV higher energy *1s* orthoexciton triplet state has single-photon transitions that are dipole-forbidden but quadrupole-allowed through an exceptionally narrow polariton resonance [185, 186]. The optical selection rules are so strict that, despite the direct gap, the strongest transitions require the participation of a phonon [186, 187, 188, 189].

Bound pairs of *1s* yellow orthoexcitons (i.e. bi-orthoexcitons) are expected to be forbidden from coupling to light to all orders, similar to paraexcitons [190]. Previously, luminescence data were interpreted as evidence of a decay chain of "green" series biexcitons [191]. Now, most of these features are interpreted as transitions from yellow excitons to the ground electronic state occupied by phonons [192]. A few lines still remain unexplained and may be caused by unidentified impurities [193].

Despite the lack of existing experimental evidence for biexcitons in $Cu_2O$, recombination of exciton pairs by Auger scattering has been invoked to explain exciton kinetics [194, 195]. In Auger scattering, one exciton in a pair is annihilated while the second exciton is ionized. Auger scattering is believed to be responsible for suppressing the Bose-Einstein condensation of excitons and for creating relaxation "explosions" in ultracold traps in $Cu_2O$ [195, 196, 197]. While measured exciton density-dependent dynamics are consistent with the Auger model [198], the values of the Auger proportionality coefficient reported by different experimental sources vary by two orders of magnitude [199]. The variation is explained in part by differences in the total exciton number, the volume occupied inhomogeneously by the excitons, the exciton temperature [194], strain [200], and spin state [194, 201].

In general, there are two Auger mechanisms: one in which the exciton pair forms a bound

state before decaying (i.e. biexciton-Auger) and one in which it does not (i.e. free exciton-Auger) [194]. When the exciton temperature $T_{Ex}$ is low compared to the biexciton binding energy $\Delta E_{Bx}$, i.e. $k_B T_{Ex} \ll \Delta E_{Bx}$, the condition relevant for Bose-Einstein condensation [195, 202], we expect the biexciton-Auger behavior to dominate. When the exciton temperature is high compared to the biexciton binding energy, i.e. $k_B T_{Ex} \gg \Delta E_{Bx}$, the condition relevant for most ultrafast and high intensity experiments, we expect the free exciton-Auger behavior to dominate [203].

In the free exciton-Auger model, the decay rate of the exciton density $n$ is expected to be linearly proportional to the exciton temperature [204], i.e. $dn/dt \propto -T_{Ex} n^2$, which is qualitatively consistent with the results at high $T_{Ex}$ [205]. In the biexciton-Auger model, the decay rate is expected to be inversely proportional to the exciton temperature, i.e. $dn/dt \propto -n^2/T_{Ex}$, as has been previously observed at low $T_{Ex}$ [206]. This indirect evidence is the strongest indication for the existence and significant influence of biexcitons in $Cu_2O$. Thus, direct observation of biexcitons and measurement of the biexciton binding energy is necessary to support any biexciton-based model of exciton kinetics and resolve differences among Auger kinetics measurements [200, 207, 208, 209, 210, 211, 212].

## 7.2 Cuprous Oxide Crystal Growth

A $Cu_2O$ crystal was grown by our collaborators using their previously reported method for producing relatively large, phase pure crystals with minimal point defects [213, 214, 215]. A 0.9999 pure Cu rod with a 6.35 mm diameter was oxidized at 1045 °C in air for 3 days with a heating and cooling rate of 5 °C/min. It was crystallized in air at a rate of 3.5 mm/hr in an optical floating zone furnace. The feed and support rods were counter-rotating at 7 RPM. A 2 cm section of the crystal was annealed at 1045 °C for 5 days with a heating and cooling rate of 5 °C/min. The crystal was then cut perpendicular to the [110] axis, the relative orientation of the laser polarization in our measurements. A slice of the oriented

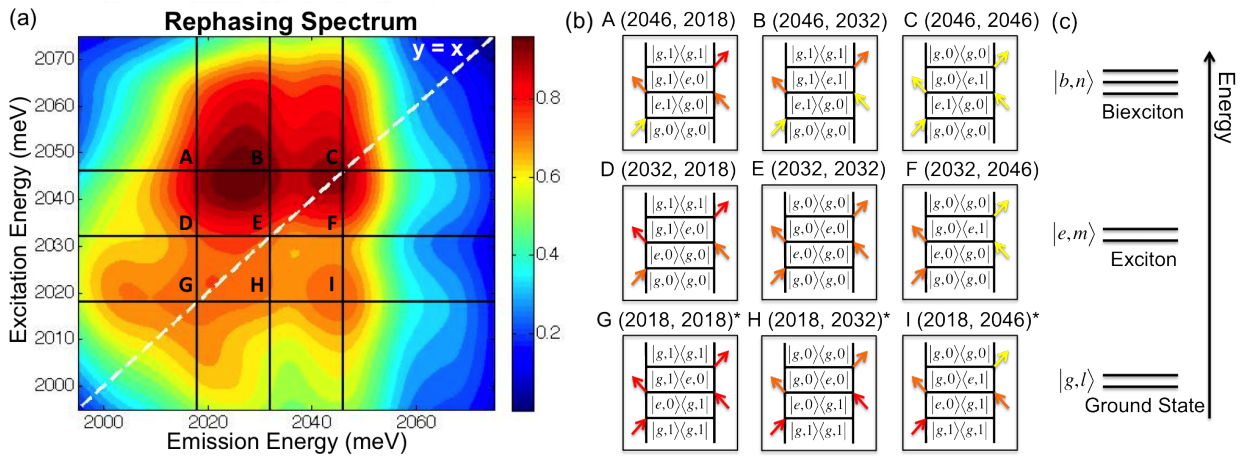


Figure 7.1: Two-dimensional rephasing spectrum of cuprous oxide at 10 K. (a) Rephasing spectrum at 10 K. (b) Representative Feynman diagrams for orthoexciton-polariton and phonon-assisted orthoexciton pathways, where red, orange, and yellow arrows denote field interactions involving the changes in phonon occupation number by -1, 0, and +1 which are nominally at photon energies of 2018, 2032, and 2046 meV, respectively. See Appendix B for full elucidation of Feynman diagrams. (c) Energy level diagram for orthoexcitons.

crystal was polished, resulting in a sample 0.401 mm thick. For the experiment, the $Cu_2O$ crystal was cooled to 10 K in a Janis ST-100-H cryostat and controlled by a Lake Shore 331 Temperature Controller.

## 7.3 One-Quantum Rephasing Spectrum

To accurately identify the features of the two-quantum spectrum, we first discuss the one-quantum (1Q) optical response of the *1s* yellow orthoexciton revealed by the two-dimensional (2D) rephasing spectrum. The data gave no evidence of any contribution from the optically forbidden paraexciton. Figure 7.1a shows the rephasing spectrum with four qualitatively distinct features (locations A, C, G, and I).

The two diagonal features near 2046 meV (C) and 2018 meV (G) are approximately 14 meV from the 2032 meV orthoexciton-polariton energy, $E_{Ex}$. This energy difference corresponds to the $\Gamma_{12}^{-}$ optical phonon energy, $E_{ph}$ [192]. Exciton-phonon coupling has been shown to substantially aid optical excitation by phonon creation or annihilation [196]. Therefore,

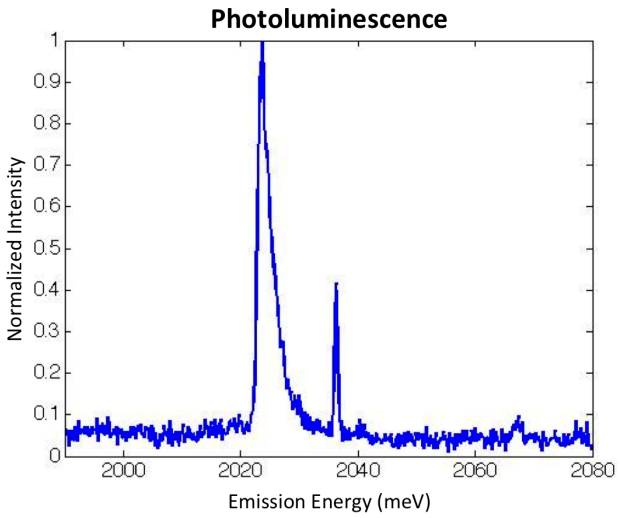


Figure 7.2: Photoluminescence spectrum. Pumping at 3100 meV and detecting polarizations parallel to [110] reveals the weak, higher energy exciton-polariton emission and the strong, lower energy phonon-assisted emission (i.e. phonon creation).

the 2046 meV diagonal peak is consistent with a transition between the ground vibronic state $|g,0\rangle$ and an orthoexciton state with one $\Gamma_{12}^{-}$ phonon $|e,1\rangle$ (i.e. phonon creation: $E_{Ex}-E_{ph}$). The 2018 meV diagonal peak is consistent with a transition between a phonon-populated ground electronic state $|g,1\rangle$ and the ground vibrational state of the orthoexciton $|e,0\rangle$ (i.e. phonon annihilation: $E_{Ex}-E_{ph}$). The 2046 meV absorption is much stronger because it originates from the ground vibronic state while the 2018 meV transition requires at least one phonon in the ground electronic state, which is less probable for experiments at 10 K but possible due to a large phonon density of states [196]. As expected, the 2032 meV orthoexciton-polariton diagonal peak (E) does not distinctly appear because it is a weakly allowed quadrupole resonance.

The two off-diagonal features with emission near 2018 meV (A) and 2046 meV (I) are crosspeaks between the phonon-assisted diagonal peaks (C and G). However, the 2018 meV crosspeak is shifted toward the 2032 meV orthoexciton-polariton emission energy (B). One reason for the shift is non-zero kinetic energy of the phonon-assisted orthoexcitons [196]. Due to the flatness of the phonon dispersion around the gamma point, phonon-assisted orthoexcitons can gain kinetic energy from high wavevector phonons, resulting in a high

energy tail along both the absorption and emission axes. The higher energy tail is also observed in the photoluminescence spectrum in figure 7.2, where the strong, lower energy $E_{Ex} - E_{ph}$ emission is phonon-assisted and creates a phonon on the ground electronic state ($|e,0\rangle \rightarrow |g,1\rangle$) and the weak, higher energy $E_{Ex}$ emission is purely excitonic ($|e,0\rangle \rightarrow |g,0\rangle$). A second possible reason is weak crosspeaks (B, D, F, and H) between the orthoexciton-polariton and phonon-assisted orthoexcitons. These crosspeaks gain oscillator strength from the phonon-assisted transition dipole moments and may contribute to the overall spectrum even though the orthoexciton-polariton diagonal peak (E) is not directly observed.

## 7.4 Two-Quantum Spectrum

Based on the participation of the $\Gamma_{12}^{-}$ phonon in the 1Q spectrum, we now discuss the two-quantum (2Q) spectrum shown in Figure 7.3a. First, we note there are strong 2Q coherences that unambiguously demonstrate significant two-exciton correlations. Additionally, the spectral density lies almost entirely below the $y = 2x$ line, indicating the bi-orthoexciton is lower in energy than twice the orthoexciton energy and thus possesses a finite binding energy, $\Delta E_{Bx} = 2E_{Ex} - E_{Bx}$. However, a quantitative estimate of the bi-orthoexciton binding energy requires detailed analysis of the exciton-phonon coupling.

In the 2Q spectrum, we observe a major and a minor feature. The major feature emits near 2046 meV and is consistent with a phonon-assisted orthoexciton transition in which a phonon is annihilated upon emission ($E_{Ex} + E_{ph}$). The 2Q energy of the major feature is centered at 4066 meV and has a FWHM of approximately 80 meV but extends over more than 100 meV. Under the assumptions that at most one phonon can be created or annihilated per field interaction and the initial transition originates from the ground electronic state with 0 or 1 phonons (based on the 1Q spectrum), we can identify three excitation paths from the ground electronic state $|g,0\rangle$ into a bi-orthoexciton coherence with 0, 1, and 2 phonons $|b,n\rangle$ that can emit with transition $E_{Ex}+E_{ph}$. Neglecting the biexciton binding energy, these three

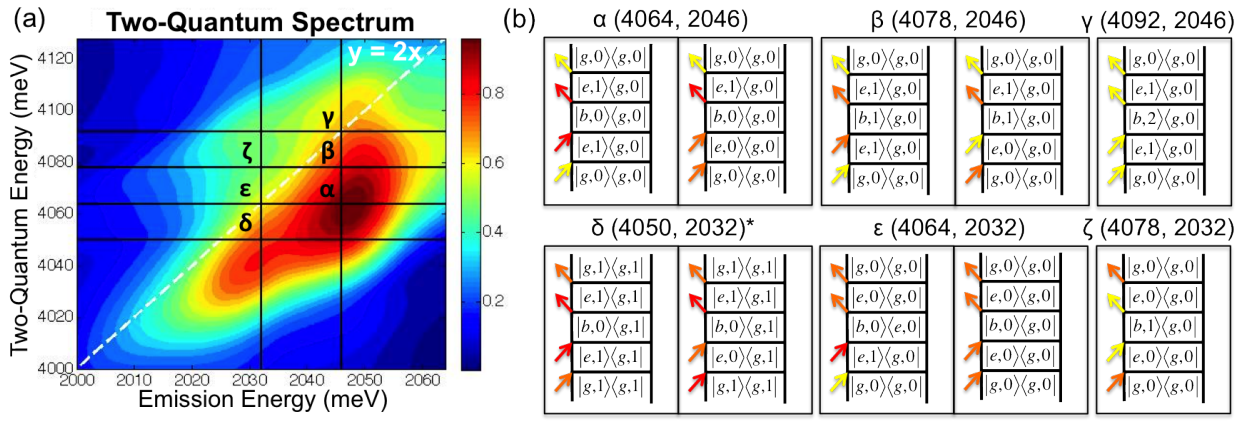


Figure 7.3: Two-dimensional two-quantum spectrum of cuprous oxide at 10 K. (a) Two-quantum spectrum at 10 K. (b) Representative Feynman diagrams for orthoexciton-polariton and phonon-assisted orthoexciton pathways, where red, orange, and yellow arrows denote field interactions involving the changes in phonon occupation number by -1, 0, and +1 which are nominally at photon energies of 2018, 2032, and 2046 meV, respectively. See Appendix C for full elucidation of Feynman diagrams.

paths give rise to signals at $2E_{Ex}$, $2E_{Ex}+E_{ph}$, $2E_{Ex}+2E_{ph}$, which are indicated in figure 7.3a at locations α, β, and γ, respectively. These three features have similar oscillator strength and overlap to form one broad peak centered at the average 2Q energy: $2E_{Ex}+E_{ph}-\Delta E_{Bx}$. The 2Q spectrum shows the corresponding spectral feature is shifted down in 2Q energy by some biexciton binding energy $\Delta E_{Bx}$. The location of the major feature indicates a bi-orthoexciton binding energy of 12 meV, within the range of theoretically predicted values [190, 216, 217].

To better understand the determination of the biexciton binding energy, figure 7.4 illustrates the analysis for extracting $\Delta E_{Bx}$ from three overlapping 2Q signals with the same emission energy. Figure 7.4a illustrates the case where the non-overlapping signals of three unbound biexcitons at 2Q energy $2E_{Ex}+2E_{ph}$, $2E_{Ex}+E_{ph}$, and $2E_{Ex}$ emit from $E_{Ex}+E_{ph}$. We observe there are three distinct peaks each separated in 2Q energy by the phonon energy $E_{ph}$. Figure 7.4b demonstrates how the three biexciton peaks shift to lower 2Q energy for a positive biexciton binding energy. Figure 7.4c illustrates the case where the overlapping signals of three unbound biexcitons at 2Q energy $2E_{Ex}+2E_{ph}$, $2E_{Ex}+E_{ph}$, and $2E_{Ex}$ emit

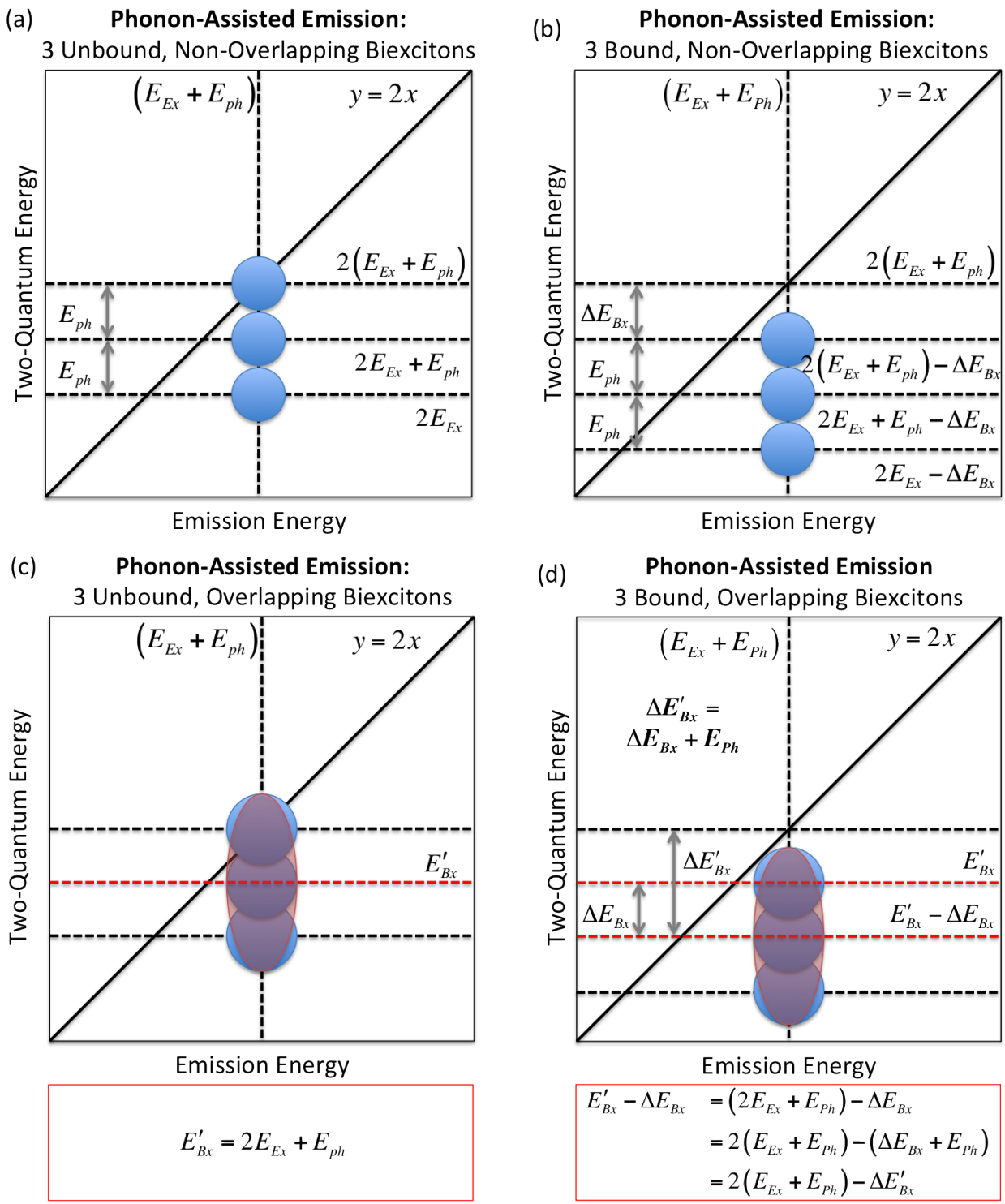


Figure 7.4: Three overlapping two-quantum vibronic peaks. Bi-orthoexciton binding energy illustrations for the 3 overlapping vibronic signals of the 2Q phonon-assisted emission peak.

from $E_{Ex} + E_{ph}$. In this case, the three distinct peaks in figure 7.4a become one peak elongated along the 2Q energy direction. The center of the overlapping peak no longer lies on the $y = 2x$ line even for the case of unbound biexcitons but is situated at the average 2Q energy of the three overlapping peaks: $E'_{Bx} = 2E_{Ex} + E_{ph}$. Figure 7.4d demonstrates how the elongated biexciton peak shifts to lower 2Q energy for a positive biexciton binding energy. The energy difference between the $y = 2x$ line and the center of the elongated peak is now $\Delta E'_{Bx} = \Delta E_{Bx} + E_{ph}$. Thus, the energy difference between the $y = 2x$ line and the elongated biexciton peak must be adjusted by $E_{ph}$ to determine $\Delta E_{Bx}$ for three overlapping vibronic peaks.

The minor feature emits near 2032 meV and is consistent with orthoexciton-polariton emission ($E_{Ex}$). The 2Q energy of the minor feature is centered at 4043 meV and has a FWHM of approximately 50 meV but extends over approximately 90 meV. We can identify three excitation paths that can emit with transition energy $E_{Ex}$: one from the phonon-populated ground electronic state $|g, 1\rangle$ into a bi-orthoexciton coherence including zero phonons $|b, 0\rangle$ and two from the ground vibronic state $|g, 0\rangle$ into a bi-orthoexciton coherence with 0 or 1 phonons $|b, n\rangle$. Neglecting the biexciton binding energy, these three paths give rise to signals with 2Q energies of $2E_{Ex} - E_{ph}$, $2E_{Ex}$, and $2E_{Ex} + E_{ph}$, which are indicated in figure 7.3a at locations δ, ε, and ζ, respectively.

However, there is no substantial signal intensity on or above the $y = 2x$ line at the $E_{Ex}$ emission energy and the signal is much narrower than the phonon-assisted emission peak. This suggests the bi-orthoexciton with one phonon (ζ) is not observed in the 2Q spectrum because of destructive interference with the excited state emission from pathway α. Thus, we postulate the minor feature originates mostly from the overlapping signals of the two bi-orthoexciton ground vibrational state pathways (δ and ε). These two features have similar oscillator strength and overlap to form one peak centered at the average energy: $2E_{Ex} - \frac{1}{2}E_{ph} - \Delta E_{Bx}$. The location of the minor feature indicates a bi-orthoexciton binding energy of 13 meV, which is in agreement with the binding energy of the phonon-assisted

peak.

To better understand the determination of the biexciton binding energy, figure 7.5 illustrates the analysis for extracting $\Delta E_{Bx}$ from two overlapping 2Q signals with the same emission energy. Figure 7.5a illustrates the case where the non-overlapping signals of two unbound biexcitons at 2Q energy $2E_{Ex}$ and $2E_{Ex} - E_{ph}$ emit from $E_{Ex}$. We observe there are two distinct peaks separated in 2Q energy by the phonon energy $E_{ph}$. Figure 7.5b demonstrates how the two biexciton peaks shift to lower 2Q energy for a positive biexciton binding energy. Figure 7.5c illustrates the case where the overlapping signals of two unbound biexcitons at 2Q energy $2E_{Ex}$ and $2E_{Ex} - E_{ph}$ emit from $E_{Ex}$. In this case, the two distinct peaks in figure 7.5a become one peak elongated along the 2Q energy direction. The center of the overlapping peak no longer lies on the $y = 2x$ line even for the case of unbound biexcitons but is situated at the average 2Q energy of the two overlapping peaks: $E'_{Bx} = 2E_{Ex} - \frac{1}{2}E_{ph}$. Figure 7.5d demonstrates how the elongated biexciton peak shifts to lower 2Q energy for a positive biexciton binding energy. The energy difference between the $y = 2x$ line and the center of the elongated peak is now $\Delta E'_{Bx} = \Delta E_{Bx} + \frac{1}{2}E_{ph}$. Thus, the energy difference between the $y = 2x$ line and the elongated biexciton peak must be adjusted by $\frac{1}{2}E_{ph}$ to determine $\Delta E_{Bx}$ for two overlapping vibronic peaks.

From the lineshapes of the 2Q spectrum, we can also determine a bi-orthoexciton coherence lifetime of approximately 70 fs.

### 7.4.1 Feynman Diagram Analysis

To validate our assumptions about the number and relative strengths of the 2Q signals, we construct the set of all possible pathways, each presented by a distinct double-sided Feynman diagram, that constitute the 2Q signal at each emission energy, including phonon creation (2018 meV), exciton-polariton emission (2032 emV), and phonon annihilation (2048 meV). We enumerate all the possible 2Q Feynman diagrams under the assumptions that a field interaction can create or annihilate at most one phonon and the initial transition originates

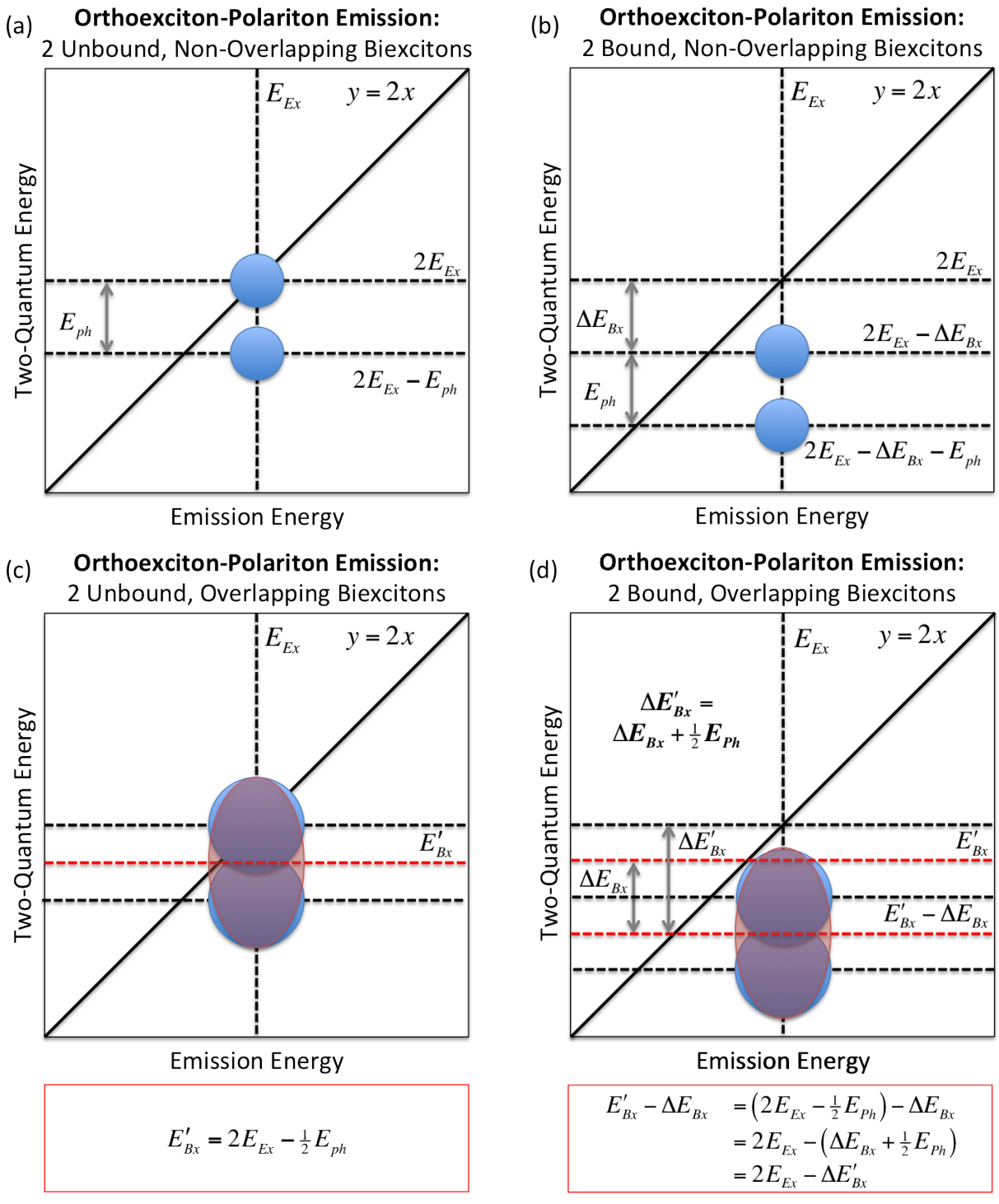


Figure 7.5: Two overlapping two-quantum vibronic peaks. Bi-orthoexciton binding energy illustrations for the 2 overlapping vibronic signals of the 2Q orthoexciton-polariton emission peak.

(a) **Non-Overlapping Pathways**

| Two-Quantum Energy (meV) | Emission Energy (meV) | | | | | |
|---|---|---|---|---|---|---|
| | 2018 | | 2032 | | 2046 | |
| 4092 | | | | | γ' | γ |
| | | | | | -81 | 81 |
| | | | | | -81* | 81* |
| 4078 | | | ζ' | ζ | β' | β |
| | | | -18 | 18 | -18 | 18 |
| | | | -18* | 18* | -18* | 18* |
| 4064 | θ' | θ | ε' | ε | α' | α |
| | -90 | 0 | -10 | 10 | 0 | 90 |
| | -171* | 171* | -19* | 19* | -171* | 171* |
| 4050 | η' | η | δ' | δ | | |
| | 0 | 0 | 0 | 0 | | |
| | -18* | 18* | -18* | 18* | | |

(b) **Overlapping Pathways**

| Two-Quantum Energy (meV) | Emission Energy (meV) | | | |
|---|---|---|---|---|
| | 2004 | 2018 | 2032 | 2046 |
| 4092 | | | γ' | γ |
| | | | -85 | 85 |
| 4078 | | ζ' | Z | β |
| | | -19 | 0 | 19 |
| 4064 | θ' | Θ | E | α |
| | -99 | -2 | 2 | 99 |
| 4050 | η' | N | δ | |
| | -1 | 0 | 1 | |

Figure 7.6: Graphical displays of two-quantum signal via Feynman diagram analysis. Graphical displays for non-overlapping (a) and overlapping (b) pathway strengths for all possible 2Q Feynman diagrams. * indicates pathways involving a phonon-populated ground electronic state. ‘ indicates excited state absorption pathways.

from the ground electronic state with 0 or 1 phonons. All the 2Q Feynman diagrams are enumerated in Appendix C.

For our qualitative estimate of the 2Q signal strengths, we assign the orthoexciton-polariton transition dipole moment a strength of 1 and the phonon-assisted transition dipole moment a strength of 3. This 3:1 ratio is estimated from the photoluminescence spectrum in figure 7.2, which demonstrates a 9:1 ratio of the phonon-assisted to orthoexciton-polariton emission intensity. We also assume the transition dipole moments between the ground and exciton states and between the exciton and biexciton states are equivalent. For pathways originating from the phonon-populated ground electronic state, we assume 5% of electrons experience sufficient thermal excitation at 10 K, due to the large phonon density of states, to involve a phonon. The strength of a single pathway is given by the product of the four transition dipole moments and the initial thermal population. If multiple pathways exist for the same signal, they are summed to produce the total signal strength.

Each 2Q signal strength is graphically organized in figure 7.6a first assuming there is

no signal overlap. A plain Greek letter X indicates the stimulated emission pathway at a given 2Q and emission energy. X' indicates the excited state absorption pathway, which is shifted by the biexciton binding energy (13 meV) along the emission axis. A plain number Y indicates the total strength of transitions from the ground vibronic state, while Y* indicates the total strength of transitions involving an optical phonon on the ground electronic state.

Because the biexciton binding energy (13 meV) is close to the optical phonon energy (14 meV), the excited state absorption (ESA) of a given pathway should destructively interfere with the stimulated emission (SE) of the pathway at the next lowest emission energy. The destructive interference is due to the SE and ESA pathways being out of phase with each other. This can readily seen in the SE and ESA polarizations generated by the three excitation pulses:

$$P_{SE}(t') = \left(\frac{-i}{\hbar}\right)^3 \int_0^\infty dt \int_0^\infty dT \int_0^\infty d\tau \overrightarrow{E}_3^*(t'-t)\,\overrightarrow{E}_2(t'-t-T)\,\overrightarrow{E}_1(t'-t-T) \times Tr\left(\left[\left[\left[\overrightarrow{\mu}_{eg}(T+t),\overrightarrow{\mu}_{be}(T)\right],\overrightarrow{\mu}_{eb}(0)\right],\overrightarrow{\mu}_{ge}(0)\right]\rho(0)\right) \quad (7.1)$$

$$P_{ESA}(t') = \left(\frac{i}{\hbar}\right)\left(\frac{-i}{\hbar}\right)^2 \int_0^\infty dt \int_0^\infty dT \int_0^\infty d\tau \overrightarrow{E}_3^*(t'-t)\,\overrightarrow{E}_2(t'-t-T)\,\overrightarrow{E}_1(t'-t-T) \times Tr\left(\left[\left[\left[\overrightarrow{\mu}_{be}(T+t),\overrightarrow{\mu}_{ge}^*(T)\right],\overrightarrow{\mu}_{eb}(0)\right],\overrightarrow{\mu}_{ge}(0)\right]\rho(0)\right) \quad (7.2)$$

Figure 7.6b shows the expected 2Q signal strengths if neighboring stimulated emission and excited state absorption pathways perfectly cancel. We observe the excited state absorption pathway of peak β exactly cancels with the stimulated emission pathway of ζ (figure 7.6b, position Z).

$$E_{SE}^{\zeta}(4078\ meV,\ 2032\ meV) = E_{ESA}^{\beta}(4078\ meV,\ 2046\ meV - \Delta E_{Bx}) \quad (7.3)$$

Thus we expect to see little or no spectral density above the $y = 2x$ line at the 2032

meV emission energy. This is consistent with the measured 2Q spectrum and supports our assumption that only the overlapping E and δ pathways in figure 7.6b contribute to the minor feature. Additionally, the strength of the overlapping signal at E is 2, while the strength at δ is 1. These two signal strengths are similar, so the minor feature in the 2Q spectrum should be nearly symmetric about the two pathways.

The strength of the signals at α and γ are comparable at 99 and 85, respectively. The near equivalence of the expected spectral densities of the stimulated emission pathways of α and γ in figure 7.6b supports our assumption that the major feature in the 2Q spectrum is symmetric about pathway β.

A similar Feynman diagram analysis was performed for the rephasing spectrum and can be found in Appendix B.

## 7.5 One- and Two-Quantum Spectrum Simulations

To corroborate our interpretation of the 1Q and 2Q spectrum, the third-order response functions of $Cu_2O$ were simulated using the density matrix formalism and assuming a 13 meV biexciton binding energy [41]. The third-order response functions of 2D spectra are discussed in more detail in chapter 4. Here, we merely give the expression for the matrix elements of the rephasing and 2Q response functions, including the ground state bleach (GSB), stimulated emission (SE), and excited state absorption (ESA) terms:

$$R^{(3)}_{R:GSB}\left(\omega_{ge}, T, \omega_{eg}\right) = \rho\left(0\right)\left|\mu_{ge}\right|^4 \exp\left[-\left(i\omega_{ge} + \Gamma_{ge}\right)\tau\right] \exp\left[-\left(i\omega_{eg} + \Gamma_{eg}\right)t\right] \tag{7.4}$$

$$R^{(3)}_{R:SE}\left(\omega_{ge}, T, \omega_{eg}\right) = \rho\left(0\right)\left|\mu_{ge}\right|^4 \times \exp\left[-\left(i\omega_{ge} + \Gamma_{ge}\right)\tau\right] \exp\left[-\Gamma_{ee}T\right] \exp\left[-\left(i\omega_{eg} + \Gamma_{eg}\right)t\right] \tag{7.5}$$

$$R^{(3)}_{R:ESA}(\omega_{ge}, T, \omega_{be}) = -\rho(0)\,|\mu_{ge}|^2\,|\mu_{eb}|^2 \times \exp[-(i\omega_{ge} + \Gamma_{ge})\,\tau]\exp[-\Gamma_{ee}T]\exp[-(i\omega_{be} + \Gamma_{be})\,t] \quad (7.6)$$

$$R^{(3)}_{2Q:SE}(\omega_{gb},\omega_{ge}) = \rho(0)\,|\mu_{ge}|^2\,|\mu_{eb}|^2\exp[-(i\omega_{gb} + \Gamma_{gb})\,T_{2Q}]\exp[-(i\omega_{ge} + \Gamma_{ge})\,t] \quad (7.7)$$

$$R^{(3)}_{2Q:ESA}(\omega_{gb},\omega_{eb}) = -\rho(0)\,|\mu_{ge}|^2\,|\mu_{eb}|^2\exp[-(i\omega_{gb} + \Gamma_{gb})\,T_{2Q}]\exp[-(i\omega_{eb} + \Gamma_{eb})\,t] \quad (7.8)$$

where $\omega_{ij}$ is the resonance frequency between states $i$ and $j$, $\mu_{ij}$ is the transition dipole moment, and $\Gamma_{ij}$ is the dephasing time. An asymmetric Lorentzian lineshape was used to reproduce the high-energy tails of the phonon-assisted peaks observed in the photoluminescence in figure 7.2 [218]. In this model, the full width at half maximum ($\gamma$) of the Lorentzian lineshape function $f(\omega)$ varies as a function of frequency:

$$\gamma(\omega) = \frac{\gamma_0}{1 + \exp[a\,(\omega - \omega_0)]} \quad (7.9)$$

$$f(\omega) = \frac{1}{\pi\gamma(\omega)}\left[\frac{\gamma^2(\omega)}{(\omega - \omega_0)^2 + \gamma^2(\omega)}\right] \quad (7.10)$$

where $\gamma_0$ is the full width at half maximum at the center frequency $\omega_0$ and $a$ is a measure of the asymmetry of the lineshape. These simulations are qualitative in nature and only attempt to reproduce the general features of the rephasing and 2Q spectra.

The simulation of the rephasing spectrum is shown in figure 7.7a. The calculation of the response function reproduces the relative spectral intensities of the phonon creation (2046 meV) and phonon annihilation (2018 meV) absorption paths. The high-energy tails are also clearly visible. The [2046 meV, 2018 meV] crosspeak (figure 7.1a, peak A) is clearly shifted toward the 2032 meV orthoexciton-polariton emission energy, while the [2018 meV, 2046 meV] crosspeak (C) is shifted slightly away. The off-diagonal peak associated with phonon annihilation at [2018 meV, 2046 meV] (I) is weaker in the simulation then in the experimental data, but the diagonal peak at [2018 meV, 2018 meV] (G) is reproduced fairly well. Overall, the simulation qualitatively reproduces the data well enough to support our interpretations

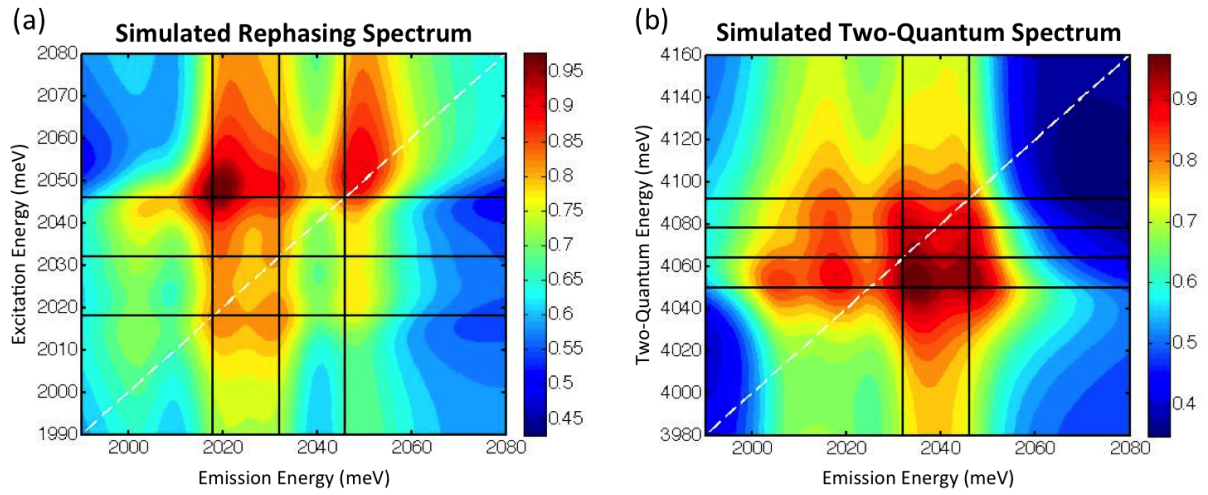


Figure 7.7: Rephasing and two-quantum spectra simulations. Simulations of the third-order response function for the rephasing (a) and 2Q spectra (b) using a combination of symmetric and asymmetric Lorentzian lineshapes and assuming the experimentally determined 13 meV bi-orthoexciton binding energy.

of the 1Q spectrum and to validate our assumptions for the analysis of the 2Q spectrum.

In figure 7.7b, we show the simulation of the 2Q spectrum. The calculation reproduces the 2046 meV 2Q signal emission fairly well. However for the 2032 meV 2Q signal emission, there is some simulated spectral intensity above the $y = 2x$ line, possibly due to incomplete destructive interference of the 4078 meV peak with the excited state absorption pathway from the [4078 meV, 2046 meV] peak (figure 7.3a, peak $\alpha$). The 2Q energy of the 2032 meV emission is also only slightly lower in 2Q energy than the 2046 meV emission, possibly due to weak signal from the phonon-populated ground electronic state pathway ($\delta$). The 2032 meV emission is also more intense compared to the 2046 meV emission. The lower emission energy features are mainly from the excited state absorption pathways of the 2032 meV 2Q signal emission, which we do not observe experimentally. Overall, the simulation qualitatively reproduces the major feature of the 2Q spectrum but breaks down for the minor feature. We are confident in our interpretation of the experimental data, particularly of the major feature, but quantitative simulation of the 2Q spectrum requires many unknown and difficult to optimize parameters, including some dephasing rates and the difference between

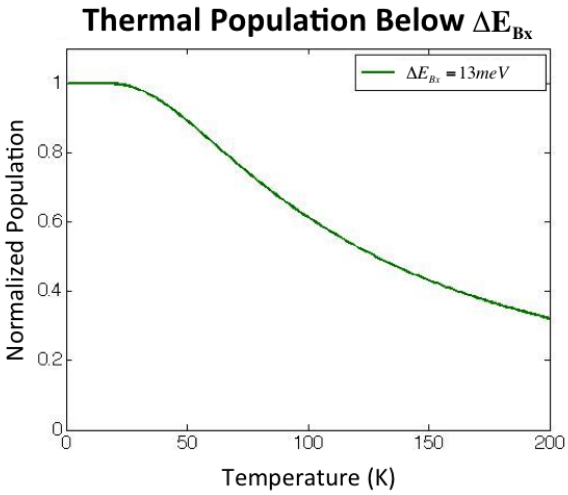


Figure 7.8: Temperature-dependent, integrated Maxwell-Boltzmann distribution of biexciton energies. Temperature-dependent population fraction of bi-orthoexcitons with thermal energy less than the 13 meV bi-orthoexciton binding energy.

the ground to exciton and exciton to biexciton transition dipole moments.

## 7.6 Temperature-Dependent Experiments

Temperature-dependent 2Q spectra were recorded in the 10-200 K range to further study the bi-orthoexcitons in $Cu_2O$. Figure 7.10 shows the normalized integrated signal intensity of the entire 2Q spectrum as a function of temperature. As the temperature of the system increases and the kinetic energy of the bi-orthoexcitons exceeds their binding energy, the total 2Q signal intensity decreases. A Maxwell-Boltzmann distribution can be used to model the population of bi-orthoexcitons below the binding energy as a function of temperature:

$$f^{MB}_{E<\Delta E_{Bx}}(T) = \int_0^{\Delta E_{Bx}} f^{MB}(E,T)\, dE \tag{7.11}$$

$$f^{MB}(E,T) = 2\left(\frac{1}{k_B T}\right)^{\frac{3}{2}} \sqrt{\frac{E}{\pi}} \exp\left[\frac{-E}{k_B T}\right] \tag{7.12}$$

Figure 7.8 shows the calculation of the percentage of the bi-orthoexciton thermal popu-

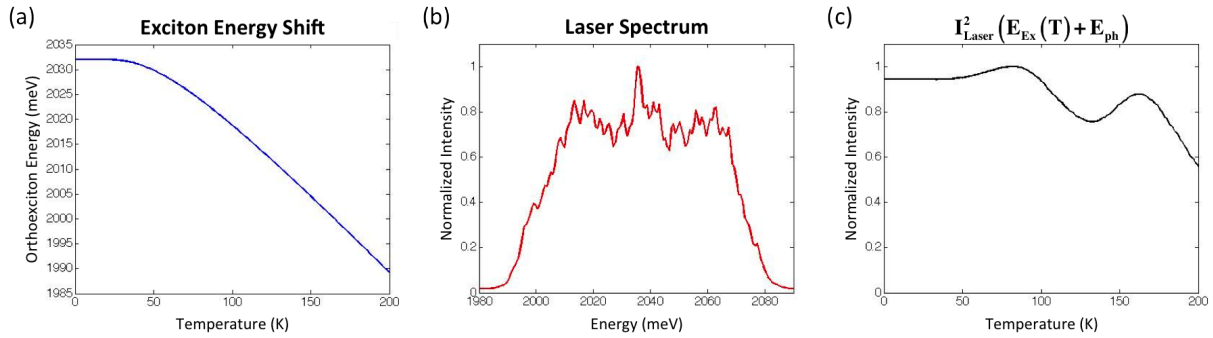


Figure 7.9: Laser intensity at the temperature-dependent exciton energy. (a) Temperature-dependent orthoexciton-polariton energy. (b) Laser spectrum used in the 2D experiments. (c) Temperature-dependent laser intensity squared at 2046 meV, $I^2_{Laser}(E_{Ex}(T) + E_{ph})$.

lation below the bi-orthoexciton binding energy (13 meV) as a function of temperature using equation 7.11. It is assumed any biexciton with a thermal energy equal to or greater than the biexciton binding energy ($E_{Bx}(T) \geq \Delta E_{Bx}$) dissociates and does not contribute to the 2Q signal intensity.

The orthoexciton-polariton energy is also temperature-dependent and decreases with temperature. At high temperatures, the transition frequency begins to move out of the laser pulse bandwidth. A model developed by Itoh and Narita for the temperature dependence of the band gap energy ($E_{BG}(T)$) and the orthoexciton binding energy ($\Delta E_{Ex}(T)$) describes the orthoexciton-polariton energy as a function of the temperature [219]:

$$E_{Ex}(T) = E_{BG}(T) - \Delta E_{Ex}(T) + E_{O-P} \tag{7.13}$$

$$E_{BG}(T) = 2,195\,meV - 26\,meV \times \coth\left[\frac{E_{ph}}{2k_BT}\right] \tag{7.14}$$

$$\Delta E_{Ex}(T) = 150\,meV + 0.64\,meV \times \coth\left[\frac{E_{ph}}{2k_BT}\right] \tag{7.15}$$

where $E_{O-P}$ is the ortho-para exchange splitting energy. We assume $E_{O-P}$ is temperature independent because it is an order of magnitude smaller than $\Delta E_{Ex}(T)$ and two orders of magnitude smaller than $E_{BG}(T)$, both of which vary around 1% in this temperature range [219]. We can account for the temperature-dependent orthoexciton-polariton energy

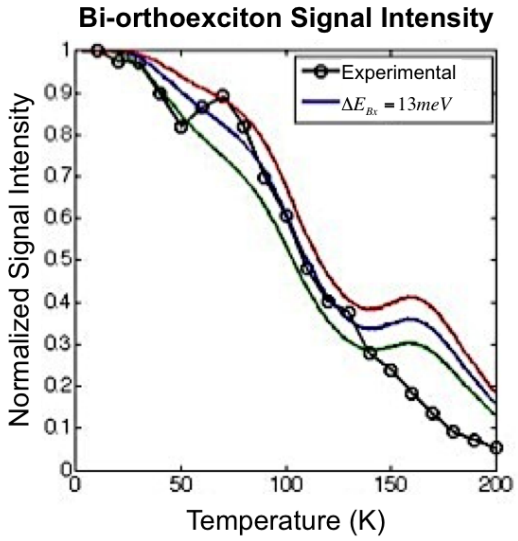


Figure 7.10: Temperature-dependent bi-orthoexciton signal intensity. Model predictions are based on bi-orthoexciton binding energies of 11 (green), 13 (blue), and 15 (red) meV.

by normalizing the bi-orthoexciton signal intensity to the laser intensity squared at the energy of the strongest transition: $I^2_{Laser}\left(E_{Ex}\left(T\right)+E_{ph}\right)$. We assume $E_{ph}$ is temperature independent because it is also two orders of magnitude smaller than $E_{Ex}\left(T\right)$ and is likely to only vary around 1%, as in other semiconductors in this temperature range [220, 221]. Figure 7.9a plots the temperature-dependent orthoexciton-polariton energy $E_{Ex}\left(T\right)$ using the Itoh-Narita model expressed in equation 7.13. Figure 7.9b shows the laser pulse spectrum used in the 2D experiments. Figure 7.9c shows the laser intensity squared at the strongest transition energy as a function of temperature, $I^2_{Laser}\left(E_{Ex}\left(T\right)+E_{ph}\right)$.

The effects of the bi-orthoexcitons thermal energy (figure 7.8) and the shifting of the orthoexciton energy out of the laser pulse bandwidth (figure 7.9c) are combined to model the temperature-dependent bi-orthoexciton 2Q signal intensity. We multiply the results from figures 7.8 and 7.9c to produce the model presented in figure 7.10. Figure 7.10 superimposes the temperature-dependent bi-orthoexciton signal intensity with the theoretical prediction of our model. For the 13 meV bi-orthoexciton binding energy determined in the 2Q spectrum at 10 K, the model agrees well with the temperature-dependent data. The deviation of the theoretical bi-orthoexciton signal intensity from the experimental intensity above 130 K can

be seen to arise from the non-Gaussian profile of the laser spectrum in figures 7.9a-c. The 2Q signal intensity must deviate from the expected behavior as the resonances move out of the laser pulse bandwidth and depend less on the laser pulse profile.

## 7.7 Conclusions

From the 2Q spectrum of $Cu_2O$, we directly observe two-exciton correlations. We measure a bi-orthoexciton binding energy of 12-13 meV and a coherence lifetime of approximately 70 fs. Our model of the temperature-dependent bi-orthoexciton signal intensity is also consistent with a 13 $\pm$ 2 meV bi-orthoexciton binding energy. Our estimate is much greater than the 4.7 meV value calculated from third-order central cell corrected predictions [190] and the 6.2 meV value calculated with a variational method [216] but is in agreement with the 13 meV Feynman path integral prediction [217]. Overall, our results support the suggestion that biexcitons play a key role in Auger recombination of excitons below 150 K and thus in the suppression of exciton-polariton Bose-Einstein condensation.

# Chapter 8

# Exciton-Phonon and Exciton-Exciton Interactions in Monolayer Transition Metal Dichalcogenides

In chapter 8, we discuss preliminary experiments exploring the extent of exciton-exciton and exciton-phonon interactions in monolayer transition metal dichalcogenides. Our samples were grown using chemical vapor deposition by our collaborators at the National Tsing Hua University in the group of Yi-Hsien Lee. Characterization of the samples by microscopy and reflectance were performed by Edbert Sie at MIT in the group of Nuh Gedik. Two-dimensional spectroscopy was performed by myself, Jake Siegel, and Yoseob Yoon.

## 8.1 Monolayer Transition Metal Dichalcogenides Physics

Recent advancements in the isolation of monolayer transition metal dichalcogenides (TMDs: $MX_2$) by exfoliation and chemical vapor deposition (CVD) have led to the discovery of new and exciting semiconductor physics [222, 223, 82, 85]. This class of materials is most commonly composed of the group VI transition metals (M) molybdenum (Mo) or tungsten (W) and the group XVI chalcogens (X) sulfur (S), selenium (Se), or tellurium (Te). Bulk TMDs

are characterized by strongly bound layers weakly coupled through van der Waals forces, similar to graphite. Each layer is three atoms thick and comprised of a layer of transition metals sandwiched between two layers of chalcogen atoms (i.e. $XMX$), illustrated in figure 8.1a. Each monolayer is arranged in a hexagonal structure that results in a hexagonal Brillouin zone with six $K$-point valleys, similar to the band structure of graphene. Unlike graphene, the chemical composition of TMDs leads to a finite band gap of approximately 1-2 eV. In the bulk, TMDs are indirect band gap semiconductors. In the monolayer limit, TMDs become direct band gap semiconductors, due to quantum confinement of their $d$-electrons, and exhibit strong absorption and photoluminescence [224, 83]. Monolayer TMDs also do not possess an inversion center, unlike bulk and even numbered multi-layer TMDs, and results in non-equivalent $K$ and $-K$ valleys in the Brillouin zone.

### 8.1.1 Emergence of Valley Polarization

The emergence of non-equivalent $K$ valleys in monolayer TMDs has garnered significant interest because of the potential to carry quantum information in the valley indices of electrons and holes. In this design, electrons or holes of the same energy but binary positions in momentum space can be used to build "valleytronic" devices, similar to electronic and spintronic devices. The large atomic weight of the transition metal in TMDs also produces strong spin-orbit coupling that splits the valence and conduction bands into two bands each. The excitons formed by holes in each of the valence bands are clearly observed in the linear absorption spectrum (figure 8.1b) [225, 226]. The lower- and higher-energy excitons are commonly referred to as $A$ and $B$, respectively.

The spin-orbit coupling also couples the spin and valley states and allows a single spin or valley to be accessed via circularly polarized light due to stringent optical selection rules, summarized in figure 8.1c [84]. In the $K$ valley, electrons from the higher (lower) energy valence band with positive $|\uparrow\rangle$ (negative $|\downarrow\rangle$) spin are selectively excited by right-handed $\sigma^+$ (left-handed $\sigma^-$) circular polarized light into the conduction band; while in the $-K$ valley,

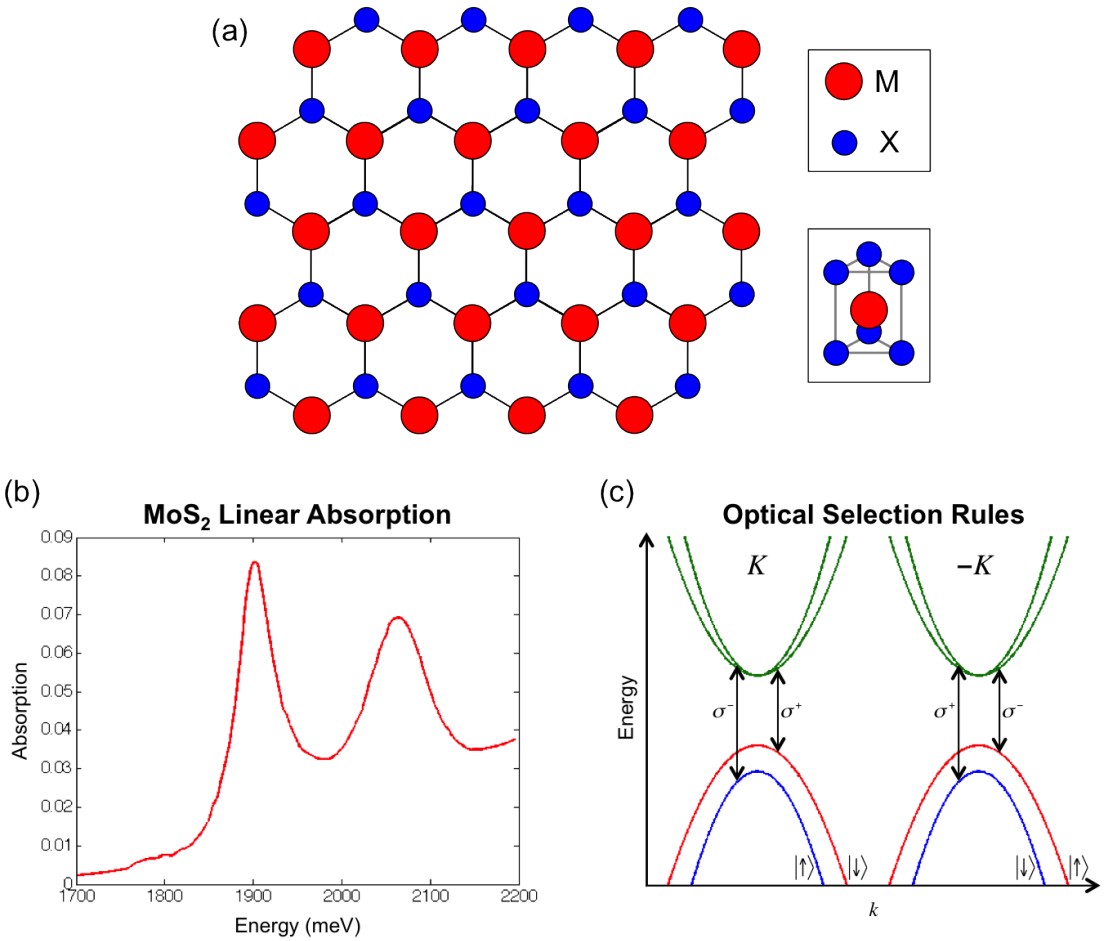


Figure 8.1: Monolayer transition metal dichalcogenides. (a) Hexagonal lattice structure, with one layer of transition metals (M: red) sandwiched between two layer of chalcogen atoms (X: blue). (b) Linear absorption spectrum of monolayer $MoS_2$, where the $A$ and $B$ exciton states absorb at 1.90 eV and 2.06 eV, respectively [98]. (d) Optical selection rules. Positive $|\uparrow\rangle$ and negative $|\downarrow\rangle$ spin electrons in the $K$ and $-K$ valleys are selectively excited from the upper (red) and lower (blue) valences bands into the conduction bands (green) by either right-handed $\sigma^+$ or left-handed $\sigma^-$ circularly polarized light.

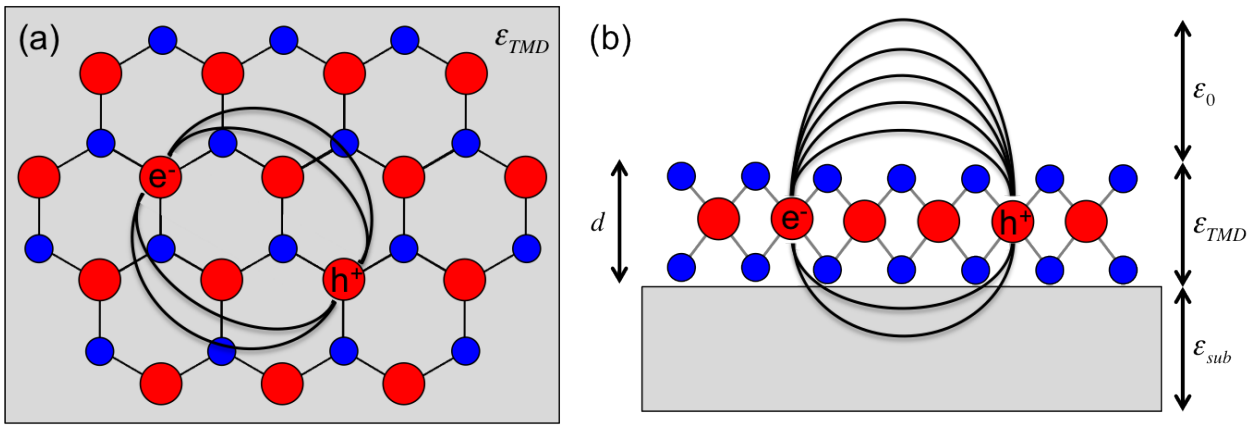


Figure 8.2: Coulombic interactions in two-dimensional materials. (a) In-plane Coulombic interactions are determined by the in-plane bulk dielectric constant $\varepsilon_{TMD}$, which is large and decreases electron ($e^-$) and hole ($h^+$) interactions as indicated by the curved electric field lines. (b) Out-of-plane Coulombic interactions are determined by the dielectric constants of the substrate $\varepsilon_{sub}$ and vacuum $\varepsilon_0$ and the thickness of the TMD monolayer $d$.

electrons from the higher (lower) energy valence band with negative $|\downarrow\rangle$ (positive $|\uparrow\rangle$) spin are selectively excited by left-handed $\sigma^-$ (right-handed $\sigma^+$) circular polarized light into the conduction band. Numerous experimental measurements have demonstrated the generation of robust valley polarizations of over 50% by circular dichroism lasting longer than 1 ns [227, 228, 229].

### 8.1.2 Enhancement of Coulombic Interactions

Monolayer TMDs are also of significant interest because of their unprecedented Coulombic interactions for inorganic semiconductors. Coulombic interactions in the plane of a monolayer are analogous to the in-plane interaction of the bulk due to their large dielectric constants. However, charged particles can also interact out of the plane and the interaction strength is dependent on the dielectric constants of the substrate and vacuum. This out-of-plane Coulombic interaction allows for much stronger charged particle correlations when the surrounding dielectric constants are small and screening of electrons and holes decreases, as depicted in figure 8.2. The dielectric constant of our sapphire substrates $\varepsilon_{sub} = 3.2$ reduces the interaction of charged particles through the substrate, but the small vacuum dielectric

**Dielectric Constants and Multi-Particle Interactions**

| Materials | $\varepsilon$ | $\Delta E_X$ (meV) | $\Delta E_{X^-}$ (meV) | $\Delta E_{XX}$ (meV) |
|---|---|---|---|---|
| $MoS_2$ WL | 11.6 [86] | 850 [230] | 20 [98] | 70 [231] |
| $WS_2$ ML | 13.0 [86] | 710 [232] | 30 [233] | 65 [234] |
| GaAs QW | 12.3 [235] | 9 [236] | 1 [237] | 1 [61] |

Table 8.1: Dielectric constants and multi-particle interactions in monolayer transition metal dichalcogenides. Monolayer (ML) $MoS_2$ and $WS_2$ and GaAs quantum well (QW) dielectric constants $\varepsilon$, exciton $\Delta E_X$, trion $\Delta E_{X^-}$, and biexciton $\Delta E_{XX}$ binding energies.

constant $\varepsilon_0 = 1$ allows strong charged particle interactions above the plane of the monolayer. The dielectric constants of monolayer $MoS_2$ and $WS_2$ and GaAs quantum wells are summarized in table 8.1 along with their exciton $\Delta E_X$, trion $\Delta E_{X^-}$, and biexciton $\Delta E_{XX}$ binding energies. The binding energies of all the multi-particle correlations in monolayer TMDs are more than an order of magnitude larger than those in quasi-two-dimensional quantum wells, demonstrating significantly stronger Coulombic interactions in the atomic limit.

The Hamiltonian of charged particles in a two-dimensional material on a substrate can easily written down.

$$\hat{H} = -\frac{1}{2\mu}\nabla_r^2 - \hat{V}_{2D}\left(\overrightarrow{r}\right) \tag{8.1}$$

where $\mu^{-1} = m_e^{-1} + m_h^{-1}$ is the reduced mass of the exciton and $m_e$ and $m_h$ are the masses of an electron and hole, respectively. The Coulomb potential $\hat{V}_{2D}$ is characterized by the dielectric constants of the monolayer $\varepsilon_{TMD}$, substrate $\varepsilon_{sub}$, and vacuum $\varepsilon_0$ and takes the form:

$$\hat{V}_{2D}\left(\overrightarrow{r}\right) = \frac{\pi e^2}{\left(\varepsilon_{sub} + \varepsilon_0\right) r_0}\left[\frac{\overrightarrow{r}}{r_0}\left(H_0 - Y_0\right)\right] \tag{8.2}$$

$$r_0 = \frac{\varepsilon_{TMD} d}{\varepsilon_{sub} + \varepsilon_0} \tag{8.3}$$

where $e$ is the charge of an electron, $r_0$ is the screening length that is dependent on $d$ the thickness of the TMD monolayer (6.5 Å in $MoS_2$), and $H_0$ and $Y_0$ are the Struve function and the Bessel function of the second kind, respectively [238]. At long range, the Coulombic interaction behaves like a screened potential $1/r$; while at short range, the Coulombic

interaction has a weaker logarithmic divergence and allows for stronger charged-particle correlations. The transition between short and long range interactions is determined by the screening length $r_0$.

For photovoltaic devices, strong electron-hole interactions are unfavorable because excitons must be dissociated, usually at an interface, in order to extract charge and generate a current. Thus, the large binding energies of excitons in monolayer TMDs make them less suited for light-harvesting devices. However, the high charge-carrier mobilities in monolayer TMDs are highly favorable and allow for fabrication of larger devices, the size of which can increase their quantum efficiency [239].

## 8.2 Monolayer Transition Metal Dichalcogenide Characterization

Prior to performing two-dimensional (2D) spectroscopy experiments to investigate exciton-phonon and exciton-exciton interactions in monolayer TMDs, we characterized our samples using microscopy and reflection measurements. First, we took microscope images of our CVD-grown monolayer $WS_2$ sample on sapphire, shown in figure 8.3a. From the image, we can clearly distinguish the characteristic triangular single domains (light green) approximately 20 μm across with a nucleation site (white) in the center. In this sample, many domains have grown together, forming a monolayer film covering the majority of the the substrate (dark green). Second, we used a microscope to measure the reflectance of white light off single domains of monolayer $WS_2$ at 10 K. Using the Kramers-Kronig relations, we calculated the linear absorption spectrum from the reflectance [240, 241]. Figure 8.3b shows a representative linear absorption spectrum of a single domain. In this spectrum, the absorption is centered at 2.07 eV with a full width at half maximum (FWHM) of approximately 0.04 eV. However, the central energy of the linear absorption changed significantly from domain to domain with greater than 0.02 eV variation, more than half the FWHM. The

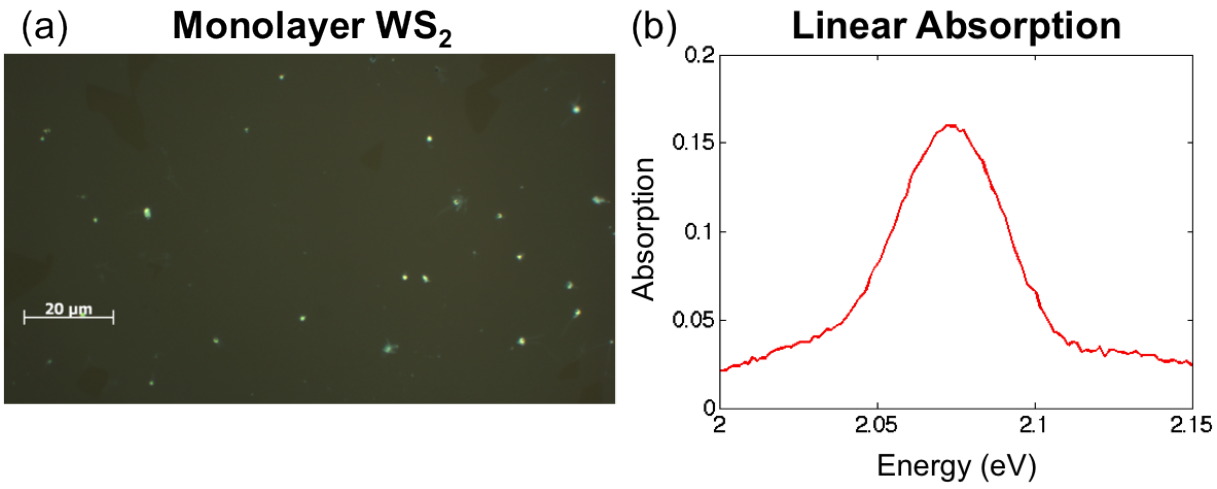


Figure 8.3: Monolayer transition metal dichalcogenide characterization. (a) Microscopic image of CVD-grown monolayer $WS_2$ on sapphire with 100x magnification at 295 K. Light green regions indicate monolayer $WS_2$, dark green regions the substrate, and white regions nucleation sites for single domains. (b) Representative linear absorption spectrum of a single domain of monolayer $WS_2$ at 10 K. The central energy of the absorption changes more than 0.02 eV in different domains, while the 0.04 eV full width at half maximum and lineshape remains relatively constant.

FHWM was relatively constant from domain to domain. The lineshape was also relatively constant, but some domains exhibited small shoulders that were redshifted 0.04 eV from the main peak, which could be due to trion or biexciton formation [233, 234].

## 8.3 Exciton-Phonon Interactions in Monolayer Transition Metal Dichalcogenides

The interaction of excitons and phonons is strongly dependent on the structure and dimensionality of the material. As the width of a material decreases and approaches the 2D limit, exciton-phonon coupling is predicted to significantly increase [242, 243]. Experiments using Raman spectroscopy to study the phonon modes in graphene, the most widely studied 2D material, have shown strong and layer-dependent electron-phonon interactions at and near the atomic limit [244, 245]. Thus, investigation of exciton-phonon coupling in mono-

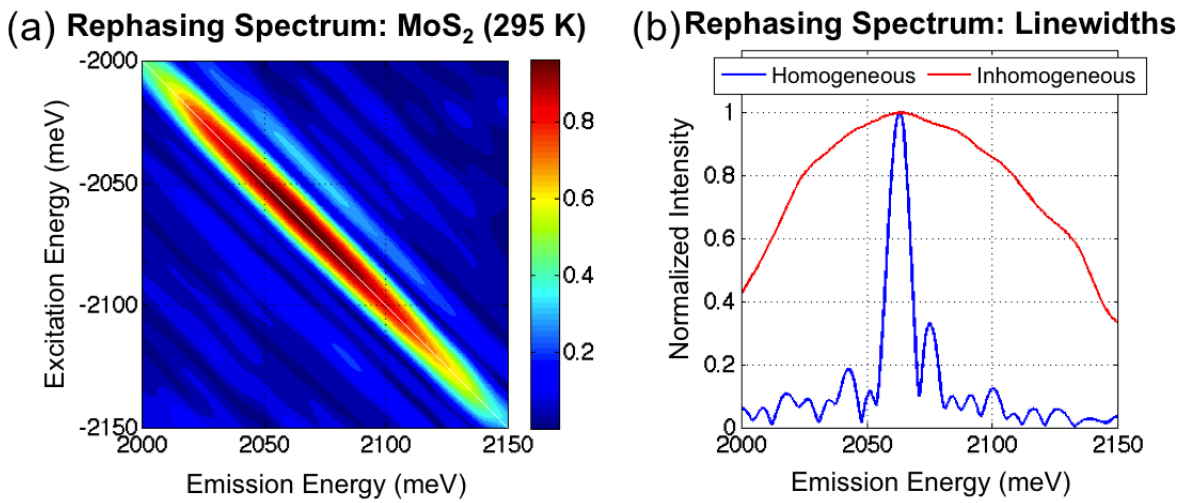


Figure 8.4: Two-dimensional rephasing spectrum of monolayer $MoS_2$ at 295 K. (a) 2D rephasing spectrum of monolayer $MoS_2$ at 295 K. (b) Diagonal and anti-diagonal line cuts of the 2D rephasing spectrum reveal inhomogeneous and homogeneous linewidths of 130 and 10 meV, respectively.

layer TMDs is important to understand the interactions and dynamics of their elementary excitations.

### 8.3.1 Large Inhomogeneous Broadening in Chemical Vapor Deposition-Grown Monolayer Transition Metal Dichalcogenides

To study the interactions of excitons and phonons, we first used 2D rephasing spectroscopy to measure the homogeneous and inhomogeneous linewidths of the B exciton in monolayer $MoS_2$ at 295 K. Figure 8.4a clearly shows substantial inhomogeneous broadening in the rephasing spectrum. The homogeneous (i.e. anti-diagonal) and inhomogeneous (i.e. diagonal) lineshapes, plotted in figure 8.4b, are 10 and 130 meV, respectively. Substantial inhomogeneous broadening demonstrates that static disorder dominates the absorption linewidths of the monolayer. Static disorder generally occurs due to structural defects within a single domain (e.g. vacancies and interstitials) and variations from domain to domain (i.e. multiple domain illumination in the 30 μm focus spot size) [246]. Dynamic disorder generally occurs due to exciton-phonon and exciton-exciton interactions and population recombination,

which determines the homogeneous linewidth. Even at 295 K and large phonon population, the static rather than dynamic disorder is the major contributor to exciton dephasing. 2D rephasing measurements by Moody and co-workers also demonstrate significant inhomogeneous broadening in single domain monolayer $WSe_2$ at cryogenic temperatures [57]. Temperature-dependent experiments revealed exciton-phonon interactions due to acoustic phonon scattering were enhanced by a factor of 5 to 10 compared to quasi-2D GaAs quantum wells.

CVD-grown TMD monolayers generally exhibit more static disorder than exfoliated monolayers. Thus, exfoliated TMDs may reveal substantially less inhomogeneous broadening and significantly different 2D rephasing spectra. Large densities of structural defects can significantly hinder the electrical properties, such as charge transport. However, structural defects also increase the exciton radiative lifetime in monolayer TMDs due to exciton localization, which is beneficial for device fabrication [247].

### 8.3.2 Exciton Coupling to In-Plane Optical and Acoustic Phonon Modes

Second, we used 2D correlation spectroscopy to measure the primary phonons contributing to the dephasing of A excitons in monolayer $WS_2$ at 10 K. Figure 8.5a shows clear structure in the correlation spectrum along both the absorption and emission axes. Fitting the excitation energy-integrated projection of the correlation spectrum onto the emission axis reveals a progression of peaks equally separated by 22 meV with a FWHM of 26 meV, shown in figure 8.5b. Thripuranthaka M and Late conducted temperature-dependent Raman experiments and assigned their 22 meV peak to an optical/acoustic phonon combination band $E^1_{2g} - LA\,(M)$, where $E^1_{2g}$ is an in-plane optical phonon mode at the Γ-point and $LA\,(M)$ is an in-plane longitudinal acoustic phonon mode at the M-point [220]. The phonon progression observed in the correlation spectrum is not observed in the linear absorption spectrum. So it is unclear why the phonon progression is observed in the 2D spectrum, but it is clear

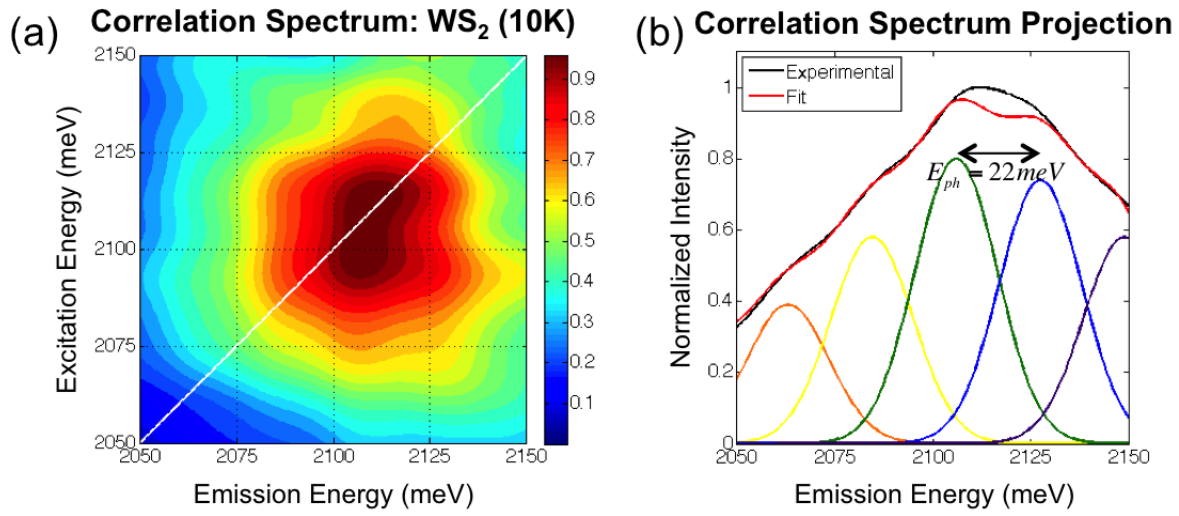


Figure 8.5: Two-dimensional correlation spectrum of monolayer $WS_2$ at 10 K. (a) Correlation spectrum of monolayer $WS_2$ at 10 K. (b) Excitation energy-integrated projection of the correlation spectrum amplitude onto the emission axis reveals a phonon progression of the 22 meV combination band $E^1_{2g} - LA\,(M)$.

the $E^1_{2g} - LA\,(M)$ combination phonon band is playing an important role in the optical response of excitons in monolayer $WS_2$ at 10 K. Temperature-dependent and population time-dependent measurements can further interrogate the role of phonons in modulating the excitonic properties of monolayer TMDs.

## 8.4 Exciton-Exciton Interactions in Monolayer Transition Metal Dichalcogenides

### 8.4.1 Biexciton Binding Energy via One-Quantum Measurements

From the absorptive (i.e. imaginary) component of the 2D correlation spectrum of A excitons in monolayer $WS_2$ at 10 K, we can determine the biexciton binding energy by the separation of the stimulated emission and excited state absorption peaks. Figure 8.6a illustrates the stimulated emission and excited state absorption Feynman diagrams. The stimulated emission pathway radiates from an exciton-ground state coherence $|e\rangle\langle g|$ with the exciton

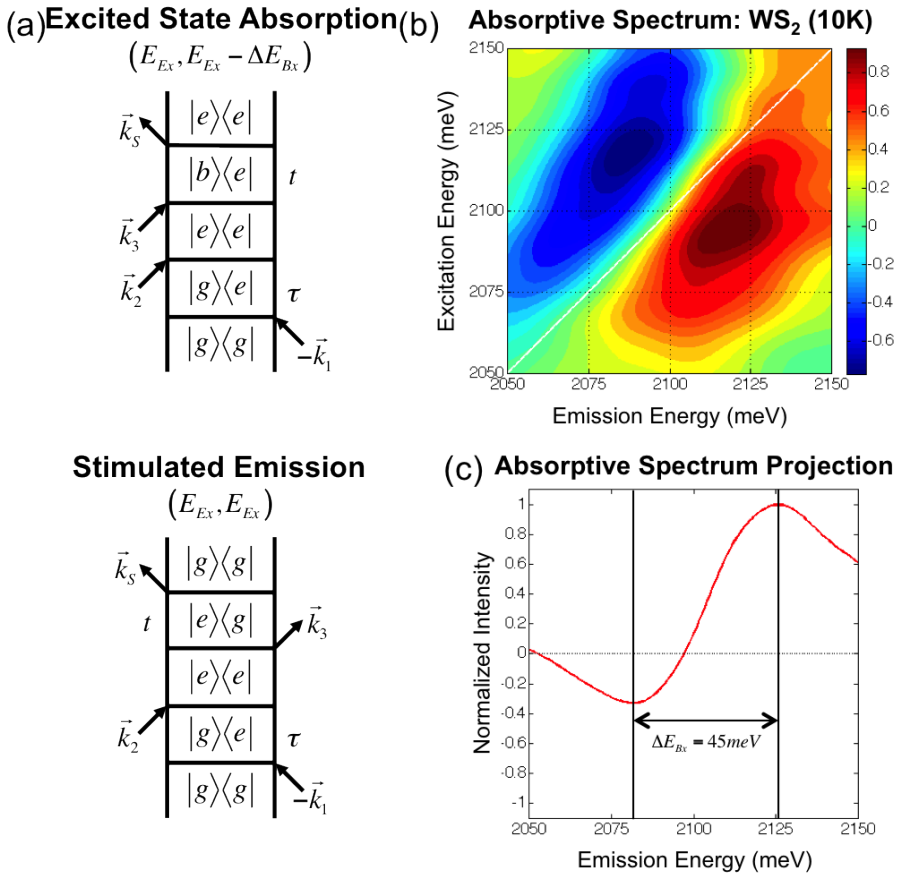


Figure 8.6: Two-dimensional absorptive spectrum of monolayer $WS_2$ at 10 K. (a) Feynman diagrams for stimulated emission and excited state absorption pathways emitting at $E_{Ex}$ and $E_{Ex} - \Delta E_{Bx}$, respectively. (b) 2D absorptive spectrum of monolayer $WS_2$ at 10 K with stimulated emission (positive) and excited state absorption (negative) peaks. (c) Excitation energy-integrated projection of the 2D absorptive spectrum amplitude onto the emission axis reveals a 45 $\pm$ 3 meV biexciton binding energy by the difference of the stimulated emission and excited state absorption peak emission energies.

energy $E_{Ex}$, while the excited state absorption pathway radiates from a biexciton-exciton coherence $|b\rangle\langle e|$ with energy $E_{Bx}-E_{Ex}=E_{Ex}-\Delta E_{Bx}$, where $\Delta E_{Bx}$ is the biexciton binding energy. Thus, the difference in emission energy between the stimulated emission and excited state absorption peaks is a measure of the biexciton binding energy. Figure 8.6b shows the 2D absorptive spectrum with the stimulated emission (negative) and excited state absorption (positive) peaks. The excitation energy-integrated projection of the 2D absorptive spectrum onto the emission axis, plotted in figure 8.6c, reveals the characteristic absorptive lineshape and a biexciton binding energy of 45 ± 3 meV, equivalent to a thermal energy of $\Delta E_{Bx}/k_B = 520K$.

### 8.4.2 Biexciton Dephasing Time via Two-Quantum Measurements

We also used two-quantum (2Q) spectroscopy to directly measure biexciton coherences and determine the AA biexciton binding energy and dephasing time in monolayer $WS_2$ at 10 K. The deviation of the 2Q signal from the $y = 2x$ line directly reveals the biexciton binding energy ($\Delta E_{Bx} = 2E_{Ex} - E_{Bx}$) without interference from single-exciton signals. Figure 8.7 shows the 2Q spectrum and reveals a biexciton binding energy of 38 ± 8 meV, equivalent to a thermal energy of $\Delta E_{Bx}/k_B = 460K$. The linewidth of the 2Q signal also reveals a biexciton dephasing time faster than 100 fs. The low 2Q energy peak is a small contribution from the single-exciton signal in the 2Q spectrum.

The biexciton binding energies measured in the one-quantum absorptive and 2Q spectra are in good agreement and are more than an order of magnitude greater than the biexciton binding energies in GaAs quantum wells [61]. Power-dependent experiments by Moody and co-workers also revealed that exciton-exciton coupling in monolayer $WSe_2$ is enhanced by an order of magnitude or more compared to GaAs quantum wells [57]. Our measurements of unprecedentedly large biexciton binding energies are also in good agreement with other one-quantum measurements in monolayer TMDs [231, 234, 248]. Large biexciton binding energies make them relevant at room temperature and may allow them to significantly affect

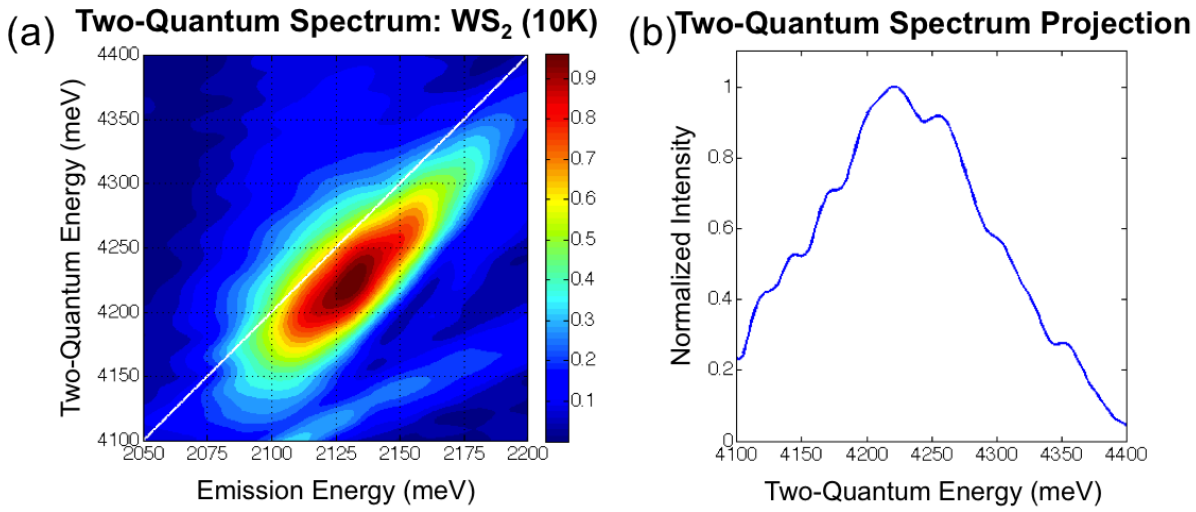


Figure 8.7: Two-dimensional two-quantum spectrum of monolayer $WS_2$ at 10 K. (a) Two-quantum spectrum of monolayer $WS_2$ at 10 K. (b) Emission energy-integrated projection of the two-quantum spectrum amplitude onto the two-quantum axis reveals a biexciton dephasing rate faster than 100 fs.

the quantum efficiency of monolayer TMD-based devices.

## 8.5 Conclusions

From our preliminary experiments on monolayer TMDs, we were able to measure large inhomogeneous broadening in a CVD-grown monolayer TMD at 295 K, revealing that static disorder dominates the linear absorption spectrum and is the main contributor to exciton dephasing even at room temperature. 2D correlation spectroscopy also demonstrated strong contributions from the in-plane $E^1_{2g}$ optical and $LA\,(M)$ acoustic phonon modes leading to modulation of the 2D spectrum. The absorptive component of the correlation spectrum and the two-quantum spectrum revealed an AA biexciton binding energy in monolayer $WS_2$ of 40-45 meV, orders of magnitude greater than quasi-two-dimensional GaAs quantum wells, and a biexciton dephasing time faster than 100 fs.

There are many more experiments planned for monolayer TMDs. First, we plan to measure the homogeneous and inhomogeneous linewidths of exfoliated TMD monolayers and

investigate the contribution of static disorder to the linear absorption spectrum compared to CVD-grown monolayers. Second, we plan to use 2D correlation spectroscopy to elucidate the mechanisms of the exciton-phonon interaction by measuring temperature-dependent and population time-dependent 2D spectra. Third, we plan to use higher-order spectroscopies to measure 3-, 4-, ..., n-exciton interactions and determine the full extent of the multi-particle interactions, their binding energies, and coherence times. Finally, bilayers of different TMDs can also be synthesized to form heterostructures. We plan to investigate the extent of exciton-exciton interactions in these heterostructures and determine if interlayer biexcitons or higher-order correlations exist.

# Chapter 9

# Conclusions and Outlook

In this thesis, we discussed ultrafast spectroscopic experiments exploring the exciton dynamics and exciton-exciton and exciton-phonon interactions in organic and inorganic, nanostructured semiconductors. In chapter 5, we measured the weak coupling of excitons on the inner and outer walls of isolated and bundled double-walled J-aggregate nanotubes in solution. We determined exciton dephasing in solution-based nanotubes at room temperature is dominated by dynamic disorder, while glass nanotubes at cryogenic temperature is dominated by static disorder. We also observed photo-induced degradation and recovery in glass nanotubes at cryogenic temperature and the lowest possible excitation fluence, the mechanism for which is still being studied by our collaborators in the Bawendi group at MIT. In chapter 6, we utilized quantum process tomography to unambiguously characterize the secular processes of population decay and transfer and coherence decay, unequivocally determine the weak coupling of inner and outer wall excitons, and demonstrate the absence of non-secular processes in isolated J-aggregate nanotubes. In chapter 7, we made the first direct experimental measurement of biexcitons in cuprous oxide and provided evidence to support a biexciton-Auger mechanism that effectively suppresses Bose-Einstein condensation of excitons. In chapter 8, we discussed preliminary experiments exploring the strength of exciton-phonon and exciton-exciton interactions in monolayer transition metal dichalcogenides.

We plan to continue experiments exploring the exciton dynamics in monolayer transition metal dichalcogenides. First, we plan to measure the homogeneous and inhomogeneous linewidths of exfoliated monolayers and investigate the contribution of static disorder to the linear absorption spectrum as compared to chemical vapor deposition-grown monolayers. Second, we plan to elucidate the mechanisms of exciton-phonon interaction by measuring temperature-dependent and population time-dependent two-dimensional correlation spectra. Third, we plan to determine the full extent of multi-exciton correlations, their binding energies, and their coherence times using higher-order, multi-quantum spectroscopy. Finally, bilayers of different transition metal dichalcogenides can be synthesized to form unique heterostructures. We plan to investigate the extent of exciton-exciton interactions in these heterostructures and determine if interlayer multi-exciton correlations exist.

Another class of exciting nanoscale semiconductors is organic-inorganic hybrid materials such as quantum dot-J-aggregate systems [249, 250, 251]. Using sensitizing media to enhance optical and electronic properties is a common technique for improving the efficiency of devices. The improvement in efficiency is generally determined by the electronic coupling between the media. We plan to use two-dimensional spectroscopy to explore the coupling of excitons in quantum dot-J-aggregate hybrid systems.

The emergence of relatively high efficiency perovskite solar cells, such as methyl ammonium lead halides, have renewed interest in these semiconducting materials [252, 253]. The synthesis of new lead halide perovskite nanoplatelets has also garnered attention due to their tunability via quantum confinement [254, 255]. We plan to use multi-quantum spectroscopies to investigate the extent of multi-exciton correlations in this new class of nanoscale materials.

Exciton transport is also an important process in determining the efficiency of optical and electronic devices. More specifically, excitons in a photovoltaic device must diffuse to an interface in order to dissociate into electrons and holes and generate a current. If excitons cannot diffuse to an interface within their lifetime, charge separation does not efficiently

occur and a substantial current cannot be generated. Excitons generally do not diffuse more than a micron within their lifetime, thus exciton transport should be measured directly on the nanoscale. However, most exciton transport measurements are made indirectly on the micro-scale [256]. Currently, we are working on performing transient grating measurements of exciton transport on the nanoscale. However, these experiments are hindered by exciton-exciton annihilation even at the lowest possible excitation fluences. Thus, we are developing a new fluorescence-detected transient grating technique to further reduce the necessary excitation fluences while maintaing high spatial resolution.

The ultrafast spectroscopic experiments performed and proposed in this thesis are designed to investigate the interactions and time evolution of elementary excitations in organic and inorganic nanostructured semiconductors. Elucidating the ultrafast and nanoscale dynamics of excitons and phonons is crucial to understanding the physics of optical and electronic devices operating on these length and timescales. The results in this thesis will hopefully help guide the design of next generation optical and electronic devices utilizing nanoscale semiconductors.

# Appendix A

# Transient Grating Feynman Diagrams for Quantum Process Tomography

Appendix A enumerates all the possible transient grating Feynman diagrams for quantum process tomography of the inner and outer wall excitons of double-walled J-aggregate nanotubes. The Feynman diagrams are organized by experiment $XYZ$ ($X$, $Y$, $Z \in I$, $O$), where the initial state $|X\rangle\langle Y|$ is selectively excited and the state $|Z\rangle$ is interrogated. During the delay $T$, we allow secular and non-secular processes to occur or any initial state $|X\rangle\langle Y|$ to evolve into any other final state $|X'\rangle\langle Y'|$ and determine the emission energy associated with the corresponding process matrix elements $\chi_{X'Y'XY}$ for each experiment.

## Experiment: OOO

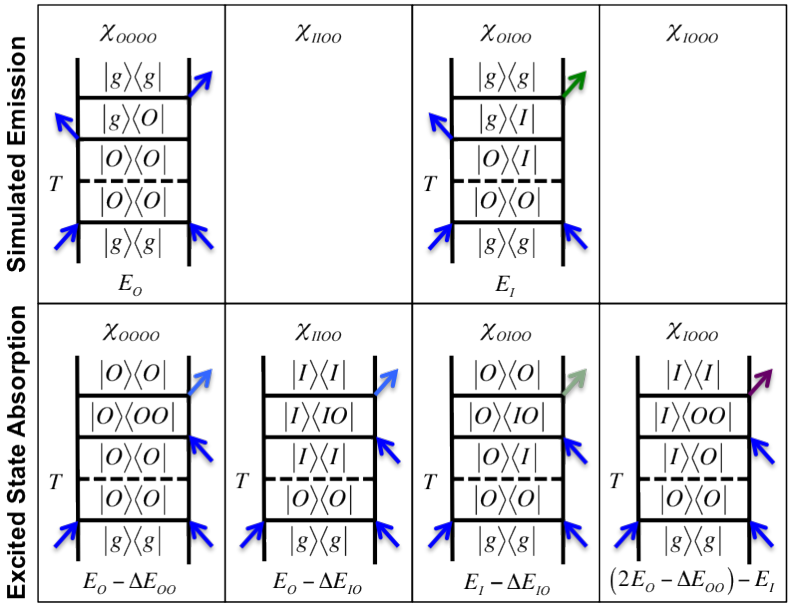


## Experiment: OOI

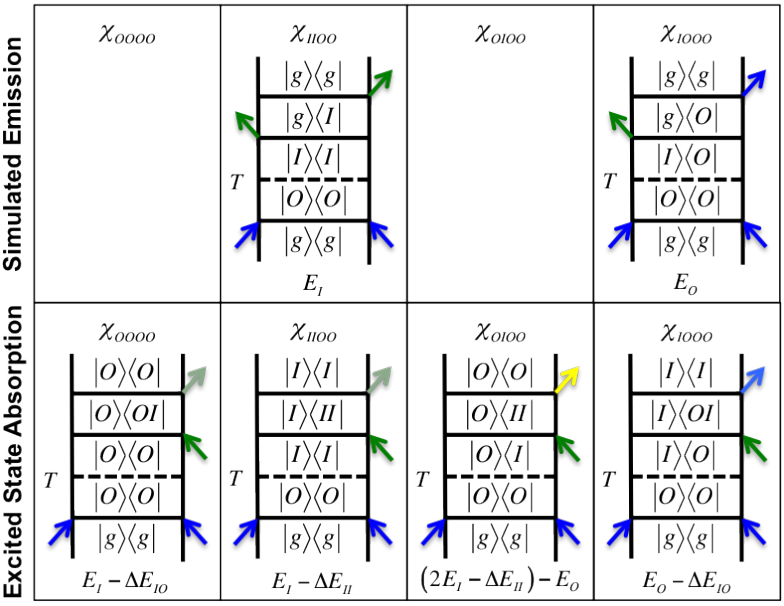

## Experiment: IIO

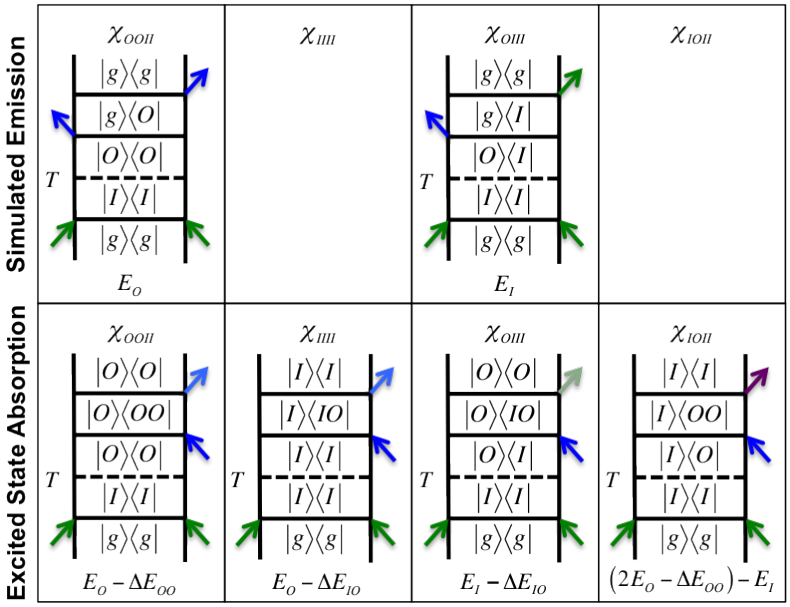


## Experiment: III

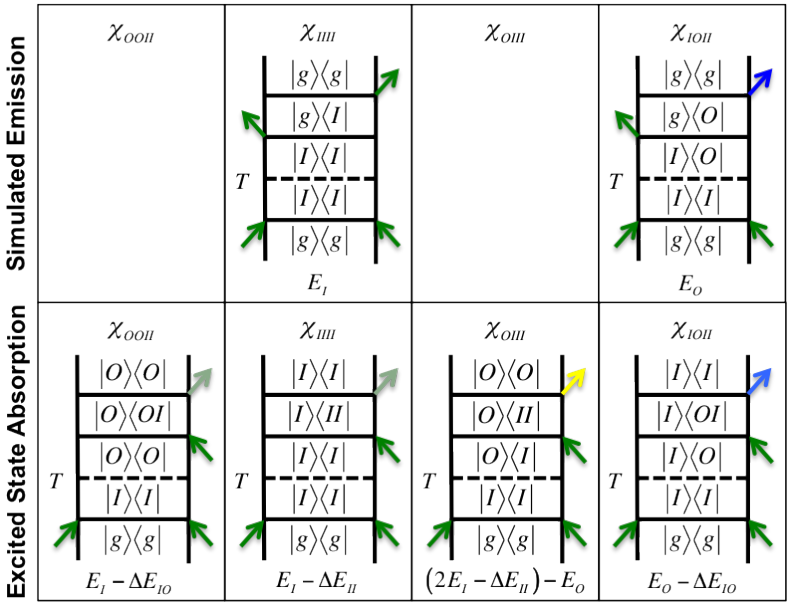

## Experiment: OIO

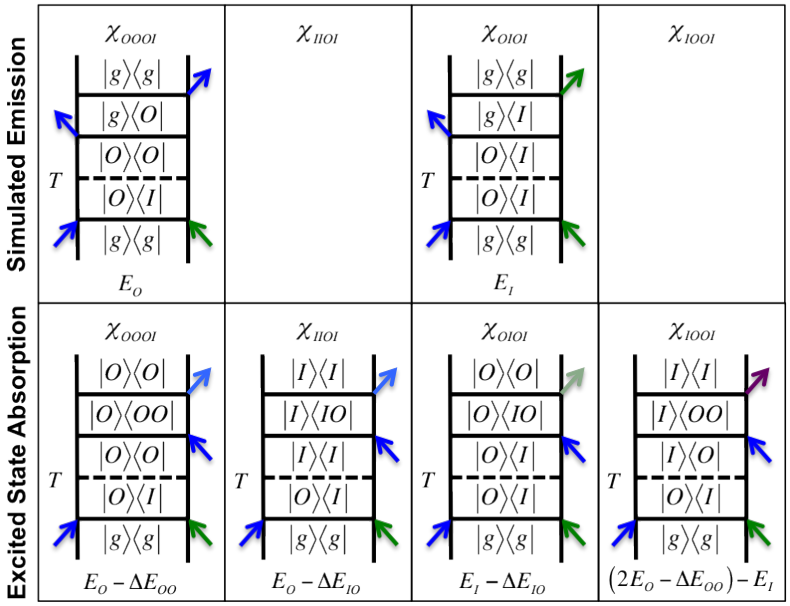


## Experiment: OII

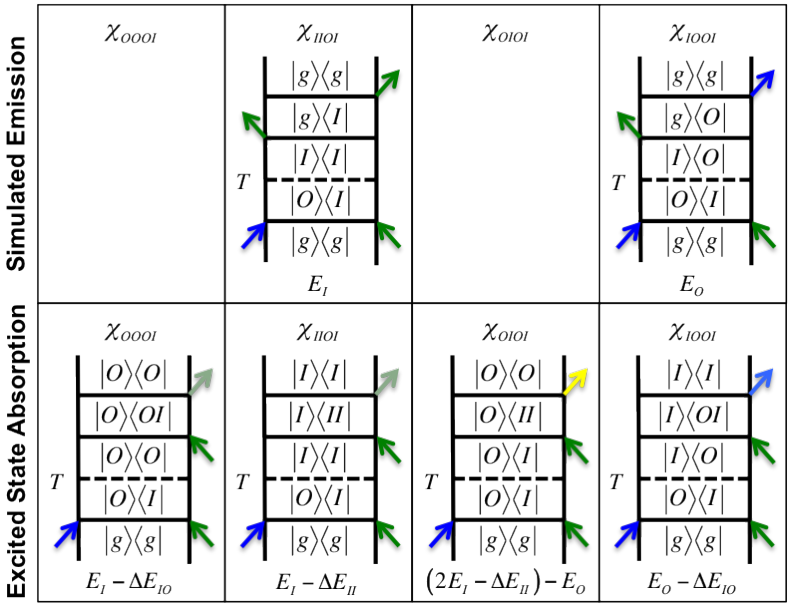

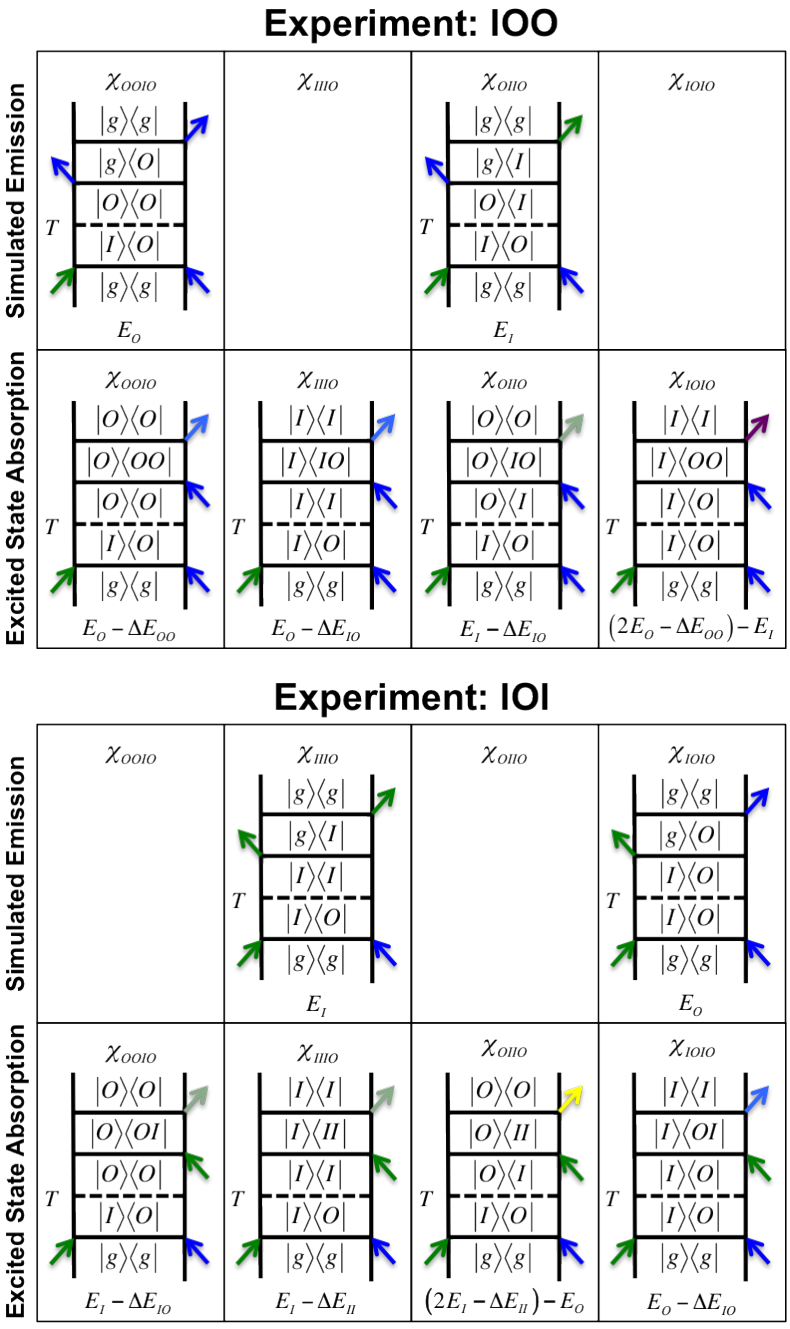


Figure A.1: Transient grating Feynman diagrams for quantum process tomography in double-walled J-aggregate nanotubes. All possible Feynman diagrams pathways including secular and non-secular processes occurring during the delay time $T$. Green and blue arrows indicate interactions with energies $E_I$ and $E_O$, respectively. Light green and light blue arrows indicate interactions with energies shifted by the biexciton binding energies $E_I - \Delta E$ and $E_O - \Delta E$, respectively. Yellow and purple arrows indicate interactions with energies $(2E_I - \Delta E_{II}) - E_O$ and $(2E_O - \Delta E_{OO}) - E_I$, respectively. $\Delta E_{xy}$ denotes the binding energy of the $|xy\rangle$ biexciton.

# Appendix B

# Two-Dimensional Rephasing Feynman Diagrams and Analysis for Cuprous Oxide

Appendix B enumerates all the possible Feynman diagrams for the two-dimensional rephasing spectrum of cuprous oxide, including transitions for pure exciton-polariton creation and destruction and phonon-assisted creation and destruction. Appendix B also includes the graphical maps of the two-dimensional rephasing signal intensity via Feynman diagram analysis.

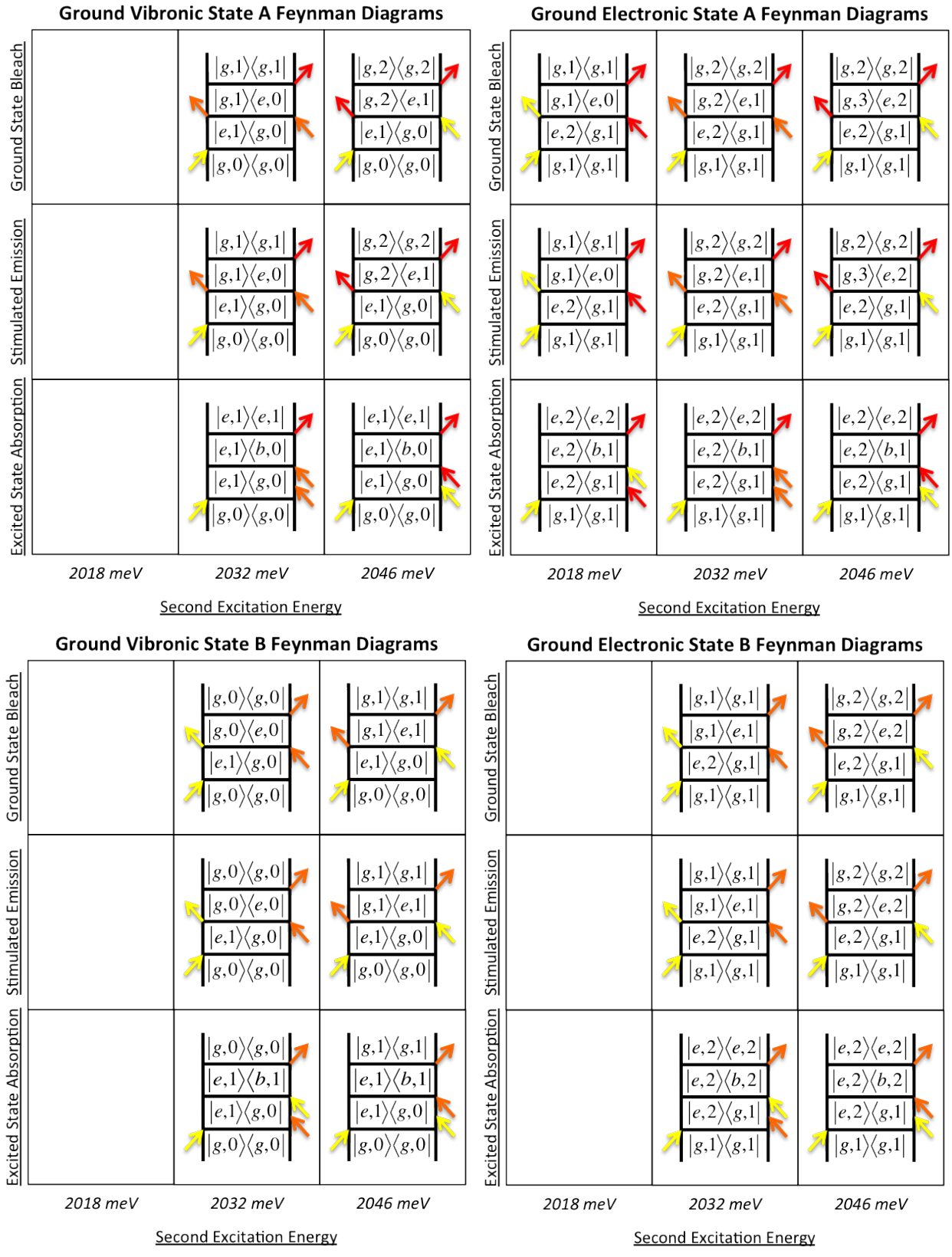
Ground Vibronic State A Feynman Diagrams
Ground Electronic State A Feynman Diagrams
Ground Vibronic State B Feynman Diagrams
Ground Electronic State B Feynman Diagrams
Ground State Bleach
Stimulated Emission
Excited State Absorption
2018 meV
2032 meV
2046 meV
Second Excitation Energy

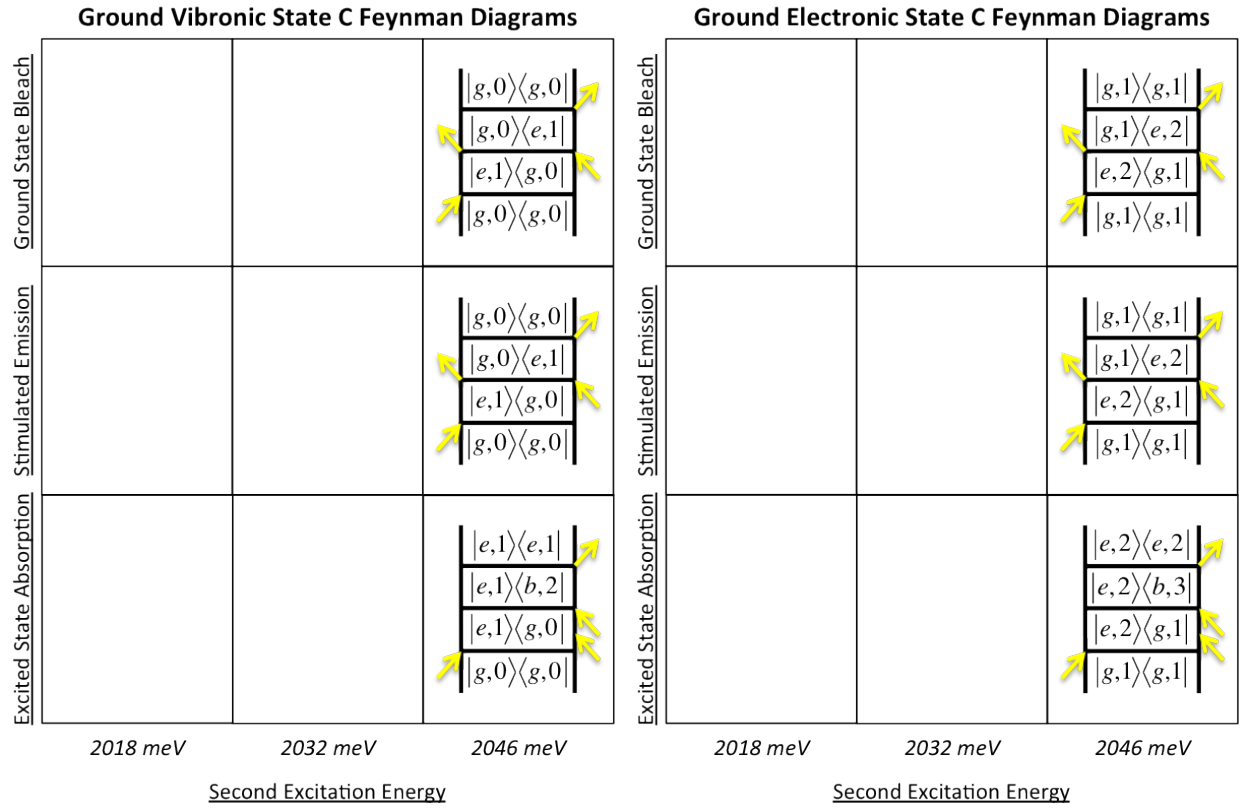
Ground Vibronic State C Feynman Diagrams
Ground Electronic State C Feynman Diagrams
Ground State Bleach
Stimulated Emission
Excited State Absorption
$|g,0\rangle\langle g,0|$
$|g,0\rangle\langle e,1|$
$|e,1\rangle\langle g,0|$
$|g,0\rangle\langle g,0|$
$|e,1\rangle\langle e,1|$
$|e,1\rangle\langle b,2|$
$|g,1\rangle\langle g,1|$
$|g,1\rangle\langle e,2|$
$|e,2\rangle\langle g,1|$
$|e,2\rangle\langle e,2|$
$|e,2\rangle\langle b,3|$
2018 meV
2032 meV
2046 meV
Second Excitation Energy

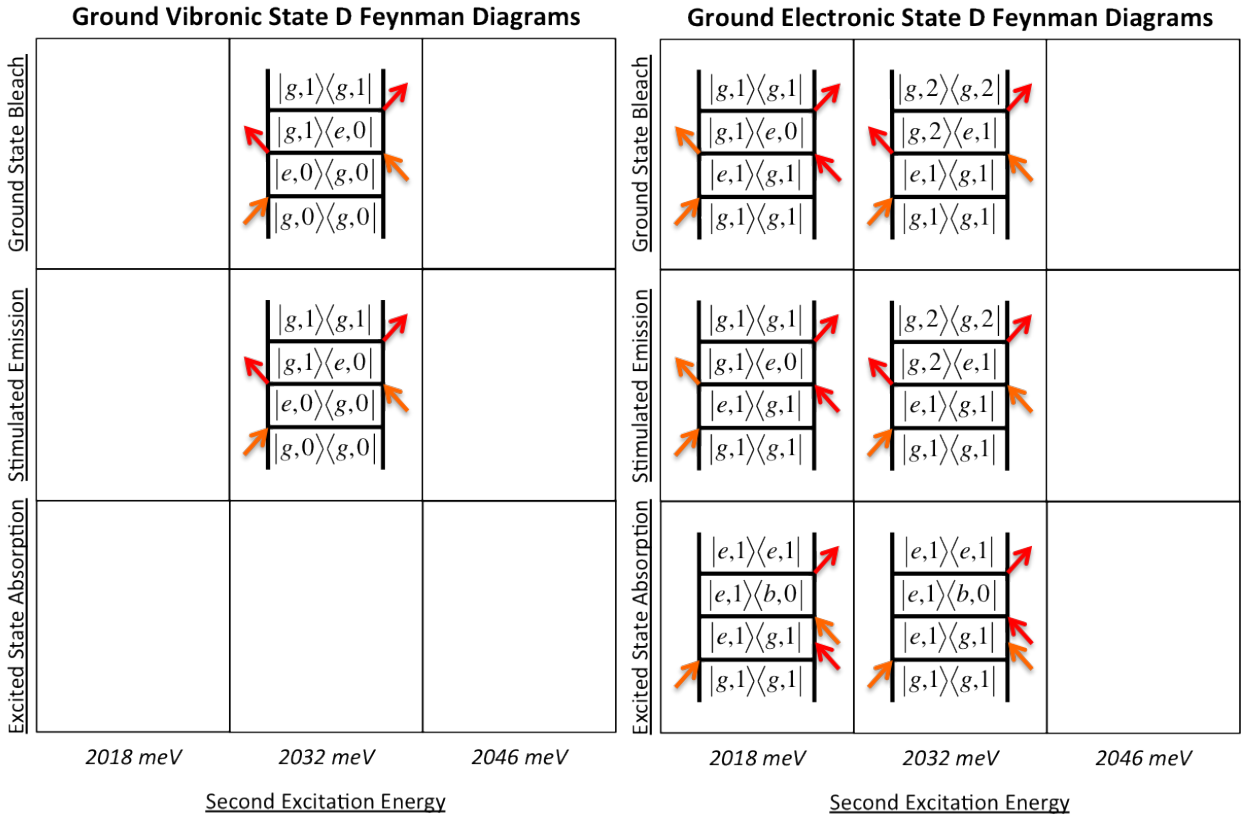
Ground Vibronic State D Feynman Diagrams
Ground Electronic State D Feynman Diagrams
Ground State Bleach
Stimulated Emission
Excited State Absorption
$|g,1\rangle\langle g,1|$
$|g,1\rangle\langle e,0|$
$|e,0\rangle\langle g,0|$
$|g,0\rangle\langle g,0|$
$|g,2\rangle\langle g,2|$
$|g,2\rangle\langle e,1|$
$|e,1\rangle\langle g,1|$
$|e,1\rangle\langle e,1|$
$|e,1\rangle\langle b,0|$
2018 meV
2032 meV
2046 meV
Second Excitation Energy

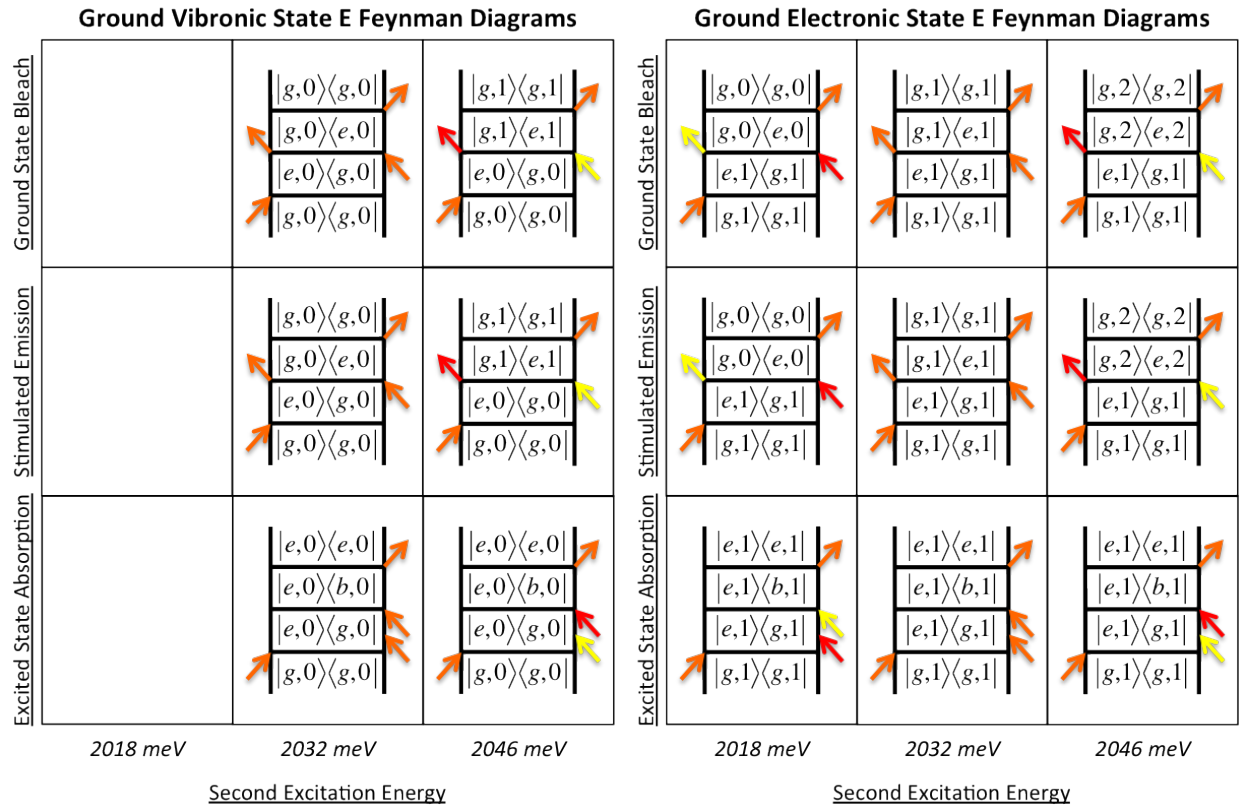
Ground Vibronic State E Feynman Diagrams
Ground State Bleach
Stimulated Emission
Excited State Absorption
2018 meV
2032 meV
2046 meV
Second Excitation Energy
Ground Electronic State E Feynman Diagrams
Ground State Bleach
Stimulated Emission
Excited State Absorption
2018 meV
2032 meV
2046 meV
Second Excitation Energy

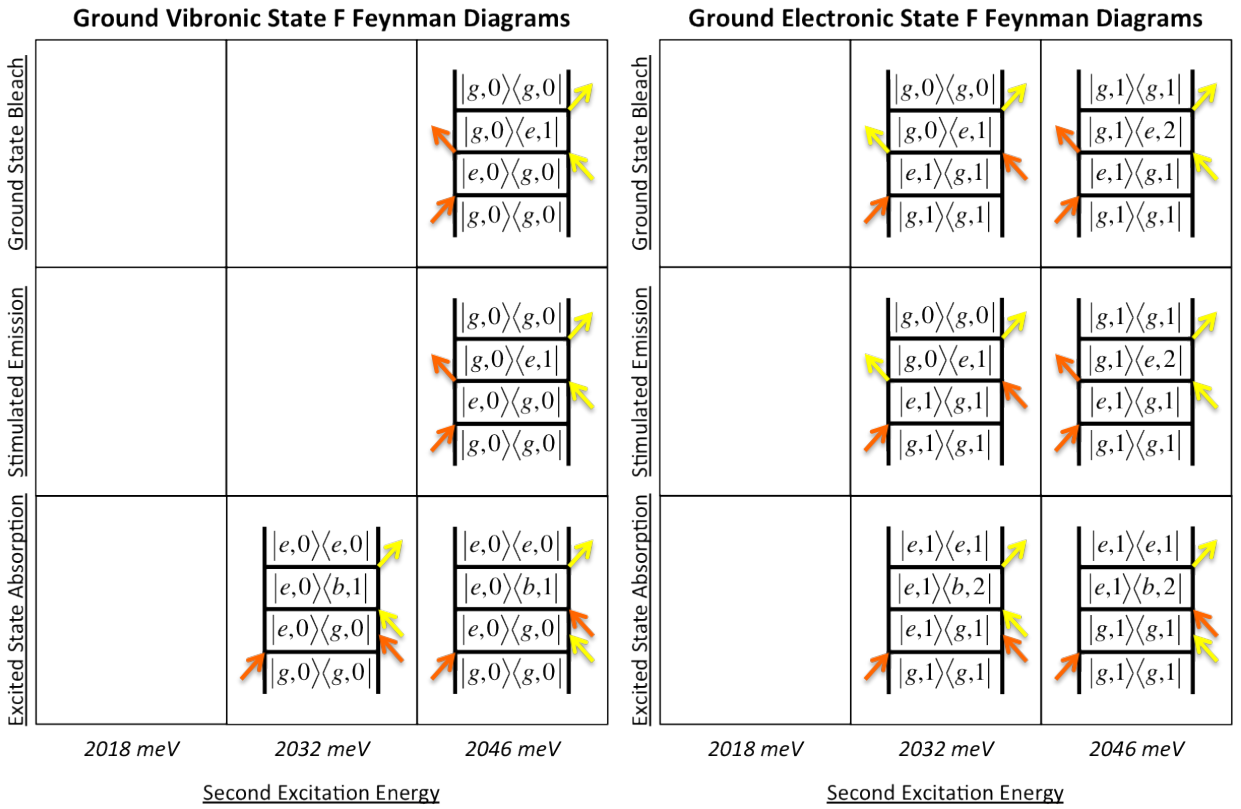
Ground Vibronic State F Feynman Diagrams
Ground State Bleach
Stimulated Emission
Excited State Absorption
2018 meV
2032 meV
2046 meV
Second Excitation Energy
Ground Electronic State F Feynman Diagrams
Ground State Bleach
Stimulated Emission
Excited State Absorption
2018 meV
2032 meV
2046 meV
Second Excitation Energy

**Ground Vibronic State G Feynman Diagrams**

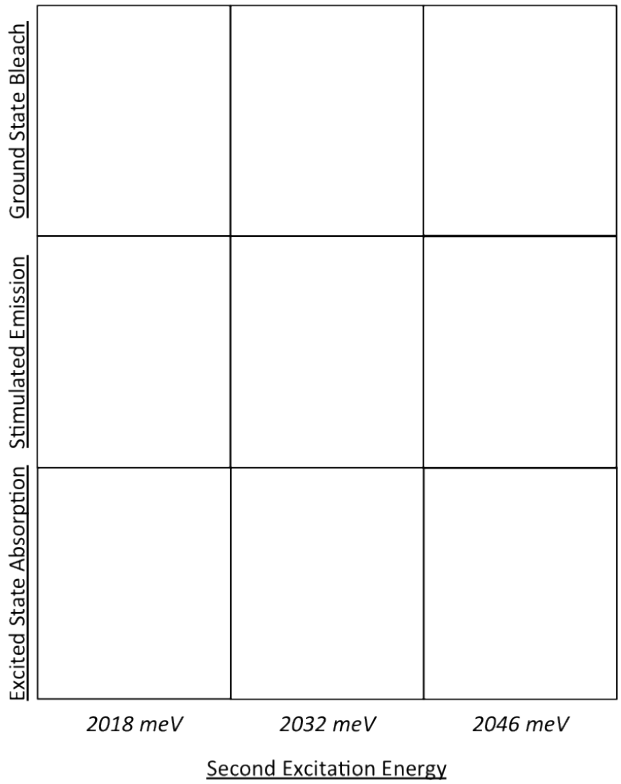


**Ground Electronic State G Feynman Diagrams**

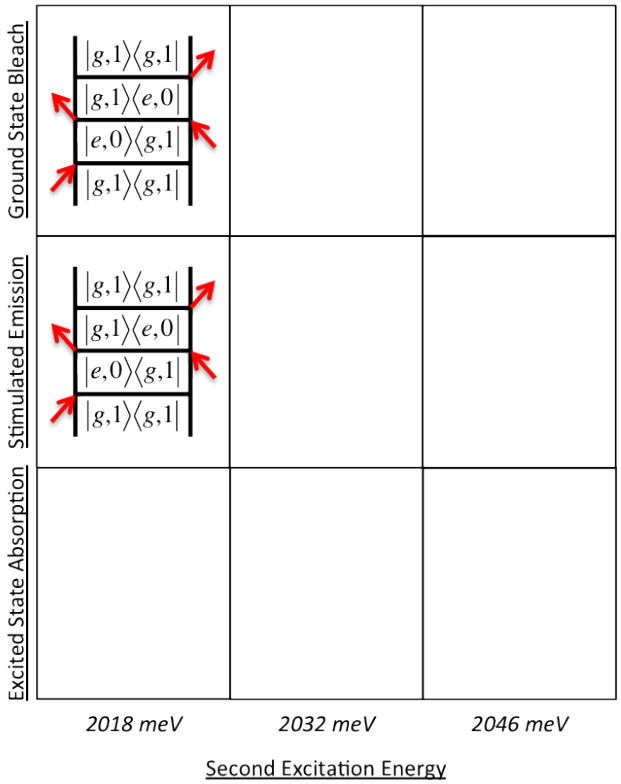


**Ground Vibronic State H Feynman Diagrams**

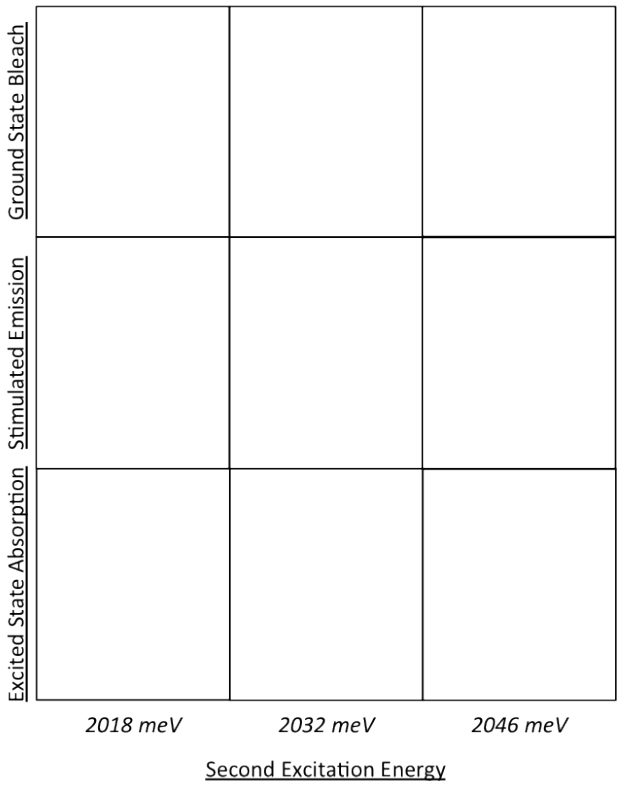


**Ground Electronic State H Feynman Diagrams**

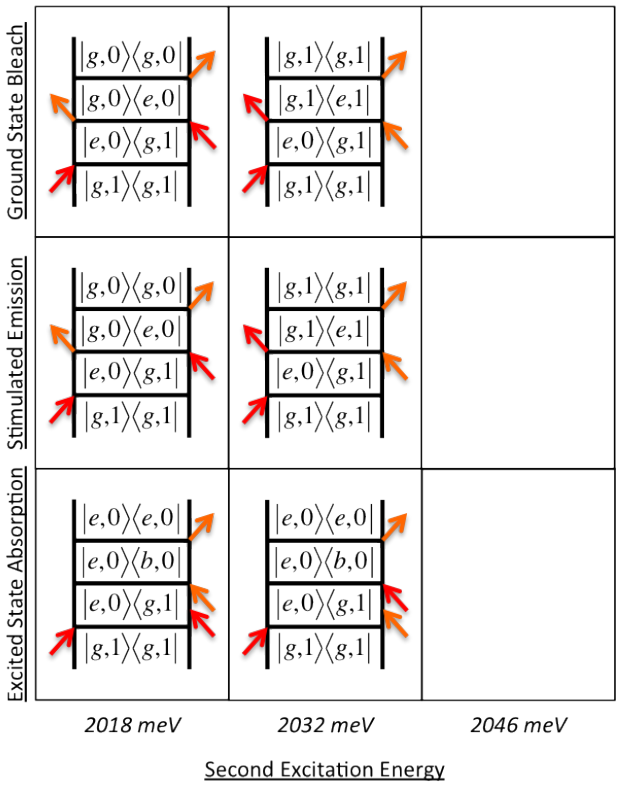

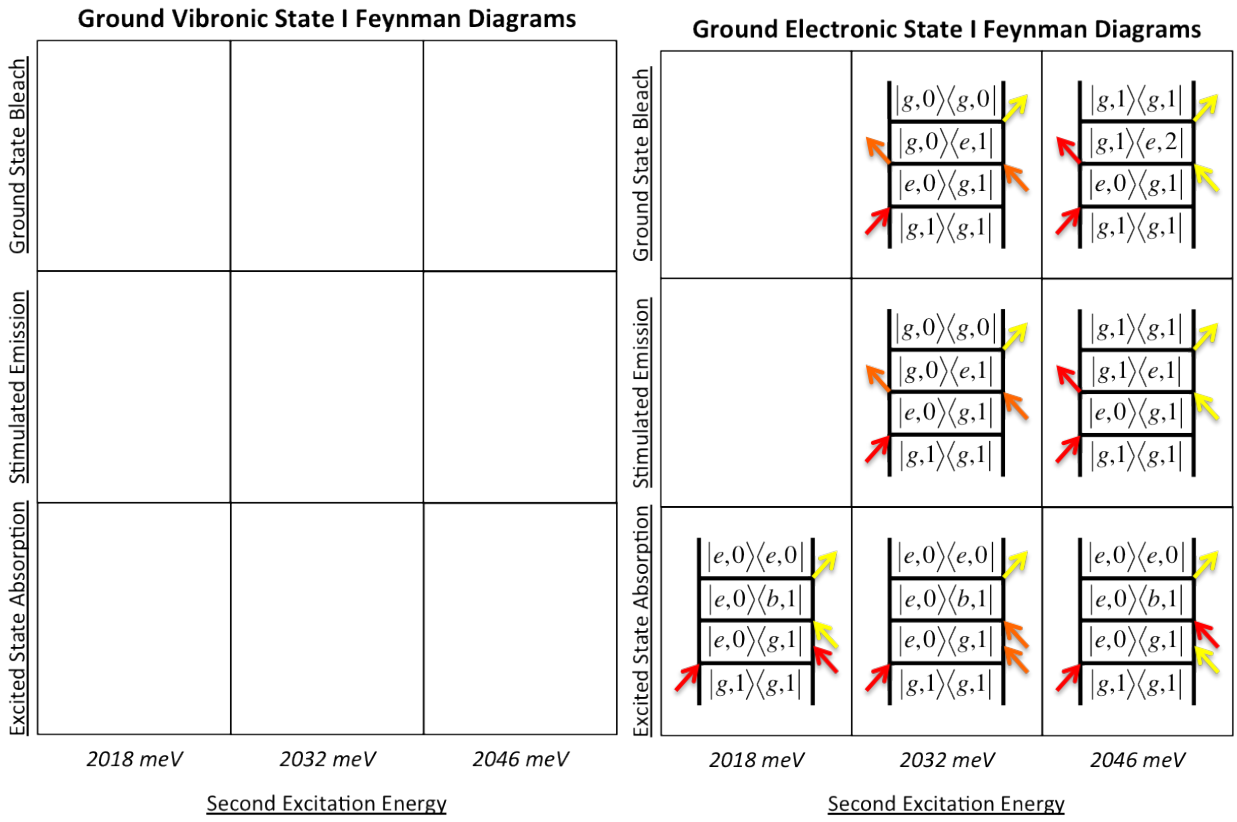


Figure B.1: Two-dimensional rephasing Feynman diagrams in cuprous oxide. All possible orthoexciton pathways originating from the ground vibronic and phonon-populated ground electronic states. In the bra-ket notation, $|n, m\rangle$ represents a state occupied by $n$ excitons and $m$ phonons. Red, orange, and yellow arrows denote field interactions involving the changes in phonon occupation number by -1, 0, and +1, respectively.

(a) **Non-Overlapping Pathways**

| Excitation Energy (meV) | Emission Energy (meV) | | | | | |
|---|---|---|---|---|---|---|
| | 2018 | | 2032 | | 2046 | |
| 2046 | A' | A | B' | B | C' | C |
| | -90 | 180 | -18 | 36 | -81 | 162 |
| | -171* | 342* | -18* | 36* | -81* | 162* |
| 2032 | D' | D | E' | E | F' | F |
| | 0 | 200 | -10 | 20 | -18 | 18 |
| | -18* | 36* | -19* | 38* | -18* | 36* |
| 2018 | G' | G | H' | H | I' | I |
| | 0 | 0 | 0 | 0 | 0 | 0 |
| | 0* | 162* | -18* | 36* | -171* | 180* |

(b) **Overlapping Pathways**

| Excitation Energy (meV) | Emission Energy (meV) | | | |
|---|---|---|---|---|
| | 2004 | 2018 | 2032 | 2046 |
| 2046 | A' | a | b | C |
| | -99 | 178 | -72 | 170 |
| 2032 | D' | d | e | F |
| | -1 | 191 | 3 | 20 |
| 2018 | G' | g | h | I |
| | 0 | 7 | 7 | 10 |

Figure B.2: Graphical displays for two-dimensional rephasing signal via Feynman diagram analysis. Graphical displays for non-overlapping (a) and overlapping (b) pathway strengths for all possible rephasing Feynman diagrams. * indicates pathways involving a phonon-populated ground electronic state. ‘ indicates excited state absorption pathways.

# Appendix C

# Two-Dimensional Two-Quantum Feynman Diagrams for Cuprous Oxide

Appendix C enumerates all the possible Feynman diagrams for the two-dimensional two-quantum spectrum of cuprous oxide, including transitions for pure exciton-polariton creation and destruction and phonon-assisted creation and destruction.

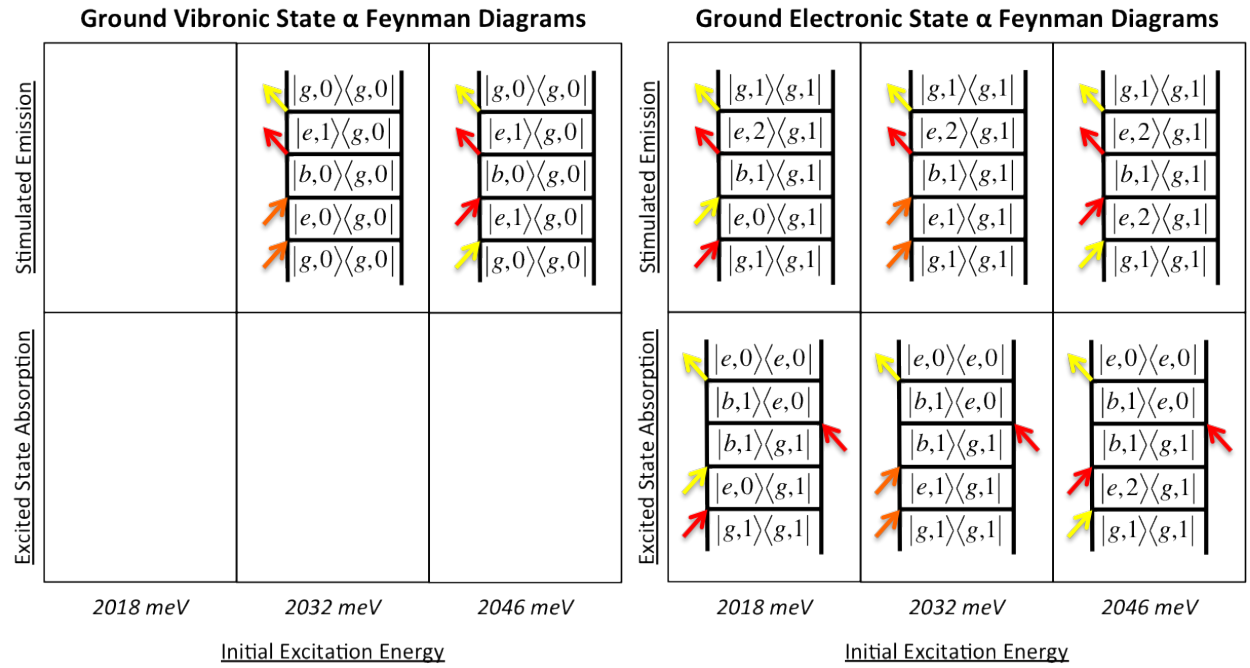
Ground Vibronic State α Feynman Diagrams
Stimulated Emission
Excited State Absorption
2018 meV
2032 meV
2046 meV
Initial Excitation Energy
Ground Electronic State α Feynman Diagrams
Stimulated Emission
Excited State Absorption
2018 meV
2032 meV
2046 meV
Initial Excitation Energy

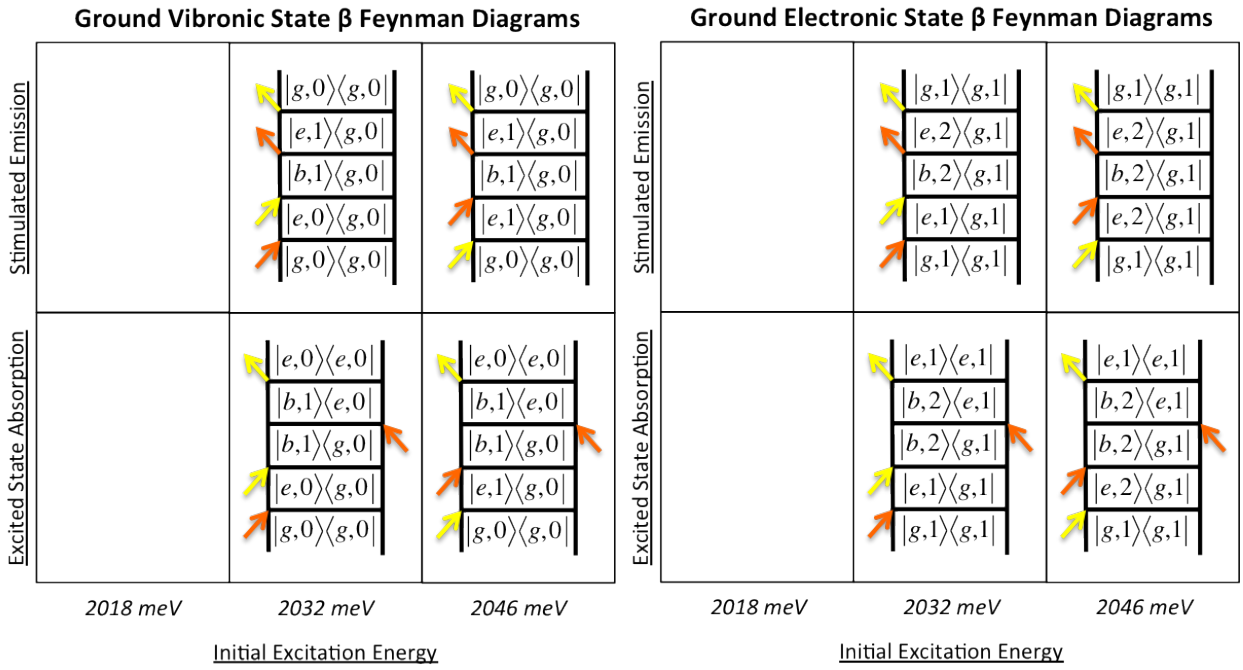
Ground Vibronic State β Feynman Diagrams
Stimulated Emission
Excited State Absorption
2018 meV
2032 meV
2046 meV
Initial Excitation Energy
Ground Electronic State β Feynman Diagrams
Stimulated Emission
Excited State Absorption
2018 meV
2032 meV
2046 meV
Initial Excitation Energy

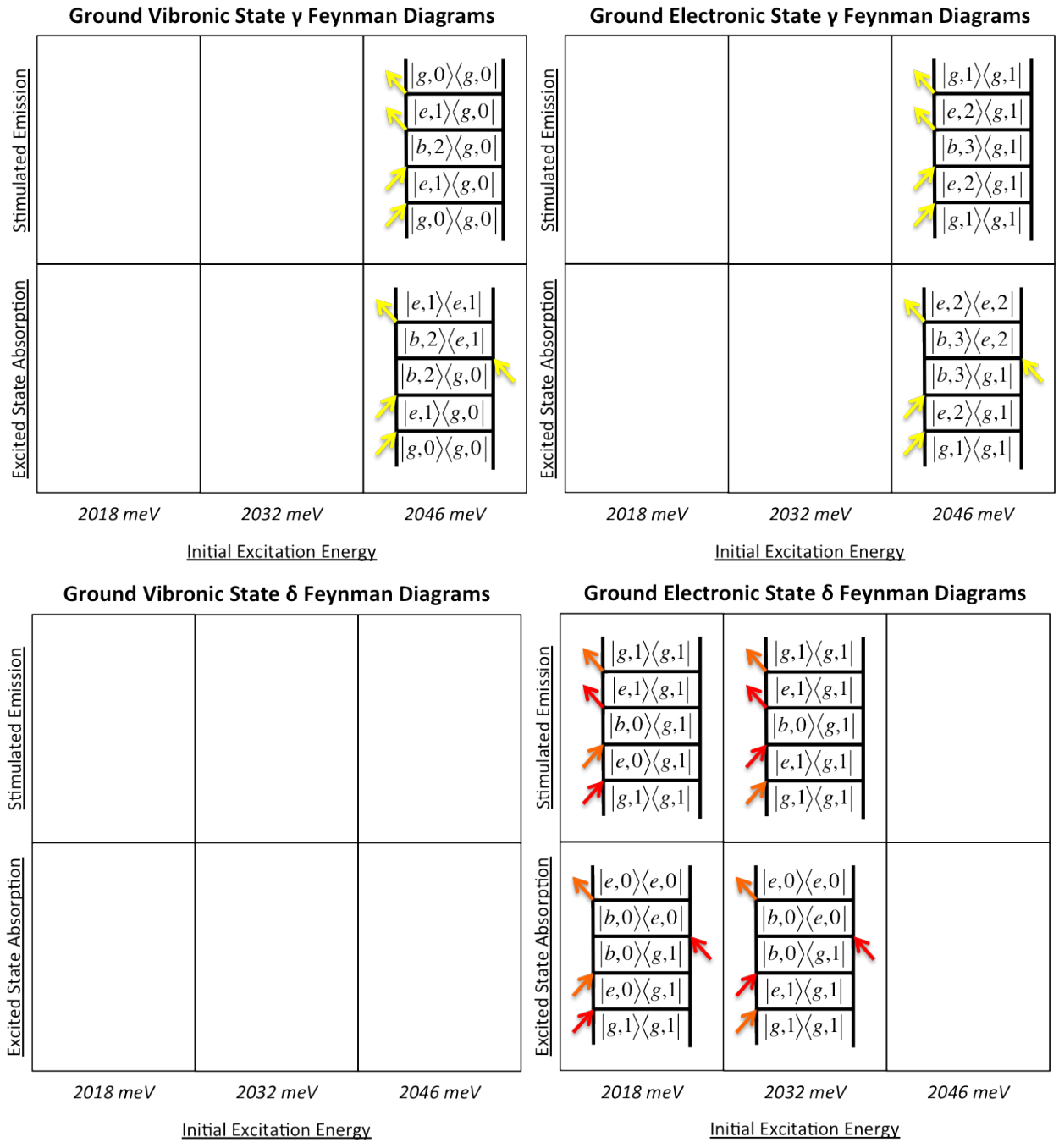
Ground Vibronic State γ Feynman Diagrams
Stimulated Emission
Excited State Absorption
$|g,0\rangle\langle g,0|$
$|e,1\rangle\langle g,0|$
$|b,2\rangle\langle g,0|$
$|e,1\rangle\langle g,0|$
$|g,0\rangle\langle g,0|$
$|e,1\rangle\langle e,1|$
$|b,2\rangle\langle e,1|$
$|b,2\rangle\langle g,0|$
$|e,1\rangle\langle g,0|$
$|g,0\rangle\langle g,0|$
2018 meV
2032 meV
2046 meV
Initial Excitation Energy
Ground Electronic State γ Feynman Diagrams
Stimulated Emission
Excited State Absorption
$|g,1\rangle\langle g,1|$
$|e,2\rangle\langle g,1|$
$|b,3\rangle\langle g,1|$
$|e,2\rangle\langle g,1|$
$|g,1\rangle\langle g,1|$
$|e,2\rangle\langle e,2|$
$|b,3\rangle\langle e,2|$
$|b,3\rangle\langle g,1|$
$|e,2\rangle\langle g,1|$
$|g,1\rangle\langle g,1|$
2018 meV
2032 meV
2046 meV
Initial Excitation Energy
Ground Vibronic State δ Feynman Diagrams
Stimulated Emission
Excited State Absorption
2018 meV
2032 meV
2046 meV
Initial Excitation Energy
Ground Electronic State δ Feynman Diagrams
Stimulated Emission
Excited State Absorption
$|g,1\rangle\langle g,1|$
$|e,1\rangle\langle g,1|$
$|b,0\rangle\langle g,1|$
$|e,0\rangle\langle g,1|$
$|g,1\rangle\langle g,1|$
$|e,0\rangle\langle e,0|$
$|b,0\rangle\langle e,0|$
$|b,0\rangle\langle g,1|$
$|e,0\rangle\langle g,1|$
$|g,1\rangle\langle g,1|$
2018 meV
2032 meV
2046 meV
Initial Excitation Energy

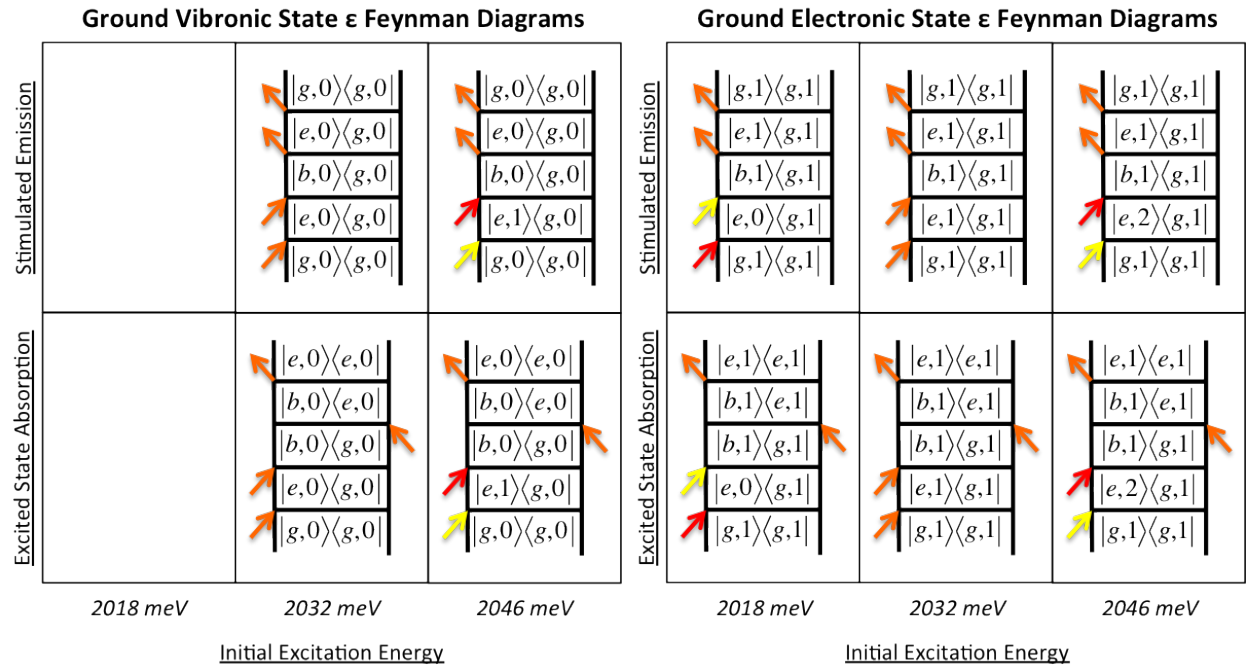
Ground Vibronic State ε Feynman Diagrams
Stimulated Emission
Excited State Absorption
|g,0⟩⟨g,0|
|e,0⟩⟨g,0|
|b,0⟩⟨g,0|
|e,0⟩⟨g,0|
|g,0⟩⟨g,0|
|g,0⟩⟨g,0|
|e,0⟩⟨g,0|
|b,0⟩⟨g,0|
|e,1⟩⟨g,0|
|g,0⟩⟨g,0|
|e,0⟩⟨e,0|
|b,0⟩⟨e,0|
|b,0⟩⟨g,0|
|e,0⟩⟨g,0|
|g,0⟩⟨g,0|
|e,0⟩⟨e,0|
|b,0⟩⟨e,0|
|b,0⟩⟨g,0|
|e,1⟩⟨g,0|
|g,0⟩⟨g,0|
2018 meV
2032 meV
2046 meV
Initial Excitation Energy
Ground Electronic State ε Feynman Diagrams
Stimulated Emission
Excited State Absorption
|g,1⟩⟨g,1|
|e,1⟩⟨g,1|
|b,1⟩⟨g,1|
|e,0⟩⟨g,1|
|g,1⟩⟨g,1|
|g,1⟩⟨g,1|
|e,1⟩⟨g,1|
|b,1⟩⟨g,1|
|e,1⟩⟨g,1|
|g,1⟩⟨g,1|
|g,1⟩⟨g,1|
|e,1⟩⟨g,1|
|b,1⟩⟨g,1|
|e,2⟩⟨g,1|
|g,1⟩⟨g,1|
|e,1⟩⟨e,1|
|b,1⟩⟨e,1|
|b,1⟩⟨g,1|
|e,0⟩⟨g,1|
|g,1⟩⟨g,1|
|e,1⟩⟨e,1|
|b,1⟩⟨e,1|
|b,1⟩⟨g,1|
|e,1⟩⟨g,1|
|g,1⟩⟨g,1|
|e,1⟩⟨e,1|
|b,1⟩⟨e,1|
|b,1⟩⟨g,1|
|e,2⟩⟨g,1|
|g,1⟩⟨g,1|
2018 meV
2032 meV
2046 meV
Initial Excitation Energy

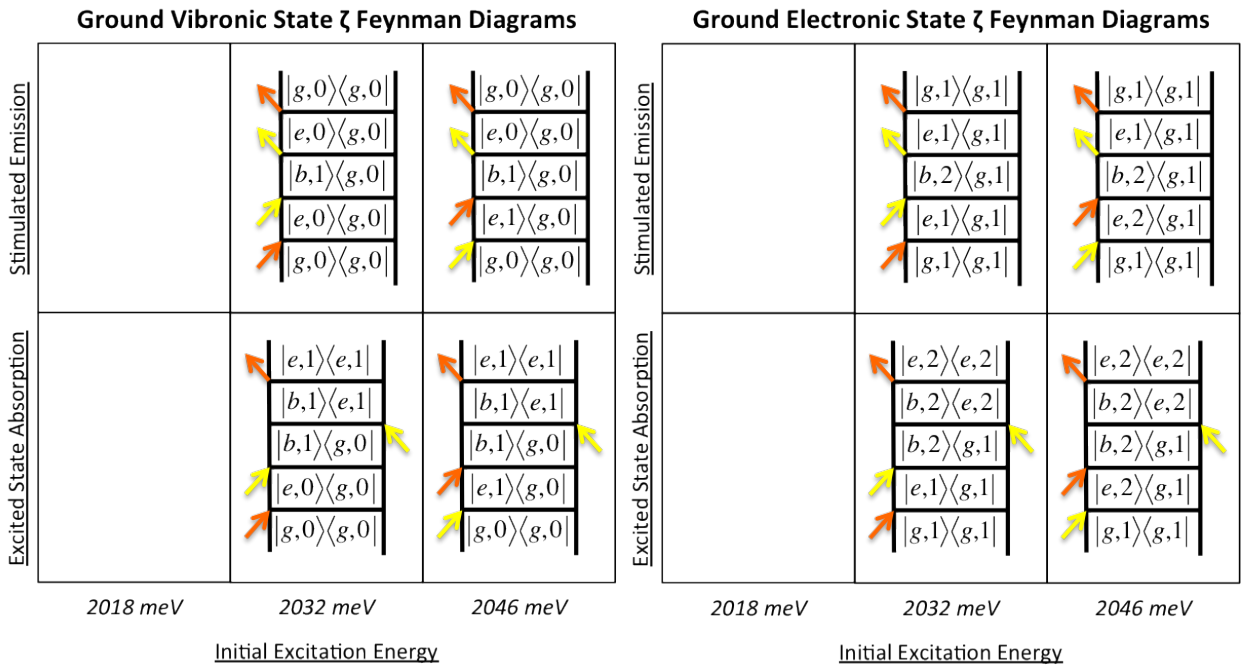
Ground Vibronic State ζ Feynman Diagrams
Stimulated Emission
Excited State Absorption
|g,0⟩⟨g,0|
|e,0⟩⟨g,0|
|b,1⟩⟨g,0|
|e,0⟩⟨g,0|
|g,0⟩⟨g,0|
|g,0⟩⟨g,0|
|e,0⟩⟨g,0|
|b,1⟩⟨g,0|
|e,1⟩⟨g,0|
|g,0⟩⟨g,0|
|e,1⟩⟨e,1|
|b,1⟩⟨e,1|
|b,1⟩⟨g,0|
|e,0⟩⟨g,0|
|g,0⟩⟨g,0|
|e,1⟩⟨e,1|
|b,1⟩⟨e,1|
|b,1⟩⟨g,0|
|e,1⟩⟨g,0|
|g,0⟩⟨g,0|
2018 meV
2032 meV
2046 meV
Initial Excitation Energy
Ground Electronic State ζ Feynman Diagrams
Stimulated Emission
Excited State Absorption
|g,1⟩⟨g,1|
|e,1⟩⟨g,1|
|b,2⟩⟨g,1|
|e,1⟩⟨g,1|
|g,1⟩⟨g,1|
|g,1⟩⟨g,1|
|e,1⟩⟨g,1|
|b,2⟩⟨g,1|
|e,2⟩⟨g,1|
|g,1⟩⟨g,1|
|e,2⟩⟨e,2|
|b,2⟩⟨e,2|
|b,2⟩⟨g,1|
|e,1⟩⟨g,1|
|g,1⟩⟨g,1|
|e,2⟩⟨e,2|
|b,2⟩⟨e,2|
|b,2⟩⟨g,1|
|e,2⟩⟨g,1|
|g,1⟩⟨g,1|
2018 meV
2032 meV
2046 meV
Initial Excitation Energy

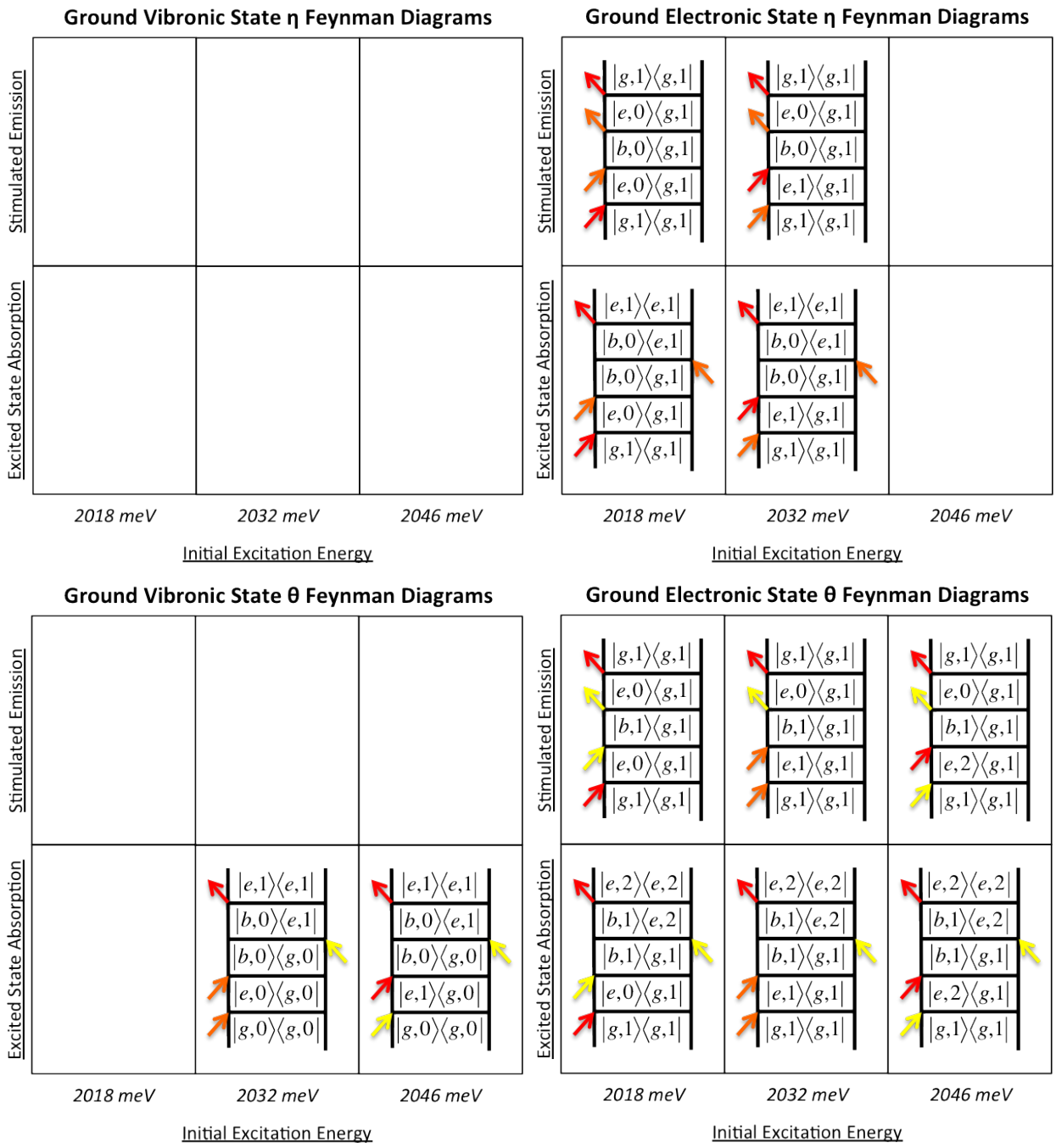


Figure C.1: Two-dimensional two-quantum Feynman diagrams in cuprous oxide. All possible orthoexciton pathways originating from the ground vibronic and phonon-populated ground electronic states. In the bra-ket notation, $|n, m\rangle$ represents a state occupied by $n$ excitons and $m$ phonons. Red, orange, and yellow arrows denote field interactions involving the changes in phonon occupation number by -1, 0, and +1, respectively.

# Bibliography


[1] Gregory D. Scholes and Garry Rumbles. Excitons in nanoscale systems. *Nature Materials*, 5(9):683–696, 2006.

[2] Gregory D. Scholes. Insights into excitons confined to nanoscale systems: Electron–hole interaction, binding energy, and photodissociation. *American Chemical Society Nanotechnology*, 2(3):523–537, 2008.

[3] Gang Li, Vishal Shrotriya, Jinsong Huang, Yan Yao, Tom Moriarty, Keith Emery, and Yang Yang. High-efficiency solution processable polymer photovoltaic cells by self-organization of polymer blends. *Nature Materials*, 4(11):864–868, 2005.

[4] P. Peumans and S.R. Forrest. Very-high-efficiency double-heterostructure copper phthalocyanine/C60 photovoltaic cells. *Applied Physics Letters*, 79(1):126–128, 2001.

[5] Akihiro Kojima, Kenjiro Teshima, Yasuo Shirai, and Tsutomu Miyasaka. Organometal halide perovskites as visible-light sensitizers for photovoltaic cells. *Journal of the American Chemical Society*, 131(17):6050–6051, 2009.

[6] Zhihong Huang, James E. Carey, Mingguo Liu, Xiangyi Guo, Eric Mazur, and Joe C. Campbell. Microstructured silicon photodetector. *Applied Physics Letters*, 89(3):033506, 2006.

[7] Shiang-Feng Tang, Shih-Yen Lin, and Si-Chen Lee. Near-room-temperature operation of an InAs/GaAs quantum-dot infrared photodetector. *Applied Physics Letters*, 78(17):2428–2430, 2001.

[8] G.A. O'brien, A.J. Quinn, D.A. Tanner, and G. Redmond. A single polymer nanowire photodetector. *Advanced Materials*, 18(18):2379–2383, 2006.

[9] J.H. Burroughes, D.D.C. Bradley, A.R. Brown, R.N. Marks, K. Mackay, R.H. Friend, P.L. Burns, and A.B. Holmes. Light-emitting diodes based on conjugated polymers. *Nature*, 347(6293):539–541, 1990.

[10] Shuji Nakamura, Takashi Mukai, and Masayuki Senoh. Candela-class high-brightness InGaN/AlGaN double-heterostructure blue-light-emitting diodes. *Applied Physics Letters*, 64(13):1687–1689, 1994.

[11] Yong-Jae Lee, Se-Heon Kim, Joon Huh, Guk-Hyun Kim, Yong-Hee Lee, Sang-Hwan Cho, Yoon-Chang Kim, and Young Rag Do. A high-extraction-efficiency nanopatterned organic light-emitting diode. *Applied Physics Letters*, 82(21):3779–3781, 2003.

[12] V.L. Colvin, M.C. Schlamp, and A.P. Alivisatos. Light-emitting diodes made from cadmium selenide nanocrystals and a semiconducting polymer. *Nature*, 370(6488):354–357, 1994.

[13] Yoshitaka Taniyasu, Makoto Kasu, and Toshiki Makimoto. An aluminium nitride light-emitting diode with a wavelength of 210 nanometres. *Nature*, 441(7091):325–328, 2006.

[14] M.A. Haase, J. Qiu, J.M. DePuydt, and H. Cheng. Blue-green laser diodes. *Applied Physics Letters*, 59(11):1272–1274, 1991.

[15] Bryan Ellis, Marie A. Mayer, Gary Shambat, Tomas Sarmiento, James Harris, Eugene E. Haller, and Jelena Vuckovic. Ultralow-threshold electrically pumped quantum-dot photonic-crystal nanocavity laser. *Nature Photonics*, 5(5):297–300, 2011.

[16] Xiangfeng Duan, Yu Huang, Ritesh Agarwal, and Charles M. Lieber. Single-nanowire electrically driven lasers. *Nature*, 421(6920):241–245, 2003.

[17] Y. Yang, G.A. Turnbull, and I.D.W. Samuel. Hybrid optoelectronics: A polymer laser pumped by a nitride light-emitting diode. *Applied Physics Letters*, 92(16):163306, 2008.

[18] Daryl M. Beggs, Thomas P. White, Liam O'Faolain, and Thomas F. Krauss. Ultracompact and low-power optical switch based on silicon photonic crystals. *Optics Letters*, 33(2):147–149, 2008.

[19] Slawomir Z. Janicki and Gary B. Schuster. A liquid crystal opto-optical switch: Nondestructive information retrieval based on a photochromic fulgide as trigger. *Journal of the American Chemical Society*, 117(33):8524–8527, 1995.

[20] Mike Heilemann, Emmanuel Margeat, Robert Kasper, Markus Sauer, and Philip Tinnefeld. Carbocyanine dyes as efficient reversible single-molecule optical switch. *Journal of the American Chemical Society*, 127(11):3801–3806, 2005.

[21] Zhiyong Fan, Dawei Wang, Pai-Chun Chang, Wei-Yu Tseng, and Jia G. Lu. ZnO nanowire field-effect transistor and oxygen sensing property. *Applied Physics Letters*, 85(24):5923–5925, 2004.

[22] David L. Klein, Richard Roth, Andrew K.L. Lim, A. Paul Alivisatos, and Paul L. McEuen. A single-electron transistor made from a cadmium selenide nanocrystal. *Nature*, 389(6652):699–701, 1997.

[23] Francis Garnier, Ryad Hajlaoui, Abderrahim Yassar, and Pratima Srivastava. All-

polymer field-effect transistor realized by printing techniques. *Science*, 265(5179):1684–1686, 1994.

[24] C.D. Dimitrakopoulos, A.R. Brown, and A. Pomp. Molecular beam deposited thin films of pentacene for organic field effect transistor applications. *Applied Physics Letters*, 80(40):2501–2508, 1996.

[25] Nathan S. Lewis and Daniel G. Nocera. Powering the planet: Chemical challenges in solar energy utilization. *Proceedings of the National Academy of Sciences*, 103(43):15729–15735, 2006.

[26] Robert E. Blankenship, David M. Tiede, James Barber, Gary W. Brudvig, Graham Fleming, Maria Ghirardi, M.R. Gunner, Wolfgang Junge, David M. Kramer, Anastasios Melis, Thomas A. Moore, Christopher C. Moser, Daniel G. Nocera, Arthur J. Nozik, Donald R. Ort, William W. Parson, Roger C. Prince, and Richard T. Sayre. Comparing photosynthetic and photovoltaic efficiencies and recognizing the potential for improvement. *Science*, 332(6031):805–809, 2011.

[27] Yasuhiro Tachibana, Lionel Vayssieres, and James R. Durrant. Artificial photosynthesis for solar water-splitting. *Nature Photonics*, 6(8):511–518, 2012.

[28] A.K. Ringsmuth, G.J. Milburn, and T.M. Stace. Multiscale photosynthetic and biomimetic excitation energy transfer. *Nature Physics*, 8(7):562–567, 2012.

[29] Carsten Kulheim, Jon Agren, and Stefan Jansson. Rapid regulation of light harvesting and plant fitness in the field. *Science*, 297(5578):91–93, 2002.

[30] R.E. Fenna and B.W. Matthews. Chlorophyll arrangement in a bacteriochlorophyll protein from chlorobium limicola. *Nature*, 258(5536):573–577, 1975.

[31] Gregory S. Engel, Tessa R. Calhoun, Elizabeth L. Read, Tae-Kyu Ahn, Tomas Mancal, Yuan-Chung Cheng, Robert E. Blankenship, and Graham R. Fleming. Evidence for wavelike energy transfer through quantum coherence in photosynthetic systems. *Nature*, 446(7137):782–786, 2007.

[32] Gitt Panitchayangkoon, Dugan Hayes, Kelly A. Fransted, Justin R. Caram, Elad Harel, Jianzhong Wen, Robert E. Blankenship, and Gregory S. Engel. Long-lived quantum coherence in photosynthetic complexes at physiological temperature. *Proceedings of the National Academy of Sciences*, 107(29):12766–12770, 2010.

[33] Hohjai Lee, Yuan-Chung Cheng, and Graham R. Fleming. Coherence dynamics in photosynthesis: Protein protection of excitonic coherence. *Science*, 316(5830):1462–1465, 2007.

[34] Gregory D. Scholes, Graham R. Fleming, Alexandra Olaya-Castro, and Rienk van Grondelle. Lessons from nature about solar light harvesting. *Nature Chemistry*,

3(10):763–774, 2011.

[35] Graham R. Fleming and Gregory D. Scholes. Physical chemistry: Quantum mechanics for plants. *Nature*, 431(7006):256–257, 2004.

[36] Edwin E. Jelley. Spectral absorption and fluorescence of dyes in the molecular state. *Nature*, 138:1009–1010, 1936.

[37] Frank Wurthner, Theo E. Kaiser, and Chantu R. Saha-Moller. J-aggregates: From serendipitous discovery to supramolecular engineering of functional dye materials. *Angewandte Chemie International Edition*, 50(15):3376–3410, 2011.

[38] Takayoshi Kobayashi. *J-Aggregates*. World Scientific Publishing Company, Hackensack, NJ, 1996.

[39] Minhaeng Cho. *Two-Dimensional Optical Spectroscopy*. CRC Press, Boca Raton, FL, 2009.

[40] Peter Hamm and Martin Zanni. *Concepts and Methods of 2D Infrared Spectroscopy*. Cambridge University Press, Cambridge, UK, 2011.

[41] Shaul Mukamel. *Principles of Nonlinear Optical Spectroscopy*. Oxford University Press, New York, NY, 1995.

[42] Tobias Brixner, Jens Stenger, Harsha M. Vaswani, Minhaeng Cho, Robert E. Blankenship, and Graham R. Fleming. Two-dimensional spectroscopy of electronic couplings in photosynthesis. *Nature*, 434(7033):625–628, 2005.

[43] Donatas Zigmantas, Elizabeth L. Read, Tomas Mancal, Tobias Brixner, Alastair T. Gardiner, Richard J. Cogdell, and Graham R. Fleming. Two-dimensional electronic spectroscopy of the B800-B820 light-harvesting complex. *Proceedings of the National Academy of Sciences*, 103(34):12672–12677, 2006.

[44] Jakub Dostal, Tomas Mancal, Ramunas Augulis, Frantisek Vacha, Jakub Psencik, and Donatas Zigmantas. Two-dimensional electronic spectroscopy reveals ultrafast energy diffusion in chlorosomes. *Journal of the American Chemical Society*, 134(28):11611–11617, 2012.

[45] Evgeny E. Ostroumov, Rachel M. Mulvaney, Richard J. Cogdell, and Gregory D. Scholes. Broadband 2D electronic spectroscopy reveals a carotenoid dark state in purple bacteria. *Science*, 340(6128):52–56, 2013.

[46] Elisabetta Collini, Cathy Y. Wong, Krystyna E. Wilk, Paul M.G. Curmi, Paul Brumer, and Gregory D. Scholes. Coherently wired light-harvesting in photosynthetic marine algae at ambient temperature. *Nature*, 463(7281):644–647, 2010.

[47] Alexandra Nemeth, Franz Milota, Jaroslaw Sperling, Darius Abramavicius, Shaul

Mukamel, and Harald F. Kauffmann. Tracing exciton dynamics in molecular nanotubes with 2D electronic spectroscopy. *Chemical Physics Letters*, 469(1-3):130–134, 2009.

[48] F. Milota, J. Sperling, A. Nemeth, D. Abramavicius, S. Mukamel, and H.F. Kauffmann. Excitonic couplings and interband energy transfer in a double-wall molecular aggregate imaged by coherent two-dimensional electronic spectroscopy. *The Journal of Chemical Physics*, 131(5):054510, 2009.

[49] Jaroslaw Sperling, Alexandra Nemeth, Jurgen Hauer, Darius Abramavicius, Shaul Mukamel, Harald F. Kauffmann, and Franz Milota. Excitons and disorder in molecular nanotubes: A 2D electronic spectroscopy study and first comparison to a microscopic model. *The Journal of Physical Chemistry A*, 114(32):8179–8189, 2010.

[50] James Lim, David Palecek, Felipe Caycedo-Soler, Craig N. Lincoln, Javier Prior, Hans von Berlepsch, Susana F. Huelga, Martin B. Plenio, Donatas Zigmantas, and Jurgen Hauer. Vibronic origin of long-lived coherence in an artificial molecular light harvester. *Nature Communications*, 6:7755, 2015.

[51] Darius Abramavicius, Alexandra Nemeth, Franz Milota, Jaroslaw Sperling, Shaul Mukamel, and Harald F. Kauffmann. Weak exciton scattering in molecular nanotubes revealed by double-quantum two-dimensional electronic spectroscopy. *Physical Review Letters*, 108:067401, 2012.

[52] Elisabetta Collini and Gregory D. Scholes. Coherent intrachain energy migration in a conjugated polymer at room temperature. *Science*, 323(5912):369–373, 2009.

[53] Yin Song, Scott N. Clafton, Ryan D. Pensack, Tak W. Kee, and Gregory D. Scholes. Vibrational coherence probes the mechanism of ultrafast electron transfer in polymer–fullerene blends. *Nature Communications*, 5:4933, 2014.

[54] Cristina Consani, Federico Koch, Fabian Panzer, Thomas Unger, Anna Kohler, and Tobias Brixner. Relaxation dynamics and exciton energy transfer in the low-temperature phase of MEH-PPV. *The Journal of Chemical Physics*, 142(21):212429, 2015.

[55] Artem A. Bakulin, Sarah E. Morgan, Tom B. Kehoe, Mark W.B. Wilson, Alex W. Chin, Donatas Zigmantas, Dassia Egorova, and Akshay Rao. Real-time observation of multiexcitonic states in ultrafast singlet fission using coherent 2D electronic spectroscopy. *Nature Chemistry*, 8(1):16–23, 2016.

[56] V.M. Huxter, T.A.A. Oliver, D. Budker, and G.R. Fleming. Vibrational and electronic dynamics of nitrogen-vacancy centres in diamond revealed by two-dimensional ultrafast spectroscopy. *Nature Physics*, 9(11):744–749, 2013.

[57] Galan Moody, Chandriker Kavir Dass, Kai Hao, Chang-Hsiao Chen, Lain-Jong Li, Akshay Singh, Kha Tran, Genevieve Clark, Xiaodong Xu, Gunnar Berghauser, Ermin

Malic, Andreas Knorr, and Xiaoqin Li. Intrinsic homogeneous linewidth and broadening mechanisms of excitons in monolayer transition metal dichalcogenides. *Nature Communications*, 6:8315, 2015.

[58] Irina Kuznetsova, Peter Thomas, Torsten Meier, Tianhao Zhang, and Steven T. Cundiff. Determination of homogeneous and inhomogeneous broadenings of quantum-well excitons by 2DFTS: An experiment-theory comparison. *Physica Status Solidi (c)*, 6(2):445–448, 2009.

[59] Gael Nardin, Galan Moody, Rohan Singh, Travis M. Autry, Hebin Li, Francois Morier-Genoud, and Steven T. Cundiff. Coherent excitonic coupling in an asymmetric double InGaAs quantum well arises from many-body effects. *Physical Review Letters*, 112:046402, 2014.

[60] Daniel B. Turner, Patrick Wen, Dylan H. Arias, Keith A. Nelson, Hebin Li, Galan Moody, Mark E. Siemens, and Steven T. Cundiff. Persistent exciton-type many-body interactions in GaAs quantum wells measured using two-dimensional optical spectroscopy. *Physical Review B*, 85:201303, 2012.

[61] Katherine W. Stone, Kenan Gundogdu, Daniel B. Turner, Xiaoqin Li, Steven T. Cundiff, and Keith A. Nelson. Two-quantum 2D FT electronic spectroscopy of biexcitons in GaAs quantum wells. *Science*, 324(5931):1169–1173, 2009.

[62] Daniel B. Turner and Keith A. Nelson. Coherent measurements of high-order electronic correlations in quantum wells. *Nature*, 466(7310):1089–1092, 2010.

[63] Daniel B. Turner, Katherine W. Stone, Kenan Gundogdu, and Keith A. Nelson. Three-dimensional electronic spectroscopy of excitons in GaAs quantum wells. *The Journal of Chemical Physics*, 131(14):144510, 2009.

[64] G. Moody, M.E. Siemens, A.D. Bristow, X. Dai, D. Karaiskaj, A.S. Bracker, D. Gammon, and S.T. Cundiff. Exciton-exciton and exciton-phonon interactions in an interfacial GaAs quantum dot ensemble. *Physical Review B*, 83:115324, 2011.

[65] Elad Harel, Sara M. Rupich, Richard D. Schaller, Dmitri V. Talapin, and Gregory S. Engel. Measurement of electronic splitting in PbS quantum dots by two-dimensional nonlinear spectroscopy. *Physical Review B*, 86:075412, 2012.

[66] Daniel B. Turner, Yasser Hassan, and Gregory D. Scholes. Exciton superposition states in CdSe nanocrystals measured using broadband two-dimensional electronic spectroscopy. *Nano Letters*, 12(2):880–886, 2012.

[67] Justin R. Caram, Haibin Zheng, Peter D. Dahlberg, Brian S. Rolczynski, Graham B. Griffin, Dmitriy S. Dolzhnikov, Dmitri V. Talapin, and Gregory S. Engel. Exploring size and state dynamics in CdSe quantum dots using two-dimensional electronic spectroscopy. *The Journal of Chemical Physics*, 140(8):084701, 2014.

[68] Justin R. Caram, Haibin Zheng, Peter D. Dahlberg, Brian S. Rolczynski, Graham B. Griffin, Andrew F. Fidler, Dmitriy S. Dolzhnikov, Dmitri V. Talapin, and Gregory S. Engel. Persistent inter-excitonic quantum coherence in CdSe quantum dots. *The Journal of Physical Chemistry Letters*, 5(1):196–204, 2014.

[69] Daniel B. Turner, Krystyna E. Wilk, Paul M.G. Curmi, and Gregory D. Scholes. Comparison of electronic and vibrational coherence measured by two-dimensional electronic spectroscopy. *The Journal of Physical Chemistry Letters*, 2(15):1904–1911, 2011.

[70] Vaclav Perlik, Craig Lincoln, Frantisek Sanda, and Jurgen Hauer. Distinguishing electronic and vibronic coherence in 2D spectra by their temperature dependence. *The Journal of Physical Chemistry Letters*, 5(3):404–407, 2014.

[71] Joel Yuen-Zhou, Jacob J. Krich, and Alan Aspuru-Guzik. A witness for coherent electronic vs vibronic-only oscillations in ultrafast spectroscopy. *The Journal of Chemical Physics*, 136(23):234501, 2012.

[72] Patrick Rebentrost, Sangwoo Shim, Joel Yuen-Zhou, and Alan Aspuru-Guzik. Characterization and quantification of the role of coherence in ultrafast quantum biological experiments using quantum master equations, atomistic simulations, and quantum process tomography. *Procedia Chemistry*, 3(1):332–346, 2011.

[73] Francesca Fassioli, Alexandra Olaya-Castro, and Gregory D. Scholes. Coherent energy transfer under incoherent light conditions. *The Journal of Physical Chemistry Letters*, 3(21):3136–3142, 2012.

[74] Paul Brumer and Moshe Shapiro. Molecular response in one-photon absorption via natural thermal light vs. pulsed laser excitation. *Proceedings of the National Academy of Sciences*, 109(48):19575–19578, 2012.

[75] Daniel B. Turner, Paul C. Arpin, Scott D. McClure, Darin J. Ulness, and Gregory D. Scholes. Coherent multidimensional optical spectra measured using incoherent light. *Nature Communications*, 4:2298, 2013.

[76] K.B. Davis, M.-O. Mewes, M.R. Andrews, N.J. van Druten, D.S. Durfee, D.M. Kurn, and W. Ketterle. Bose-Einstein condensation in a gas of sodium atoms. *Physical Review Letters*, 75:3969–3973, 1995.

[77] M.H. Anderson, J.R. Ensher, M.R. Matthews, C.E. Wieman, and E.A. Cornell. Observation of Bose-Einstein condensation in a dilute atomic vapor. *Science*, 269(5221):198–201, 1995.

[78] J.P. Eisenstein and A.H. MacDonald. Bose-Einstein condensation of excitons in bilayer electron systems. *Nature*, 432(7018):691–694, 2004.

[79] J. Kasprzak, M. Richard, S. Kundermann, A. Baas, P. Jeambrun, J.M.J. Keeling,

F.M. Marchetti, M.H. Szymanska, R. Andre, J.L. Staehli, V. Savona, P.B. Littlewood, B. Deveaud, and Le Si Dang. Bose-Einstein condensation of exciton polaritons. *Nature*, 443(7110):409–414, 2006.

[80] Markus Greiner, Cindy A. Regal, and Deborah S. Jin. Emergence of a molecular Bose-Einstein condensate from a fermi gas. *Nature*, 426(6966):537–540, 2003.

[81] J.R. Abo-Shaeer, C. Raman, J.M. Vogels, and W. Ketterle. Observation of vortex lattices in Bose-Einstein condensates. *Science*, 292(5516):476–479, 2001.

[82] Manish Chhowalla, Hyeon Suk Shin, Goki Eda, Lain-Jong Li, Kian Ping Loh, and Hua Zhang. The chemistry of two-dimensional layered transition metal dichalcogenide nanosheets. *Nature Chemistry*, 5(4):263–275, 2013.

[83] Kin Fai Mak, Changgu Lee, James Hone, Jie Shan, and Tony F. Heinz. Atomically thin $MoS_2$: A new direct-gap semiconductor. *Physical Review Letters*, 105:136805, 2010.

[84] Di Xiao, Gui-Bin Liu, Wanxiang Feng, Xiaodong Xu, and Wang Yao. Coupled spin and valley physics in monolayers of $MoS_2$ and other group-VI dichalcogenides. *Physical Review Letters*, 108:196802, 2012.

[85] Qing Hua Wang, Kourosh Kalantar-Zadeh, Andras Kis, Jonathan N. Coleman, and Michael S. Strano. Electronics and optoelectronics of two-dimensional transition metal dichalcogenides. *Nature Nanotechnology*, 7(11):699–712, 2012.

[86] A. Thilagam. Two-dimensional charged-exciton complexes. *Physical Review B*, 55:7804–7808, 1997.

[87] Claude Cohen-Tannoudji, Bernard Diu, and Franck Lalo. *Quantum mechanics*. Wiley-Interscience, Hoboken, NJ, 2005.

[88] Neil W. Ashcroft and N. David Mermin. *Solid State Physics*. Mermin-Brooks Cole, Belmont, CA, 1976.

[89] David L. Dexter and Robert S. Knox. *Excitons*. Interscience Publishers, New York, NY, 1965.

[90] R.S. Knox and N. Inchauspe. Exciton states in ionic crystals. *Physical Review*, 116:1093–1099, 1959.

[91] M. Knupfer. Exciton binding energies in organic semiconductors. *Applied Physics A*, 77(5):623–626, 2003.

[92] Martin A. Green. Improved value for the silicon free exciton binding energy. *American Institute of Physics Advances*, 3(11):112104, 2013.

[93] Solomon Zwerdling, Benjamin Lax, Laura M. Roth, and Kenneth J. Button. Exciton and magneto-absorption of the direct and indirect transitions in germanium. *Physical Review*, 114:80–89, 1959.

[94] Ronald L. Greene and K.K. Bajaj. Binding energies of wannier excitons in GaAs-GaAlAs quantum well structures. *Solid State Communications*, 45(9):831 – 835, 1983.

[95] Michael H. Huang, Samuel Mao, Henning Feick, Haoquan Yan, Yiying Wu, Hannes Kind, Eicke Weber, Richard Russo, and Peidong Yang. Room-temperature ultraviolet nanowire nanolasers. *Science*, 292(5523):1897–1899, 2001.

[96] Robert W. Meulenberg, Jonathan R.I. Lee, Abraham Wolcott, Jin Z. Zhang, Louis J. Terminello, and Tony van Buuren. Determination of the exciton binding energy in CdSe quantum dots. *American Chemical Society Nanotechnology*, 3(2):325–330, 2009.

[97] Feng Wang, Gordana Dukovic, Louis E. Brus, and Tony F. Heinz. The optical resonances in carbon nanotubes arise from excitons. *Science*, 308(5723):838–841, 2005.

[98] Kin Fai Mak, Keliang He, Changgu Lee, Gwan Hyoung Lee, James Hone, Tony F. Heinz, and Jie Shan. Tightly bound trions in monolayer $MoS_2$. *Nature Materials*, 12(3):207–211, 2013.

[99] J.G. Tischler, A.S. Bracker, D. Gammon, and D. Park. Fine structure of trions and excitons in single GaAs quantum dots. *Physical Review B*, 66:081310, 2002.

[100] P. Wen, G. Christmann, J.J. Baumberg, and Keith A. Nelson. Influence of multi-exciton correlations on nonlinear polariton dynamics in semiconductor microcavities. *New Journal of Physics*, 15(2):025005, 2013.

[101] Shigeji Fujita, Kei Ito, and Salvador Godoy. *Quantum Theory of Conducting Matter*. Springer-Verlag, New York, NY, 2009.

[102] A.P. Alivisatos. Semiconductor clusters, nanocrystals, and quantum dots. *Science*, 271(5251):933–937, 1996.

[103] Robert W. Boyd. *Nonlinear Optics*. Academic Press, Burlington, MA, 2008.

[104] Andrei Tokmakoff. Nonlinear and two-dimensional spectroscopy notes. University of Chicago.

[105] Peter Hamm. Principles of nonlinear optical spectroscopy: A practical approach or: Mukamel for dummies. Univesity of Zurich, August 2005.

[106] David J. Griffiths. *Introduction to Electromagnetism*. Prentice-Hall, Upper Saddle River, NJ, 1999.

[107] B.E.A Saleh and M.C. Teich. *Fundamentals of Photonics*. John Wiley & Sons, Hobo-

ken, NJ, 2007.

[108] Jeremy A. Johnson, Alexei A. Maznev, Mayank T. Bulsara, Eugene A. Fitzgerald, T.C. Harman, S. Calawa, C.J. Vineis, G. Turner, and Keith A. Nelson. Phase-controlled, heterodyne laser-induced transient grating measurements of thermal transport properties in opaque material. *Journal of Applied Physics*, 111(2):023503, 2012.

[109] Jeremy A. Johnson. *Optical characterization of complex mechinical and thermal transport properties.* PhD thesis, Massachusetts Institute of Technology, 2011.

[110] Jeffrey K. Eliason. *Optical transient grating measurements of micro/nanoscale thermal transport and mechanical properties.* PhD thesis, Massachusetts Institute of Technology, 2015.

[111] Keith A. Nelson, Roger Casalegno, R.J. Dwayne Miller, and M.D. Fayer. Laser-induced excited state and ultrasonic wave gratings: Amplitude and phase grating contributions to diffraction. *The Journal of Chemical Physics*, 77(3), 1144-1152 1982.

[112] Richard R. Ernst, Geoffrey Bodenhausen, and Alexander Wokaun. *Principles of nuclear magnetic resonance in one and two dimensions.* Oxford University Press, Oxford, UK, 1987.

[113] David M. Jonas. Two-dimensional femtosecond spectroscopy. *Annual Review of Physical Chemistry*, 54(1):425–463, 2003.

[114] Daniel B. Turner, Katherine W. Stone, Kenan Gundogdu, and Keith A. Nelson. Invited article: The coherent optical laser beam recombination technique (COLBERT) spectrometer: Coherent multidimensional spectroscopy made easier. *Review of Scientific Instruments*, 82(8):081301, 2011.

[115] M. Wegener, D.S. Chemla, S. Schmitt-Rink, and W. Schafer. Line shape of time-resolved four-wave mixing. *Physical Review A*, 42:5675–5683, 1990.

[116] K. Leo, M. Wegener, J. Shah, D.S. Chemla, E.O. Gobel, T.C. Damen, S. Schmitt-Rink, and W. Schafer. Effects of coherent polarization interactions on time-resolved degenerate four-wave mixing. *Physical Review Letters*, 65:1340–1343, 1990.

[117] K. Bott, O. Heller, D. Bennhardt, S.T. Cundiff, P. Thomas, E.J. Mayer, G.O. Smith, R. Eccleston, J. Kuhl, and K. Ploog. Influence of exciton-exciton interactions on the coherent optical response in GaAs quantum wells. *Physical Review B*, 48:17418–17426, 1993.

[118] Justin M. Shacklette and Steven T. Cundiff. Role of excitation-induced shift in the coherent optical response of semiconductors. *Physical Review B*, 66:045309, 2002.

[119] Xiaoqin Li, Tianhao Zhang, Camelia N. Borca, and Steven T. Cundiff. Many-body interactions in semiconductors probed by optical two-dimensional fourier transform

spectroscopy. *Physical Review Letters*, 96:057406, 2006.

[120] Hailin Wang, Kyle Ferrio, Duncan G. Steel, Y.Z. Hu, R. Binder, and S.W. Koch. Transient nonlinear optical response from excitation induced dephasing in GaAs. *Physical Review Letters*, 71:1261–1264, 1993.

[121] H. Wang, K.B. Ferrio, D.G. Steel, P.R. Berman, Y.Z. Hu, R. Binder, and S.W. Koch. Transient four-wave-mixing line shapes: Effects of excitation-induced dephasing. *Physical Review A*, 49:R1551–R1554, 1994.

[122] Giulio Cerulloa and Sandro De Silvestri. Ultrafast optical parametric amplifiers. *Review of Scientific Instruments*, 74:1, 2003.

[123] A.M. Weiner. Femtosecond pulse shaping using spatial light modulators. *Review of Scientific Instruments*, 71:1929, 2000.

[124] S.R. Hartmann and E.L. Hahn. Nuclear double resonance in the rotating frame. *Physical Review*, 128:2042–2053, 1962.

[125] L. Lepetit, G. Cheriaux, and M. Joffre. Linear techniques of phase measurement by femtosecond spectral interferometry for applications in spectroscopy. *Journal of the Optical Society of America B*, 12(12):2467–2474, 1995.

[126] Dorine Keusters, Howe-Siang Tan, and Warren S. Warren. Role of pulse phase and direction in two-dimensional optical spectroscopy. *The Journal of Physical Chemistry A*, 103(49):10369–10380, 1999.

[127] Anthony E. Siegman. *Lasers*. University Science Books, Palo Alto, CA, 1986.

[128] T.F. Crimmins A.A. Maznev and K.A. Nelson. How to make femtosecond pulses overlap. *Optics Express*, 23(17):1378–1380, 1998.

[129] Joshua C. Vaughan, T. Feurer, Katherine W. Stone, and Keith A. Nelson. Analysis of replica pulses in femtosecond shaping with pixelated devices. *Optics Express*, 14(3):1314–1328, 2006.

[130] Joshua C. Vaughan, Thomas Hornung, T. Feurer, and Keith A. Nelson. Diffraction-based femtosecond pulse shaping with a two-dimensional spatial light modulator. *Optics Express*, 30(3):323–325, 2005.

[131] Andrius Baltuska, Maim S. Pshenichnikov, and Douwe A. Wiersma. Second-harmonic generation frequency-resolved optical gating in the single-cyle regime. *IEEE Journal of Quantum Electronics*, 35(4):459–478, 1999.

[132] M.J. Collett, R. Loudon, and C.W. Gardiner. Quantum theory of optical homodyne and heterodyne detection. *Journal of Modern Optics*, 34(6-7):881–902, 1987.

[133] Joshua C. Vaughan, T. Hornung, K.W. Stone, and Keith A. Nelson. Coherently controlled ultrafast four-wave mixing spectroscopy. *The Journal of Physical Chemistry A*, 111(23):4873–4883, 2007.

[134] A.S. Davydov. *Theory of Molecular Excitons.* Plenum Press, New York, NY, 1971.

[135] Robin M. Hochstrasser and John D. Whiteman. Exciton band structure and properties of a real linear chain in a molecular crystal. *Journal of Chemical Physics*, 56:5945, 1972.

[136] H. von Berlepsch, C. Bottcher, A. Ouart, C. Burger, S. Dahne, and S. Kirstein. Supramolecular structures of J-aggregates of carbocyanine dyes in solution. *The Journal of Physical Chemistry B*, 104(22):5255–5262, 2000.

[137] H. von Berlepsch, C. Bottcher, A. Ouart, M. Regenbrecht, S. Akari, U. Keiderling, H. Schnablegger, S. Dahne, and S. Kirstein. Surfactant-induced changes of morphology of J-aggregates: Superhelix-to-tubule transformation. *Langmuir*, 16(14):5908–5916, 2000.

[138] H. von Berlepsch, S. Kirstein, and C. Bottcher. Effect of alcohols on J-aggregation of a carbocyanine dye. *Langmuir*, 18(20):7699–7705, 2002.

[139] Catalin Didraga, Audrius Pugzlys, P. Ralph Hania, Hans von Berlepsch, Koos Duppen, and Jasper Knoester. Structure, spectroscopy, and microscopic model of tubular carbocyanine dye aggregates. *The Journal of Physical Chemistry B*, 108(39):14976–14985, 2004.

[140] Catalin Didraga and Jasper Knoester. Chiral exciton wave functions in cylindrical J aggregates. *Journal of Chemical Physics*, 121:946, 2004.

[141] Catalin Didraga, Joost A. Klugkist, and Jasper Knoester. Optical properties of helical cylindrical molecular aggregates: The homogeneous limit. *The Journal of Physical Chemistry B*, 106(44):11474–11486, 2002.

[142] Stefan Kirstein and Siegfried Daehne. J-aggregates of amphiphilic cyanine dyes: Self-organization of artificial light harvesting complexes. *International Journal of Photoenergy*, 2006:20363, 2006.

[143] G. Scheibe. Uber die veranderlichkeit der absorptionsspektren in losungen und die nebenvalenzen als ihre ursache. *Angewandte Chemie*, 50(11):212–219, 1937.

[144] H. Fidder and D.A. Wiersma. Collective optical response of molecular aggregates. *Physica Status Solidi (b)*, 188(1):285–295, 1995.

[145] Johannes Moll, Siegfried Daehne, James R. Durrant, and Douwe A. Wiersma. Optical dynamics of excitons in J aggregates of a carbocyanine dye. *Journal of Chemical Physics*, 102:6362, 1995.

[146] D.M. Eisele, C.W. Cone, E.A. Bloemsma, S.M. Vlaming, C.G.F. van der Kwaak, R.J. Silbey, M.G. Bawendi, J. Knoester, J.P. Rabe, and D.A. Vanden Bout. Utilizing redox-chemistry to elucidate the nature of exciton transitions in supramolecular dye nanotubes. *Nature Chemistry*, 4(8):655–662, 2012.

[147] Dorthe M. Eisele, Jasper Knoester, Stefan Kirstein, Jurgen P. Rabe, and David A. Vanden Bout. Uniform exciton fluorescence from individual molecular nanotubes immobilized on solid substrates. *Nature Nanotechnology*, 4(10):658–663, 2009.

[148] Bengt Norden, Alison Rodger, and Tim Dafforn. *Linear Dichroism and Circular Dichroism*. The Royal Society of Chemistry, London, UK, 2010.

[149] Naomi S. Ginsberg, Yuan-Chung Cheng, and Graham R. Fleming. Two-dimensional electronic spectroscopy of molecular aggregates. *Accounts of Chemical Research*, 42(9):1352–1363, 2009.

[150] F. Milota, J. Sperling, A. Nemeth, and H.F. Kauffmann. Two-dimensional electronic photon echoes of a double band J-aggregate: Quantum oscillatory motion versus exciton relaxation. *Chemical Physics*, 357(1-3):45–53, 2009.

[151] Jordan M. Womick, Stephen A. Miller, and Andrew M. Moran. Probing the dynamics of intraband electronic coherences in cylindrical molecular aggregates. *The Journal of Physical Chemistry A*, 113(24):6587–6598, 2009.

[152] J.L. Green and C.A. Angell. Phase relations and vitrification in saccharide-water solutions and the trehalose anomaly. *The Journal of Physical Chemistry*, 93(8):2880–2882, 1989.

[153] Wendell Q. Sun and Paul Davidson. Protein inactivation in amorphous sucrose and trehalose matrices: effects of phase separation and crystallization. *Biochimica et Biophysica Acta (BBA) - General Subjects*, 1425(1):235 – 244, 1998.

[154] Liuquan Chang, Deanna Shepherd, Joanna Sun, David Ouellette, Kathleen L. Grant, Xiaolin Tang, and Michael J. Pikal. Mechanism of protein stabilization by sugars during freeze-drying and storage: Native structure preservation, specific interaction, and/or immobilization in a glassy matrix? *Journal of Pharmaceutical Sciences*, 94(7):1427–1444, 2005.

[155] Dylan H. Arias, Katherine W. Stone, Sebastiaan M. Vlaming, Brian J. Walker, Moungi G. Bawendi, Robert J. Silbey, Vladimir Bulovic, and Keith A. Nelson. Thermally-limited exciton delocalization in superradiant molecular aggregates. *The Journal of Physical Chemistry B*, 117(16):4553–4559, 2013.

[156] G.M. Akselrod, Y.R. Tischler, E.R. Young, D.G. Nocera, and V. Bulovic. Exciton-exciton annihilation in organic polariton microcavities. *Physical Review B*, 82:113106, 2010.

[157] Feng Zhu, Jianbing Yang, De Song, Chunhong Li, and Donghang Yan. Single-crystal-like organic heterojunction with 40 nm thick charge accumulation layers. *Applied Physics Letters*, 94(14):143305, 2009.

[158] Brent F. Howell and Mark G. Kuzyk. Amplified spontaneous emission and recoverable photodegradation in polymer doped with disperse orange 11. *Journal of the Optical Society of America B*, 19(8):1790–1793, 2002.

[159] Natnael B. Embaye, Shiva K. Ramini, and Mark G. Kuzyk. Mechanisms of reversible photodegradation in disperse orange 11 dye doped in PMMA polymer. *The Journal of Chemical Physics*, 129(5):054504, 2008.

[160] Benjamin Anderson, Shiva K. Ramini, and Mark G. Kuzyk. Imaging studies of photodamage and self-healing in disperse orange 11 dye-doped PMMA. *Journal of the Optical Society of America B*, 28(3):528–532, 2011.

[161] Gethin H. Richards, Krystyna E. Wilk, Paul M. Curmi, and Jeffrey A. Davis. Disentangling electronic and vibrational coherence in the phycocyanin-645 light-harvesting complex. In *19th International Conference on Ultrafast Phenomena*. Optical Society of America, 2014.

[162] Masoud Mohseni, Patrick Rebentrost, Seth Lloyd, and Alan Aspuru-Guzik. Environment-assisted quantum walks in photosynthetic energy transfer. *The Journal of Chemical Physics*, 129(17):174106, 2008.

[163] Michael A. Nielsen and Isaac L. Chuang. *Quantum Computation and Quantum Information*. Cambridge University Press, New York, NY, 2000.

[164] Joel Yuen-Zhou and Alan Aspuru-Guzik. Quantum process tomography of excitonic dimers from two-dimensional electronic spectroscopy. i. general theory and application to homodimers. *The Journal of Chemical Physics*, 134(13):134505, 2011.

[165] Joel Yuen-Zhou, Jacob J. Krich, Masoud Mohseni, and Alan Aspuru-Guzik. Quantum state and process tomography of energy transfer systems via ultrafast spectroscopy. *Proceedings of the National Academy of Sciences*, 108(43):17615–17620, 2011.

[166] Karl Blum. *Density Matrix Theory and Applications*. Springer-Verlag, New York, NY, 2012.

[167] Stephan Hoyer and K. Birgitta Whaley. Inverting pump-probe spectroscopy for state tomography of excitonic systems. *The Journal of Chemical Physics*, 138(16):164102, 2013.

[168] Travis S. Humble and Jeffrey A. Cina. Nonlinear wave-packet interferometry and molecular state reconstruction in a vibrating and rotating diatomic molecule. *The Journal of Physical Chemistry B*, 110(38):18879–18892, 2006.

[169] David Avisar and David J. Tannor. Complete reconstruction of the wave function of a reacting molecule by four-wave mixing spectroscopy. *Physical Review Letters*, 106:170405, 2011.

[170] Andrew M. Childs, Isaac L. Chuang, and Debbie W. Leung. Realization of quantum process tomography in NMR. *Physical Review A*, 64:012314, 2001.

[171] R.C. Bialczak, M. Ansmann, M. Hofheinz, E. Lucero, M. Neeley, A.D. O'Connell, D. Sank, H. Wang, J. Wenner, M. Steffen, A.N. Cleland, and J.M. Martinis. Quantum process tomography of a universal entangling gate implemented with Josephson phase qubits. *Nature Physics*, 6(6):409–413, 2010.

[172] M. Howard, J. Twamley, C. Wittmann, T. Gaebel, F. Jelezko, and J. Wrachtrup. Quantum process tomography and Linblad estimation of a solid-state qubit. *New Journal of Physics*, 8(3):33, 2006.

[173] M. Riebe, K. Kim, P. Schindler, T. Monz, P.O. Schmidt, T.K. Korber, W. Hansel, H. Haffner, C.F. Roos, and R. Blatt. Process tomography of ion trap quantum gates. *Physical Review Letters*, 97:220407, 2006.

[174] S.H. Myrskog, J.K. Fox, M.W. Mitchell, and A.M. Steinberg. Quantum process tomography on vibrational states of atoms in an optical lattice. *Physical Review A*, 72:013615, 2005.

[175] Joel Yuen-Zhou, Dylan H. Arias, Dorthe M. Eisele, Colby P. Steiner, Jacob J. Krich, Moungi G. Bawendi, Keith A. Nelson, and Alan Aspuru-Guzik. Coherent exciton dynamics in supramolecular light-harvesting nanotubes revealed by ultrafast quantum process tomography. *American Chemical Society Nanotechnology*, 8(6):5527–5534, 2014.

[176] Dorthe M. Eisele, Dylan H. Arias, Xiaofeng Fu, Erik A. Bloemsma, Colby P. Steiner, Russell A. Jensen, Patrick Rebentrost, Holger Eisele, Andrei Tokmakoff, Seth Lloyd, Keith A. Nelson, Daniela Nicastro, Jasper Knoester, and Moungi G. Bawendi. Robust excitons inhabit soft supramolecular nanotubes. *Proceedings of the National Academy of Sciences*, 111(33):E3367–E3375, 2014.

[177] Michael C. Grant and Stephen P. Boyd. Graph implementations for nonsmooth convex programs. In *Recent Advances in Learning and Control*, pages 95–110. Springer-Verlag, 2008.

[178] Michael C. Grant and Stephen P. Boyd. CVX: Matlab software for disciplined convex programming, version 1.21, 2011.

[179] R. Augulis, A. Pugzlys, and P.H.M. van Loosdrecht. Exciton dynamics in molecular aggregates. *Physica Status Solidi (c)*, 3(10):3400–3403, 2006.

[180] Jordan M. Womick, Stephen A. Miller, and Andrew M. Moran. Correlated exciton fluctuations in cylindrical molecular aggregates. *The Journal of Physical Chemistry B*, 113(19):6630–6639, 2009.

[181] Franz Milota, Valentyn I. Prokhorenko, Tomas Mancal, Hans von Berlepsch, Oliver Bixner, Harald F. Kauffmann, and Jurgen Hauer. Vibronic and vibrational coherences in two-dimensional electronic spectra of supramolecular J-aggregates. *The Journal of Physical Chemistry A*, 117(29):6007–6014, 2013.

[182] T. Kazimierczuk, D. Frohlich, S. Scheel, H. Stolz, and M. Bayer. Giant rydberg excitons in the copper oxide $Cu_2O$. *Nature*, 514(7522):343–347, 2014.

[183] S.A. Moskalenko and D.W. Snoke. *Bose-Einstein Condensation of Excitons and Biexcitons: And Coherent Nonlinear Optics with Excitons*. Cambridge University Press, New York, NY, 2000.

[184] D. Fishman, C. Faugeras, M. Potemski, A. Revcolevschi, and P.H.M. van Loosdrecht. Magneto-optical readout of dark exciton distribution in cuprous oxide. *Physical Review B*, 80:045208, 2009.

[185] D. Frohlich, A. Kulik, B. Uebbing, A. Mysyrowicz, V. Langer, H. Stolz, and W. von der Osten. Coherent propagation and quantum beats of quadrupole polaritons in $Cu_2O$. *Physical Review Letters*, 67:2343–2346, 1991.

[186] R.J. Elliott. Symmetry of excitons in $Cu_2O$. *Physical Review*, 124:340–345, 1961.

[187] Y. Petroff, P.Y. Yu, and Y.R. Shen. Study of photoluminescence in $Cu_2O$. *Physical Review B*, 12:2488–2495, 1975.

[188] Philip W. Baumeister. Optical absorption of cuprous oxide. *Physical Review*, 121:359–362, 1961.

[189] Peter Y. Yu and Y.R. Shen. Resonance Raman studies in $Cu_2O$. I. The phonon-assisted 1s yellow excitonic absorption edge. *Physical Review B*, 12:1377–1394, 1975.

[190] Oleksiy Roslyak, Upali Aparajita, Joseph L. Birman, and Shaul Mukamel. Coherent manipulation of quadrupole biexcitons in cuprous oxide by 2D femtosecond spectroscopy. *Physica Status Solidi (b)*, 249(3):435–447, 2012.

[191] E.F. Gorss and F.I. Kreingold. Biexcitons in $Cu_2O$ crystal. *Journal of Experimental and Theoretical Physics Letters*, 12(2):98–100, 1970.

[192] Y. Petroff, P.Y. Yu, and Y.R. Shen. Luminescence of $Cu_2O$-excitonic molecules, or not? *Physical Review Letters*, 29:1558–1562, 1972.

[193] J.I. Jang, Y. Sun, B. Watkins, and J.B. Ketterson. Bound excitons in $Cu_2O$: Efficient internal free exciton detector. *Physical Review B*, 74:235204, 2006.

[194] James P. Wolfe and Joon I. Jang. The search for Bose-Einstein condensation of excitons in $Cu_2O$: exciton-Auger recombination versus biexciton formation. *New Journal of Physics*, 16(12):123048, 2014.

[195] Kosuke Yoshioka, Eunmi Chae, and Makoto Kuwata-Gonokami. Transition to a Bose-Einstein condensate and relaxation explosion of excitons at sub-Kelvin temperatures. *Nature Communications*, 2:328, 2011.

[196] K.E. O'Hara and J.P. Wolfe. Relaxation kinetics of excitons in cuprous oxide. *Physical Review B*, 62:12909–12922, 2000.

[197] Kosuke Yoshioka, Yusuke Morita, Kenta Fukuoka, and Makoto Kuwata-Gonokami. Generation of ultracold paraexcitons in cuprous oxide: A path toward a stable Bose-Einstein condensate. *Physical Review B*, 88:041201, 2013.

[198] Nobuko Naka, Ikuko Akimoto, and Masanobu Shirai. Free-carrier generation by two-photon resonant excitation to the excitonic states in cuprous oxide. *Physica Status Solidi (b)*, 250(9):1773–1776, 2013.

[199] S. Sobkowiak, D. Semkat, and H. Stolz. Hydrodynamic description of trapped ultracold paraexcitons in $Cu_2O$. *Physical Review B*, 91:075209, 2015.

[200] S. Denev and D.W. Snoke. Stress dependence of exciton relaxation processes in $Cu_2O$. *Physical Review B*, 65:085211, 2002.

[201] J.I. Jang and J.P. Wolfe. Exciton decay in $Cu_2O$ at high density and low temperature: Auger recombination, spin-flip scattering, and molecule formation. *Solid State Communications*, 137(1-2):91–96, 2006.

[202] Heinrich Stolz, Rico Schwartz, Frank Kieseling, Sunipa Som, Maria Kaupsch, Siegfried Sobkowiak, Dirk Semkat, Nobuko Naka, Thomas Koch, and Holger Fehske. Condensation of excitons in $Cu_2O$ at ultracold temperatures: experiment and theory. *New Journal of Physics*, 14(10):105007, 2012.

[203] N. Laszlo Frazer, Richard D. Schaller, and J.B. Ketterson. Unexpectedly slow two particle decay of ultra-dense excitons in cuprous oxide. *Solid State Communications*, 170:34–38, 2013.

[204] G.M. Kavoulakis and Gordon Baym. Auger decay of degenerate and Bose-condensed excitons in $Cu_2O$. *Physical Review B*, 54:16625–16636, 1996.

[205] J.T. Warren, K.E. O'Hara, and J.P. Wolfe. Two-body decay of thermalized excitons in $Cu_2O$. *Physical Review B*, 61:8215–8223, 2000.

[206] J.I. Jang and J.P. Wolfe. Auger recombination and biexcitons in $Cu_2O$: A case for dark excitonic matter. *Physical Review B*, 74:045211, 2006.

[207] A. Jolk, M. Jorger, and C. Klingshirn. Exciton lifetime, Auger recombination, and exciton transport by calibrated differential absorption spectroscopy in $Cu_2O$. *Physical Review B*, 65:245209, 2002.

[208] K.E. O'Hara, J.R. Gullingsrud, and J.P. Wolfe. Auger decay of excitons in $Cu_2O$. *Physical Review B*, 60:10872–10885, 1999.

[209] Rico Schwartz, Nobuko Naka, Frank Kieseling, and Heinrich Stolz. Dynamics of excitons in a potential trap at ultra-low temperatures: paraexcitons in $Cu_2O$. *New Journal of Physics*, 14(2):023054, 2012.

[210] Kosuke Yoshioka, Takuro Ideguchi, Andre Mysyrowicz, and Makoto Kuwata-Gonokami. Quantum inelastic collisions between paraexcitons in $Cu_2O$. *Physical Review B*, 82:041201, 2010.

[211] J.I. Jang and J.B. Ketterson. Suppression of molecule formation for orthoexciton-polaritons in $Cu_2O$. *Solid State Communications*, 146(3-4):128–132, 2008.

[212] S. Mani, J.I. Jang, and J.B. Ketterson. Nonlinear optical processes at quadrupole polariton resonance in $Cu_2O$ as probed by a Z-scan technique. *Physical Review B*, 82:113203, 2010.

[213] Kelvin B. Chang, Laszlo Frazer, Johanna J. Schwartz, John B. Ketterson, and Kenneth R. Poeppelmeier. Removal of copper vacancies in cuprous oxide single crystals grown by the floating zone method. *Crystal Growth and Design*, 13(11):4914–4922, 2013.

[214] Laszlo Frazer, Erik J. Lenferink, Kelvin B. Chang, Kenneth R. Poeppelmeier, Nathaniel P. Stern, and John B. Ketterson. Evaluation of defects in cuprous oxide through exciton luminescence imaging. *Journal of Luminescence*, 159:294–302, 2015.

[215] Laszlo Frazer, Kelvin B. Chang, Kenneth R. Poeppelmeier, and John B. Ketterson. Cupric oxide inclusions in cuprous oxide crystals grown by the floating zone method. *Science and Technology of Advanced Materials*, 16(3):034901, 2015.

[216] A.I. Bobrysheva and S.A. Moskalenko. Biexcitons in crystals with large ortho-para-exciton splitting. *Physica Status Solidi (b)*, 119(1):141–146, 1983.

[217] Wei-Teh Huang. Binding energy of excitonic molecules in isotropic semiconductors. *Physica Status Solidi (b)*, 60(1):309–317, 1973.

[218] Aaron L. Stancik and Eric B. Brauns. A simple asymmetric lineshape for fitting infrared absorption spectra. *Vibrational Spectroscopy*, 47(1):66–69, 2008.

[219] Tadashi Itoh and Shinichiro Narita. Study of absorption spectra of excitons in $Cu_2O$ by wavelength modulation technique. *Journal of the Physical Society of Japan*, 39(1):132–139, 1975.

[220] Dattatray J. Late. Temperature dependent phonon shifts in few-layer black phosphorus. *American Chemical Society Applied Materials and Interfaces*, 7(10):5857–5862, 2015.

[221] Thripuranthaka M and Dattatray J. Late. Temperature dependent phonon shifts in single-layer $WS_2$. *American Chemical Society Applied Materials and Interfaces*, 6(2):1558–1163, 2014.

[222] K.S. Novoselov, D. Jiang, F. Schedin, T.J. Booth, V.V. Khotkevich, S.V. Morozov, and A.K. Geim. Two-dimensional atomic crystals. *Proceedings of the National Academy of Sciences*, 102(30):10451–10453, 2005.

[223] Yi-Hsien Lee, Xin-Quan Zhang, Wenjing Zhang, Mu-Tung Chang, Cheng-Te Lin, Kai-Di Chang, Ya-Chu Yu, Jacob Tse-Wei Wang, Chia-Seng Chang, Lain-Jong Li, and Tsung-Wu Lin. Synthesis of large-area $MoS_2$ atomic layers with chemical vapor deposition. *Advanced Materials*, 24(17):2320–2325, 2012.

[224] A. Kuc, N. Zibouche, and T. Heine. Influence of quantum confinement on the electronic structure of the transition metal sulfide $TS_2$. *Physical Review B*, 83:245213, 2011.

[225] Z.Y. Zhu, Y.C. Cheng, and U. Schwingenschlogl. Giant spin-orbit-induced spin splitting in two-dimensional transition-metal dichalcogenide semiconductors. *Physical Review B*, 84:153402, 2011.

[226] K. Kosmider, J.W. Gonzalez, and J. Fernandez-Rossier. Large spin splitting in the conduction band of transition metal dichalcogenide monolayers. *Physical Review B*, 88:245436, 2013.

[227] Kin Fai Mak, Keliang He, Jie Shan, and Tony F. Heinz. Control of valley polarization in monolayer $MoS_2$ by optical helicity. *Nature Nanotechnology*, 7(8):494–498, 2012.

[228] Hualing Zeng, Junfeng Dai, Wang Yao, Di Xiao, and Xiaodong Cui. Valley polarization in $MoS_2$ monolayers by optical pumping. *Nature Nanotechnology*, 7(8):490–493, 2012.

[229] Ting Cao, Gang Wang, Wenpeng Han, Huiqi Ye, Chuanrui Zhu, Junren Shi, Qian Niu, Pingheng Tan, Enge Wang, Baoli Liu, and Ji Feng. Valley-selective circular dichroism of monolayer molybdenum disulphide. *Nature Communications*, 3:887, 2012.

[230] Ashwin Ramasubramaniam. Large excitonic effects in monolayers of molybdenum and tungsten dichalcogenides. *Physical Review B*, 86:115409, 2012.

[231] Cong Mai, Andrew Barrette, Yifei Yu, Yuriy G. Semenov, Ki Wook Kim, Linyou Cao, and Kenan Gundogdu. Many-body effects in valleytronics: Direct measurement of valley lifetimes in single-layer $MoS_2$. *Nano Letters*, 14(1):202–206, 2014.

[232] Bairen Zhu, Xi Chen, and Xiaodong Cui. Exciton binding energy of monolayer $WS_2$. *Scientific Reports*, 5:9218, 2015.

[233] AA. Mitioglu, P. Plochocka, J.N. Jadczak, W. Escoffier, G.L.J.A. Rikken, L. Kulyuk, and D.K. Maude. Optical manipulation of the exciton charge state in single-layer tungsten disulfide. *Physical Review B*, 88:245403, 2013.

[234] Gerd Plechinger, Philipp Nagler, Julia Kraus, Nicola Paradiso, Christoph Strunk, Christian Schuller, and Tobias Korn. Identification of excitons, trions and biexcitons in single-layer $WS_2$. *Physica Status Solidi Rapid Research Letters (RRL)*, 9(8):457–461, 2015.

[235] Chih-Hsiang Lin, J.M. Meese, M.L. Wroge, and Chun-Jen Weng. Effect of GaAs/AlGaAs quantum-well structure on refractive index. *IEEE Photonics Technology Letters*, 6:623–625, 1994.

[236] D.A.B. Miller, D.S. Chemla, T.C. Damen, A.C. Gossard, W. Wiegmann, T.H. Wood, and C.A. Burrus. Band-edge electroabsorption in quantum well structures: The quantum-confined stark effect. *Physical Review Letters*, 53:2173–2176, 1984.

[237] Axel Esser, Erich Runge, Roland Zimmermann, and Wolfgang Langbein. Photoluminescence and radiative lifetime of trions in GaAs quantum wells. *Physical Review B*, 62:8232–8239, 2000.

[238] Timothy C. Berkelbach, Mark S. Hybertsen, and David R. Reichman. Theory of neutral and charged excitons in monolayer transition metal dichalcogenides. *Physical Review B*, 88:045318, 2013.

[239] Branimir Radisavljevic and Andras Kis. Mobility engineering and a metal-insulator transition in monolayer $MoS_2$. *Nature Materials*, 12(9):815–820, 2013.

[240] R. de L. Kronig. On the theory of dispersion of x-rays. *Journal of the Optical Society of America*, 12(6):547–557, 1926.

[241] George B. Arfken, Hans J. Weber, and Frank E. Harris. *Mathematical methods for physicists: a comprehensive guide*. Academic Press, Waltham, MA, 2013.

[242] U. Bockelmann and G. Bastard. Phonon scattering and energy relaxation in two-, one-, and zero-dimensional electron gases. *Physical Review B*, 42:8947–8951, 1990.

[243] B.K. Ridley. The electron-phonon interaction in quasi-two-dimensional semiconductor quantum-well structures. *Journal of Physics C: Solid State Physics*, 15(28):5899, 1982.

[244] S. Piscanec, M. Lazzeri, Francesco Mauri, A.C. Ferrari, and J. Robertson. Kohn anomalies and electron-phonon interactions in graphite. *Physical Review Letters*, 93:185503, 2004.

[245] A.C. Ferrari, J.C. Meyer, V. Scardaci, C. Casiraghi, M. Lazzeri, F. Mauri, S. Piscanec, D. Jiang, K.S. Novoselov, S. Roth, and A.K. Geim. Raman spectrum of graphene and graphene layers. *Physical Review Letters*, 97:187401, 2006.

[246] Wu Zhou, Xiaolong Zou, Sina Najmaei, Zheng Liu, Yumeng Shi, Jing Kong, Jun Lou, Pulickel M. Ajayan, Boris I. Yakobson, and Juan-Carlos Idrobo. Intrinsic structural defects in monolayer molybdenum disulfide. *Nano Letters*, 13(6):2615–2622, 2013.

[247] Wenjuan Zhu, Tony Low, Yi-Hsien Lee, Han Wang, Damon B. Farmer, Jing Kong, Fengnian Xia, and Phaedon Avouris. Electronic transport and device prospects of monolayer molybdenum disulphide grown by chemical vapour deposition. *Nature Communications*, 5:3087, 2014.

[248] Yumeng You, Xiao-Xiao Zhang, Timothy C. Berkelbach, Mark S. Hybertsen, David R. Reichman, and Tony F. Heinz. Observation of biexcitons in monolayer $WSe_2$. *Nature Physics*, 11(6):477–481, 2015.

[249] Jonathan E. Halpert, Jonathan R. Tischler, Gautham Nair, Brian J. Walker, Wenhao Liu, Vladimir Bulovic, and Moungi G. Bawendi. Electrostatic formation of quantum dot/J-aggregate FRET pairs in solution. *The Journal of Physical Chemistry C*, 113(23):9986–9992, 2009.

[250] Brian J. Walker, Vladimir Bulovic, and Moungi G. Bawendi. Quantum dot/J-aggregate blended films for light harvesting and energy transfer. *Nano Letters*, 10(10):3995–3999, 2010.

[251] Brian J. Walker, August Dorn, Vladimir Bulovic, and Moungi G. Bawendi. Color-selective photocurrent enhancement in coupled J-aggregate/nanowires formed in solution. *Nano Letters*, 11(7):2655–2659, 2011.

[252] Julian Burschka, Norman Pellet, Soo-Jin Moon, Robin Humphry-Baker, Peng Gao, Mohammad K. Nazeeruddin, and Michael Gratzel. Sequential deposition as a route to high-performance perovskite-sensitized solar cells. *Nature*, 499(7458):316–319, 2013.

[253] Mingzhen Liu, Michael B. Johnston, and Henry J. Snaith. Efficient planar heterojunction perovskite solar cells by vapour deposition. *Nature*, 501(7467):395–398, 2013.

[254] Son Tung Ha, Xinfeng Liu, Qing Zhang, David Giovanni, Tze Chien Sum, and Qihua Xiong. Synthesis of organic-inorganic lead halide perovskite nanoplatelets: Towards high-performance perovskite solar cells and optoelectronic devices. *Advanced Optical Materials*, 2(9):838–844, 2014.

[255] Kevin G. Stamplecoskie, Joseph S. Manser, and Prashant V. Kamat. Dual nature of the excited state in organic-inorganic lead halide perovskites. *Energy and Environmental Science*, 8:208–215, 2015.

[256] Gleb M. Akselrod, Parag B. Deotare, Nicholas J. Thompson, Jiye Lee, William A. Tisdale, Marc A. Baldo, Vinod M. Menon, and Vladimir Bulovic. Visualization of exciton transport in ordered and disordered molecular solids. *Nature Communications*, 5:3646, 2014.